INSTITUTO
UNIVERSITÁRIO
DE LISBOA

Design of Terahertz Transceiver Schemes for Ultrahigh-Speed Wireless Communications

João Pedro Calado Barradas Branco Pavia

PhD in Information Science and Technology, specialization in Telecommunications and Networks

Supervisors:

Doctor Marco Alexandre dos Santos Ribeiro, Assistant Professor,
Iscte - Instituto Universitário de Lisboa

Doctor Nuno Manuel Branco Souto, Associate Professor (with Habilitation),
Iscte - Instituto Universitário de Lisboa

May, 2022

TECNOLOGIAS
E ARQUITETURA

Department of Information Science and Technology

Design of Terahertz Transceiver Schemes for Ultrahigh-Speed Wireless Communications

João Pedro Calado Barradas Branco Pavia

PhD in Information Science and Technology, specialization in Telecommunications and Networks

Supervisors:
Doctor Marco Alexandre dos Santos Ribeiro, Assistant Professor,
Iscte - Instituto Universitário de Lisboa

Doctor Nuno Manuel Branco Souto, Associate Professor (with Habilitation),
Iscte - Instituto Universitário de Lisboa

May, 2022

TECNOLOGIAS
E ARQUITETURA

Department of Information Science and Technology

Design of Terahertz Transceiver Schemes for Ultrahigh-Speed Wireless Communications

João Pedro Calado Barradas Branco Pavia

PhD in Information Science and Technology, specialization in Telecommunications and Networks

Jury:
Doctor Sara Eloy, Assistant Professor, Iscte-Instituto Universitário de Lisboa (President)
Doctor Adão Paulo Soares da Silva, Associate Professor, Universidade de Aveiro
Doctor Rui Miguel Henriques Dias Morgado Dinis, Associate Professor (with Habilitation), Faculdade de Ciências e Tecnologia - Universidade Nova de Lisboa
Doctor Francisco António Bucho Cercas, Full Professor, Iscte - Instituto Universitário de Lisboa
Doctor Nuno Manuel Branco Souto, Associate Professor (with Habilitation), Iscte-Instituto Universitário de Lisboa

May, 2022

"Learn from yesterday, live for today, hope for tomorrow. The important thing is not to stop questioning."

Albert Einstein

Acknowledgments

My greater acknowledgement is for Professor Nuno Souto and Professor Marco Ribeiro for giving me the opportunity of developing this thesis as my research mentors, and for their continuous advice on different subject matters, such as communications schemes, signal processing, metamaterials, experimental work tips and many others. They provided me with all the required conditions to develop this work and their contributions augmented the value of this thesis. I want to thank Professor Américo Correia, Professor Rui Dinis and Professor Pedro Sebastião for the collaboration opportunities, for their teachings, and for challenging me to put into practice the work I have been developing over the years. I would also like to leave a word of appreciation to the administrative staff of Iscte - Instituto Universitário de Lisboa and Instituto de Telecomunicações that made many unavoidable burocracies so much easier to handle. Sometimes, the PhD journey can be a lonely one, but it was also thanks to my colleagues and friends of the radio systems research group that I always felt supported and encouraged throughout this experience. Their personal opinions and helpful advices increased this thesis' value on various aspects.

From a personal perspective, my first acknowledgement goes to my family, I would like to express my gratitude for their continuous support, confidence, love and for encouraging me to follow my dreams. Who I am today and what I have accomplished is only a consequence of all they have given and taught me. I also want to pay a heartfelt tribute to those who already passed away, but who have always believed in me and motivated me to go further. I have no doubt that wherever they are, they will surely be proud of my path. To my beautiful girlfriend for her love, comprehension, motivation and for believing and being there for me every day. To all my closest friends, who were always present during my entire path. Their support made me feel more confident and more committed so as not to disappoint all those around me.

Finally, I would also like to acknowledge the financial support of Iscte - Instituto Universitário de Lisboa, since they provided me my first funding through their merit scholarship programme when I applied for the doctoral program in 2019 (ISTA-BM-PDCTI-2019). I must also acknowledge the financial support of Fundação para a Ciência e Tecnologia, under the doctoral grant 2020.05621.BD, which allowed me to focus on my research until I finished this cycle of studies.

Abstract

Future ultra-high-speed wireless communication systems face difficult challenges due to the fundamental limitations of current technologies operating at microwave frequencies. Supporting high transmission rates will require the use of more spectral resources that are only available at higher frequencies. Within this context, terahertz (THz) communications have been attracting more and more attention, being considered by the research community as one of the most promising research fields on the topic due to the availability of extensive unused bandwidth segments. However, its widespread use is not yet possible due to some obstacles, such as the high propagation losses that occur in this band and the difficulty in designing devices that can effectively perform both transmission and detection tasks.

The purpose of this dissertation is to contribute for the solution of both of the aforementioned problems and to propose novel THz transceiver schemes for ultra-high-speed wireless communications. Three main research areas were addressed: device modelling for the THz; index modulation (IM) based schemes for Beyond 5G (B5G) networks and hybrid precoding designs for THz ultra massive (UM) – multiple input multiple output (MIMO) systems. The main contributions of this work include the creation of a new design for a reconfigurable THz filter; the proposal of a precoded generalized spatial modulation scheme for downlink MIMO transmissions in B5G networks; the creation of a low-complexity hybrid design algorithm with a near fully-digital performance for multiuser (MU) mmWave/THz ultra massive MIMO systems that can incorporate different analog architectures; and the system-level assessment of cloud radio access network (C-RAN) deployments based on low-complexity hybrid precoding designs for massive MIMO downlink transmissions in B5G networks. The first contribution is especially suited for the implementation of reconfigurable THz filters and optical modulators, since it is based on a simple design, which transits from situations in which it presents a full transparency to situations where it achieves full opacity. Moreover, this approach can also be used for the implementation of simultaneously transmitting and reflecting (STAR) reconfigurable intelligent surfaces (RIS) which are important for enabling flexible system designs in RIS-assisted networks. The second contribution showed that the implementation of precoding schemes based on generalised spatial modulations is a solution with a considerable potential for future B5G systems, since it can provide larger throughputs when compared to conventional MU-MIMO

schemes with identical spectral efficiencies.The last two contributions showed that through the proposed hybrid design algorithm it becomes possible to replace a fully digital precoder/combiner by a fully-connected or even by a partially-connected architecture (array of subarrays and dynamic array of subarrays), while achieving good tradeoffs between spectral efficiency, power consumption and implementation complexity. These proposals are particularly relevant for the support of UM-MIMO in severely hardware constrained THz systems. Moreover, the capability of achieving significant improvements in terms of throughput performance and coverage over typical cellular networks, when considering hybrid precoding-based C-RAN deployments in two indoor office scenarios at the THz band, was demonstrated.

Keywords: Frequency Selective Surfaces; Filters; Terahertz; Generalized Spatial Modulation, Hybrid Precoding; Ultra-Massive MIMO; B5G; 6G.

Resumo

Os futuros sistemas de comunicação sem fios de velocidade ultra-elevada enfrentam desafios difíceis devido às limitações fundamentais das tecnologias atuais que funcionam a frequências de microondas. O suporte de taxas de transmissão altas exigirá a utilização de mais recursos espectrais que só estão disponíveis em frequências mais elevadas. A banda Terahertz (THz) é uma das soluções mais promissoras devido às suas enormes larguras de banda disponíveis no espectro eletromagnético. No entanto, a sua utilização generalizada ainda não é possível devido a alguns obstáculos, tais como as elevadas perdas de propagação que se verificam nesta banda e a dificuldade em conceber dispositivos que possam desempenhar eficazmente as tarefas de transmissão e deteção.

O objetivo desta tese de doutoramento, é contribuir para ambos os problemas mencionados anteriormente e propor novos esquemas de transcetores THz para comunicações sem fios de velocidade ultra-elevada. Três grandes áreas de investigação foram endereçadas, contribuindo individualmente para um todo: a modelação do dispositivo para o THz; esquemas baseados em modulações de índice (IM) para redes pós-5G (B5G) e desenhos de pré-codificadores híbridos para sistemas THz MIMO ultra-massivos. As principais contribuições deste trabalho incluem a criação de um novo design para um filtro THz reconfigurável; a proposta de uma nova tipologia de modulação espacial generalizada pré-codificada para transmissões MIMO de ligação descendente para redes B5G; a criação de um algoritmo de design híbrido de baixa complexidade com desempenho quase totalmente digital para sistemas MIMO multi-utilizador (MU) mmWave/THz ultra massivos que podem incorporar diferentes arquiteturas analógicas e a avaliação das implementações da rede de acesso de rádio na nuvem (C-RAN) com base em designs de pré-codificação híbridos de baixa complexidade para transmissões MIMO de ligação descendente massivas em redes B5G. A primeira contribuição é especialmente adequada para a implementação de filtros THz reconfiguráveis e moduladores óticos, uma vez que se baseia numa concepção mais simples, que transita de situações em que apresenta uma transparência total para situações em que atinge uma opacidade total. Para além disso, esta abordagem também pode ser utilizada para a implementação de superfícies inteligentes reconfiguráveis (RIS) de transmissão e reflexão simultânea (STAR). A segunda contribuição mostrou que a implementação de esquemas de pré-codificação baseados em modulações espaciais generalizadas é uma solução com um potencial considerável para futuros sistemas B5G, uma vez que permite alcançar maiores

ganhos em termos de débito binário quando comparado com esquemas convencionais MU-MIMO com eficiências espectrais idênticas. As duas últimas contribuições mostraram que através do algoritmo proposto torna-se possível substituir a utilização de uma arquitectura totalmente digital por uma arquitetura totalmente conectada ou mesmo por uma arquitetura parcialmente conectada (arrays de subarrays e arrays dinâmicos de subarrays), conseguindo-se bons *tradeoffs* entre eficiência espectral, consumo de energia e complexidade de implementação. Estas propostas são particularmente relevantes para dar suporte a sistemas THz UM-MIMO com restrições severas ao nível de hardware. Demonstrou-se também a capacidade de se alcançar melhorias significativas em termos de débito binário e cobertura em relação a redes celulares típicas, considerando dois cenários na banda THz.

Palavras-Chave: Superfícies Seletivas na Frequência; Filtros; Terahertz; Modulação Espacial Generalizada, Pré-Codificação Híbrida; MIMO Ultra-massivo; B5G; 6G.

Contents

Acknowledgments……. i

Abstract……. ii

Resumo…….. iv

Contents……. vi

Listo of Figures……. vii

List of Tables……. x

List of Acronyms……... xi

List of Symbols…….. xv

Chapter 1 – Introduction…….. 18

1.1. Motivation and Scope……. 18

1.2. Goals…… 22

1.3. Contributions of Research……. 23

1.4. Thesis Overview…….. 27

1.4.1. Devices for the THz……. 27

1.4.2. Index Modulations…….. 28

1.4.3. Hybrid Precoding Designs for the THz……. 31

Chapter 2 – Design of a Reconfigurable THz Filter Based on Metamaterial Wire Resonators with Applications on Sensor Devices…….. 34

Chapter 3 – Precoded Generalized Spatial Modulation for Downlink MIMO Transmissions in Beyond 5G Networks…….. 53

Chapter 4 – Low Complexity Hybrid Precoding Designs for Multiuser mmWave/THz Ultra Massive MIMO Systems……... 71

Chapter 5 – System-Level Assessment of Low Complexity Hybrid Precoding Designs for Downlink MIMO Transmissions for Beyond 5G…… 96

Chapter 6 – Conclusions and Future Work…… 116

6.1. Summary……. 116

6.2. Future Work……... 118

References……. 120

List of Figures

Figure 1.1 – Summary Activities…… 23
Figure 2.1 – Overview of the working principle of the proposed reconfigurable filter…… 37
Figure 2.2 – Equivalent microwave network circuit of the terahertz (THz) filter. 37
Figure 2.3 – Reflection and transmission from an array of wires…….. 38
Figure 2.4 – Scheme of the magnetic circuit to be modeled on a finite element method magnetics (FEMM) solver……. 42
Figure 2.5 – Return loss in the frequency domain as a function of applied compression for high-density polyethylene (HDPE) host medium…… 43
Figure 2.6 – Insertion loss in the frequency domain as a function of applied compression for HDPE host medium……. 44
Figure 2.7 – Return loss in the frequency domain as a function of applied compression for polytetrafluoroethylene (PTFE) host medium……. 45
Figure 2.8 – Insertion loss in the frequency domain as a function of applied compression for PTFE host medium…….. 45
Figure 2.9 – Reduction in the distance between wires as a function of applied force and current for 10, 30, 50 and 70 wires and a filter assembled with HDPE. 46
Figure 2.10 – Reduction in the distance between wires as a function of applied current for 10, 30, 50 and 70 wires and a device assembled with HDPE…….. 46
Figure 2.11 – Reduction in the distance between wires as a function of applied force and current for 10, 30, 50 and 70 wires and a filter assembled with PTFE.. 47
Figure 2.12 – Reduction in the distance between wires as a function of applied current for 10, 30, 50 and 70 wires and a device assembled with PTFE…… 47
Figure 2.13 – Reflectance as a function of applied force for 10, 30, 50 and 70 wires and a filter assembled with HDPE…… 48
Figure 2.14 – Transmittance as a function of applied force for 10, 30, 50 and 70 wires and a filter assembled with HDPE…… 48
Figure 2.15 – Reflectance as a function of applied force for 10, 30, 50 and 70 wires and a filter assembled with PTFE……. 49
Figure 2.16 – Transmittance as a function of applied force for 10, 30, 50 and 70 wires and a filter assembled with PTFE……. 50
Figure 3.1 – Transmitter and receiver scheme……... 58
Figure 3.2 – Equivalent microwave network circuit of the terahertz (THz) filter. Cloud radio access network (C-RAN) considered for the system level simulations. RRU = radio remote unit…… 61
Figure 3.3 – Bit error rate (BER) performance of ADMM in a MU-MIMO scenario with N_{tx} = 255, N_{rx} = 10, N_u = 15, N_s = 17 and N_a = 2, 256-QAM……... 62
Figure 3.4 – BER performance of ADMM in a MU-MIMO scenario with N_{tx} = 255, N_{rx} = 10, N_u = 15, N_s = 17 and N_a = 2, 1024-QAM…… 62
Figure 3.5 – BER performance of a precoder based on GSM MU-MIMO and a precoder based on conventional MU-MIMO……. 63
Figure 3.6 – Block error rate (BLER) vs. E_s/N_0 for N_a=2, N_{sc}=256, N_u=15, N_{tx}=17 antennas/user, and N_{rx}=16 antennas/user…… 64
Figure 3.7 – Perfect and imperfect estimation of BLER vs. E_s/N_0 for N_a=3, N_{sc}=256, N_u=15, N_{tx}=17 antennas/user, and N_{rx}=16 antennas/user…….. 64
Figure 3.8 – Coverage vs percentage of transmitted power for N_a=2, N_{sc}=256, N_u=15, N_{tx}=17 antennas/user and N_{rx}=16 antennas/user……. 65

Figure 3.9 – Average throughput vs percentage of transmitted power for N_a=2, N_{sc}=256, N_u=15, N_{tx}=17 antennas/user and N_{rx}=16 antennas/user……... 66
Figure 3.10 – Average throughput vs number of users for N_{sc}=256, N_{tx}=17 antennas/user and N_{rx}=16 antennas/user with perfect channel estimation……... 67
Figure 3.11 – Average throughput vs number of users for N_{sc}=256, N_{tx}=17 antennas/user, and N_{rx}=16 antennas/user with imperfect channel estimation…….. 67
Figure 3.12 – CDF of throughput for 100% transmitted power for N_a=2, N_{sc}=256, N_u=15, N_{tx}=17 antennas/user, and N_{rx}=16 antennas/user…… 68
Figure 4.1 – A multiuser OFDM mmWave/THz MIMO system with hybrid precoding……..... 77
Figure 4.2 – Different precoder architectures for a mmWave/THz MIMO system based on phase shifters ……... 82
Figure 4.3 – Alternative implementations to single phase shifters based on array-of-subarrays for a mmWave/THz MIMO system……... 83
Figure 4.4 – Spectral efficiency versus SNR achieved by different methods with N_u=4, N_s=1, N_{RF}^{tx}=4, F=1, N_{tx}=100 and N_{rx}=4 (only NLOS)……. 86
Figure 4.5 – Spectral efficiency versus SNR achieved by different methods with N_u=4, N_s=1, N_{RF}^{tx}=8, F=64, N_{tx}=100 and N_{rx}=4 (only NLOS)……... 87
Figure 4.6 – Spectral efficiency versus SNR achieved by different methods with N_u=2, N_s=2, N_{RF}^{tx}=4, F=64, N_{tx}=256 and N_{rx}=4 (with LOS component)……... 88
Figure 4.7 – Spectral efficiency versus SNR achieved by the proposed precoder using different fully-connected architectures for N_u=4, N_s=2, N_{RF}^{tx}=8, F=1, N_{tx}=256 and N_{rx}=4 (only NLOS)……. 88
Figure 4.8 – Spectral efficiency versus SNR achieved by the proposed precoder using different AoSA architectures with L_{max} = 1, N_u=4, N_s=2, N_{RF}^{tx}=8, F=1, N_{tx}=256 and N_{rx}=4 (with LOS component)……. 89
Figure 4.9 – Spectral efficiency versus SNR achieved by the proposed precoder considering an architecture based on DAoSAs and the variation of the maximum number of subarrays that can be connected to an RF chain (L_{max}) for N_u=4, N_s=2, N_{RF}^{tx}=8, F=1, N_{tx}=256 and N_{rx}=4 (with LOS component)……... 90
Figure 4.10 – Spectral efficiency versus SNR achieved by the proposed precoder and by the EBE algorithm considering an architecture based on DAoSAs and the variation of the maximum number of subarrays that can be connected to an RF chain (L_{max}) for N_u=1, N_s=2, N_{RF}^{tx}=8, F=1, N_{tx}=256 and Nrx=4 (with LOS component)……..... 91
Figure 4.11 – Spectral efficiency versus SNR achieved by the proposed precoder and by the EBE algorithm considering an architecture based on DAoSAs and the variation of the maximum number of subarrays that can be connected to an RF chain (L_{max}) for a mmWave/THz system with N_u=4, N_s=2, N_{RF}^{tx} =8, F=1, N_{tx}=256 and N_{rx}=4 (with LOS component)……... 92
Figure 4.12 – Spectral efficiency versus SNR achieved by different methods for a mmWave/THz MIMO-OFDM system with N_u=4, N_s=1, N_{RF}^{tx}=4, F=1, N_{tx}=100 and N_{rx}=4 considering an uncorrelated channel…….. 92
Figure 5.1 – Transmitter and receiver structure of a multiuser OFDM mmWave/THz MIMO system with hybrid precoding for an InD scenario……..... 102
Figure 5.2 – Different precoder architectures for a mmWave/THz MIMO system based on phase shifters……..... 103
Figure 5.3 – Indoor Office scenario layout……. 105

Figure 5.4 – BER performance versus SNR achieved by different methods by changing the number of subcar-riers and considering a system with N_{tx}=100, N_{rx}=4, N_{RF}^{tx}=12, N_u=4 and Ns=2 (only NLOS component)…… 106
Figure 5.5 – BER performance versus SNR achieved by the proposed precoder with N_{tx}=256, N_{rx}=4, N_u=4, and N_s=2, by changing the number of subcarriers and the number of RF chains (only NLOS component)……..... 106
Figure 5.6 – BER performance versus SNR achieved by the proposed precoder with N_{tx}=256, N_{rx}=4, N_u=4, N_{RF}^{tx}=14, F=828 and N_s=2, considering several versions of the algorithm (only NLOS component)……..... 107
Figure 5.7 – Throughput (Gbps) vs number of users for different methods with N_{tx}=100, N_{rx}=4, N_{RF}^{tx}=12 and N_s=2, by changing the number of subcarriers (only NLOS component)…….. 108
Figure 5.8 – Throughput (Gbps) vs number of users for different number of subcarriers, RF chains and cluster sizes, considering the proposed precoder with N_{tx}=256, N_{rx}=4 and N_s=2 (only NLOS component)……. 109
Figure 5.9 – Throughput (Gbps) vs number of subcarriers for different versions of the algorithm (SPS and DPS) and cluster sizes, considering the proposed precoder with N_{tx}=256, N_{rx}=4, N_{RF}^{tx}=14, N_s=2 and N_u=180 (with LOS component)……. 109
Figure 5.10 – Throughput (Gbps) vs number of subcarriers for different versions of the algorithm (with and without quatization) and cluster sizes, considering the proposed precoder with N_{tx}=256, N_{rx}=4, N_{RF}^{tx}=14, N_s=2 and N_u=180 (only NLOS component)……. 110
Figure 5.11 – Throughput (Mbps) versus mean value of power required by each user (mW), considering the proposed precoder with N_{tx}=256, N_{rx}=4, N_{RF}^{tx}=14, N_s=2, F=828 and the quantization effect (with LOS component)…….. 111
Figure 4.12 – Coverage (%) versus mean value of power required by each user (mW), considering the proposed precoder with N_{tx}=256, N_{rx}=4, N_{RF}^{tx}=14, N_s=2, F=828 and the quantization effect (with LOS component)……. 111
Figure 5.13 – Throughput (Gbps) vs number of subcarriers for different versions of the algorithm (SPS or DPS) as a function of L_{max}, considering the proposed precoder with N_{tx}=256, N_{rx}=4, N_{RF}^{tx}=14, N_s=2 and N_u=180 (with LOS component) and 1C……. 112
Figure 5.14 – Throughput (Gbps) vs number of subcarriers for different versions of the algorithm (SPS or DPS) as a function of L_{max}, considering the proposed precoder with N_{tx}=256, N_{rx}=4, N_{RF}^{tx}=14, N_s=2 and N_u=180 (with LOS component) and 3C……. 113

List of Tables

Table 1.1 – Timeline of contributions…… 24
Table 2.1 – Simulation parameters of the materials of the proposed filter…… 42
Table 2.2 – Simulation parameters of the magnetic circuit in FEMM……... 42
Table 2.3 – Filter quality and performance parameters considering a distance between wires d = 17.5 µm…… 48
Table 2.4 – Calculation of the sensitivity of the filter considering a distance between wires d = 17.5 µm…… 49
Table 2.5 – Filter quality and performance parameters considering a distance between wires d = 18.5 µm…… 50
Table 2.6 – Calculation of the sensitivity of the filter considering a distance between wires d = 18.5 µm a reflectance S_{11} = 0.6553…….. 50
Table 3.1 – Comparison between the reference conventional multi-user multiple input multiple output (MU-MIMO) and the proposed generalized spatial modulations multi-user multiple input multiple output (GSM MU-MIMO)…….. 57
Table 3.2 – Iterative GSM detection algorithm for each user k……..... 60
Table 3.3 – Solution refinement algorithm based on a closest neighbor search for user k……...…… 61
Table 3.4 – Average throughput per user with perfect and imperfect channel estimation and the corresponding throughput gain. CSI = channel status information.…… 68
Table 4.1 – General Iterative Hybrid Design Algorithm…… 81
Table 4.2 – Overall Complexity of Different Hybrid Precoding Algorithms (per subcarrier)……... 85
Table 4.3 – Power Consumption for Different Implementations of the Proposed Precoder for N_u=4, N_s=2, N_{tx}^{RF}=8, F=1, N_{tx}=256……... 91
Table 5.1 – Table of acronyms……... 99
Table 5.2 – Evaluation parameters for indoor-office scenario……... 104
Table 5.3 – Influence of the variation of the transmitted power of the APs on the system results…… 112

List of Acronyms

3D – Three-dimensional

3GPP – 3rd Generation Partnership Project (3GPP)

3G – 3th Generation Network of Mobile Communication

4G – 4th Generation Network of Mobile Communication

5G – 5th Generation Network of Mobile Communication

6G – 6th Generation Network of Mobile Communication

ADC – Analog Digital Converter

ADMM – Alternating Direction Method of Multipliers

AM – Alternating Minimization

ANACOM – Autoridade Nacional de Comunicações

AOA – Average Angle of Arrival

AOD – Average Angle of Departure

AoSA – Array of SubArrays

AP – Access Point

B5G – Beyond 5G

BC – Book Chapter

BD – Block Diagonalization

BER – Bit Error Rate

BEREC – Body of European Regulators for Electronic Communications

BLER – Block Error Rate

BPCU – Bits Per Channel Use

BS – Base Station

CDL – Cluster Delay Line

C-RAN – Cloud Radio Access Network

CRM – Complex Rotation Matrices

CSI – Channel State Information

CU – Central Unit

DAoSA – Dynamic Array of SubArrays

DOI – Digital Object Identifier

DPS – Double Phase Shifters

EBE – Element-By-Element

EC – Energy Consumption

EE – Energy Efficiency

FC – Fully-Connected

FDD – Frequency Division Multiplexing

FEMM – Finite Element Magnetics Method

FoM – Figure of Merit

FSS – Frequency Selective Surface

GDD – Glow Discharge Detector

GHz – Gigahertz

GSFIM – Generalized Space–Frequency Index Modulation

GSM – Generalized Spatial Modulation

HDPE –High-Density PolyEthylene

HSS – Highly Selective Structure

IC – International Conferences

IJ – International Journals

IM – Index Modulation

InD-MO – InDoor-Mixed Office

InD-OO – InDoor-Open Office

IR – Infrared Radiation

IT – Instituto de Telecomunicações

IL – Insertion Loss

LASSO – Least Absolute Shrinkage and Selection Operator

LoS – Line of Sight

LTE – Long Term Evolution

MATLAB – MATrix LABoratory

MDPI – Multidisciplinary Digital Publishing Institute

MIMO – Multipli Input, Multiple Output

MLD – Maximum Likelihood Detection

MR – Microwave Radiation

MU – MultiUser

MU-MIMO – MultiUser MIMO

NLoS – Non-Line of Sight

OFDM – Orthogonal Frequency Division Multiplexing

PC – Partially-Connected

PL – PathLoss

PTFE – PolyTetraFluoroEthylene

QoS – Quality of Service

QAM – Quadrature Amplitude Modulation

QPS – Quantized Phase Shifters

QPSK – Quadrature Phase Shift Keying

RAN – Radio Access Network

RF – Radio Frequency

RL – Return Loss

RRU – Radio Remote Unit

SE – Spectral Efficiency

SI – The International System of Units

SISO – Single Input, Single Output

SNR– Signal-to-Noise Ratio

SPS – Single Phase Shifters

SSD – Signal Space Diversity

SU– Single User

TDD – Time Division Multiplexing

TDL – Tapped Delay Line

THz – Terahertz

TRP – Transmission and Reception Point

UE – User Equipment

UM-MIMO – Ultra Massive MIMO

UPA – Uniform Planar Array

ZF – Zero Forcing

List of Symbols

α – Attenuation Constant

β – Propagation Constant

ε – Electric Permitivity

k – Magnitude of the Wave Vector

λ– Wavelength

μ – Magnetic Permeability

Y – Admittance

ω – Angular Frequency

ω_0 – Resonance Frequency

c – Speed of Light in Vacuum

D – Electric Displacement

E – Electric Field

f_0 – Operating Frequency

f_s – Frequency Shift

f_t – Resonance Frequency

H – Magnetic Field

J – Electric Current Density

∇ – Nabla Operator

a – radius of the wires

d – distance between wires

l – length of the structure

Q – Quality Factor

R – Reflection Coefficient

T – Transmission Coefficient

z – Characteristic Impedance of the Dielectric Slab Material

Z_p – Impedance of the Port

$\alpha_{i,l,u}$ – Complex gain of the l^{th} ray from cluster i of the user u

α_u^{LOS} – Complex gain of the LOS component of the user u

ρ_u – Average received power at the u^{th} receiver

γ – normalizing factor

$\prod_D(.)$ – Projection operation onto set D

$\mathbf{a}_t\left(\phi_{i,l,u}^t, \theta_{i,l,u}^t\right)$ – Transmit antenna array responses at the azimuth and elevation angles of $\left(\phi_{i,l,u}^t, \theta_{i,l,u}^t\right)$

$\mathbf{a}_r\left(\phi_{i,l,u}^r, \theta_{i,l,u}^r\right)$ – Receive antenna array response at the azimuth and elevation angles of $\left(\phi_{i,l,u}^r, \theta_{i,l,u}^r\right)$

$\mathbf{a}_t\left(\phi_{i,l,u}^{t,LoS}, \theta_{i,l,u}^{t,LoS}\right)$ – Transmit antenna array responses of the LoS path at the azimuth and elevation angles of $\left(\phi_{i,l,u}^{t,LoS}, \theta_{i,l,u}^{t,LoS}\right)$

$\mathbf{a}_r\left(\phi_{i,l,u}^{r,LoS}, \theta_{i,l,u}^{r,LoS}\right)$ – Receive antenna array response of the LoS path at the azimuth and elevation angles of $\left(\phi_{i,l,u}^r, \theta_{i,l,u}^r\right)$

B_t – Bandwidth

f_c – Central frequency

f_k – k^{th} subcarrier frequency

$\mathbf{F}_{\text{RF}}$ – Analog precoder matrix

$\mathbf{F}_{\text{BB}}$ – Digital precoder matrix

$\mathbf{F}_{\text{opt}}$ – Optimal precoder matrix

$\mathbf{H}_{k,u}$ – Frequency domain channel matrix between the base station and the u^{th} receiver at subcarrier k.

h_{AP} – Height of the access point

h_{UE} – Height of the user equipment

L_{max} – Maximum number of subarrays that can be connected to an RF chain

M – Constellation Index of QAM

N_a – Number of positions of $\mathbf{s}_k$ that are nonzero

N_b – Number of bits

N_{cl} – Number of scattering clusters

N_{comb} – Number of active index combinations

N_{RF}^{tx} – Number of RF chains at the BS

N_{RF}^{rx} – Number of RF chains at the user

N_{ray} – Number of propagation paths

N_{rx} – Number of receiving antennas

N_s – Number of data streams

N_{sc} – Number of subcarriers

N_{tx} – Number of transmission antennas

N_u – Number of users

$\mathbf{n}_{k,u}$ – Independent zero-mean circularly symmetric gaussian noise sample matrix

P_C – Total power consumption

$\mathbf{R}$ – Projection matrix

$\mathbf{s}_{k,u}$ – Vector containing the symbols of user u at subcarrier k

$\mathbf{Y}_{k,u}$ – Received signal vector of user u at subcarrier k

$\mathbf{W}_{\mathrm{RF}}$ – Analog combiner matrix

$\mathbf{W}_{\mathrm{BB}}$ – Digital combiner matrix

$\mathbf{W}_{\mathrm{opt}}$ – Optimal combiner matrix

Chapter 1 – Introduction

This chapter introduces all the work developed in this research, namely the motivation, the goals, the contributions and provides an overview of the work.

1.1. Motivation and Scope

Telecommunications are crucial for the development of societies and maintenance of human relations. Over the last two decades, the telecommunications field experienced a fast growth, which allowed its global proliferation and the constant evolution of the services that can delivered to the subscribers. In fact, this sector was fundamental during the COVID-19 pandemic, since it allowed remote work and accelerated the digital transformation of businesses through the internet. Considering the data of the study performed by the Autoridade Nacional de Comunicações Portuguesa (ANACOM) in [1], it was verified that in the begining of the pandemic in Portugal, there was a growth of the voice traffic around 94% and an increase of 52% of the data traffic, when compared to the numbers of the pre-COVID19 period. Such event made the European Commission (EC) and the Body of European Regulators for Electronic Communications (BEREC) make efforts in order to provide a set of recommendations aiming to avoid network congestion and maintain a good Quality of Service (QoS) to answer to the increased demand for network connectivity [2]. Despite the existence of some fluctuations in the use of telecommunication services due to the effect of the application of confinements and deconfinements, in general, the usage of the services has shown an increasing trend in 2020 and 2021 and this is expected to continue in 2022 [3], [4]. Such an event can be justified by the implementation of some working practices (fully remote or hybrid) that have come to last and by the fact that users can do most of their daily tasks with minimal effort [5].

Although telecom operators in Portugal have been able to respond to the challenges in the pandemic in the face of increasingly demanding user requirements, it is unlikely that current technologies will be able to respond adequately in a more demanding scenario. The traditional approach used to obtain higher transmission rates in wireless communication systems is to employ advanced modulation schemes and signal processing techniques in order to increase the spectral efficiency [6]. However, supporting transmission rates above 10 Gbps or higher will require more spectral

resources which are not available in the common RF bands. According to [7], within in the 300 GHz band, the data capacity can be 150 times larger than for 3G/4G cellular systems (1.9~2.1 GHz) enabling rates over 10 Gbps. For that reason, Terahertz (THz) waves have recently joined the race towards ultrahigh-speed future wireless communications systems as an appealing alternative against other investigated candidates, such as ultra-wideband (UWB), 60-GHz radio, free-space optical communications (FSO) and IrDA [8], [9], [10], [11] . In fact, the THz band is envisioned as one of the key enablers for this type of communications [10] but, in order to build an effective THz communication system, further advancements on the devices and transceivers architectures are still required [11].

The THz gap (1 THz = 1×10^{12} Hz) lies between the microwave (MR) and the infrared (IR) regions in the electromagnetic spectrum, ranging from 0.1 THz to 10 THz. Nevertheless the first research works in the frequency region of THz date to 1975 and, since then, there has been a significant progress in the fields of instrumentation, imaging and spectroscopy [12], [13]. The main reasons behind this event are the considerable advances in several key issues such as THz sources and detectors (e.g., quantum cascade lasers [14], photomixers [15], deuterated triglycine sulphate (DTGS) crystals [16], bolometers and single photon detectors [17]) and, as recently pointed out in the literature [18], the increasing demand for high quality electromagnetic components for the THz domain. It was also pointed out in [19], that such components cannot be easily manufactured resorting to natural materials, because they largely do not respond to THz radiation. Therefore, researchers began to focus on novel artificial materials called metamaterials. These novel materials offer many opportunities to explore unprecedented applications and led recently to major research breakthroughs, such as superlenses with enhanced resolution not limited by diffraction [20], [21], invisibility cloaks that aim at the concealment of an object [22], and the design of novel devices by Transformation Optics (TO) [23]. This last one is a very powerful technique that relies on the form invariance of Maxwell's equations to control the electromagnetic field at will [24], [25]. The first metamaterial for the THz domain was demonstrated in [26], consisting of a single planar structure composed of double split-ring resonators (SRR) arrays. The authors of [27] demonstrated a very fast electrically-driven THz modulator with modulation depth as high as 50% (at room temperature). This device completely outperforms conventional THz modulators based on semiconductors, without even

requiring cryogenic refrigeration. Other successful achievements have been highly selective band pass filters [19] and ultrafast optical switches that exhibit recovery time as short as 20ps, which it is very promising if we consider that the bit rate is proportional to the repetition rate of the optical pulses [28]. However, the fields of TO and metamaterials require further developments, as they are not yet fully consolidated to be used as a basis for efficient technologies for the THz domain. For example, TO has dealt mostly with simple geometries such as idealized 2D spheres, cylinders, and squares and the resulting designs usually vary spatially in an uncontrolled manner, presenting serious difficulties in practical implementations. The proposal of low-loss broadband metamaterials for TO is also a great challenge in the THz domain, since metamaterials are constituted of small metal inclusions. Those inclusions can induce strong resonances with undesirable effects, such as narrow band functionality and losses.

Another major challenge to achieve reliable THz communications lies on the high spreading loss and molecular absorption that are typical at the millimeter-wave (mmWave) (30–300 GHz) and THz (0.1–10 THz) frequency bands, which limit the signal coverage range. In [29], the problem of distance limitation was addressed considering four possible directions, namely, a physical layer distance-aware design, ultra-massive MIMO communication, reflectarrays, and intelligent surfaces. As discussed in [30], by adopting a joint design methodology it should be possible to combine the benefits of each solution and further extend the communication distance. In order to obtain the promised mmWave and THz throughput gains, novel systems with large-scale antennas capable of overcoming the severe path loss should be designed. The use of multiple antennas allows the adoption of beamforming (BF) architectures. Due to the small wavelengths and the related small-sized antenna elements, a large number of antenna elements could be installed to form powerful BF systems. Such BF architectures for THz communications have been discussed in [31]. It is important to note that large-scale antennas systems must respect the hardware challenges of mmWave and THz circuits. Although hardware components for these bands present good capabilities, their high complexity and power cost impose more constraints on large-antenna systems, precluding the adoption of the same designs used in lower frequencies. Thus, conventional systems with one dedicated radio frequency (RF) chain for one antenna are no longer feasible and have to be replaced by a system design based on a limited number of RF chains. This leads to the adoption of a hybrid digital-analog architecture. The hybrid structure splits signal processing into two

separate digital and analog parts, which contributes to the reduction of the overall circuit complexity and power consumption. In fact, it was shown in [30] and [32] that when hybrid precoding and an array-of-subarrays architecture (where each RF chain uniquely activates a disjoint subset of antennas) are employed, both the spectral and energy efficiency in the THz communications can be improved. One additional approach that can be explored for achieving power efficient transmission in THz systems relies on the use of index modulation (IM) techniques [31]. IM has attracted tremendous attention in the last decades since these techniques convey additional information bits contained implicitly in the index of the selected element (in the spatial, frequency, and temporal domain) among several possible combinations [32]. As an example, the element could be the active antenna subset as is done in generalized spatial modulations (GSM) [33]. Cloud radio access network (C-RAN) is a promising enabling technology that can cope with the increasing mobile traffic demand, while reducing the surging costs experienced by service operators [34]. Moreover, it is also considered as key to overcome the differences among solutions for the new generation of communication networks, and further support dynamical network resource utilization and slicing [35]. According to [36], B5G networks using radio access virtualization strategies and advanced computational platforms will exploit network densification. This concept of virtual cell removes the traditional cell boundary for the device, while providing a consequent reduction in the detrimental "cell-edge experience" by the terminal. In the previous paradigm, devices were associated with a cell and, as a consequence, the link performance could degrade as a terminal moves away from the cell center. However, when concerning a virtualized C-RAN, the network determines which base stations (BSs) or access points (APs) are to be associated with each terminal. The cell moves with and always surrounds the terminal in order to provide a cell-center experience throughout the entire network. Each terminal designated as user equipment (UE) is served by its preferred set of APs. The actual serving set for a UE may contain one or multiple APs and the terminal's data are partially or fully available at some cluster with potential serving APs. The AP controller (central processor) will accommodate each UE with its preferred cluster and transmission mode at every communication instance while considering load and channel state information (CSI) knowledge associated with the cluster of APs. Although it is possible to find in the literature, at system level, the evaluation of mmWave schemes in realistic scenarios [37], [38] as far as we are aware there are no published data so far for frequencies at the THz

level, in particular there is a lack of system-level evaluations of robust hybrid algorithms with different architectures (fully-connected (FC) structures, arrays of subarrays (AoSAs) and dynamic arrays of subarrays (DAoSAs), etc.) for this band.

1.2. Goals

After a careful reflection, one comes to the conclusion that the development of communication systems for the THz band needs to overcome several technological difficulties since a communication link will typically suffer very high propagations losses at these frequencies. Such systems require adequate beamforming, modulation and equalization schemes, while, at the same time, devices for performing these tasks efficiently in the THz band have to be designed.

The main objective of this thesis is, thus, to propose and evaluate solutions that enable ultra-high speed wireless communications in the THz band. Considering this main goal, three types of approaches were explored:

- design of THz devices – we intended to design a new reconfigurable THz filter that outperforms the filters mentioned in the current literature and that can be used in the communication schemes in order to enable THz communications;
- IM based schemes for B5G networks – we intended to explore IM based communication schemes for B5G systems, since these schemes allow us to transmit more bits of information while keeping good tradeoffs between spectral and energy efficiency. Although this study was carried out in common RF bands, this concept has the potential to be applied to the THz in the future.
- hybrid precoding designs for THz Ultra Massive (UM) – Multiple Input Multiple Output (MIMO) systems – we aimed to propose low complexity hybrid precoding designs for multiuser (MU) UM-MIMO systems that can be used not only at mmWave but also at THz bands, since a significant part of the designs reported in the literature present some implementation complexity and a considerable power consumption when extended for the THz band.

Figure 1 summarizes the flow of activities that were undertaken and that will be presented in the following subsections. For each one of the research areas, specific goals were defined, and models were developed and evaluated. The accomplishement of these tasks gave rise to several results and research contributions in each one of the research

areas. Such research contributions and their detailed information are listed in subsection 1.3, in which we also provide a chronogram showing how the work progressed during the PhD. In subsection 1.4, an overview of the work developed during this research and the explanation of how each scientific contribution is related with the goals, is presented. Following the completion of the work associated with each of the three research areas, suggestions for future work were generated.

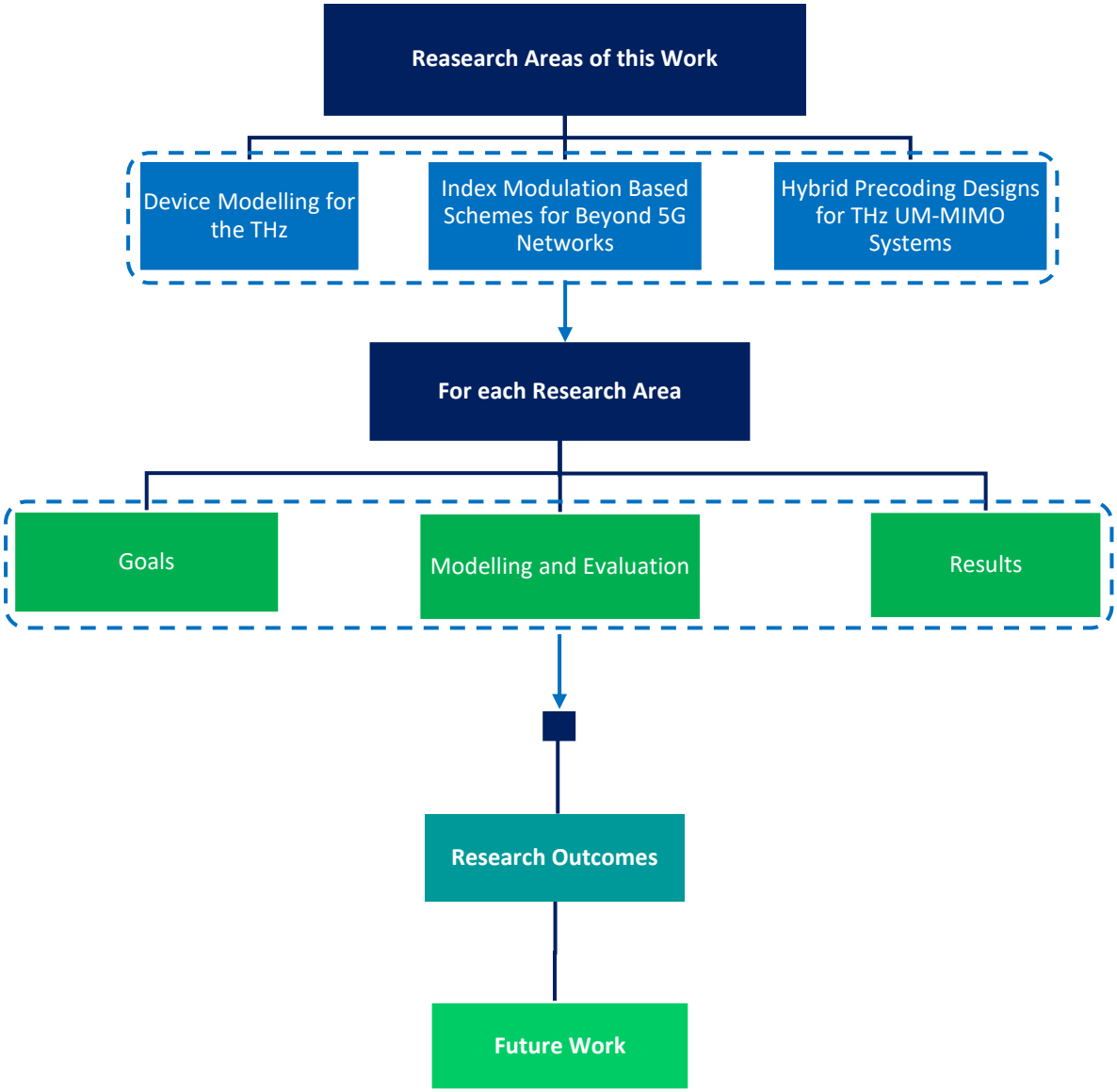

Figure 1.1 – Summary of activities.

1.3. Contributions of Research

The research developed over these years has allowed some research questions to be answered, which have resulted in several publications. This research also allowed the

development of other types of scientific materials with great relevance, such as a new theoretical model for a reconfigurable THz filter based on metamaterial wire resonators, a new MU-MIMO scheme based on generalized spatial modulations and a new design algorithm developed for low complexity hybrid precoding in MU mmWave/THz UM-MIMO systems. The last one was also the basis for parallel research in system planning for indoor environments. Although the most important articles resulting from this research are presented in the following chapters, it is important to highlight all the contributions of this research work in the next subsection. In summary, the work developed in the research for this thesis resulted in a total of 11 publications in International Jounals (IJ), International Conferences (IC) and Book Chapters (BC) as follows:

- **IJ** - 4 publications as first author and 4 as co-author;
- **IC** - 1 publication as first author and 1 as co-author;
- **BC** - 1 publication as co-author;

Table 1 presents in chronological order the contributions achieved during the execution of the work plan of the PhD programme.

Table 1.2 – Timeline of contributions.

Chronological time	Publication
March 2019	**IJ1** An alternating direction algorithm for hybrid precoding and combining in millimeter wave MIMO systems
May 2020	**IC1** Hybrid precoding and combining algorithm for reduced complexity and power consumption architectures in mmWave communications
July 2020	**IJ2** Design of a reconfigurable THz filter based on metamaterial wire resonators with applications on sensor devices
September 2020	**IJ3** Precoded Generalized Spatial Modulation for Downlink MIMO Transmissions in Beyond 5G Networks
October 2020	**IC2** Precoder and Combiner Design for Generalized Spatial Modulation based Multiuser MIMO Systems
May 2021	**BC1** Development of Stand-Off Imaging Systems using Low Cost Plasma Detectors that Work in the GHz to THz range
August 2021	**IJ4** A generalized space-frequency index modulation scheme for downlink MIMO transmissions with improved diversity

September 2021	**IJ5** Low Complexity Hybrid Precoding Designs for Multiuser mmWave/THz Ultra Massive MIMO Systems
December 2021	**IJ6** Phase Shift Optimization Algorithm for Achievable Rate Maximization in Reconfigurable Intelligent Surface Assisted THz Communications
February 2022	**IJ7** System-Level Assessment of a C-RAN based on Generalized Space-Frequency Index Modulation for 5G New Radio and Beyond
March 2022	**IJ8** System-Level Assessment of Low Complexity Hybrid Precoding Designs for Downlink MIMO Transmissions for Beyond 5G

The information of each one of the contributions is now detailed, including the Scimago/Scopus Journal Ranking, beginning with the publications in peer reviewed IJ:

- **IJ1** - N. Souto, J. Silva, J.P. Pavia and M. Ribeiro, " **An alternating direction algorithm for hybrid precoding and combining in millimeter wave MIMO systems**", Physical Communication, vol. 34, p. 165, March 2019, Quartile 2, Digital Object Identifier (DOI): 10.1016/j.phycom.2019.03.012 [39].
- **IJ2** - J.P. Pavia, N. Souto and M. Ribeiro, "**Design of a Reconfigurable THz Filter Based on Metamaterial Wire Resonators with Applications on Sensor Devices**", Photonics, vol. 7, no. 3, p. 48, July 2020, Quartile 2, DOI: 10.3390/photonics7030048 [40].
- **IJ3** - J.P. Pavia, V. Velez, B. Brogueira, N. Souto and A. Correia, "**Precoded Generalized Spatial Modulation for Downlink MIMO Transmissions in Beyond 5G Networks**", Applied Sciences, vol. 10, no. 18, p. 6617, September 2020, Quartile 2, DOI: 10.3390/app10186617 [41].
- **IJ4** - V. Velez, J.P. Pavia, N. Souto, P. Sebastião and A. Correia, "**A generalized space-frequency index modulation scheme for downlink MIMO transmissions with improved diversity**", IEEE Access, vol. 9, p. 118996, August 2021, Quartile 1, Digital Object Identifier (DOI): 10.1109/ACCESS.2021.3106547 [42].
- **IJ5** - J.P. Pavia, V. Velez, R. Ferreira, N. Souto, M. Ribeiro, J. Silva and R. Dinis, "**Low Complexity Hybrid Precoding Designs for Multiuser mmWave/THz**

Ultra Massive MIMO Systems", Sensors, vol. 21, no. 18, p. 6054, September 2021, Quartile 1, DOI: 10.3390/s21186054 [43].

- **IJ6** – J. Praia, J.P. Pavia, N. Souto and M. Ribeiro, "**Phase Shift Optimization Algorithm for Achievable Rate Maximization in Reconfigurable Intelligent Surface Assisted THz Communications**", Electronics, vol. 11, no. 1, p. 18, December 2021, Quartile 2, DOI: 10.3390/electronics11010018 [44].
- **IJ7** – V. Velez, J.P. Pavia, C. Rita, C. Gonçalves, N. Souto, P. Sebastião and A. Correia, "**System-Level Assessment of a C-RAN based on Generalized Space-Frequency Index Modulation for 5G New Radio and Beyond**", Applied Sciences, vol. 12, no. 3, p. 1592, February 2022, Quartile 2, DOI: 10.3390/app12031592 [45].
- **IJ8** - J.P. Pavia, V. Velez, N. Souto, M. Ribeiro, P. Sebastião and A. Correia, "**System-Level Assessment of Low-Complexity Hybrid Precoding Designs for Downlink MIMO Transmissions for 5G New Radio and Beyond** ", Applied Sciences, vol. 12, no. 6, p. 2812, March 2022, Quartile 2, DOI: 10.3390/app12062812 [46].

The publications in peer reviewed ICs are the following:

- **IC1** - J.P. Pavia, N. Souto, M. Ribeiro, J. Silva and R. Dinis, "**Hybrid Precoding and Combining Algorithm for Reduced Complexity and Power Consumption Architectures in mmWave Communications**", 2020 IEEE 91st Vehicular Technology Conference (VTC2020-Spring), May 2020, pp. 5207, DOI: 10.1109/VTC2020-Spring48590.2020.9128553 [47].
- **IC2** - B. Brogueira, J.P. Pavia, N. Souto and A. Correia, "**Precoder and Combiner Design for Generalized Spatial Modulation based Multiuser MIMO Systems**", 2020 23rd International Symposium on Wireless Personal Multimedia Communications (WPMC), October 2020, pp. 8296, DOI: 10.1109/WPMC50192.2020.9309474 [48].

The publication of BC the peer reviewed BC is the following:

- **BC1** - D. Akbar, H. Altan, J.P. Pavia, M.A. Ribeiro, A.B. Sahin, C.K. Sarikaya, "**Development of Stand- Off Imaging Systems using Low-Cost Plasma Detectors that Work in the GHz to THz range**" in Terahertz (THz), Mid

Infrared (MIR) and Near Infrared (NIR) Technologies for Protection of Critical Infrastructures Against Explosives and CBRN, NATO Science for Peace and Security Series B: Physics and Biophysics, Dordrecht, Springer, May 2021, pp. 275-285, DOI: 10.1007/978-94-024-2082 [49].

1.4. Thesis Overview

As referred previously, the work developed in the scope of this thesis focuses on three research areas. Although the main chapters of this thesis are based on publications as first author in IJs, the research in each area was directed linked to other co-authored publications. Therefore, in this section we provide a general overview of the thesis, highlighting and interconnecting all the contributions identified in the previous subsection.

1.4.1. Devices for the THz Band (IJ2 and BC1)

Modelling devices for THz is a crucial task, as it allows to provide and optimize their ability to perform the purpose for which they were designed. Because THz is a rapidly emerging field with many potential applications, there is an urgent need for new ways of producing sources, detectors and other devices such as filters, sensors and modulators. The main contributions in this research area are **IJ2** and **BC1**. These contributions are related to two particular classes of devices for THz, such as filters and detectors. In **IJ2** [40], a reconfigurable THz filters based on metamaterial wire resonators with applications on sensor devices was proposed. In this publication, we discussed the general need of applications where these filters are required for and introduced the required tools to design a highly selective structure (HSS), which in this case are the metamaterial wire resonators, the center piece of our filter. This structure works as a reconfigurable selective THz window in which only radiation of certain desired frequencies is allowed to pass. To provide this behavior, a much simpler approach when compared to the literature, where the resonances are obtained from the propagation in a THz HSS composed by two arrays of gold wires, is used [50]. These two arrays of wires allow us to provide greater cancellation of harmonics, higher dynamic range and enhanced frequency selectivity to our filter. In order to optimize its performance, a study on the interaction between the waves and the wires was required to understand the principle of operation of the HSS. Through this study, a method to optimize the relation between the radius of the wires and

the distance between wires and adjust the sensitivity and selectivity of the device was devised. Considering its simplicity, this filter design is especially suited for the implementation of reconfigurable THz filters and optical modulators, since it transits from situations in which it presents a full transparency ($|S_{11}| = 0$) to situations where it achieves full opacity ($|S_{11}| = 1$). Moreover, this approach can also be used for the implementation of simultaneously transmitting and reflecting (STAR) reconfigurable intelligent surfaces (RIS) [51]. In **BC1** [49], we present a study on low-cost plasma detectors that can work from the GHz to the THz range. When talking about the detection of mmWave/THz radiation, most of the technologies can rely on temperature changes, direct/indirect transitions or those that detect through the applied electric field [52], [53]. However, most of the commercially available detectors have limitations in terms of speed and responsivity and are quite expensive. Considering these issues, glow discharge detectors (GDDs) can be a good alternative solution since they are low cost and can detect microwave to mmWave radiation with high sensitivity [54]. These detectors have shown a good response in the mmWave region of the spectrum below ~100 GHz, and in this publication, we showed that their sensitivity even extends far into the THz region. In order to allow for such a broad frequency sensitivity, a study on the detection mechanism behind the glow discharge was required. Two types of GDDs were studied, one with phosphor coating and one without but with similar geometrical dimensions. The validity of our approach is shown by obtaining plasma discharge parameters which agree well with experimental observations. The response of GDDs was studied from the mmWave to the THz range and we observed that the response decreased rapidly. After 100 GHz the decay slowed down which suggests that these types of lamps could detect even higher frequencies in the THz range.

1.4.2. Index Modulations (IJ3, IJ4, IJ7 and IC2)

Considering the technological advances over the last decades, the next generation of wireless communications is expected to follow this trend with a significant increase in system robustness (SR), spectral efficiency (SE) and energy efficiency (EE). In recent years, new emerging techniques have appeared in order to meet the increasingly challenging requirements of B5G communication systems, such as non-orthogonal multiple access (NOMA) schemes like signaling aided sparse code multiple access or index modulations (IM) [55]. IM has received significant attention due to its ability to

activate a subset of certain elements of communication resources, namely antennas, subcarriers, and slots [56], [57]. As referred before, GSM have been widely considered as potential candidate techniques for next-generation wireless networks, as they can improve both SE and EE. The work developed within the scope of index modulation-based schemes for B5G networks started with **IC2** [48]**,** where we proposed a precoder and combiner design for generalized spatial modulation based MU-MIMO system. In the adopted GSM approach, we considered that the BS transmits precoded GSM symbols to several receivers, where multiple antennas transmit different high-level quadrature amplitude modulation (QAM) symbols simultaneously. Considering the system model described in **IC2**, the information will be divided in such a way that part of the data will be used to select an active index (AI) from a total $N_{comb} = 2^{\left\lfloor \log_2\binom{N_s}{N_a} \right\rfloor}$ AI combinations (AICs) that are available per user. The remaining data will be mapped onto N_a complex-valued *M*-QAM symbols. Our precoder design can remove interference between users while an iterative algorithm is applied at the receiver to accomplish single-user GSM detection. This algorithm is based on the alternating direction method of multipliers (ADMM), since aforementioned situation (maximum likelihood detection) configures itself as a non-convex problem and ADMM allows us to split a complex problem into a sequence of smaller subproblems with simpler solution. To increase the chances of finding an optimal solution and improve the performance of the GSM detector, in that paper we also proposed the adoption of several different strategies (the complete description of each strategy can be found in **IC2**). It is important to note that those strategies can be applied together as it can be seen in our results of that paper. Furthermore, our simulation results show that the presented GSM MU-MIMO approach is capable to effectively exploit a large number of transmit antennas deployed at the transmitter and to provide performance gains over conventional MU-MIMO schemes with identical SEs. This work was extended to a system-level perspective in **IJ3** [41], where we studied the influence of perfect versus imperfect channel estimation on the performance of this massive MIMO GSM-based system, considering high-order *M*-QAM constellation with sizes reaching *M*=1024 symbols in order to increase the SE of the transmission.To remove inter-user interference and transform the MU transmission into several independent SU links, a block diagonalization (BD) precoder was applied at the BS, while a modified and improved version of the low-complexity single user (SU) GSM detector presented in [33] is used at the receiver. The system was conceived through a C-

RAN, which is comprised of a set of radio remote units (RRUs) connected through fiber to a central unit (CU). The RRUs array configuration corresponds to cylindrical arrays, where the separation between antennas of the array is half wavelength. To each pedestrian is assigned line-of-sight (LoS) or non-line-of-sight (NLoS) propagation conditions, depending on the distance to RRU (more considerations about the system can be found in **IJ3**). Through system level simulations, we observed that the deployments based on C-RAN can achieve very competitive and very promising throughput and coverage gains over conventional MU-MIMO systems with identical SEs. In fact, the system-level assessment showed potential gains of up to 155% in throughput and 139% in coverage when compared to traditional cellular networks. Such results were obtained for a system with N_a=2 active indexes, N_{sc}=256 subcarriers, N_u=15 users, N_{tx}=17 transmission antennas/user, N_{rx}=16 reception antennas/user and 100% of transmitted power for all QAM constellations (assuming clustering where the network is partitioned into three adjacent RRU sets and each user is served by three RRUs).

As mentioned in [58], IM can assume different versions and the academic community has been studying and proposing multidimensional schemes that are based on combinations of multiple one-dimensional IM. In line with this particular topic and extending the work from the previous contributions [41], [48], in **IJ4** [42] we proposed a new scheme, named precoding-aided transmitter side generalized space-frequency index modulation (PT-GSFIM), in which the information bits select the active antennas and subcarriers to carry amplitude and phase modulated symbols. This scheme was designed for MU-MIMO scenarios, and it is characterized by incorporating a precoder which removes multiuser interference (MUI) at the receivers and by integrating signal space diversity (SSD) techniques to tackle the typical poor performance of uncoded orthogonal frequency division multiplexing (OFDM) based schemes. Regarding this, we combine complex rotation matrices (CRM) and subcarrier-level interleaving, which allow us to exploit the inherent diversity in frequency selective channels and to improve the performance without additional power or bandwidth. Through our numerical simulation, we found that our proposed scheme can provide significant gains over conventional MU-MIMO and other GSM schemes. This work was extended to a system-level perspective in **IJ7** [45]. In that paper, we focused our study on the system-level assessment of a C-RAN based on the proposed PT-GSFIM scheme. The system-level evaluation was performed for numerologies 1 and 2 from 5G NR in three 3D scenarios (urban macro,

urban micro-street canyon and indoor hotspot) with different parameters, like modulation, number of transmitted antennas per user, bandwidth and frequency carrier. Through our numerical simulations, we observed that C-RAN deployments in several indoor and outdoor scenarios, can outperform both GSM and conventional MU-MIMO, exploiting its additional inherent frequency diversity.

1.4.3. Hybrid Precoding Designs for the THz (IJ1, IJ5, IJ6, IJ8 and IC1)

THz systems are becoming feasible due to the recent advances in the field of THz devices, and they are expected to ease the spectrum limitations of today's systems [59]. However, there are several issues that can affect the system performance, such as the reflection and scattering losses through the transmission path, the high dependency between range and frequency of channels in the THz band and also the need for controllable time-delay phase shifters. Such limitations require not only the proper system design but also the definition of a set of strategies to enable communications [60]. Considering the research area of hybrid precoding designs for THz UM-MIMO systems, the work developed within this scope started with **IJ1** [39] **and IC1** [47]. In these publications, we proposed a hybrid precoding and combining algorithm for reduced complexity and power consumption architectures in mmWave communications. Since the exploration of the potentialities of mmWave and THz wavelengths is closely related to the paradigm of using very large arrays of antennas in beamforming architectures, in order to achieve the maximum potential of these systems, it is necessary to consider the requirements and the challenges related to the channel characteristics and also to the hardware component. Our algorithm is based on ADMM, which allow us to split a properly formulated problem into a sequence of smaller subproblems with straightforward solutions. This approach enables the analog design part to be reduced to a simple projection operation resulting in a flexible algorithm that can easily cope with different architectures, namely variable phase shifters, switches and inverters deployed in a FC or partially-connected (PC) structure. Our numerical results showed that the proposed approach can obtain good trade-offs between SE and hardware implementation complexity. After working on mmWave communications, we decided to extend this approach to low complexity hybrid precoding designs for MU mmWave/THz ultra massive MIMO systems, as mentioned in **IJ5** [43]. In that paper, we proposed a hybrid design algorithm suitable for both mmWave and THz MU-MIMO systems, which

comprises separate computation steps for the digital precoder, analog precoder and MUI mitigation. Our design can incorporate different analog architectures such as phase shifters, switches and inverters, antenna selection and so on. Moreover, it can also be applied for different structures, (e.g. FC structures, AoSAs and DAoSAs, making it suitable for the support of UM-MIMO in severely hardware constrained THz systems. Through our results, we proved that it is possible to achieve good trade-offs between spectral efficiency and simplified implementation, even as the number of users and data streams increase. We explicitly showed how the proposed design can be applied to a DAoSAs approach where a reduced number of switches are inserted at each AoSA panel, which allows the connections to the RF chains (L_{max}) to be dynamically adjusted. One of the objectives of adopting these low-complexity solutions is to reduce overall power consumption. In Table 3 of [43] , the total power consumption of each precoding scheme considered in this study, was calculated (more information about the formula and further considerations can be seen in **IJ5**). Through this study it can be seen that the use of architectures based on DAoSAs allows us to reduce considerably the amount of power that is consumed by the precoder. In fact, it is possible to reduce the amount of consumed power up to 55% if we consider a precoder scheme based on DAoSA with double phase shifters (DPS) and L_{max} = 4 versus an FC structure precoder based on unquatized phase shifters (UPS), with only a small performance penalty. This reduction increases to 73% if a DPS structure is replaced by a single phase shifters (SPS) one. In the particular case of architectures based on quantized phase shifters (QPS), we observed that by decreasing the number of quantization bits, it is possible to substantially reduce the power consumption without excessively compromising the complexity. Moreover, we found that the architectures based on low resolution QPS, AoSAs and DAoSAs present superior energy efficiency when compared to the fully-connected structure with UPS. This last work was extended to a system-level perspective in **IJ8** [46], where we performed a thorough system level assessment of a C-RAN based on low complexity hybrid precoding designs for massive MIMO downlink transmissions for B5G systems. The system level simulations were performed based on link level results between the APs and multiple terminals, where it is considered that the ADMM algorithm from **IJ5** is applied for hybrid precoding design at the transmitter side. The study of the proposed C-RAN was centered in two 5G New Radio (NR) three-dimension (3D) scenarios, namely, the indoor mixed office (InD-MO) and indoor open office (InD-OO). For the InD-MO scenario, we

considered the fifth numerology of 5G NR with different parameters, such as the number of transmitted antennas per user and the number of subcarriers. Our evaluation demonstrated that low-complexity hybrid precoding-based C-RAN deployments in an indoor scenario can enable the practical implementation of those schemes, which rely on massive/ultra-massive antenna arrays to combat distance limitation and minimize the MUI. Although these hybrid designs sacrifice some performance, significant throughput performance and coverage improvements can still be achieved over typical cellular networks. The use of PC architectures (AoSA and DAoSA) when compared with FC structures tends to achieve good performances in terms of the trade-off between spectral efficiency and energy consumption. InD-MO scenario can provide higher throughput and coverage performances in comparison to the InD-OO scenario independently of the cluster size, due to a lower inter-site interference. Another aspect that could effectively address the challenges related to the peculiarities of communications in THz when implementing MU mmWave/THz ultra massive MIMO systems in indoor environments is the use of RIS panels. In line with this topic in **IJ6** [44], we studied an UM-MIMO THz communication system operating in a typical indoor scenario where the direct link between the transmitter and receiver is obstructed due to surrounding obstacles. In this problem, we assumed the aid of a nearby RIS whose phase shifts can be adjusted in order to help establish communication. The configuration of the individual phase shifts of the RIS elements requires a proper formulation in order to maximize the achievable rate. Due to the complexity of this optimization problem, we applied the accelerated proximal gradient (APG) method, which results in a low complexity algorithm that copes with the non-convex phase shift constraint through simple element-wise normalization. Through our numerical results, we demonstrated the effectiveness of the proposed algorithm even when considering realistic discrete phase shifts' quantization and imperfect channel knowledge.

Chapter 2 – Design of a Reconfigurable THz Filter Based on Metamaterial Wire Resonators with Applications on Sensor Devices

As referred previously, THz is a rapidly emerging field with many potential applications but also one where there is an urgent need for new ways of producing sources, detectors and other devices such as filters, sensors and modulators. Artificial materials, such as metamaterials, play an important role in THz because they make it possible to design and manufacture very compact, sensitive and extremely selective structures surpassing the existing materials in nature. THz filters are a key component in optimizing the performance of THz sensing devices, since they can eliminate undesirable background radiation and enhance the signal-to-noise ratio as well as spectral resolution in practical applications. Considering their architectures, several approaches related to the design of THz filters can be followed in order to optimize their tunability and control their response according to a set of specific requirements. The article presented in this chapter introduces the fundamental concepts on the design, simulation and characterization of a reconfigurable THz filter based on two FSSs. Through our theoretical model, we found out that, by careful tuning the wire parameters, it is possible to control the filter sensitivity and also the energy transmission and reflection that passes through the structure. Due to its characteristics, this THz filter might be an interesting solution not only for THz sensors based on reconfigurable filters but also for optical modulators for the THz domain. Moreover, this approach can also be used for the implementation of simultaneously transmitting and reflecting (STAR) reconfigurable intelligent surfaces (RIS) [52].

Some paper details:

- Title: Design of a Reconfigurable THz Filter Based on Metamaterial Wire Resonators with Applications on Sensor Devices;
- Date of publication: 10 July 2020;
- Journal: Photonics;
- Scimago/Scopus Journal Ranking: Quartile 2;
- Publisher: MDPI.

photonics

MDPI

Article

Design of a Reconfigurable THz Filter Based on Metamaterial Wire Resonators with Applications on Sensor Devices

João Pedro Pavia [1,2,*], Nuno Souto [1,2] and Marco Alexandre Ribeiro [1,2]

[1] Department of Information Science and Technology, ISCTE—Instituto Universitário de Lisboa, Av. das Forças Armadas, 1649-026 Lisbon, Portugal; Nuno.Souto@iscte-iul.pt (N.S.); Marco.Ribeiro@iscte-iul.pt (M.A.R.)

[2] Radio Systems Group, Instituto de Telecomunicações, Av. Rovisco Pais, 1049-001 Lisbon, Portugal

* Correspondence: Joao_Pedro_Pavia@iscte-iul.pt

Photonics 2020, 7(3), 48; https://doi.org/10.3390/photonics7030048

Received: 31 May 2020 / Revised: 1 July 2020 / Accepted: 7 July 2020 / Published: 10 July 2020

Abstract: A study on the design, simulation and characterization of a reconfigurable terahertz (THz) filter, composed of two frequency-selective surfaces (FSSs) with applications on sensor devices in general and highly sensitive stress sensors, is presented in this paper. Using the developed theoretical model, we found out that by careful tuning the wire parameters, it is possible to control the filter sensitivity and also the energy transmission and reflection that passes through the structure. Numerical modelling of both the mechanical and electromagnetic components (using the elasticity equation and Maxwell's equations, respectively) has been undertaken for two types of the device assemblies based on different thermoplastic polymers transparent to the THz radiation, namely: high-density polyethylene (HDPE) and polytetrafluoroethylene (PTFE), operating in a THz window from 395 to 455 GHz. The numerical results allowed us to characterize the relation between the reflectance/transmittance and the amount of force required to obtain a specific frequency shift along that window. It was found that the device assembled with HDPE presents a more linear response and it is able to pass from a full transparency to almost full opacity using only its linear operating zone. Due to its characteristics, this THz filter might be an interesting solution not only for THz sensors based on reconfigurable filters but also for optical modulators for the THz domain.

Keywords: filters; metamaterials; frequency-selective surfaces (FSSs); stress sensors; terahertz (THz)

1. Introduction

Terahertz (THz) is a rapidly emerging field in science with many potential applications but where there is an urgent need for new ways of producing sources, detectors and other devices such as filters, sensors and modulators. Artificial materials, such as metamaterials, play an important role in THz because they make it possible to design and manufacture very compact, sensitive and extremely selective structures surpassing the existing materials in nature [1,2]. Over the last few years, the scientific community has focused on several research areas, such as all-dielectric metamaterials, reconfigurable metamaterials, flexible metamaterials, metadevices, graphene metamaterials, tunable metamaterials and metasurfaces [1,3]. According to [2], for sensing applications, it is necessary that metamaterials are capable of fulfilling a set of requirements such as the ability to provide spoof surface plasmons with localized electric field enhancement and have high quality factor values (*Q*-factor), while preserving a high sensitivity, even when subjected to minor changes due to external factors. Some classes of metamaterials have gained a significant prominence for this type of applications, namely metasurfaces, absorbers, metallic mesh devices and metamaterial-based thin films, due to their potentialities in terms of shape design, geometry, orientation, maximization of the excited electric/magnetic field, tuneability, sensitivity and also the possibility of being manufactured using lithography and nanoprinting technologies [1,3]. Successful applications have been reported in the literature with an emphasis on biosensing, microfluid devices, THz detectors and plasmonic toroidal metamodulators [2–5]. Architectonically speaking, most of these devices are based on split ring resonators (SRRs) and frequency-selective surfaces (FSSs), whose geometric and quality parameters can be adjusted to efficiently control resonant modes, quality factor, sensitivity, selectivity, responsivity and also to minimize losses. However, new trends in this field report a paradigm change in which the inclusion of nanomaterials in metamaterial

sensors and the use of graphene plasmon and graphene metamaterial devices and topological insulators induced THz surface are expected in the near future [1].

THz filters are a key component in optimizing the performance of THz sensing devices, since they can eliminate undesirable background radiation and enhance the signal-to-noise ratio as well as spectral resolution in practical applications such as THz spectroscopy and imaging [6,7]. Several designs of broadband and narrowband THz bandpass filters based on metamaterials have been studied over the last decade [8–12]. Narrowband THz filters are especially important since they are the centerpiece of a wide range of ultrasensitive THz sensors due to their capability for selecting the radiation only in a narrow spectrum around a target frequency [10]. There is a wide range field where those sensors are essential, such as health, industry, science, telecommunications and security [6,7,10]. Several approaches related to the design of THz filters as well as to their tunability, have been reported since then. Some examples that stand out include the architectures based on photonic crystals, thin-film stacks, Bragg reflectors, FSSs, waveguides and resonant cavities [13–17]. The performance of most of these filters can be controlled following the same methodologies used in metamaterials, being also possible to control them mechanically (by adjusting the thickness or the distance of the components of the unit cells) or through the action of temperature as described in [6,15]. Metrics such as dynamic range, *Q*-factor, full width at average maximum (FWHM), dephasing time of the induced spectral line shapes (t_d), figure of merit (*FoM*) and insertion loss (IL) are widely used to evaluate THz filters [5,6,13,14,17].

The utilization of THz technologies for stress sensing applications is very recent, but some approaches have already been reported in the literature [18–21]. The sensors of those systems must be accessible, light and discrete, so as not to impose cost and weight on the structure as well as not to interfere with the structural resistance [19]. Most of these requirements can be easily accomplished through the use of FSSs in the design of micro-electro-mechanical system (MEMS) sensors, since they can offer higher sensitivity and resolution and also possess a greater potential to deliver the strong enhancement and localization of fields, being especially suitable for the development of wireless strain sensors that can operate in the microwave and terahertz ranges [18,21]. The development of THz stress sensors based on metal mesh filters and FSSs is described in [21]. The resonances of this type of sensor are obtained thanks to the periodicity of the unit cells in the direction of propagation and, according to the authors, can be used in several applications, including structural health monitoring (SHM). Their integration into the structures allow us to detect cracks and other kinds of damage, since, in this type of critical situation, it is known that the reflectance/transmittance values of the sensors decrease abruptly.

This paper aims to present a detailed study about the characterization, design and simulation of a reconfigurable THz filter with high sensitivity and selectivity for sensor devices such as stress sensors. Our filter has a simpler design when compared to the approaches referred above, since it is composed by only two FSSs based on metamaterial wire resonators. Despite being a novel approach, the proposed device can provide a higher dynamic range, an enhanced frequency selectivity and requires less force to cause a frequency shift. The remainder of the paper is organized as follows: Section 2 describes the filter theory and respective design. The mechanical model and respective simulation method is introduced in Section 3, while Section 4 presents the numerical results obtained from the electromagnetic and mechanical point of view. Finally, the conclusions are outlined in Section 5.

2. Filter Theory and Design Decisions

In this section, the required tools are introduced in order to design a highly selective structure (HSS) that is the centerpiece of the sensor. This HSS works as a reconfigurable selective THz window in which only radiation of certain desired frequencies is allowed to pass. In literature, as described in [21], this kind of behavior is obtained using a technique related to the periodicity of the unit cells of the structure in the direction of propagation. Here, a much simpler approach, where the resonances are obtained from the propagation in a THz HSS composed by two arrays of gold wires, is used. The goal is therefore to study the interaction between the waves and the wires to be able to understand the principle of operation of the HSS. More specifically we intend to devise a method to optimize the relation between the radius of the wires and the distance between wires and adjust the sensitivity and selectivity of the device. Moreover, for simplicity, we shall assume that the structure is composed by two arrays of wires because using a single array would not be sufficient to achieve the desired degree of selectivity. Based on the variation of the distance between wires and the mechanical stress experienced by the structure, it will be possible to predict how the transmittance is decreasing to the operating frequency, since, when the transmittance is very low when compared to the initial one, it is known that the structure has a problem.

2.1. Working Principle

In this paper, we propose a new design for a reconfigurable THz filter that can be used to implement an electro-mechanical sensor. As can be seen in Figure 1, the device is composed of two FSSs (arrays of wires) within a dielectric host material. Note that the selective character of the wire arrays gives rise to a bell-shaped frequency response. The working principle is presented in Figure 1, in which it can be seen that by applying compression along the x axis, the distance between wires d will decrease and, therefore, the frequency response of the sensor will change, as does its transmittance. The sensor is settled to operate at the target frequency and, as it experiences compression, it becomes possible to adjust the sensor response from full transparency to complete opacity, including all degrees of transparency in between. The red curve corresponds to maximum compression and the green curve to half compression.

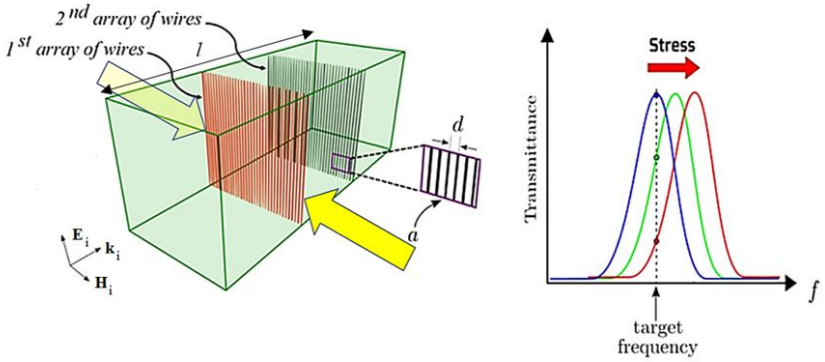

Figure 1. Overview of the working principle of the proposed reconfigurable filter.

By allowing a lateral compression instead of a uniaxial compression, the device becomes more functional and easier to implement. It is also more selective since its working principle is based on the resonance of two arrays in the propagation directions. This selectivity can be accomplished through the careful design of the d/a ratio of the wire arrays (a is the radius of the wires), which also enhances the Q-factor of the filter.

This double grid structure can be represented by a simplified two-port network model, as can be seen Figure 2 [22]. The arrays of wires are described as admittances Y in the equivalent circuit and the dielectric slab is represented by three sections of transmission line with equal length $l/3$ (note that the total length of the structure is l).

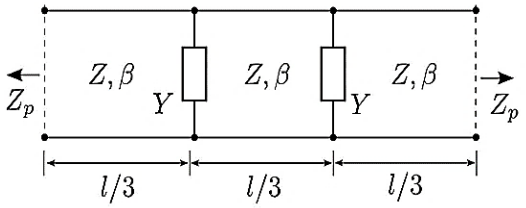

Figure 2. Equivalent microwave network circuit of the terahertz (THz) filter.

In this model, Z_p is the impedance of the port, z is the characteristic impedance of the dielectric slab material and β is the propagation constant. In the next section, we will show how to determine the expression for admittance Y.

2.2. Circuit Theory

In all wave propagation problems, where there are transitions between media, we can always identify incident waves at the interface, which give rise to reflected and transmitted waves. As it is well known from electromagnetic theory, the reflectance and transmittance of a dielectric slab have a comb like frequency response [22]. However, in this situation, the arrays of wires will introduce a filter-like response in the frequency domain. We must study this problem in order to understand the interactions between electromagnetic waves and the array of wires, as can be seen in Figure 3.

By studying the problem, we will be able to find out what will be the structure's response in the frequency domain and how can we tune the filter.

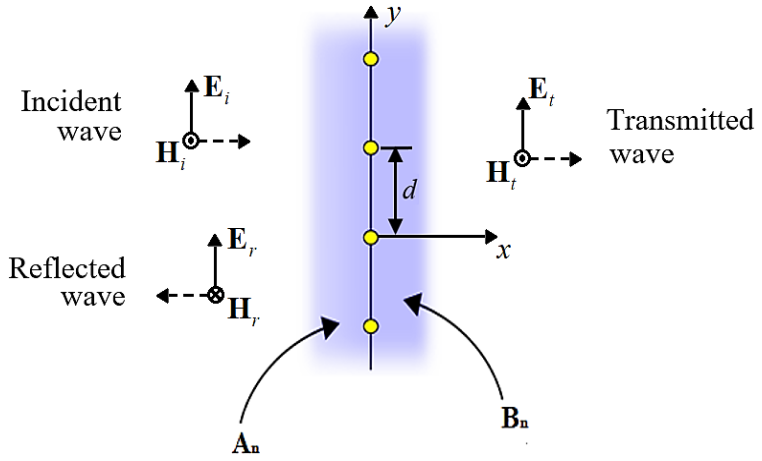

Figure 3. Reflection and transmission from an array of wires.

2.2.1. Equivalent Circuit Admittance for the Wire Arrays

For propagation in the *z* direction and for time harmonic fields of the form $e^{j\omega t}$, the Helmholtz equation is:

$$\frac{\partial^2 E_z}{\partial x^2}+\frac{\partial^2 E_z}{\partial y^2}+k^2 E_z=0\,, \tag{1}$$

where $k=\omega/c$ is the magnitude of the wave vector and E_z is the *z* component of the electric field, parallel to the wires. Solutions of (1) can be written in the form $E_z(x,y)=X(x)Y(y)$, where

$$Y\left(y\right)=c_1\cos\left(k_y y\right)+c_2\sin\left(k_y y\right). \tag{2}$$

The second term on the right-hand side vanishes because $Y(y)=Y\left(-y\right)$. This condition results from the symmetry along the *y* axis. Moreover, since the structure is periodic in the *y* direction with lattice constant *d*, the possible solutions for k_y, in the Fourier plane are restricted to $k_y=2n\pi/d$, where *n* is the number of the propagation mode. The condition in this case is $Y(y+d)=Y\left(y\right)$. Thus, we can write:

$$Y(y)=c_1\cos\left(\frac{2n\pi y}{d}\right). \tag{3}$$

For the *x* component of the wavevector, we have $k_x=\pm j\alpha_x$, where

$$\alpha_x=\sqrt{\frac{4n^2\pi^2}{d^2}-k^2}\approx\frac{2n\pi}{d}\,. \tag{4}$$

This follows from $k^2=k_x{}^2+k_y{}^2$ if we take into account that $d\ll\lambda/2$, which corresponds to the case where it is not possible to resolve details in the structure according to Abbe limit. The solutions for $X(x)$ are of the form $e^{-\alpha_x x}$ and $e^{\alpha_x x}$, which describe evanescent waves that only exist in the vicinity of the wires. The electric field for $x<0$ is then given by:

$$E_z=\left[E_{0i}e^{-jkx}+E_{0r}e^{jkx}+\sum_{n=1}^{\infty}A_n e^{\alpha_x x}\cos\left(\frac{2n\pi y}{d}\right)\right]e^{j\omega t}\,, \tag{5}$$

where E_{0i} and E_{0r} are the complex amplitudes of the incident and reflected waves, respectively, and the coefficients A_n account for the evanescent fields. For $x>0$ the electric field is obtained by combining the transmitted wave with the evanescent field:

$$E_z = \left[E_{0t} e^{-jkx} + \sum_{n=1}^{\infty} B_n e^{-\alpha_x x} \cos\left(\frac{2n\pi y}{d}\right) \right] e^{j\omega t} . \tag{6}$$

Close to the wires we have $|x| \ll \lambda$, where

$$E_z\left(x<0\right)e^{-j\omega t} \approx E_{0i}(1-jkx) + E_{0r}(1+jkx) + \sum_{n=1}^{\infty} A_n e^{\frac{2n\pi x}{d}} \cos\left(\frac{2n\pi y}{d}\right), \tag{7}$$

and

$$E_z\left(x>0\right)e^{-j\omega t} \approx E_{0t}(1-jkx) + \sum_{n=1}^{\infty} B_n e^{-\frac{2n\pi x}{d}} \cos\left(\frac{2n\pi y}{d}\right). \tag{8}$$

At the wires ($x=0$), the tangential component of the electric field must be continuous. We have:

$$E_{oi} + E_{0r} + \sum_{n=1}^{\infty} A_n \cos\left(\frac{2n\pi y}{d}\right) = E_{0t} + \sum_{n=1}^{\infty} B_n \cos\left(\frac{2n\pi y}{d}\right), \tag{9}$$

Which, according to Fourier's theory implies that:

$$E_{0t} = E_{0i} + E_{0r} \,,\; B_n = A_n \,. \tag{10}$$

For cylindrical wires, it is convenient to introduce the following function:

$$u(x,y) = \frac{1}{2}\ln\left[2\left(\cosh\left(\frac{2\pi x}{d}\right) - \cos\left(\frac{2\pi y}{d}\right)\right)\right], \tag{11}$$

which has the geometric property of being approximately constant on the surface of the thin wires. By Taylor expansion we find:

$$u = \pm\frac{\pi x}{d} - \sum_{n=1}^{\infty} \frac{e^{-\frac{2n\pi x}{d}}}{n} \cos\left(\frac{2n\pi y}{d}\right), \tag{12}$$

where the + sign holds for $x \geq 0$ and the - sign for $x \leq 0$. Based on this expansion, we can assume $A_n = B_n = A_1/n$ and write the electric field E_z in terms of *u* as

$$e^{-j\omega t} \approx \begin{cases} E_{0i}(1-jkx) + E_{0r}(1+jkx) - A_1\left(u\left(x,y\right) + \dfrac{\pi x}{d}\right), & x<0 \\ E_{0t}(1-jkx) - A_1\left(u\left(x,y\right) - \dfrac{\pi x}{d}\right). & x>0 \end{cases} . \tag{13}$$

To determine A_1 in terms of E_{0t} , we impose the continuity of $\frac{\partial E_z}{\partial x}$ at $x=0$. With the aid of the Equations (10) and (13), we find:

$$A_1 = \frac{jkd}{\pi} E_{0r} \,. \tag{14}$$

Up to this point, we have neglected the boundary conditions on the surface of the wires, where the tangential component of the electric field E_z must vanish. Considering wires with radius *a*, it results from (14) and using (13) with $x=0$ and $y=a$ that:

$$S_{11} = \frac{E_{0r}}{E_{0i}} = -\frac{1}{1 - \dfrac{jkd}{2\pi}\ln\left[2\left(1-\cos\left(\dfrac{2\pi a}{d}\right)\right)\right]} , \tag{15}$$

where we have also used (11) to determine $u(0,a)$. From network theory [22], we known that the *ABCD* parameters of a two port circuit consisting of an admittance $Y = G + jB$ are $A = D = 1$, $B = 0$ and $D = Y$, such that:

$$S_{11} = \frac{A + \frac{B}{Z_0} - CZ_0 - D}{A + \frac{B}{Z_0} + CZ_0 + D} = -\frac{1}{1 + \frac{2}{YZ_0}}. \tag{16}$$

Here, Z_0 is the characteristic impedance of the dielectric slab material. Hence, (16) is compatible with (15) and we can easily determine the admittance.

$$Y = j\frac{\lambda}{d}\frac{2Z_0^{-1}}{\ln\left[2\left(1-\cos\left(\frac{2\pi a}{d}\right)\right)\right]}. \tag{17}$$

2.2.2. Transmission Matrix of the Filter

Let T_1 and T_2 be the transmission matrices of a section of the slab of size $l/3$ and of a two-port network consisting of an admittance *Y*, respectively. Then, the *ABCD* parameters for the equivalent circuit in Figure 2 can be written in the form:

$$\begin{pmatrix} A & B \\ C & D \end{pmatrix} = T_1 T_2 T_1 T_2 T_1 = \begin{pmatrix} 1 + \frac{z_1}{z_3} & \left(z_1 + z_2 + \frac{z_1 z_2}{z_3}\right)Z \\ \frac{1}{Zz_3} & 1 + \frac{z_2}{z_3} \end{pmatrix}, \tag{18}$$

where z_1, z_2 and z_3 are the following normalized impedances:

$$z_1 = z_2 = EF^{-1},\ z_3 = F^{-1} \tag{19}$$

with coefficients *E* and *F* defined as:

$$E = \left(4 + Z^2Y^2\right)\cos^3\left(\beta l\right) - \left(3 + Z^2Y^2\right)\cos^3\left(\beta l\right) + j3ZY\sin\left(\beta l\right) - j4ZY\sin^3\left(\beta l\right) - 1, \tag{20}$$

and

$$F = 4ZY\cos^3\left(\beta l\right) - 2ZY\cos\left(\beta l\right) + j\left(3 + Z^2Y^2\right)\sin\left(\beta l\right) - j\left(4 + Z^2Y^2\right)\sin^3\left(\beta l\right). \tag{21}$$

Knowing the *ABCD* parameters of the network, one can determine the scattering matrix using the formulas for the conversion between two-port network parameters [22]:

$$S_{11} = \frac{2z_1 z_3 z + z_1^2 z - z^{-1}}{2(z_1 + z_3) + 2z_1 z_3 z + z_1^2 z + z^{-1}} \tag{22}$$

and

$$S_{12} = \frac{2z_3}{2(z_1 + z_3) + 2z_1 z_3 z + z_1^2 z + z^{-1}}. \tag{23}$$

Where $z = Z/Z_0$ is the normalized impedance of the slab with respect to free-space. By symmetry and reciprocity, we have $S_{11} = S_{22}$ and $S_{12} = S_{21}$.

2.3. Parameters' Choice

The theory described above was used to determine a starting point for the device parameters assuming a frequency window in the THz range between 395 and 455 GHz. From the theoretical model, it is possible to verify that the bandwidth decreases as *Y* increases. Moreover, as we approach the limit a/d=1/6, the *Y* will grows to ∞. However, this value cannot be reached due to the resistance of the wires and because in that limit the formula is only an approximation (formula is only valid for $d \ll \lambda$ and $a \ll d$). After performing several electromagnetic simulations to fit tune the initials parameters, a set that fulfill our requirements was found:

- Length (l) = 1.42 mm;
- Radius of the wires (a) = 0.2 μm;

- Distance between wires (d) ∈ [15; 20] μm.

The distance between wires is expressed as a range, since the previous study proved that it is possible to control the behavior of the filter in the desired frequency range by varying this parameter and to compress the device without deforming or cracking the structure [21]. As mentioned above, the device must have some robustness and a good degree of sensitivity, which means that one should consider materials that will be relatively easy to compress and transparent to THz radiation. According to [18], silicon and plastics such as high-density polyethylene (HDPE) and polytetrafluoroethylene (PTFE) are key terahertz materials since they fulfil the requirements mentioned above for the frequency band over 0.1 to 5 THz [23]. Naturally, the plastic materials will be a more suitable solution since silicon requires a substantially higher rate of compression. However, it is also important to consider some specific characteristics from the materials, taking into account the working principle, the design and the assembly of the filter.

HDPE possesses a linear structure with few branches lending to its optimal strength/density ratio. This thermoplastic presents some interesting features, such as: the sensitivity to stress cracking and the possibility to customize their physical properties through the molding process that is used in its manufacturing [24,25]. On the other hand, PTFE, which is a material widely used in industrial applications, also presents some interesting features, such as: weatherability and the capability of maintaining high strength, toughness and self-lubrication at low temperatures down to 5 K, as well as good flexibility at temperatures above 194 K [26].

Considering their properties and the fact that both have low losses and low dispersion in the frequency region of the THz, as mentioned above, these materials in fact constitute good candidates to be used in the assembly of the proposed device.

3. Mechanical Simulations

In this section, the main purpose is to understand how to mechanically model the filter in order to find out how much force and current it will take to make the device compress up to 25% according to the materials used for its assembling, since beyond that ratio the device presents saturation in the frequency response. The finite element method was used for the simulation of the filter according to the geometry that was presented previously. This solving technique is an efficient method that can provide approximated solutions to partial differential equations and it is widely used to solve problems in several areas, such as: electromagnetics, structural analysis, among others [27].

3.1. Device's Modelling

Since the device response analysis lies on two components, namely electromagnetic and mechanic, it will be necessary to model the filter from both perspectives. The first one can be easily simulated based on the circuit theory presented in the previous section. However, the latter requires a realistic model according to the geometry specifications considered in the device design. To satisfy this requirement, the Gmsh and Elmer software were used to model the filter [28,29]. Through the Gmsh, it was possible to design the filter and generate its corresponding mesh. After importing the filter's mesh into the Elmer solver, materials and boundary conditions associated with the elasticity equation must be defined. Knowing the range to be tested for the wire spacing and the lateral section area of the device, it is possible to determine the level of compression needed to obtain the required wire spacing. This is possible to achieve, knowing that the materials have certain physical properties, some of which are especially important for calculating the displacement derived from the compression applied to the device, among them: density, Young's modulus and Poisson's ratio [30]. The relation between the displacement and the force applied to an elastic material is characterized by the well-known equation:

$$\frac{F}{A} = E \times \frac{\Delta l}{l}, \tag{24}$$

where F/A is the force applied per unit area (stress), E is the Young's modulus and $\Delta l/l$ is the extension per unit length (strain). The stress is expressed in Newtons per square meter (Nm-2) or in Pascals (Pa) and the Young's modulus is usually expressed in GPa. Last but not least, the strain has no units, because it is just a ratio between the extension and the original length of the object. In Table 1, the values of the properties that mechanically characterize each material that comprise the device are presented [31].

Table 1. Simulation parameters of the materials of the proposed filter.

Material	Density (Kg/m³)	Young's Modulus (GPa)	Poisson's Ratio
Gold	19300	78	0.44
HDPE	641	0.8	0.46
PTFE	2100	0.3	0.46

3.2. Generation of the Required Force to Compress the Device

Mechanical stress can be monitored based on the variation of the distance between the wires caused by the impact of external factors on the structure. The required force to compress the device can be generated by passing an electric current through a coil placed on a plunger, as can be seen in Figure 4.

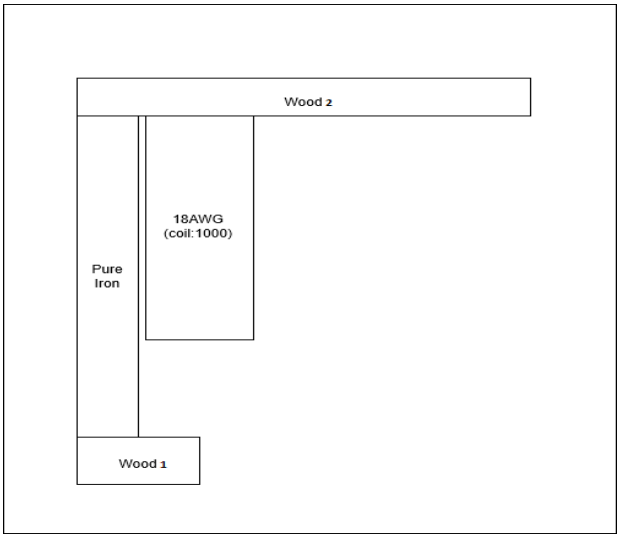

Figure 4. Scheme of the magnetic circuit to be modeled on a finite element method magnetics (FEMM) solver.

The amount of electric current to generate such force can be obtained from numerical simulations, because iron is a ferromagnetic material and, therefore, the relation between magnetic induction **B** and the magnetic field **H** is not linear. Since the FEMM solver is based on the principle of symmetry, we only draw part of the device (as shown in the Figure 4) [32]. The core of the plunger is made of iron and it is surrounded by a coil (1000 turns of copper wire), which will induce the movement of the core. The base (wood 1) and the surface (wood 2) that contacts with the device would ideally consist of wood, which in turn has air-like magnetic properties.

This circuit was simulated, according to the dimensions of the lateral section of the device and considering the data in Table 2.

Table 2. Simulation parameters of the magnetic circuit in FEMM.

L_c	W_c	L_p	Wp	σ	g	N_{turns}	$L_{wood\,1}$	$W_{wood\,1}$	$L_{wood\,2}$	$W_{wood\,2}$
0.27 mm	0.1 mm	0.05 mm	0.37 mm	10.44 MS/m	0.005 mm	1000	0.03 mm	0.079 mm	0.03 mm	0.71 mm

In this table, L_c is the coil length, W_c is the coil width, L_p is the plunger length, W_p is the plunger width, σ is the electrical conductivity of the iron, g is the length of the gap between the coil and the plunger, N_{turns} is the number of turns of the coil, L_{wood1} is the length of the base of the plunger, W_{wood1} is the width of the base of the plunger, L_{wood2} is the length of the surface of the plunger and W_{wood2} is the width of the surface of the plunger, respectively.

4. Results

In this section, the results from the simulations based on the design of the filter for each assembling hypothesis will be presented. Two analyses of the behavior from the electromagnetic and mechanical point of view will be carried out.

By analyzing the data, we will also discuss how it will be possible to apply the desired compression level to the devices and thus control the distance between wires.

4.1. Return Loss and Insertion Loss in the Frequency Domain as a Function of Distance between Wires

After the conception and presentation of the theoretical study of the working principle of the filter, it is necessary to corroborate the accuracy of the conceived theoretical model through simulations, as well as to analyse some relevant issues such as: the dynamic range, the periodicity of the shifts of resonance frequency and the evolution of the bandwidth of the device under compression.

Knowing that HDPE and PTFE have different relative permittivity constants, it will be necessary to analyse the filter for both assembling cases. Note that HDPE has a relative dielectric constant $\varepsilon_r = 2.4$ and PTFE posseses $\varepsilon_r = 2.1$ [26]. The losses were not considered due to the characteristics of these materials, as highlighted in Section 2.

The resonance frequency (f_1) will be shifted to higher frequencies as the filter is compressed. The reduction in the distance between wires occurs with a step size of 0.5 µm.

4.1.1. HDPE

Figures 5 and 6 shows return losses (RL) and insertion losses (IL) in the frequency domain as a function of applied compression for the HDPE host medium. These quantities were calculated based on the results obtained for the scattering parameters from the simulations. Since the structure is invariant to port swapping in the propagation direction, we might consider the following formulas $RL = -20\log_{10}\left(|S_{11}|\right)$ and $IL = -20\log_{10}\left(|S_{12}|\right)$, respectively [22]. The device resonance, without compression, is at 408 GHz, but, when we imposed a full compression (25%), the resonance changes to 411 GHz. In every curve, each reduction of 0.5 µm in the distance between wires causes an increase of 278 MHz in the resonance frequency, which is followed by an average bandwidth reduction at 3 dB of 111 MHz. Considering this data, it is possible to state that, between these two extreme cases, there was a shift of 3 GHz in resonant frequency and a reduction in the bandwidth at 3 dB of 1.1 GHz (a decrease of more than 50% when compared with the initial value without compression). Some saturation and distortion in the filter response are expected for this reason.

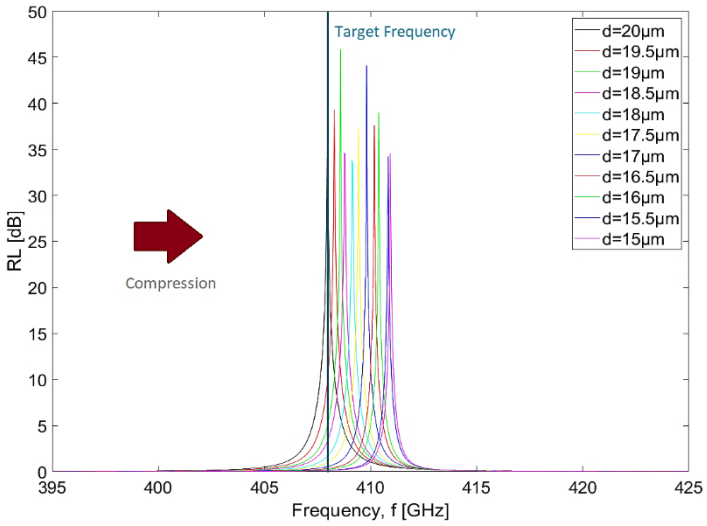

Figure 5. Return loss in the frequency domain as a function of applied compression for high-density polyethylene (HDPE) host medium.

In Figures 5 and 6, there is a vertical line identifying the target frequency (408 GHz) and, by analyzing both of them, it can be seen that the device presents an excellent dynamic range along this curve. This means that, as compression is applied to the device, it will go from full transparency ($|S_{11}|$=0) to full opacity ($|S_{11}|$=1). Therefore, it is possible to conclude that the bandwidth decreases and the selectivity increases as the compression is applied to the filter.

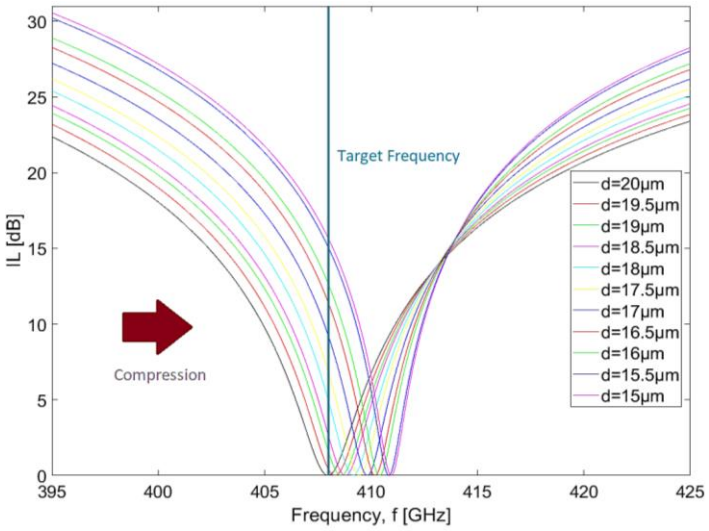

Figure 6. Insertion loss in the frequency domain as a function of applied compression for HDPE host medium.

The FWHM decreases from 1.2 GHz (without compression) to 0.55 GHz (maximum compression) [5]. The quality factor can be calculated as the ratio between the resonance frequency and the FWHM. We found that the *Q* factor ranges between *Q*≈340 for the case without compression and *Q*≈747 when maximum compression is applied. Considering the same criteria that was used to analyze the previous metrics, we found that the dephasing time (t_d) of induced line shapes decreases from 1.5797 to 0.724 μs [5]. Moreover, the figure of merit can be defined as the number of passbands inside the range of tuning, which can be computed as:

$$FoM = \frac{\omega_0^{up} - \omega_0^{low}}{\sqrt{\Delta\omega_f^{up}\Delta\omega_f^{low}}}, \tag{25}$$

where $\omega_0^{up} = 2.5824\times10^{12}$ is the uppermost resonant frequency, $\omega_0^{low} = 2.5635\times10^{12}$ is the lowermost resonant frequency, $\Delta\omega_f^{up} = 3.4558\times10^{9}$ is the uppermost passband width and $\Delta\omega_f^{low} = 7.5398\times10^{9}$ is the lowermost passband width, respectively [6]. We estimated a *FoM*≈3.6927. The insertion losses (*IL*) are practically zero as the resonance frequency is shifted by the compression on the device. The high value of the return losses (*RL*) means that the reflected energy is very small when compared to the incident wave energy. These results show that the higher the compression level applied, the greater the selectivity of the device.

4.1.2. PTFE

The results from the electromagnetic simulations for the filter assembled with PTFE are shown in Figures 7 and 8. By observing both figures, it is possible to conclude that the behavior is slightly the same when compared to the case of HDPE. However, the resonances now occur at higher frequencies, since the parameters that characterize the material are different. Note that, without compression, the device presents a resonance at 437.5 GHz, which will change to 440.7 GHz when full compression is applied. In every curve, each reduction of 0.5 μm in the distance between wires causes an increase of 320 MHz in the resonance frequency, which is followed by an average bandwidth reduction at 3 dB of 122 MHz.

Considering these data, it is possible to state that the application of maximum compression caused a total shift of 3.2 GHz in the resonance frequency and a reduction in the bandwidth at 3 dB of 1.1 GHz (a decrease of 50% when compared with the initial value without compression). In Figures 7 and 8, there is a vertical line identifying the target frequency (437.5 GHz) and, by analyzing both of them, it can be seen that the filter presents a slightly better dynamic range when compared to the case of the device assembled with HDPE. The FWHM decreased from 1.3 GHz (absence of compression) to 0.65 GHz (maximum compression), and, similar to what was observed previously, the progression of the resonance frequency as the filter is compressed is also approximately linear. The quality factor increased from *Q*≈337 (absence of compression) to *Q*≈678 (maximum compression) as the distance between wires is reduced. Considering the same criteria that was used to analyze the previous metrics, we found that the dephasing time decreases from t_d =1.7114

μs to t_d=0.8557 μs. Moreover, this filter presents an *FoM*≈3.4811, which was calculated by using Equation (25) and considering that $\omega_0^{up} = 2.7690 \times 10^{12}$, $\omega_0^{low} = 2.7489 \times 10^{12}$, $\Delta\omega_f^{up} = 4.0841 \times 10^9$ and $\Delta\omega_f^{low} = 8.1681 \times 10^9$, respectively. Globally, these results are similar to what was obtained for the HDPE.

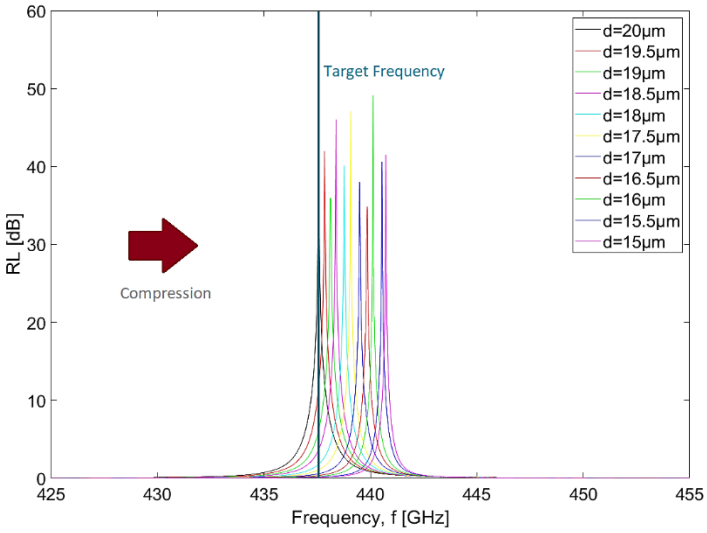

Figure 7. Return loss in the frequency domain as a function of applied compression for polytetrafluoroethylene (PTFE) host medium.

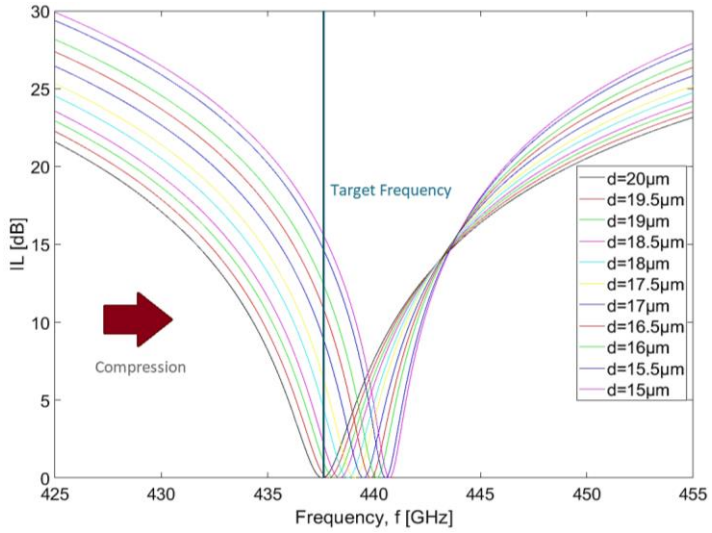

Figure 8. Insertion loss in the frequency domain as a function of applied compression for PTFE host medium.

4.2. Reduction in the Distance between Wires as a Function of Required Current

After performing the analysis of the electromagnetic component, we will focus on the analysis of the mechanical component. In the following subsections, we intend to understand how much force it will take to make the device compress up to 25% according to the materials used for its assembly and, knowing that there is a possibility of controlling the compression magnetically, what will be the current required to reach each level of compression. Through preliminary mechanical simulations, we found out that 70 wires per array are sufficient to obtain the desired behavior of the device. We also decided to study how the number of wires influences its response.

4.2.1. HDPE

Considering the theory associated with mechanical simulations, it is possible to predict the amount of force required to cause the desired distance between wires to be reduced in each case. By combining the theory used in the Elmer solver

with the theory of magnetic circuits based on which the FEMM software solves the problems, we are able to discover the current required to cause the compression that allows the distance between wires to decrease.

By analysing Figures 9 and 10, it is observed that, as expected, the higher the force to be applied to the device, the higher the current to be supplied to the magnetic circuit. To fully compress the device with 70 wires, we should supply 0.56 A to the magnetic circuit.

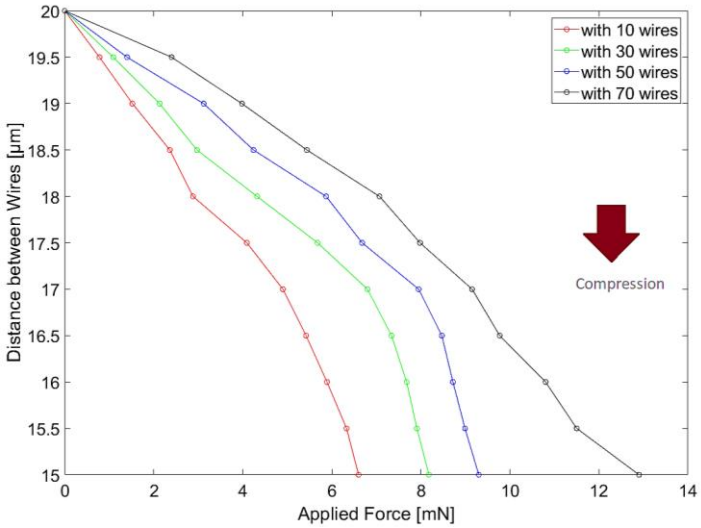

Figure 9. Reduction in the distance between wires as a function of applied force and current for 10, 30, 50 and 70 wires and a filter assembled with HDPE.

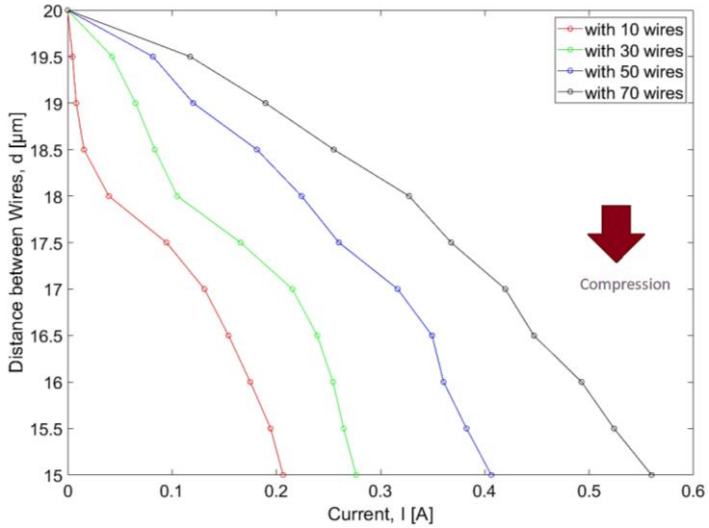

Figure 10. Reduction in the distance between wires as a function of applied current for 10, 30, 50 and 70 wires and a device assembled with HDPE.

4.2.2. PTFE

Similar to the previous case, we obtained from the Elmer solver the range of forces to be applied to the filter in order to achieve each compression state. The results are presented in Figure 11. After that, we obtained from the FEMM solver the range of currents to be supplied to the magnetic circuit in order to compress the device according to the previous data, as can be seen in Figure 12.

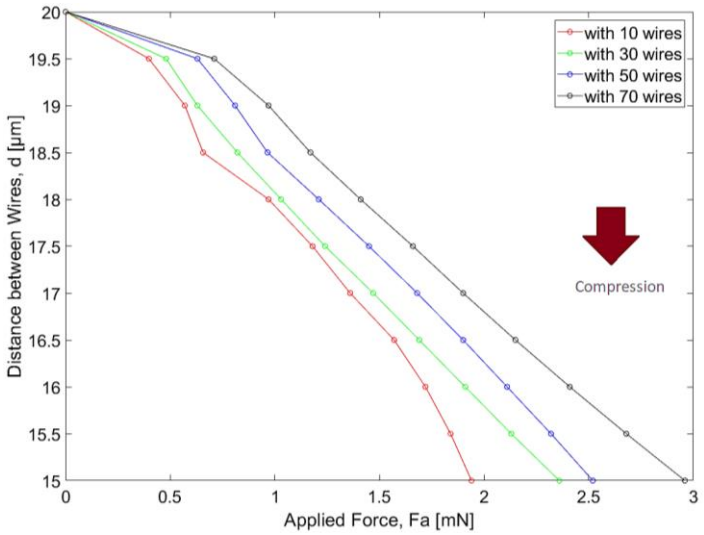

Figure 11. Reduction in the distance between wires as a function of applied force and current for 10, 30, 50 and 70 wires and a filter assembled with PTFE.

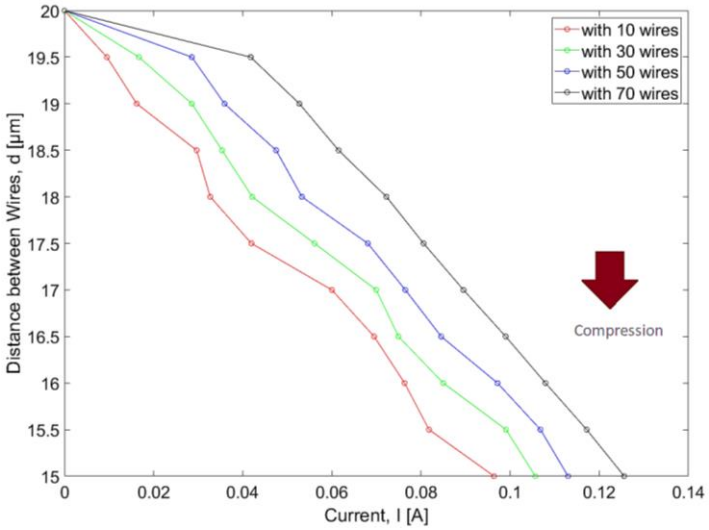

Figure 12. Reduction in the distance between wires as a function of applied current for 10, 30, 50 and 70 wires and a device assembled with PTFE.

The curves for the applied force and the required current have the same slope for each scenario, in which the number of wires is increased. However, in this case of PTFE, both the force and the current values are much lower. We should note that, as the range of forces to be applied for each typology is different, the range of currents to be supplied will also be different. In order to achieve a full compression of the device with 70 wires, we should supply the magnetic circuit with 0.125 A, which is substantially lower than the one required for HDPE.

4.3. Reflectance and Transmittance as a Function of Applied Force

Finally, after performing electromagnetic and mechanical simulations, we can now use the information we obtained from both components to illustrate the reflectance/trasmittance as a function of the force applied to the filter for each host material that can be used to build the device. The following graphs show us the relationship between these quantities. It should be noted that the resonance frequency was fixed taking into account the case without compression ($f_{t_{HDPE}}$ =408 GHz and $f_{t_{PTFE}}$ =437.5 GHZ, respectively).

4.3.1. HDPE

Through a careful analysis of Figures 13 and 14, we observe that, by increasing the number of wires per array, the more linear the response of the filter will be. Independently of the curve under analysis, the device response presents some saturation for high values of applied force. If we focus on the designs with 50 or more wires, we observe saturation for values greater than 8 mN. In spite of this fact, the device can reflect almost all of the incident wave (more than 90%) and, therefore, we can assume that the device presents an approximately linear response in the dynamic range under study.

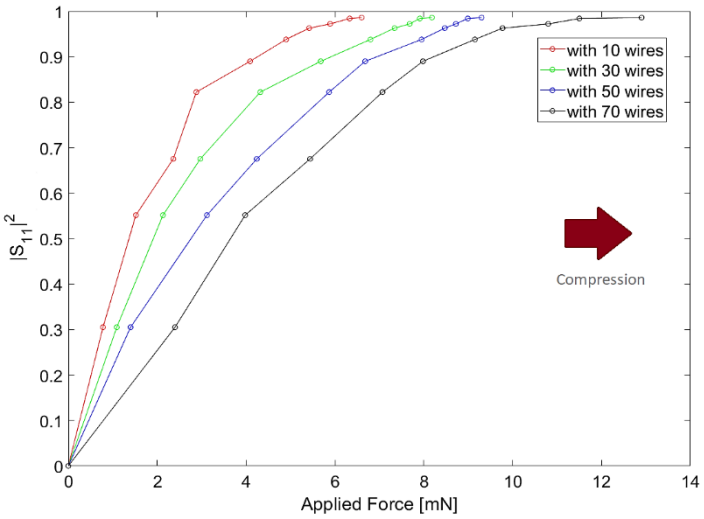

Figure 13. Reflectance as a function of applied force for 10, 30, 50 and 70 wires and a filter assembled with HDPE.

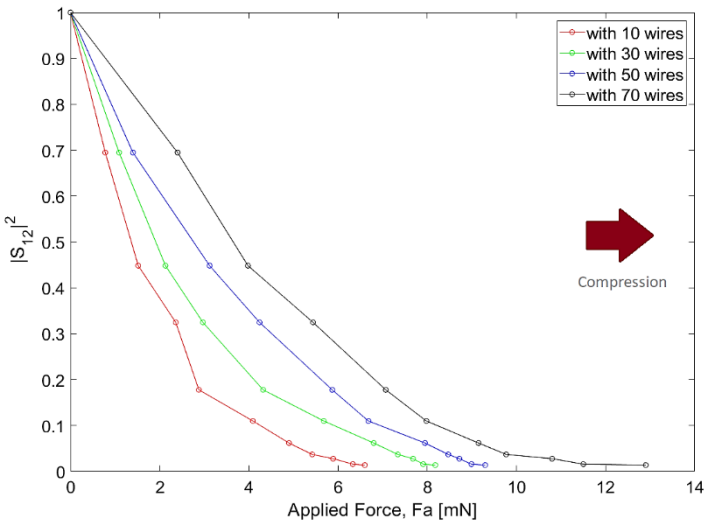

Figure 14. Transmittance as a function of applied force for 10, 30, 50 and 70 wires and a filter assembled with HDPE.

Let us consider the case, in which we have a filter with 70 wires per array and an applied force of around 8 mN (beyond this value we enter in a saturation zone). Through Figure 9, we can see that the distance between wires for 8 mN of applied force is d=17.5 μm. In turn, by analyzing Figures 5 and 6, we observe that the resonance frequency of the filter is around 409.4 GHz. Table 3 shows the filter quality and performance parameters for the scenario under study:

Table 3. Filter quality and performance parameters considering a distance between wires d = 17.5 μm.

FWHM (GHz)	Q	t_d (μs)
0.9	455	1.1848

Although these metrics do not change with the increase in the number of wires, it will be important to quantify the sensitivity of the filter $\left(S = \frac{1 - S_{11}}{\Delta F}\right)$, as we vary this parameter [21]. Table 4 illustrates the sensitivity variation, considering a distance between wires d=17.5 μm and a reflectance S_{11} =0.8901, as the number of wires per array increases:

Table 4. Calculation of the sensitivity of the filter considering a distance between wires d=17.5 μm.

Number of Wires	ΔF (mN)	Sensitivity (N)
10	4.09	26.87
30	5.68	19.35
50	6.68	16.45
70	8	13.74

The data from Table 4 shows that the sensitivity and linearity of the response of the device vary in opposite ways. Therefore, to have a sensitive device with an approximately linear response, it is necessary to establish a trade-off between these requirements.

4.3.2. PTFE

The results for the PTFE host are shown in Figures 15 and 16. As can be seen, the curves obtained for this device model are not as linear as we observed in the previous case. When compared to the device built with HDPE, this filter is more sensitive, since it can cover the entire dynamic range with much less applied force (only 21.4% of the required force to fully compress the device built with HDPE). In spite of the linearity issues, we have a linear operating region that allows us to work with reflectances between 0.25 and 0.85, depending on the requirements of the application. For values of applied force greater than 1.20 mN, some saturation of the device response (independently of the curve under analysis) is observed.

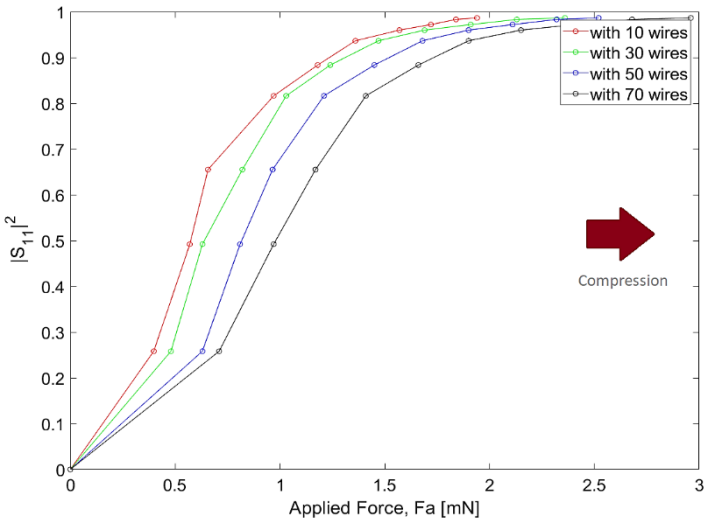

Figure 15. Reflectance as a function of applied force for 10, 30, 50 and 70 wires and a filter assembled with PTFE.

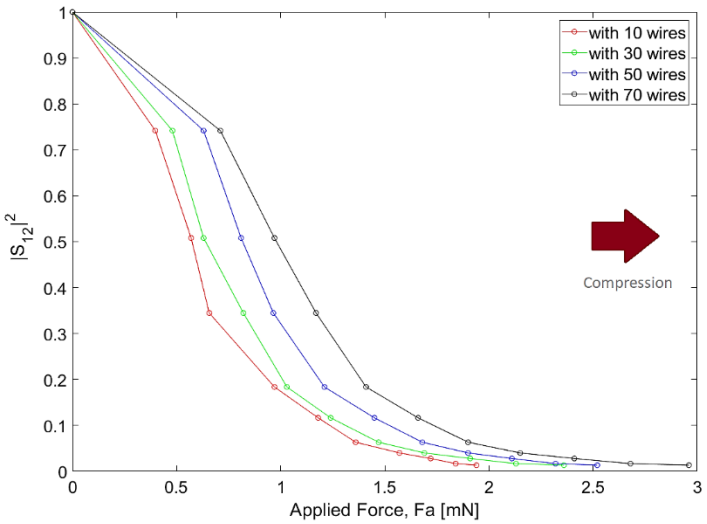

Figure 16. Transmittance as a function of applied force for 10, 30, 50 and 70 wires and a filter assembled with PTFE.

Focusing on the scenario, in which we have a filter containing 70 wires per array and a limitation of the applied force of about 1.2 mN, we can see from Figure 11 that the distance between wires for 1.2 mN of applied force is d=18.5 μm. In turn, by analyzing Figures 7 and 8, we observe that the resonance frequency of the filter is around 438.4 GHz. Table 5 shows the filter quality and performance parameters for the scenario under study:

Table 5. Filter quality and performance parameters considering a distance between wires d=18.5 μm.

FWHM (GHz)	Q	t_d (μs)
1.1	399	1.4481

In Table 6, the relationship between filter sensitivity and the increase in the number of wires is shown, considering the approach used in the previous case:

Table 6. Calculation of the sensitivity of the filter considering a distance between wires d = 18.5 μm a reflectance S_{11} =0.6553.

Number of Wires	ΔF (mN)	Sensitivity (N)
10	0.657	524.66
30	0.821	419.85
50	0.965	357.2
70	1.2	287.25

The filter assembled with PTFE requires less force to be compressed and is very sensitive. However, the data from Table 6 suggest that the relationship between sensitivity and linearity of the response of the device is the same as was observed for the case where the filter was assembled with HDPE. Given the trade-off between these requirements, we should consider the filter assembled with HDPE, since it has the same good dynamics as the filter assembled with PTFE but has a much more linear response than the latter.

5. Conclusions

This work aimed to study a reconfigurable THz filter design, using frequency selective structures based on metamaterial resonators, so that it can be used in the development of sensor devices. The proposed filter is composed by two arrays of wires to provide greater cancellation of harmonics, higher dynamic range and enhanced frequency selectivity. The resonant effects result from carefully tuning the wire radius and the distance between wires, which can be altered so that only evanescent modes exist in the vicinity of the structure, allowing us to control the energy transmission and reflection. Due to its simplicity, this filter design is especially suited for the implementation of reconfigurable THz filters and optical modulators, since it transits from situations in which it presents a full transparency $\left(|S_{11}|=0\right)$ for a full opacity $\left(|S_{11}|=1\right)$.

Two assembling hypotheses with different thermoplastic polymers materials were analyzed. The choice of these materials was essentially due to the fact that they are relatively easy to compress and exhibit low losses and low dispersion for the frequency band over 0.1 to 5 THz. Numerical simulation using the finite element method allowed us to study the variation of the electromagnetic and mechanical response of the device as compression was applied.

Our results corroborated our theoretical model by proving that it is possible to design a filter with a very good dynamic range and a high sensitivity by following the proposed methodology. The model designed with HDPE presented a quite linear response when compared to the one designed with PTFE, which is more sensitive. This might be explained by the different electromagnetic and mechanical properties of these materials.

For the model composed by HDPE, the required force to be applied to cause a reduction in the distance between wires is four times greater, when compared to the one that is required by the model with PTFE. By analyzing the data from the simulations, it was also determined that the relation between wire spacing and the required current to compress the device is the same, when compared to the amount of force that should be applied to verify a shift on the resonance frequency.

Author Contributions: All authors contributed equally to the article. All authors have read and agreed to the published version of the manuscript.

Conceptualization, J.P.P, N.S. and M.A. R.; Data curation, J.P.P; Formal analysis, J.P.P, N.S. and M.A. R.; Funding acquisition, N.S. and M.A.R.; Investigation, J.P.P, N.S. and M.A. R.; Methodology J.P.P, N.S. and M.A. R.; Project administration, N.S. and M.A.R.; Resources, N.S. and M.A.R; Software, J.P.P.; Supervision, N.S. and M.A.R; Validation, J.P.P, N.S. and M.A. R.; Visualization, J.P.P.; Writing – original draft, J.P.P.; Writing – review & editing, J.P.P, N.S. and M.A. R. All authors have read and agreed to the published version of the manuscript.

Funding: This research was partially funded by the FCT—Fundação para a Ciência e Tecnologia and Instituto de Telecomunicações (IT) under projects TUBITAK/0002/2014 and UIDB/EEA/50008/2020. Moreover, João Pedro Pavia had a funding provided by ISCTE-University Institute of Lisbon under the grant ISTA-BM-PDCTI-2019.

Acknowlegements: The authors acknowledge the support of FCT, IT and ISCTE—University Institute of Lisbon, as described above in funding.

Conflicts of Interest: The funders had no role in the design of the study; in the collection, analyses, or interpretation of data; in the writing of the manuscript, or in the decision to publish the results.

References

1. Xu, W.; Xie, L.; Ying, Y. Mechanisms and applications of terahertz metamaterial sensing: A review. *Nanoscale* **2017**, *9*, 13864–13878.
2. Salim, A.; Lim, S. Review of Recent Metamaterial Microfluidic Sensors. *Sensors* **2018**, *18*, 232.
3. Gerislioglu, B.; Ahmadivand, A.; Pala, N. Tunable plasmonic toroidal terahertz metamodulator. *Physical Review B* **2018**, *97*, 161405.
4. Ahmadivand, A.; Gerislioglu, B.; Ahuja, R.; Kumar Mishra, Y. Terahertz plasmonics: The rise of toroidal metadevices towards immunobiosensings. *Mater. Today* **2020**, *32*, 108–130.
5. Ahmadivand, A.; Gerislioglu, B.; Ramezani, Z. Gated graphene island-enabled tunable charge transfer plasmon terahertz metamodulator. *Nanoscale* **2019**, *11*, 8091–8095.
6. Ferraro, A.; Zografopoulos, D.; Caputo, R.; Beccherelli, R. Periodical Elements as Low-Cost Building Blocks for Tunable Terahertz Filters. *IEEE Photonics Technol. Lett.* **2016**, *28*, 2459–2462.
7. Ferraro, A.; Tanga, A.; Zografopoulos, D.; Messina, G.; Ortolani, M.; Beccherelli, R. Guided mode resonance flat-top bandpass filter for terahertz telecom applications. *Optics Lett.* **2019**, *44*, 4239.
8. Sun, D.; Qi, L.; Liu, Z. Terahertz broadband filter and electromagnetically induced transparency structure with complementary metasurface. *Results Phys.* **2020**, *16*, 102887.
9. Sanphuang, V.; Ghalichechian, N.; Nahar, N.; Volakis, J. Reconfigurable THz Filters Using Phase-Change Material and Integrated Heater. *IEEE Trans. Terahertz Sci. Technol.* **2016**, *6*, 583–591.
10. Chang, C.; Huang, L.; Nogan, J.; Chen, H. Invited Article: Narrowband terahertz bandpass filters employing stacked bilayer metasurface antireflection structures. *APL Photonics* **2018**, *3*, 051602.
11. Zaitsev, A.; Grebenchukov, A.; Khodzitsky, M. Tunable THz Graphene Filter Based on Cross-In-Square-Shaped Resonators Metasurface. *Photonics* **2019**, *6*, 119.
12. Ferraro, A.; Zografopoulos, D.; Caputo, R.; Beccherelli, R. Guided-mode resonant narrowband terahertz filtering by periodic metallic stripe and patch arrays on cyclo-olefin substrates. *Sci. Rep.* **2018**, *8*, 1–8.
13. Cong, L.; Tan, S.; Yahiaoui, R.; Yan, F.; Zhang, W.; Singh, R. Experimental demonstration of ultrasensitive sensing with terahertz metamaterial absorbers: A comparison with the metasurfaces. *Appl. Phys. Lett.* **2015**, *106*, 031107.
14. Zhang, N.; Song, R.; Hu, M.; Shan, G.; Wang, C.; Yang, J. A Low-Loss Design of Bandpass Filter at the Terahertz Band. *IEEE Microw. Wirel. Compon. Lett.* 2018, *28*, 573–575.

15. Němec, H.; Duvillaret, L.; Garet, F.; Kužel, P.; Xavier, P.; Richard, J.; Rauly, D. Thermally tunable filter for terahertz range based on a one-dimensional photonic crystal with a defect. *J. Appl. Phys.* **2004**, *96*, 4072–4075.
16. Ko, Y.; Magnusson, R. Flat-top bandpass filters enabled by cascaded resonant gratings. *Opt. Lett.* **2016**, *41*, 4704.
17. Yamada, K.; Lee, K.; Ko, Y.; Inoue, J.; Kintaka, K.; Ura, S.; Magnusson, R. Flat-top narrowband filters enabled by guided-mode resonance in two-level waveguides. *Opt. Lett.* **2017**, *42*, 4127.
18. Melo, A.; Gobbi, A.; Piazzetta, M.; da Silva, A. Cross-Shaped Terahertz Metal Mesh Filters: Historical Review and Results. *Adv. Opt. Technol.* **2012**, *2012*, 1–12.
19. Ozbey, B.; Unal, E.; Ertugrul, H.; Kurc, O.; Puttlitz, C.; Erturk, V.; Altintas, A.; Demir, H. Wireless Displacement Sensing Enabled by Metamaterial Probes for Remote Structural Health Monitoring. *Sensors* **2014**, *14*, 1691–1704.
20. Chen, J.; Kaushik, S. Terahertz Interferometer That Senses Vibrations Behind Barriers. *IEEE Photonics Technol. Lett.* **2007**, *19*, 486–488.
21. Pavia, J.P.; Ribeiro, M.; Souto, N. Design of Frequency Selective Devices for the THz Domain with Applications on Structural Health Monitoring. In Proceedings of the 2019 Thirteenth International Congress on Artificial Materials for Novel Wave Phenomena (Metamaterials), Rome, Italy, 16–21 September 2019.
22. Pozar, D. *Microwave Engineering*; John Wiley & Sons: Hoboken, NJ, USA, 2012.
23. Naftaly, M.; Vieweg, N.; Deninger, A. Industrial Applications of Terahertz Sensing: State of Play. *Sensors* **2019**, *19*, 4203.
24. Cunningham, P.; Valdes, N.; Vallejo, F.; Hayden, L.; Polishak, B.; Zhou, X.; Luo, J.; Jen, A.; Williams, J.; Twieg, R. Broadband terahertz characterization of the refractive index and absorption of some important polymeric and organic electro-optic materials. *J. Appl. Phys.* **2011**, *109*, 043505–043510.
25. Madhu, G.; Bhunia, H.; Bajpai, P.; Chaudhary, V. Mechanical and morphological properties of high density polyethylene and polylactide blends. *J. Polym. Eng.* **2014**, *34*, 813–821.
26. Dhanumalayan, E.; Joshi, G. Performance properties and applications of polytetrafluoroethylene (PTFE)—a review. *Adv. Compos. Hybrid Mater.* **2018**, *1*, 247–268.
27. Reddy, J. *Introduction to the Finite Element Method*; McGraw-Hill: New York, NY, USA, 2006.
28. Gmsh. Available online: http://gmsh.info/doc/texinfo/gmsh.html (accessed on 23 March 2020).
29. Råback, P.; Byckling, M.; Pursula, A.; Ruokolainen, J.; Zwinger, T.; Malinen, M. CSC-Documentation-Elmer Sover. Available online: https://www.csc.fi/web/elmer/documentation (accessed on 23 March 2020).
30. Abazari, A.; Safavi, S.; Rezazadeh, G.; Villanueva, L. Modelling the Size Effects on the Mechanical Properties of Micro/Nano Structures. *Sensors* **2015**, *15*, 28543–28562.
31. Engineering ToolBox. Available online: https://www.engineeringtoolbox.com (accessed on 23 March 2020).
32. Finite Element Method Magnetics: Documentation. Available online: http://www.femm.info/wiki/Documentation/ (accessed on 23 March 2020).

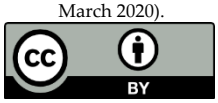

Chapter 3 – Precoded Generalized Spatial Modulation for Downlink MIMO Transmissions in Beyond 5G Networks

The design of MIMO schemes capable of achieving both high spectral and energy efficiency constitutes a challenge for next-generation wireless networks. GSM constitutes a particular case of IM, which is suitable for large scale MIMO antennas schemes enabling greater energy efficiency with ease of implementation. Considering that the information is encoded in the combination of active antennas and in the modulated symbols transmitted in the active antennas, GSM can also achieve a greater SE than single antenna communications. MIMO schemes based on GSM have been widely considered as a powerful technique to achieve that purpose. In line with this topic, we proposed a MU GSM MIMO system, which relies on the transmission of precoded symbols from a base station to multiple receivers. The information is divided in such a way that part of the data will be used to select an AI from a total $N_{comb} = 2^{\left\lfloor \log_2\left(\binom{N_s}{N_a}\right)\right\rfloor}$ AICs that are available per user. To increase the SE of the transmission, the remaining data will be mapped onto N_a different complex-valued M-QAM symbols (M=1024 symbols are considered) which are sent on different antennas. . To remove inter-user interference and transform the MU transmission into several independent SU links, a BD precoder is applied at the BS, while a modified and improved version of the low-complexity SU GSM detector presented in [33] is used at the receiver. Simulation results based on a C-RAN showed that the proposed approach can exploit efficiently a large number of antennas deployed at the transmitter and it can also provide large gains when compared to conventional MU-MIMO schemes with identical spectral efficiencies. Based on the simulated C-RAN scenario, the potential gains in terms of throughput and coverage considering perfect and imperfect channel estimation were also studied.

Some paper details:

- Title: Precoded Generalized Spatial Modulation for Downlink MIMO Transmissions in Beyond 5G Networks;
- Date of publication: 22 September 2020;
- Journal: Applied Sciences;

- Scimago/Scopus Journal Ranking: Quartile 2;
- Publisher: MDPI.

applied sciences

MDPI

Article

Precoded Generalized Spatial Modulation for Downlink MIMO Transmissions in Beyond 5G Networks

João Pedro Pavia [1,2,*], Vasco Velez [1,2], Bernardo Brogueira [1,2], Nuno Souto [1,2] and Américo Correia [1,2]

[1] Department of Information Science and Technology, ISCTE—Instituto Universitário de Lisboa, Av. das Forças Armadas, 1649-026 Lisbon, Portugal; Bernardo_Brogueira@iscte-iul.pt (B.B.); Vasco_Velez@iscte-iul.pt (V.V.); Nuno.Souto@iscte-iul.pt (N.S.); americo.correia@iscte.pt (A.C.)

[2] Radio Systems Group, Instituto de Telecomunicações, Av. Rovisco Pais, 1049-001 Lisbon, Portugal

* Correspondence: Joao_Pedro_Pavia@iscte-iul.pt

Appl. Sci. 2020, 10(18), 6617; https://doi.org/10.3390/app10186617

Received: 24 August 2020; Revised: 14 September 2020; Accepted: 16 September 2020 / Published: 22 September 2020

Abstract: The design of multiple input multiple output (MIMO) schemes capable of achieving both high spectral and energy efficiency constitutes a challenge for next-generation wireless networks. MIMO schemes based on generalized spatial modulations (GSM) have been widely considered as a powerful technique to achieve that purpose. In this paper, a multi-user (MU) GSM MIMO system is proposed, which relies on the transmission of precoded symbols from a base station to multiple receivers. The precoder's design is focused on the removal of the interference between users and allows the application of single-user GSM detection at the receivers, which is accomplished using a low-complexity iterative algorithm. Link level and system level simulations of a cloud radio access network (C-RAN) comprising several radio remote units (RRUs) were run in order to evaluate the performance of the proposed solution. Simulation results show that the proposed GSM MU-MIMO approach can exploit efficiently a large number of antennas deployed at the transmitter. Moreover, it can also provide large gains when compared to conventional MU-MIMO schemes with identical spectral efficiencies. In fact, regarding the simulated C-RAN scenario with perfect channel estimation, system level results showed potential gains of up to 155% and 139% in throughput and coverage, respectively, compared to traditional cellular networks. The introduction of imperfect channel estimation reduces the throughput gain to 125%.

Keywords: B5G; generalized spatial modulation (GSM); precoder design; massive multiple input multiple output (MIMO); quadrature amplitude modulation (QAM) constellations

1. Introduction

Considering the technological advances over the last decades, the next generation of wireless communications is expected to follow this trend with a significant increase in system robustness (SR), spectral efficiency (SE) and energy efficiency (EE). In recent years, new emerging techniques have appeared in order to meet the increasingly challenging requirements of beyond fifth generation (B5G) communication systems, such as non-orthogonal multiple access (NOMA) schemes like Signaling Aided Sparse Code Multiple Access [1] or index modulations (IM). IM has received significant attention due to its ability to activate a subset of certain elements of communication resources, namely antennas, subcarriers, and slots [2,3]. Generalized spatial modulation (GSM) constitutes a particular case of IM, which is suitable for large scale multiple input multiple output (MIMO) antennas schemes enabling greater EE with ease of implementation [4,5]. Considering that the information is encoded in the combination of active antennas and, also in the modulated symbols transmitted in the active antennas, GSM can also achieve a greater SE than single antenna communications.

GSM can be considered as a compromise between conventional MIMO and simple radio frequency (RF) transmissions, since only a subset of the available transmission antennas is active for a certain period of time, thus

reducing the number of RF chains required. Several detectors have been reported in the literature for single user scenarios. The authors of [6] proposed a minimal average square block error detector (OB-MMSE) that can achieve a close to optimal performance, while its required complexity is much lower when compared to other detectors. This detector uses an algorithm that sorts the possible transmit antenna combinations (TAC), followed by the detection in sequence of the possible signal vector for each TAC using block minimum mean square error (MMSE). A termination threshold must be applied in order to reduce the number of tested TACs. Although this detector is able to achieve near-optimal performance, it can incur in substantial complexity in large scenarios. A different GSM iterative detector is proposed in [7], which is based on dividing the problem of the maximum likelihood detection (MLD) into a sequence of simpler steps, such as the minimization of the unrestricted Euclidean distance, the projection of the elements onto the signal constellation and the projection onto the set of valid active antenna combinations. This approach allows a substantial complexity reduction when compared with the optimal MLD while still achieving near-optimal performance. Although the wide range of precoding schemes referred to in the literature for MIMO systems considering both uplink and downlink scenarios [8–12], there is a significant imbalance between the number of approaches aimed at those scenarios for GSM-based schemes. In fact, there are very few studies that have extended the use of GSM to downlink MU [13].

Despite describing a system for scalable video broadcast communications in [3], the proposed scheme also considered the use of GSM for multiple users. However, the removal of inter-user interference is made at the receiver, which demands a large number of antennas at the users. A better suited alternative for dedicated links relies on removing inter-user interference at the transmitter through a precoder. This approach is often applied for conventional MU-MIMO as presented in [14], where the authors describe a precoder that accomplishes block diagonalization (BD) of the equivalent channel matrix. The proposed BD precoding guarantees zero inter-user interference and can be thought of as a generalization of channel inversion. Despite the similarity of the approach proposed by the authors in [15], their method cannot only provide improved bit error rate (BER) and throughput performances, but also additional diversity gain by adopting a partial nulling technique for the generalized block diagonalization (GBD). A few precoded schemes have been introduced for spatial modulations (SM) and GSM since then. A new precoder scheme for the downlink of MU-SM systems was proposed in [16], which exploits the channel status information (CSI) at the base station (BS). Here, a precoding matrix is computed, which allows the MU downlink system to be broken down into several independent single user SM systems. A precoded scheme designed for multi-user (MU) GSM systems was reported in [17], with the aim of eliminating all inter-user interference while maintaining the antenna selection features of GSM, which means that only some of the antennas are active, while the rest are silenced. Both proposals of [16,17] are limited in terms of spectral efficiency, since the first one was only defined for SM, while the later was designed specifically for a version of GSM, where the *M*-quadrature amplitude modulations (M-QAM) symbols are the same in all active antennas.

CSI is fundamental in channel estimation process in order to enable uplink and downlink transmissions in MIMO systems. However, the channel estimation for downlink transmissions on massive MIMO systems operating at frequency division duplexing (FDD) represents a very complex problem, since it is unfeasible for practical applications [18,19]. Time Division Duplexing (TDD) represents an interesting solution that can be used as alternative in order to overcome the aforementioned problem in context of downlink transmission in FDD systems. Considering the use of TDD mode, it is possible to exploit the channel reciprocity, which allows the estimation of the downlink channel by the base station through the uplink channel information. In the uplink scenario, orthogonal pilot signals are sent from the users to the base station, and based on that, signals at the base station will estimate the CSI to the user equipment (UE). After accomplishing this task, the base station beamforms the downlink data towards the UE. Considering that there is a limited number of orthogonal pilots that can be reused between cells, a pilot contamination issue may appear and become a critical problem for massive MIMO channel estimation [20]. In order to overcome this issue and others, such as the increasing amount of required hardware and computational complexity cost due to use of large number of required antennas in those schemes, several channel estimation algorithms have been developed over last few years [21–23]. The success of the channel estimation process affects the performance of massive MIMO schemes [24] and, such as, should also be taken into account in the system evaluation. It is important to highlight that even though we will not cover in this paper, massive MIMO systems such as the GSM schemes addressed here are prone to several hardware impairments such as non-linear distortions from power amplifier, I/Q imbalance, sampling jitter, and finite-resolution quantization in analog digital converters (ADCs) [20]. To reduce the impact of these effects on the overall performance of the system, compensation algorithms can be developed to mitigate the impairments.

Another issue that must be considered with the introduction of 5G and beyond is the extreme densification of the network, which requires an increase in the network capacity [25,26]. Poor cell-edge coverage and throughput are the most limiting factors of 4G cellular radio access network (RAN). Some research has been dedicated to decrease inter-cell

interference by base station coordination and coordinated beamforming [27,28]. Coordinated multi-point (CoMP) transmission or reception is one of the key techniques in 5G that mitigates inter-cell interference (ICI) from neighboring cells, providing higher spectral efficiency and coverage. CoMP indeed extends the cell coverage area and improves cell edge throughput. Joint processing coordinated multipoint transmission (JP-CoMP) requires the clustering of neighboring cells and cooperative transmission within each cluster. Clustering algorithms can be static and dynamic, centralized or distributed [29,30]. Static clustering relies on a predetermined fixed base station cluster. Each static clustering algorithm utilizes different strategies to determine the efficient cluster formation. The network then decides on base station clusters. Dynamic clustering adapts to network changes, where the usual methods are designed based on centralized control on the network, which requires extensive information sharing. In our study, we only consider static clustering based on channel state information (CSI). The techniques mentioned above are essential to improve the overall spectral and energy efficiencies and also increase the throughput and coverage gains, when compared to traditional cellular networks [31].

Motivated by the work above, in this paper we provide a study on MU-MIMO systems, where GSM symbols are transmitted simultaneously to multiple users (differences between the proposed approach and a conventional MU-MIMO assumed as reference are shown in Table 1). To increase the SE of the transmission, different modulated symbols are sent on different (virtual) antennas, where high-order M-QAM constellation with sizes reaching M = 1024 symbols are considered. To remove inter-user interference and transform the MU transmission into several independent SU links, a BD precoder is applied at the BS, while a modified and improved version of the low-complexity SU GSM detector presented in [7] is used at the receiver.

Table 1. Comparison between the reference conventional multi-user multiple input multiple output (MU-MIMO) and the proposed generalized spatial modulations multi-user multiple input multiple output (GSM MU-MIMO).

	Conventional MU-MIMO	**GSM MU-MIMO**
Precoder	• Block Diagonalization	• Block Diagonalization
Detector	• conventional single user MIMO • proposed ADMM-based receiver	• Single-user GSM detector capable of operating in undetermined scenarios (sMMP, OB-MMSE, …) • proposed ADMM-based receiver
Information Mapping	• Modulated Symbols	• Modulated Symbols • (Virtual) Antenna Indices
Possibilities for improving Spectral Efficiency	• Increase modulation order • Increase number of transmit antennas → additional transmit power needed	• Increase modulation order • Increase number of transmit antennas → no additional transmit power needed

The influence of imperfect channel estimation on the performance of this massive MIMO GSM-based system is also analyzed. Link level simulations show that the presented GSM MU-MIMO approach can provide substantial performance gains over conventional MU-MIMO. Additionally, system level simulations show that deployments based on cloud-RAN (C-RAN) comprising several radio remote units (RRUs) can achieve large throughput and coverage gains over traditional cellular networks. The paper is organized as follows: Section 2 presents the model for the MU GSM system, Section 3 presents the transmitter and receiver structure followed by the numerical results obtained in Section 4. Finally, the conclusions are outlined in Section 5.

Notation: Matrices and vectors are denoted by uppercase and lowercase boldface letters, respectively, $(.)^{\mathrm{T}}$ and $(.)^{\mathrm{H}}$ denote the transpose and conjugate transpose, $\lfloor . \rfloor$ is the floor function, $\binom{N}{k}$ denotes the number of combinations of N symbols taken k at a time, and supp($\boldsymbol{x}$) returns the set of indices of nonzero elements in x (i.e., the support of x).

2. System Model

Let us consider a downlink MU-MIMO system where a BS transmits simultaneously to N_u users. The BS is equipped with N_{tx} antennas and each user has N_{rx} antennas, as illustrated in Figure 1. We assume that the signal can be represented as $\mathbf{s} = \left[s_0^{\,T}, \ldots, s_{N_u-1}^{\,T} \right]^T$, where $\mathbf{s}_k \in \mathbb{C}^{N_s \times 1}$ contains the information transmitted to user k and $N_s \le N_{tx}/N_u$.

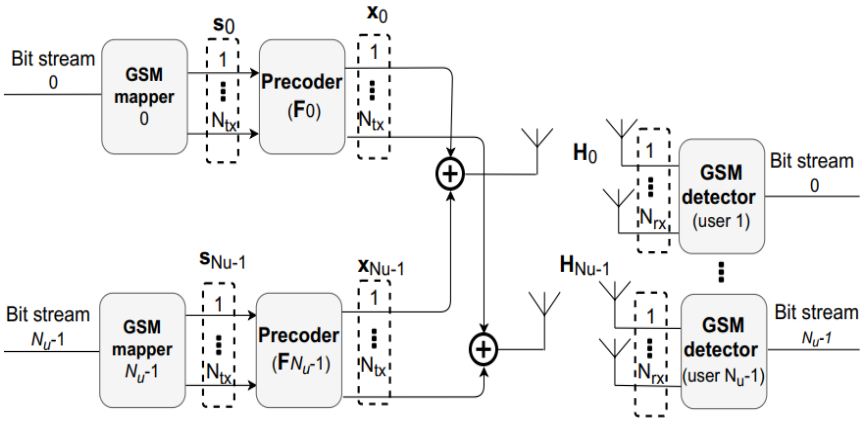

Figure 1. Transmitter and receiver scheme.

Considering that GSM is being used, only N_a positions of $\mathbf{s}_k$ are nonzero. These correspond to active indexes, which carry M-QAM modulated symbols. The signal vector of each user can be written as

$$\mathbf{s}_k = \left[...,0,s_k^0,0,...,0,s_k^{N_a-1},0,...\right]^T, \tag{1}$$

where $s_k^j \in \mathcal{A}\ (j=0,...,N_a-1)$ with $\mathcal{A}$ denoting an *M*-QAM complex valued constellation set. According to this model, the information will be divided in such a way that part of the data are used to select an active index (AI) from a total $N_{comb} = 2^{\left\lfloor \log_2\left(\binom{N_s}{N_a}\right)\right\rfloor}$ AI combinations (AICs) available per user. The remaining data are mapped onto N_a complex-valued *M*-QAM symbols. The resulting SE is then

$$N_{bits} = N_u\left\lfloor \log_2\left(\binom{N_s}{N_a}\right)\right\rfloor + N_u N_a \log_2(M) \tag{2}$$

bits per channel use (bpcu).

3. Transmitter and Receiver Structure

In this section the transmitter and receiver structures' design will be addressed. The receiver design will be based on the alternating direction method of the multipliers (ADMM), which will be explained further in Section 3.2.

3.1. Transmitter Design

Channel state information at the transmitter (CSIT) will be used to pre-process the symbols through a linear precoder $\mathbf{F} = \left[\mathbf{F}_0,...,\mathbf{F}_{N_u-1}\right]$, where $\mathbf{F}_k \in \mathbb{C}^{N_{Tx}\times N_s}$. Considering that the transmitted signal propagates through a flat fading channel, the baseband signal received by user k can be written as

$$\mathbf{y}_k = \mathbf{H}_k\mathbf{x}_k + \mathbf{H}_k\sum_{\substack{j=0\\ j\neq k}}^{N_u-1}\mathbf{x}_j + \mathbf{n}_k, \tag{3}$$

where

$$\mathbf{x} = \sum_{k=0}^{N_u-1}\mathbf{x}_k = \sum_{k=0}^{N_u-1}\mathbf{F}_k\mathbf{s}_k. \tag{4}$$

In this expression, $\mathbf{H}_k \in \mathbb{C}^{N_{rx}\times N_{Tx}}$ corresponds to the channel matrix for the link between the BS and user *k* and $\mathbf{n}_k \in \mathbb{C}^{N_{rx}\times 1}$ is the noise vector with samples taken according to a zero-mean circularly symmetric Gaussian distribution with covariance $2\sigma^2\mathbf{I}_{N_{rx}}$. The first term in (4) is related to the desired signal and the second one is the interference caused by the other users' signals. Moreover, the multiuser interference can be eliminated by using a BD method as proposed in [9]. Following this approach, the equivalent overall channel matrix **HF**, with $\mathbf{H} = \left[\mathbf{H}_0^{\ T},...,\mathbf{H}_{N_u-1}^{\ T}\right]^T$, will become block diagonal. A simple BD precoder without any power loading optimization is assumed in this paper, with each precoder

matrix $\mathbf{F}_k$ designed so as to enforce that $\mathbf{H}_i\mathbf{F}_k = 0$ for all $i \neq k$. This particular condition can be satisfied using vectors selected from the null space of matrix $\tilde{\mathbf{H}}_k$, which is defined as

$$\tilde{\mathbf{H}}_k = \left[\mathbf{H}_0^T, ..., \mathbf{H}_{k-1}^T, \mathbf{H}_{k+1}^T, ..., \mathbf{H}_{N_u-1}^T\right]^T. \quad (5)$$

$\tilde{\mathbf{H}}_k$ corresponds to the concatenation of the channel matrices between the BS and all users except user *k*. An orthonormal basis for the null space of $\tilde{\mathbf{H}}_k$ can be found by computing its singular value decomposition (SVD) as

$$\tilde{\mathbf{H}}_k = \tilde{\mathbf{U}}_k \tilde{\mathbf{\Lambda}}_k \left[\tilde{\mathbf{V}}_k^{(1)} \tilde{\mathbf{V}}_k^{(0)}\right]^H, \quad (6)$$

where $\tilde{\mathbf{U}}_k$ is the matrix with the left-singular vectors and $\tilde{\mathbf{\Lambda}}_k$ is a rectangular diagonal matrix containing the nonzero singular values. $\tilde{\mathbf{V}}_k^{(1)}$ and $\tilde{\mathbf{V}}_k^{(0)}$ contain the right singular vectors corresponding to the nonzero singular values and the null singular values, respectively. $\mathbf{F}_k$ is obtained from $\tilde{\mathbf{V}}_k^{(0)}$ by selecting its first N_s columns. In this case, the signal arriving at each receiver reduces to

$$\mathbf{y}_k = \hat{\mathbf{H}}_k \mathbf{s}_k + \mathbf{n}_k, \quad (7)$$

where $\hat{\mathbf{H}}_k = \mathbf{H}_k\mathbf{F}_k$ is the equivalent single user channel seen by the receiver.

3.2. Receiver Design

Considering the system model and the BD precoder described in the previous sections, each receiver will have to apply simple single user GSM detection. This can be seen as an attempt to solve the MLD problem related to receiver *k*, which is formulated as

$$\min_{\mathbf{s}} f(\mathbf{s}_k) \triangleq \left\|\mathbf{y}_k - \hat{\mathbf{H}}_k \mathbf{s}_k\right\|_2^2 \quad (8)$$

$$\text{subject to } \mathbf{s}_k \in \mathcal{A}_0^{N_s} \quad (9)$$

$$\text{supp}(\mathbf{s}_k) \in \mathbb{S}, \quad (10)$$

where $\mathcal{A}_0 \overset{def}{=} \mathcal{A} \cup \{0\}$ and $\mathbb{S}$ denotes the set of valid AICs, which has a size of N_{comb}. Solving this non-convex problem directly would require excessive or even unfeasible computational complexity for moderate to large problem settings. To tackle the problem, we adopt instead a similar approach to the one we applied in [7], which is based on the idea of using ADMM as an heuristic for splitting a complex problem into a sequence of simpler ones (as addressed in [32]). Being an heuristic based approach, there will be no guarantee that the resulting algorithm will converge to the solution of the original MLD problem. While this means that the detector will be suboptimal, it will require a much lower computational cost. Following a similar derivation to the one provided in [7], we can arrive at the iterative detection algorithm shown in Table 2 which can be used in each GSM receiver.

In this table, $\mathbf{u}, \mathbf{w} \in \mathbb{C}^{N_{tx}/N_u \times 1}$ are scaled dual variables and ρ_x and ρ_z are penalty parameters associated to constraints (9) and (10). A careful tuning of these parameters will ensure that the algorithm reaches a good performance during its execution. In the algorithm, *Q* is the maximum number of iterations, $\prod_{\mathcal{D}}(.)$ denotes the projection onto set $\mathcal{D} = \left\{\mathbf{s} : \text{supp}(\mathbf{s}) \in \mathbb{S}\right\}$, and $\prod_{\mathcal{A}_0^{N_s}}(.)$ is the projection over $\mathcal{A}_0^{N_s}$. The projection over set $\mathcal{D}$ can be accomplished by keeping the N_a largest magnitude elements whose indices also match a valid antenna combination, whereas $\prod_{\mathcal{A}_0^{N_s}}(.)$ can be computed as simple rounding of each component to the closest element in $\mathcal{A}_0$.

Although heuristic-based approaches as the one adopted in the proposed GSM detector can reach a solution faster, it may not be the optimal one. Therefore, it is not guaranteed that the algorithm will converge to the optimal solution of the original MLD problem (which is nonconvex). To increase the chances of finding an optimal solution and to improve the performance of the GSM detector, we present several different strategies. The first method is the simplest and consists of restarting the algorithm multiple times by using different initializations [32] for the variables $\mathbf{u}^0$, $\mathbf{w}^0$, $\mathbf{x}^{u(0)}$, $\mathbf{z}^0$ required by the algorithm.

Table 2. Iterative GSM detection algorithm for each user k.

1:	**Input:** $\mathbf{u}^0$, $\mathbf{w}^0$, $\mathbf{x}^0$, $\mathbf{z}^0$, $\hat{\mathbf{H}}_k$, $\mathbf{y}_k$, ρ_x , ρ_z, Q
2:	$f_{best} = \infty$.
3:	$\mathbf{\Phi} \leftarrow \left(\hat{\mathbf{H}}_k^H \hat{\mathbf{H}}_k + (\rho_x + \rho_z)\mathbf{I}_{N_s}\right)^{-1}$.
4:	**for** t = 0, 1, …Q-1 **do**
5:	$\mathbf{s}_k^{(t+1)} \leftarrow \mathbf{\Phi}\left(\hat{\mathbf{H}}_k^H \mathbf{y}_k + \rho_x(\mathbf{x}^{(t)} - \mathbf{u}^{(t)}) + \rho_z(\mathbf{z}^{(t)} - \mathbf{w}^{(t)})\right)$.
6:	$\mathbf{x}^{(t+1)} \leftarrow \prod_D\left(\mathbf{s}_k^{(t+1)}\right)$.
7:	$\mathbf{z}^{(t+1)} \leftarrow \prod_{\mathcal{A}_0^{N_s}}\left(\mathbf{s}_k^{(t+1)} + \mathbf{w}^{(t)}\right)$.
8:	$I \leftarrow \mathrm{supp}\left(\mathbf{x}^{(t+1)}\right)$.
9:	$\hat{\mathbf{s}}_{\bar{I}}^{candidate} \leftarrow 0, \hat{\mathbf{s}}_I^{candidate} \leftarrow \prod_{\mathcal{A}^{N_a}}\left(\mathbf{s}_I^{(t+1)}\right)$
10:	**if** $f(\hat{\mathbf{s}}^{candidate}) < f_{best}$ **then**
11:	$\hat{\mathbf{s}}_{k,\bar{I}} \leftarrow 0, \hat{\mathbf{s}}_{k,I} \leftarrow \hat{\mathbf{s}}_I^{candidate}$.
12:	$f_{best} = f(\hat{\mathbf{s}}^{candidate})$.
13:	**end if**
14:	$\mathbf{u}^{(t+1)} \leftarrow \mathbf{u}^{(t)} + \mathbf{s}_k^{(t+1)} - \mathbf{x}^{(t+1)}$.
15:	$\mathbf{w}^{(t+1)} \leftarrow \mathbf{w}^{(t)} + \mathbf{s}_k^{(t+1)} - \mathbf{u}^{(t+1)}$.
16:	**end for**.
17:	**Output:** $\hat{\mathbf{s}}_k$

Another improvement strategy that we propose relies on checking at the end of the algorithm if any of the P neighboring candidates result in an improvement of $f(\hat{\mathbf{s}}^{candidate})$. These P neighbors can be selected amongst those with the closest supports using the algorithm presented in Table 3. A last possible refinement method that we consider consists of re-solving the MLD problem with the support set fixed according to the candidate point $\hat{\mathbf{s}}_k$ generated by the main algorithm.

In this case, the resulting formulation becomes a conventional MIMO detection problem which can also be approximated by a simple projected MMSE estimate, i.e., as

$$\hat{\mathbf{s}}_I^{candidate} = \prod_{\mathcal{A}^{N_a}}\left(\left(\hat{\mathbf{H}}_{k,I}^H \hat{\mathbf{H}}_{k,I} + 2\sigma^2 \mathbf{I}_{N_a}\right)^{-1} \hat{\mathbf{H}}_{k,I} \mathbf{y}_k\right). \tag{11}$$

We refer to this third approach as the MMSE polishing step. In terms of computational complexity, the BD precoding requires the computation of N_u SVDs, which is the step with the heaviest cost resulting in a complexity order of $O\left(N_u^4 N_{rx}^3 + N_u^2 N_{tx}^2 N_{rx}\right)$. This cost is supported by the BS which typically can have higher computational capabilities. More critical is the required computational complexity at the users. Regarding the receiver, the s-update step (line 5 of Table 2) has the highest cost as it involves an $N_{tx}/N_u \times N_{tx}/N_u$ matrix inversion (although it is only computed in the beginning of the algorithm). Considering a fixed number of iterations, the total complexity order is $O\left(\left(N_{tx}/N_u\right)^3\right)$. For comparison, the complexity order of MLD is $O\left(N_{comb} M^{N_a}\right)$ (with $N_{comb} = 2^{\left\lfloor \log_2\binom{N_s}{N_a} \right\rfloor}$), of a linear MMSE is $O\left(\left(N_{tx}/N_u\right)^3\right)$, of OB-MMSE [33] is $O\left(N_{comb} N_a^3\right)$ and of multipath matching pursuit with slicing (sMMP) [34] is $O\left(\frac{N_{tx}}{N_u} N_{rx}\left(1-T^K\right)/\left(1-T\right) + \left(N_a^2 N_{rx} + N_a^3\right)T^K\right)$ (T is the number of child candidates expanded at each iteration). Therefore, the proposed approach has a similar complexity order to the linear MMSE. Note that the complexity of OB-MMSE does not grow exponentially with the signal constellation size, M, like in the case of MLD, but it still depends on $N_{comb} = 2^{\left\lfloor \log_2\binom{N_s}{N_a} \right\rfloor}$ which can restrict its use when a large number of bits are conveyed on antenna indices.

Table 3. Solution refinement algorithm based on a closest neighbor search for user k.

1:	**Input:** $\hat{\mathbf{H}}_k$, $\mathbf{y}_k$, $\hat{\mathbf{s}}$, $\mathbf{s}_k^{(Q)}$, f_{best} , P
2:	$\bar{D}_0 = D$, $I \leftarrow \text{supp}(\hat{\mathbf{s}})$
3:	**for** $p = 1, \ldots P$ **do**
4:	$\bar{D}_p = \bar{D}_{p-1} \setminus \{\mathbf{s} : \text{supp}(\mathbf{s}) = I\}$.
5:	$\mathbf{x} \leftarrow \prod_{\bar{D}_p} (\mathbf{s}_k^{(Q)})$
6:	$I \leftarrow \text{supp}(\mathbf{x})$.
7:	$\hat{\mathbf{s}}_{\bar{I}}^{\,candidate} \leftarrow 0, \hat{\mathbf{s}}_I^{\,candidate} \leftarrow \prod_{\mathcal{A}^{N_a}} (\mathbf{s}_I^{(Q)})$
8:	**if** $f(\hat{\mathbf{s}}^{candidate}) < f_{best}$ **then**
9:	$\hat{\mathbf{s}}_{k,\bar{I}} \leftarrow 0, \hat{\mathbf{s}}_{k,I} \leftarrow \hat{\mathbf{s}}_I^{\,candidate}$.
10:	$f_{best} = f(\hat{\mathbf{s}}^{candidate})$.
11:	**end if**
12:	**end for**.
13:	**Output:** $\hat{\mathbf{s}}_k$

4. Numerical Results

In this section, we present numerical simulations, both link level and system level. Link performance results, namely, block error rate (BLER), are used as input by the system level simulator. The system is illustrated in Figure 2, where the C-RAN is comprised of 19 radio remote units (RRUs) connected through fiber to a central unit (CU), each RRU with N=60 active pedestrian users. Each RRU consists of three transmission and reception points (TRP), each one equipped with $N_{tx_{total}} = 256$ antennas while users have N_{rx} antennas (i.e., each RRU corresponds to a BS according to the system model presented in Section 2). The RRUs array configuration corresponds to cylindrical arrays: 16 × 16 × 3, where the separation between antennas of the array is half wavelength [35].

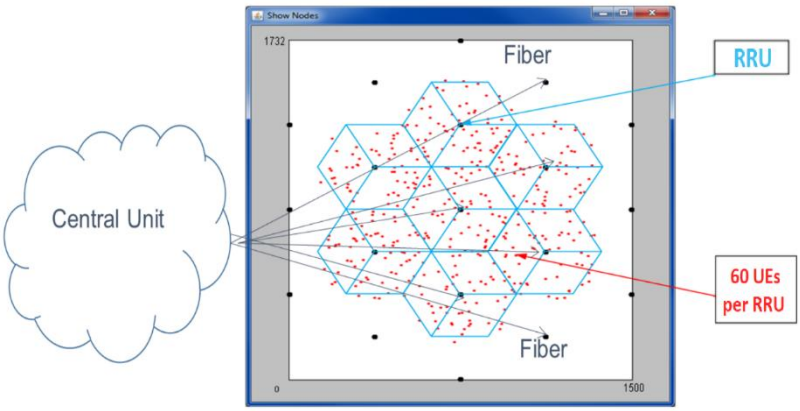

Figure 2. Cloud radio access network (C-RAN) considered for the system level simulations. RRU = radio remote unit.

The system level block diagram can be found in references [36,37]. This simulator is based on the one described in [37]. In the system level simulator, there are general parameters that must be defined, such as network layout and antenna parameters. The setup used considers several of the same parameters adopted in the case study presented in section 7.7 of [38] for the deployment of a Massive MIMO based outdoor network. Our system level simulator considers the 3D urban macro 3D-Uma scenario [36], where the BSs are mounted above rooftop levels of surrounding buildings with antenna height: 25 m and pedestrians height: 1.5–2.5 m. To each pedestrian is assigned line-of-sight (LOS) or non-line-of-sight (NLOS) propagation conditions, depending on the distance to RRU. It is generated correlated large-scale and small-scale parameters to create channel coefficients and pathloss and shadowing are applied with $\sigma_{SF} = 7.8$ dB. For the NLOS pathloss distance, we have $PL = 32.4 + 20\log(f_c) + 30\log(d_{3D})$ dB, where d_{3D} is the distance in meters [36]. Other simulator parameters are: carrier frequency $f_c = 3.5$ GHz, maximum TRP transmit power 46 dBm, receiver spectral noise power density −174dBm/Hz, cyclic prefix overhead 5%, pilots/TRP=15 and arrays with uni-polarized antennas. We choose the 5G NR numerology 1 and slot configuration parameters taken from [39]: the bandwidth is B_f=20 MHz with normal

CP where the subcarrier spacing is 30 kHz and 28 OFDM symbols are transmitted in every subframe of 1ms. Each user feedbacks all CSI and signal-to-interference-plus-noise ratio (SINR) to TRPs. The static clustering technique partitions the network into three adjacent RRUs sets where each user is served by at least one RRU, while the others perform inter-user interference. The RRU inter-site distance is 433 m corresponding to a radius of 250 m.

4.1. Link Level Simulations

The first simulation results had the objective of evaluating the behavior of the iterative GSM receiver and of the overall proposed GSM MU-MIMO transmitter/receiver scheme. Figures 3 and 4 present the results of BER performance versus the signal-to-noise ratio (SNR) in dB of the proposed GSM MU-MIMO system with N_{tx}=255, N_{rx}=10, N_u=15, N_s=17 and N_a=2, which corresponds to a spectral efficiency of 23 bpcu/user for 256-QAM and 27bpcu/user for 1024-QAM.

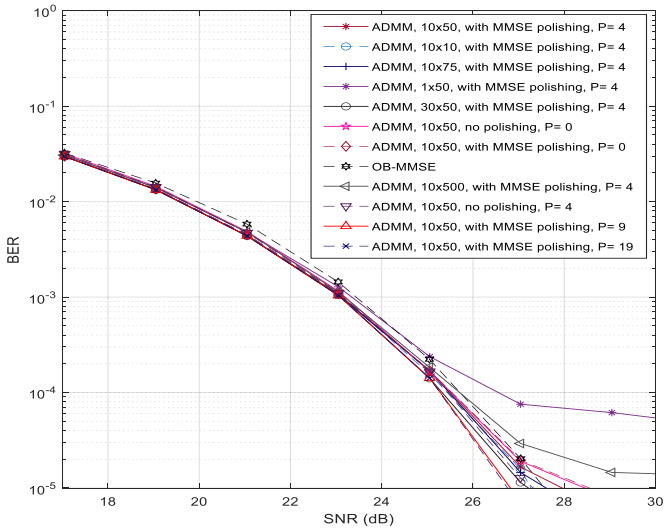

Figure 3. Bit error rate (BER) performance of ADMM in a MU-MIMO scenario with N_{tx}=255, N_{rx}=10, N_u=15, N_s= 17 and N_a=2, 256-QAM.

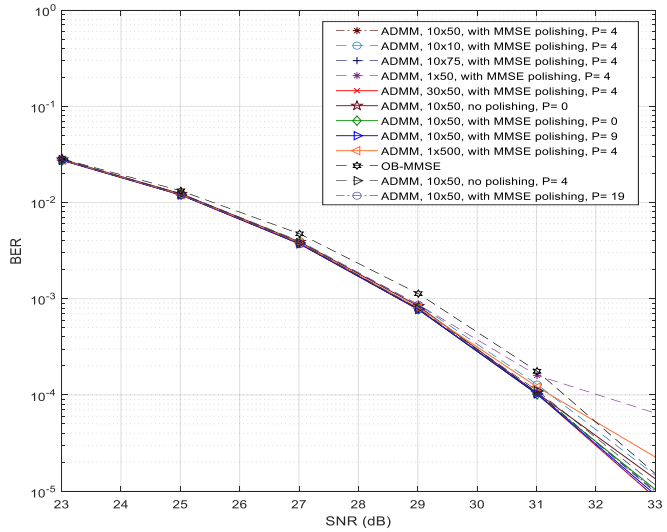

Figure 4. BER performance of ADMM in a MU-MIMO scenario with N_{tx}=255, N_{rx}=10, N_u=15, N_s= 17 and N_a=2, 1024-QAM.

The expression $n_1 \times n_2$, mentioned in the legend of both figures, denotes that the receiver algorithm was ran with n_1 restarts and n_2 iterations. The type of polishing applied as well as the number of neighbors is also shown. Besides the expected improvement when using more iterations, it can be observed that by increasing the number of algorithm restarts, we can achieve a better system performance. When considering the 1 × 500 and 10 × 50 cases, which have the same total number of iterations, it is clear that the best results are achieved by the case with more restarts (10 × 50). Considering the

scenarios where MMSE polishing is used and those where it is not, one can observe that those where polishing is applied have better performance. We also studied the impact of changing the number of neighbors on the performance of the algorithm and we concluded that the greater the number of neighbors, the better the performance will be (see the cases where P = 1, 4, 9 and 19). Moreover, the combination of the three proposed improvement strategies for the ADMM receiver lead to a better performance than the usage of the individual approaches. Globally, the proposed ADMM algorithm tends to lead to better results when compared to the case where the well-known OB-MMSE receiver (which we included as benchmark) is used [6].

Our next goal is to provide a comparison between a conventional BD precoded MU-MIMO [9] and the proposed GSM MU-MIMO. Figure 5 shows the results for two different configurations. The first case concerns a comparison between the precoded GSM MU-MIMO with with N_{tx}=160, N_{rx}=6, N_u=10, N_s=16 and N_a=1, 16-QAM and the conventional BD precoded MU-MIMO with N_{tx}=60, N_{rx}=6, N_u=10, N_s=1 and 256-QAM, both with a spectral efficiency of 8 bpcu/user. In the second case, we present a comparison between the precoder based on GSM MU-MIMO with with N_{tx}=90, N_{rx}=8, N_u=10, N_s=9 and N_a=3, quadrature phase-shift keying (QPSK) and the precoder based on conventional MU-MIMO with with N_{tx}=80, N_{rx}=8, N_u=10, N_s=3 and 16-QAM, both with a spectral efficiency of 12bpcu/user. Regarding the GSM MU-MIMO scheme, results with the proposed receiver as well as other alternative ones are included, namely with a linear MMSE and with the sMMP (from [34]). In the case of sMMP, a lower number of child nodes (T = 3) was adopted for 12 bpcu due to the very high computational complexity when operating with higher values in this scenario.

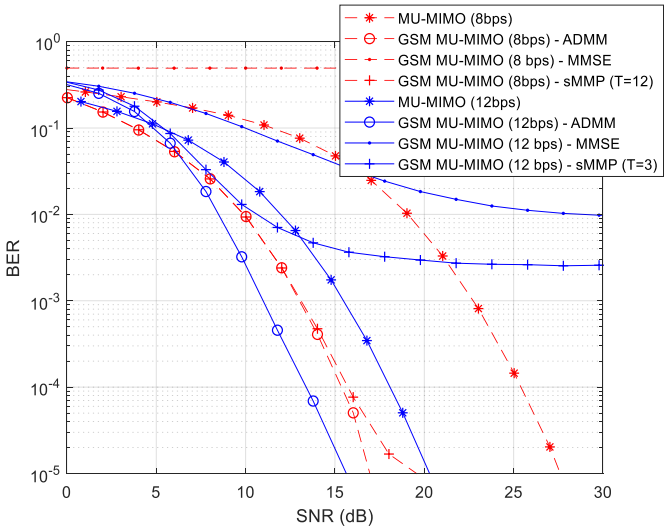

Figure 5. BER performance of a precoder based on GSM MU-MIMO and a precoder based on conventional MU-MIMO.

In the results, it is clear that the proposed ADMM receiver achieves the best results when compared against sMMP and MMSE. In the case of MMSE, it simply cannot correctly detect the information (8 bps) or it has a high irreducible BLER (12 bps). This is due to the fact that from a receiver point of view, both scenarios correspond to underdetermined systems $(N_{rx} < N_s)$, which a simple MMSE has a high difficulty to cope with. Through this figure, it can also be seen that the GSM MU-MIMO precoder with the proposed ADMM receiver achieves a better performance when compared to the conventional MU-MIMO precoder (which also uses the same receiver). When we focus on the curve's behavior for a 10^{-4} BER considering a 8bpcu/user scenario, the GSM MU-MIMO shows a gain of about 10 dB over the conventional MU-MIMO. Moving on to the 12bpcu/user scenario and maintaining the BER at 10^{-4}, the GSM MU-MIMO presents a gain of about 5 dB over the conventional MU-MIMO. These results suggest that GSM MU-MIMO can be a potential alternative to increase the SE of the system when compared with the adoption of higher-level modulations in conventional MU-MIMO.

A second set of simulations were performed in order to analyze the block error rate (BLER) performance versus the energy per symbol to noise power spectral density (E_s/N_0) in dB of the proposed GSM MU-MIMO system. These results are required for the system level evaluation in the next subsection. Both perfect channel estimation and imperfect channel estimation curves are presented. For the imperfect channel estimation results we adopted the same model as in [40]. Denoting the CSI available at the transmitter as $\bar{\mathbf{H}}$ and the CSI error as $\mathbf{H}_{error}$ we can express the channel matrix as

$\mathbf{H}=\bar{\mathbf{H}}+\mathbf{H}_{error}$. The entries of $\bar{\mathbf{H}}$ and $\mathbf{H}_{error}$ are drawn assuming complex Gaussian distributions of $\mathcal{CN}\left(0,\sigma_{\bar{h}}^2\right)$ and $\mathcal{CN}\left(0,\sigma_{h_{error}}^2\right)$, with $\sigma_{\bar{h}}^2+\sigma_{h_{error}}^2=1$. In the presented results we considered $\sigma_{h_{error}}=0.03$. In our simulations, a minimum of 25,000 blocks were transmitted for computing each BLER result. In Figures 6 and 7, we have N_{sc}=256 subcarriers, N_{tx}=17 antennas/user, N_{rx}=16 antennas/user and N_u=15 users.

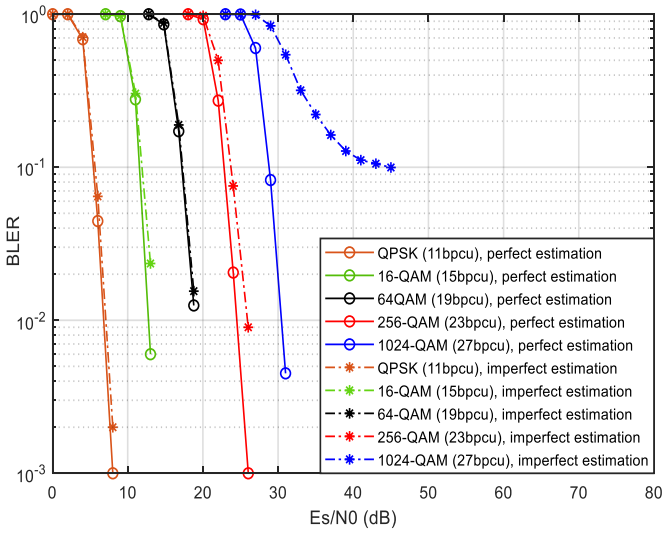

Figure 6. Block error rate (BLER) vs E_s/N_0 for N_u=2, N_{sc}=256, N_u=15, N_{tx}=17 antennas/user, and N_{rx}=16 antennas/user.

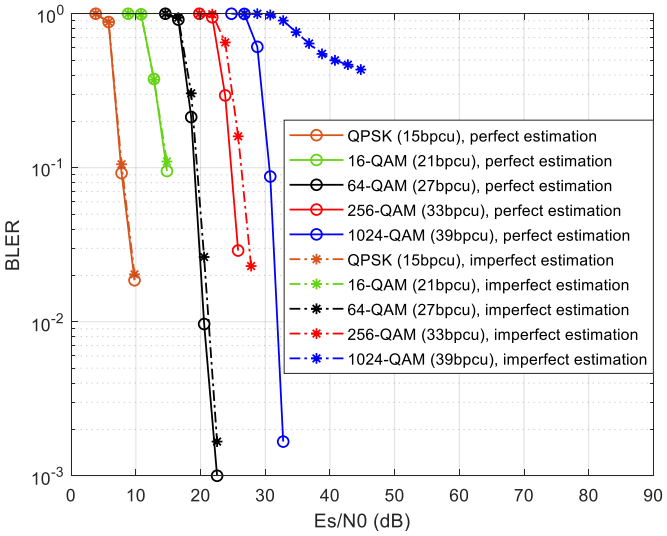

Figure 7. Perfect and imperfect estimation of BLER vs E_s/N_0 for N_u=3, N_{sc}=256, N_u=15, N_{tx}=17 antennas/user, and N_{rx}=16 antennas/user.

The number of active antennas are N_u=2 and N_u=3, respectively. The case N_u=3 and 1024-QAM corresponds to a spectral efficiency of 39bpcu/user. The peak bit rate per user achieved assuming 5G NR numerology 1 is 279.552Mbps. This means that 1bpcu/user is equivalent to bit rate of 7.168Mbps.

Doubling N_{sc}=256 to N_{sc} =512 doubles the spectral efficiency to 78 bpcu/user use which is equivalent to a bit rate of 14.336Mbps. In both figures, the BLER of GSM MU-MIMO is presented versus (E_s/N_0) in dB, for five uniform M-QAM constellations namely, M ∈ {4,16,64,256,1024}. As expected, independently of N_u, higher values of M require higher values of E_s/N_0 (dB) to reach the reference BLER=10^{-1}. In Figure 6, 1024-QAM with perfect estimation requires an additional 24dB of E_s/N_0 compared to 4-QAM(QPSK). With imperfect channel estimation there is an additional 15dB penalty to reach BLER=10^{-1} in the detection of 1024-QAM (it has a higher sensitivity to channel estimation errors).

In Figure 7, for N_a=3, it is clear the higher sensitivity of 1024-QAM, as one can notice that with imperfect estimation there is the emergence of a BLER floor. The other modulations only reveal small or negligible degradation.

4.2. System Level Simulations

Using the BLER results described previously, several system level simulations were performed. The signal-to-noise ratio in dB used in the system level simulations is obtained using $SNR=(E_s/N_0)+10\log(R_s/B)$ dB, where R_s is the total transmitted symbol rate per antenna and user, B is the total bandwidth (we considered 20MHz), and E_s/N_0 is the ratio of symbol energy to noise spectral density in dB. Values of E_s/N_0 are obtained from the link level BLER results.

In Figure 8, we have chosen N_a=2 with perfect estimation, and computed the SNR values corresponding to the BLER=10^{-1} so as to obtain the coverage results vs. the percentage of transmitted carrier power. Based on the parameters N_u=15, N_{tx}=17 transmit antennas/user and N_{rx}=16 receive antennas/user there are a total of 255 active antennas at each TRP. The coverage of each of the five different M-QAM constellations and the arithmetic average of the coverage of all constellations (labelled as AllQAM) is presented for two different clusterings. In the present cellular topology, RRUs correspond to base stations, and each user is served by one RRU while the other RRUs generate inter-interference when transmitting towards their users. The label 1C means that the cluster contains one RRU. According to BLER performance results of Figure 6, it is expected that the 1024-QAM constellation has the minimum coverage due to more demanding signal-to-noise ratio, while 4-QAM has the maximum coverage for 100% of the transmitted carrier power. Only users close to RRUs are able to decode correctly 1024-QAM symbols, whereas 4-QAM symbols are decoded everywhere. We can check in Figure 8 that only for 100% of transmitted carrier power, the average coverage of all constellations reaches 71.5% of the area. The remaining coverage curves correspond to clustering where the network is partitioned into three adjacent RRU sets and each user is served by three RRUs (labelled as 3C). It is clear that there is an improved coverage obtained for all constellations, which is due to a much lower inter-interference between RRUs. Now, the average coverage of all constellations for 100% of carrier power is 99.6%, which corresponds to a coverage gain of 139%.

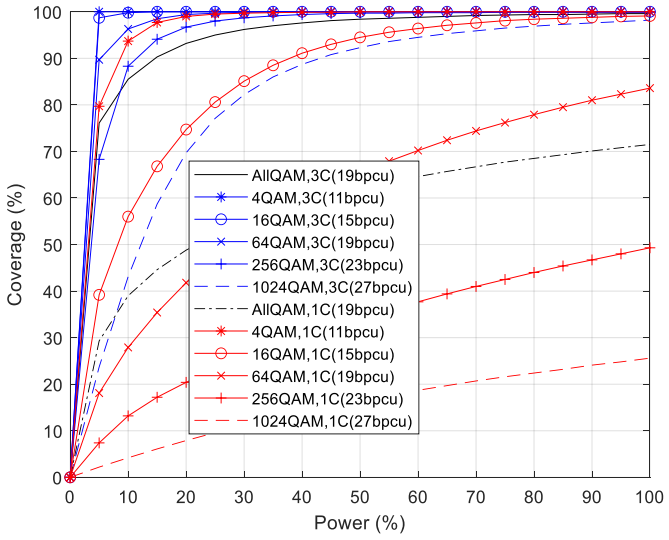

Figure 8. Coverage vs percentage of transmitted power for N_a=2, N_{sc}=256, N_u=15, N_{tx}=17 antennas/user, and N_{rx}=16 antennas/user.

In Figure 9, the average throughput results corresponding to the coverage results of the previous figure are presented. Considering the impact of clustering in which only one RRU (1C) is transmitting, the constellation with the lowest throughput is 1024-QAM and the highest result is achieved for 64-QAM. The latter presents a better tradeoff of coverage and spectral efficiency when compared to the use of 16-QAM and 4-QAM constellations. For 15 users and 100% of transmitted carrier power, the average throughput obtained with all constellations is 1306.5 Mbps (87.1Mbps/user). For the clustering where three RRUs (3C) transmit to each user, the constellation with the highest throughput is 1024-QAM, followed by 256-QAM, 64-QAM, 16-QAM, and 4-QAM. There is a match between the spectral efficiency (bpcu) of each constellation and the corresponding average throughput achieved at C-RAN system level. In fact, the same type of match is also observed for the curve of all constellations with spectral efficiency of 19 bpcu and the average throughput achieved at RAN. Notice that the spectral efficiency of 19 bpcu corresponds to a 64-QAM constellation and is equal to the average

spectral efficiency of all constellations. For 15 users and 100% of transmitted power, the average throughput of all constellations is 2031.0 Mbps (135.4 Mbps/user), which gives a throughput gain of 155%.

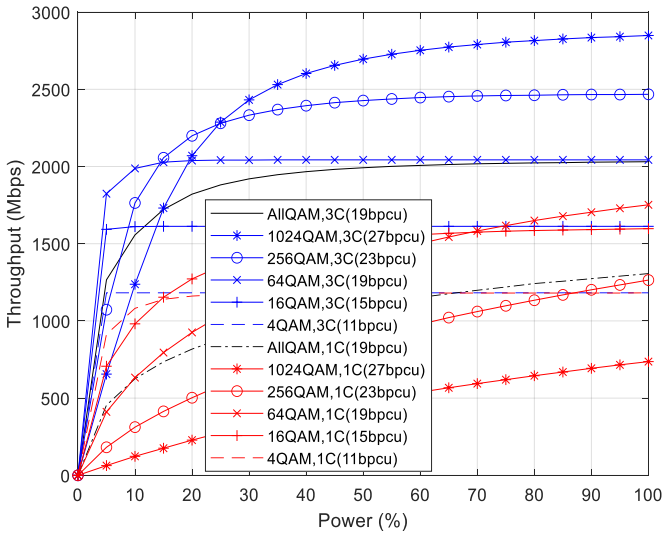

Figure 9. Average throughput vs percentage of transmitted power for N_u=2, N_{sc}=256, N_u=15, N_{tx}=17 antennas/user, and N_{rx}=16 antennas/user.

Figure 10 presents the throughput averaged over all users uniformly distributed, for the C-RAN scenario where three RRUs (3C) transmit to each user. The parameters of the previous figures are kept the same, namely N_{tx}=17 antennas/user, N_{rx}=16 antennas/user, N_{sc}=256, and we vary the number of users N_u from 1 up to 15, considering 100% of transmitted carrier power. We consider that the channel estimation is perfect. We can confirm that the BD MU precoding used at the RRUs and the ADMM receivers are operating as expected because every throughput curve is a straight line with slope dependent of the constellation but independent of N_u. The increase in throughput depends on the spectral efficiency. We present two set of results. For N_u=2, the minimum is 11 bpcu (4-QAM) and the maximum is 27 bpcu (1024-QAM). The second set of performance curves have N_u=3, starting from 15 bpcu (4-QAM) up to a maximum of 39 bpcu (1024-QAM). We observe the same throughput results for 15 bpcu with 16-QAM and N_u=2 or 4-QAM with N_u=3. The throughput results are almost the same between the average of all constellations with N_u=2 (19 bpcu) or N_u=3 (27 bpcu) and the 64-QAM constellation having the same spectral efficiencies. This can be explained because the average coverage of all constellations is only slightly lower than the coverage of 64-QAM. The ratio of throughput results for the average of all constellations with N_u=3 (27 bpcu) compared to those of N_u=2 (19 bpcu) is 2875.8/2031.0 = 1.42, the same as the expected ratio (27 bpcu/19 bpcu) = 1.42.

Figure 11 considers the same parameters of Figure 10 but the channel estimation is imperfect instead of perfect. Some performance degradation due to imperfect channel estimation can be observed. The throughput results are not anymore the same between the average of all constellations with N_u=2 (19 bpcu) or N_u=3 (27 bpcu) and the 64-QAM constellation having the same spectral efficiencies. Indeed, the simulation results indicate that the throughput of the average of all constellations is lower than the 16-QAM constellation results with N_u=2 (15 bpcu) or N_u=3 (21 bpcu). For both numbers of active antennas, the throughput results for 1024-QAM become the lowest instead of the highest and for N_u=3, the throughput is zero (does not attain a BLER of 10^{-1} as observed previously). There is an obvious decrease in the simulated throughput results compared to the expected results based on the constellation bpcu. The ratio of throughput results for the average of all constellations with N_u=3 (27 bpcu) compared to those of N_u=2 (19 bpcu) is 2062.5/1546.5 = 1.33, lower than the expected ratio (27 bpcu/19 bpcu) = 1.42. The comparison between Figures 10 and 11 indicates that the throughput reduction due to imperfect channel estimation for N_u=2 is (1-1546.5/2031.0) = 0.24 and for N_u=3 is (1-2062.5/2875.8) = 0.28. Therefore, the throughput reduction due to imperfect estimation increases with the number of GSM active antennas which was expected based on the BLER results of Figures 6 and 7.

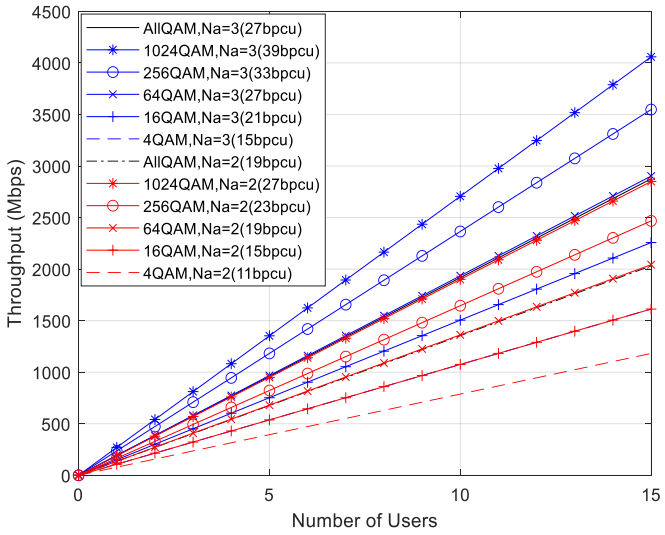

Figure 10. Average throughput vs number of users for N_{st}=256, N_{tx}=17 antennas/user and N_{rx}=16 antennas/user with perfect channel estimation.

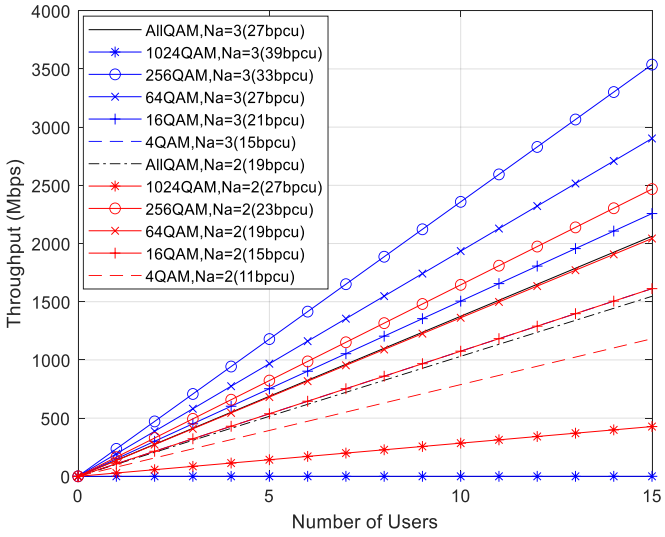

Figure 11. Average throughput vs number of users for N_{st}=256, N_{tx}=17 antennas/user and N_{rx}=16 antennas/user with imperfect channel estimation.

Figure 12 presents the cumulative distribution function (CDF) of a RRU with three TRPs, each TRP with N_{tx}=255 active antennas serving 60 users each with N_{rx}=16 antennas. The CDF of this figure corresponds to the case of 100% of carrier transmission power. We consider only the C-RAN scenario with clusters of three RRUs (3C), with curves for both perfect channel estimation and imperfect channel estimation cases. As expected, only for 1024-QAM there is an obvious difference in CDF results due to imperfect estimation compared to perfect estimation. For the other constellations, there are almost the same CDF results which is in agreement with the BLER results of Figure 6. The receiving throughput of all users exceeds 2.5 Gbps, 3.5 Gbps, 4.5 Gbps, 5.5 Gbps, and 6.5 Gbps for 10% of the users with 4-QAM, 16-QAM, 64-QAM, 256-QAM, and 1024-QAM (perfect estimation), respectively. For 50% of the users, the throughput received corresponds to the performance results presented on Figure 9. Only less than 10% of users receive a throughput level lower than 100Mbps, with the exception of 1024-QAM users with imperfect estimation.

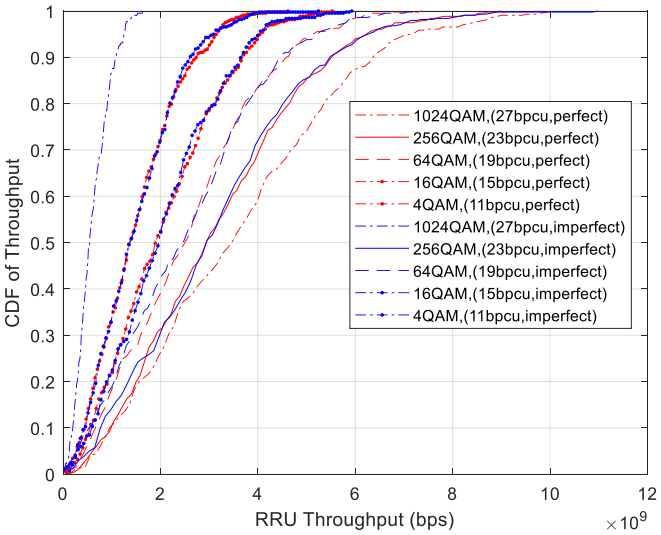

Figure 12. CDF of throughput for 100% transmitted power for N_a=2, N_{sc}=256, N_u=15, N_{tx}=17 antennas/user, and N_{rx}=16 antennas/user.

Table 4 summarizes the average throughput per user with perfect and imperfect channel estimation for C-RAN with clusters 1C and 3C and the corresponding throughput gain. The maximum throughput gain is 1.55 and the minimum is 1.25.

Table 4. Average throughput per user with perfect and imperfect channel estimation and the corresponding throughput gain. CSI = channel status information.

Na	CSI	1C	3C	Gain
2	perfect	87.1Mbps	135.4Mbps	1.55
2	imperfect	82.5Mbps	103.1Mbps	1.25
3	perfect	125.4Mbps	191.7Mbps	1.53
3	imperfect	103.4Mbps	137.5Mbps	1.33

5. Conclusions

In this paper, a novel MIMO system where GSM symbols are transmitted simultaneously to multiple users has been described. By combining large antenna settings at the BS with high-order *M*-QAM constellations, the proposed approach is capable of improving the spectral efficiency and energy efficiency. A precoder is applied at the BS to completely remove inter-user interference, while a reduced complexity iterative SU GSM detector is implemented at each receiver. Simulation results show that the proposed approach can achieve a very competitive and very promising performance compared to conventional MU-MIMO systems with identical SE. In fact, system level results based on a C-RAN scenario with multiple RRU showed potential gains of up to 155% in throughput and 139% in coverage when compared to traditional cellular networks**.** The introduction of imperfect channel estimation reduces the throughput gain to 125%. Future work will include a thorough evaluation of the impact of several hardware impairments (such as phase-noise, non-linear distortion, and I/Q imbalances) and robust mitigation algorithms.

Author Contributions: Conceptualization, J.P.P., A.C., B.B. and N.S.; methodology, J.P.P., A.C., B.B. and N.S.; software, J.P.P., A.C., V.V., B.B. and N.S.; validation, J.P.P., A.C., B.B., V.V. and N.S.; formal analysis, J.P.P., A.C., B.B., V.V. and N.S.; investigation, J.P.P., A.C., B.B., V.V. and N.S.; resources, A.C. and N.S.; data curation, J.P.P., B.B., V.V., N.S. and A.C.; writing—original draft preparation, J.P.P., A.C., B.B. and N.S.; writing—review and editing, J.P.P., A.C., B.B., V.V. and N.S.; visualization, J.P.P., A.C., B.B., V.V. and N.S.; supervision, A.C. and N.S.; project administration, A.C. and N.S.; funding acquisition, A.C. and N.S. All authors have read and agreed to the published version of the manuscript.

Funding: This research was partially funded by the ISCTE-University Institute of Lisbon under the grant ISTA-BMPDCTI-2019 and by the FCT/MCTES through national funds and when applicable co-funded by EU funds under the project UIDB/50008/2020.

Acknowledgments: The authors acknowledge the support of ISCTE—University Institute of Lisbon, Fundação para a Ciência e Tecnologia (FCT) and Instituto de Telecomunicações (IT), as described above in funding.

Conflicts of Interest: The funders had no role in the design of the study; in the collection, analyses, or interpretation of data; in the writing of the manuscript, or in the decision to publish the results.

References

1. Yuan, W.; Wu, N.; Zhang, A.; Huang, X.; Li, Y.; Hanzo, L. Iterative Receiver Design for FTN Signaling Aided Sparse Code Multiple Access. IEEE Trans. Wirel. Commun. 2020, 19, 915–928.
2. Cheng, X.; Zhang, M.; Wen, M.; Yang, L. Index Modulation for 5G: Striving to Do More with Less. *IEEE Trans. Wirel. Commun.* **2018**, *25*, 126–132.
3. Correia, A.; Souto, N.; Sebastiao, P.; Gomez-Barquero, D.; Fuentes, M. Broadcasting Scalable Video with Generalized Spatial Modulation in Cellular Networks. *IEEE Access* **2020**, *8*, 22136–22144.
4. Datta, T.; Eshwaraiah, H.; Chockalingam, A. Generalized Space-and-Frequency Index Modulation. *IEEE Trans. Veh. Technol.* **2016**, *65*, 4911–4924.
5. Murtala, S.; Holoubi, T.; Muchena, N.; Mohaisen, M.; Choi, K. On the Performance of the Multiple Active Antenna Spatial Modulation with 3-Dimensional Constellation. *Appl. Sci.* **2020**, *10*, 3718.
6. Jiang, Y.; Xu, Y.; Xie, Y.; Hong, S.; Wu, X. Low-Complexity Detection Scheme for Generalized Spatial Modulation. *J. Commun.* **2016**, *11*, 726–732.
7. Lopes, H.; Souto, N. Iterative Signal Detection for Large-Scale GSM-MIMO Systems. *IEEE Trans. Veh. Technol.* **2018**, *67*, 7734–7738.
8. Castaneda, E.; Silva, A.; Gameiro, A.; Kountouris, M. An Overview on Resource Allocation Techniques for Multi-User MIMO Systems. *IEEE Commun. Surv. Tutor.* **2017**, *19*, 239–284.
9. Zu, K.; de Lamare, R.; Haardt, M. Generalized Design of Low-Complexity Block Diagonalization Type Precoding Algorithms for Multiuser MIMO Systems. *IEEE Trans. Commun.* **2013**, *61*, 4232–4242.
10. Lopes, P.; Gerald, J. Leakage-based precoding algorithms for multiple streams per terminal MU-MIMO systems. *Digit. Signal Process.* **2018**, *75*, 38–44.
11. Guerreiro, J.; Dinis, R.; Montezuma, P.; Marques da Silva, M. On the Achievable Performance of Nonlinear MIMO Systems. *IEEE Commun. Lett.* **2019**, *23*, 1725–1729.
12. Chataut, R.; Akl, R. Massive MIMO Systems for 5G and beyond Networks—Overview, Recent Trends, Challenges, and Future Research Direction. *Sensors* **2020**, *20*, 2753.
13. Souto, N.; Correia, A. Frequency Domain Equalization for Single and Multiuser Generalized Spatial Modulation Systems in Time Dispersive Channels. *IEEE Wirel. Commun. Lett.* **2020**, *9*, 316–320.
14. Spencer, Q.; Swindlehurst, A.; Haardt, M. Zero-Forcing Methods for Downlink Spatial Multiplexing in Multiuser MIMO Channels. *IEEE Trans. Signal Process.* **2004**, *52*, 461–471.
15. Lee, W.; Ro, J.; You, Y.; Hwang, D.; Song, H. An Enhanced Precoder for Multi User Multiple-Input Multiple-Output Downlink Systems. *Appl. Sci.* **2020**, *10*, 4547.
16. Li, X.; Zhang, Y.; Xiao, L.; Xu, X.; Wang, J. A novel precoding scheme for downlink multi-user spatial modulation system. In Proceedings of the IEEE 24th Annual International Symposium on Personal, Indoor, and Mobile Radio Communications (PIMRC), London, UK, 8–11 September 2013; pp. 1361–1365.
17. Zhang, H.; Ma, M.; Shao, Z. Multi-User Linear Precoding for Downlink Generalized Spatial Modulation Systems. *IEEE Commun. Lett.* **2020**, *24*, 212–216.
18. Marques da Silva, M.; Dinis, R.; Guerreiro, J. Energy-Efficient and Spectrally-Efficient MIMO. In *Wiley 5G Ref. Online,* **2019**, 1–18, doi:10.1002/9781119471509.w5GRef017.
19. Marques da Silva, M.; Dinis, R.; Guerreiro, J. Implicit Pilots for an Efficient Channel Estimation in Simplified Massive MIMO Schemes with Precoding. *Int. J. Antennas Propag.* **2019**, 2019, 1–11.
20. Gustavsson, U.; Sanchez-Perez, C.; Eriksson, T.; Athley, F.; Durisi, G.; Landin, P.; Hausmair, K.; Fager, C.; Svensson, L. On the impact of hardware impairments on massive MIMO. In Proceedings of the IEEE Globecom Workshops (GC Wkshps), Austin, TX, USA, 8–12 December 2014.
21. Souto, N.; Dinis, R. Efficient MIMO Detection for High-Order QAM Constellations in Time Dispersive Channels. In Proceedings of the IEEE International Conference on Communications (ICC), Kansas City, MO, USA, 20–24 May 2018.
22. Marques da Silva, M.; Dinis, R.; Guerreiro, J. A Low Complexity Channel Estimation and Detection for Massive MIMO Using SC-FDE. *Telecom* **2020**, *1*, 3–17.
23. Guerreiro, J.; Dinis, R.; Montezuma, P. Analytical Performance Evaluation of Precoding Techniques for Nonlinear Massive MIMO Systems with Channel Estimation Errors. *IEEE Trans. Commun.* **2018**, *66*, 1440–1451.
24. Mokhtari, Z.; Sabbaghian, M.; Dinis, R. A Survey on Massive MIMO Systems in Presence of Channel and Hardware Impairments. *Sensors* **2019**, *19*, 164.

25. Tullberg, H.; Popovski, P.; Li, Z.; Uusitalo, M.; Hoglund, A.; Bulakci, O.; Fallgren, M.; Monserrat, J. The METIS 5G System Concept: Meeting the 5G Requirements. *IEEE Commun. Mag.* **2016**, *54*, 132–139.
26. Cerwall, P. Ericsson Mobility Report. June 2019. Available online: https://www.ericsson.com/49d1d9/assets/local/mobility-report/documents/2019/ericsson-mobility-report-june-2019.pdf (accessed on 30 July 2020).
27. 3rd Generation Partnership Project (3GPP). TR 36819 v11.2.0, Coordinated Multi-Point Operation for LTE Physical Layer Aspects, Release 11. September 2013. Available online: http://www.3gpp.org/ftp/Specs/archive/36_series/36.819/36819-b20.zip (accessed on 30 July 2020).
28. Karakayali, M.; Foschini, G.; Valenzuela, R. Advances in smart antennas—Network coordination for spectrally efficient communications in cellular systems. *IEEE Wirel. Commun.* **2006**, *13*, 56–61.
29. Zhang, J.; Chen, R.; Andrews, J.; Ghosh, A.; Heath, R. Networked MIMO with clustered linear precoding. *IEEE Trans. Wirel. Commun.* **2009**, *8*, 1910–1921.
30. Dewa, G.; Park, C.; Sohn, I. Distributed Cell Clustering Based on Multi-Layer Message Passing for Downlink Joint Processing Coordinated Multipoint Transmission. *Appl. Sci.* **2020**, *10*, 5154.
31. Jabbar, S.; Li, Y. Analysis and Evaluation of Performance Gains and Tradeoffs for Massive MIMO Systems. *Appl. Sci.* **2016**, *6*, 268.
32. Boyd, S.; Parikh, N.; Chu, E. Distributed Optimization and Statistical Learning via the Alternating Direction Method of Multipliers; In *Foundations and Trends in Machine Learning Series*; Now Publishers Inc.: Delft, The Netherlands, 2010; pp. 1–122.
33. Xiao, Y.; Yang, Z.; Dan, L.; Yang, P.; Yin, L.; Xiang, W. Low-Complexity Signal Detection for Generalized Spatial Modulation. *IEEE Commun. Lett.* **2014**, *18*, 403–406.
34. Shim, B.; Kwon, S.; Song, B. Sparse Detection with Integer Constraint Using Multipath Matching Pursuit. *IEEE Commun. Lett.* **2014**, *18*, 1851–1854.
35. Van Chien, T.; Björnson, E. Massive MIMO Communications. In *5G Mobile Communications*; Xiang, W., Zheng, K., Shen, X., Eds.; Springer: Berlin, Germany, 2017,.
36. 3rd Generation Partnership Project (3GPP). TR 38.901 v. 14.3.0. "5G: Study on Channel Model for Frequencies from 0.5 to 100 GHz". Release 14. May 2017. Available online: http://www.3gpp.org/ftp/Specs/archive/38_series/38.901/38901-e11.zip (accessed on 9 September 2020).
37. Correia, A.; Silva, M.M. Link and system level simulation for MIMO. In *MIMO Processing for 4G and Beyond: Fundamentals and Evolution*; Silva, M.M., Monteiro, F.A., Eds.; CRC Press: Boca Raton, FL, USA, 2014.
38. Björnson, E.; Hoydis, J.; Sanguinetti, L. Massive MIMO Networks: Spectral, Energy and Hardware Efficiency. 2017. Available online: https://www.nowpublishers.com/article/Details/SIG-093 (accessed on 9 September 2020).
39. 3rd Generation Partnership Project (3GPP). TS 38211 v15.2.0. 5G/NR Physical Channels and Modulation, Release 15. July 2018. Available online: http://www.3gpp.org/ftp/Specs/archive/38_series/38.221/ 38211-f20.zip (accessed on 30 July 2020).
40. Stavridis, A.; Sinanovic, S.; Di Renzo, M.; Haas, H. Transmit precoding for receive spatial modulation using imperfect channel knowledge. In Proceedings of the IEEE 75th Vehicular Technology Conference (VTC Spring), Yokohama, Japan, 6–9 May 2012.

Chapter 4 – Low Complexity Hybrid Precoding Designs for Multiuser mmWave/THz Ultra Massive MIMO Systems

As mentioned earlier, the exploration of the potentialities of millimeter and terahertz wavelengths is closely related to the paradigm of using very large arrays of antennas in beamforming architectures. However, to achieve the maximum potential of these systems, it is necessary to consider the requirements and the challenges related not only to the channel characteristics but also to the hardware component. The adoption of hybrid digital/analog architectures is crucial to overcome issues such as high complexity and power usage, since these designs require a reduced number of dedicated RF chains and allow us to split the signal processing into two distinct components, which results in a substantial reduction in the overall circuit complexity and power consumption.

The article presented in this chapter proposes a hybrid design algorithm suitable for both mmWave and THz MU-MIMO systems that comprises separate computation steps for the digital precoder, analog precoder and MUI mitigation. This design can also incorporate different analog architectures such as phase shifters, switches and inverters and antenna selection. Due to its carachteristics, it is also applicable to different structures, namely, FC structures, AoSAs and DAoSAs, making it suitable for the support of UM-MIMO in severely hardware constrained THz systems.

Some paper details:

- Title: Low Complexity Hybrid Precoding Designs for Multiuser mmWave/THz Ultra Massive MIMO Systems;
- Date of publication: 9 September 2021;
- Journal: Sensors;
- Scimago/Scopus Journal Ranking: Quartile 1;
- Publisher: MDPI.

sensors

MDPI

Article

Low Complexity Hybrid Precoding Designs for Multiuser mmWave/THz Ultra Massive MIMO Systems

João Pedro Pavia [1,2,*], Vasco Velez [1,2], Renato Ferreira [1,2], Nuno Souto [1,2], Marco Ribeiro [1,2], João Silva [1,2] and Rui Dinis [2,3]

[1] Department of Information Science and Technology, ISCTE-Instituto Universitário de Lisboa,
1649-026 Lisboa, Portugal; Vasco_Velez@iscte-iul.pt (V.V.); Renato_Ferreira@iscte-iul.pt (R.F.);
Nuno.Souto@iscte-iul.pt (N.S.); Marco.Ribeiro@iscte-iul.pt (M.R.); Joao.Silva@iscte-iul.pt (J.S.)
[2] Instituto de Telecomunicações, 1049-001 Lisboa, Portugal; rdinis@fct.unl.pt
[3] Department of Electrical and Computer Engineering, Faculty of Science and Technology, Universidade Nova de Lisboa, 1099-085 Lisboa, Portugal
* Correspondence: jpavia@lx.it.pt

Sensors 2021, 21(18), 6054; https://doi.org/10.3390/s21186054

Received: 14 July 2021 / Revised: 25 August 2021 / Accepted: 8 September 2021 / Published: 9 September 2021

Abstract: Millimeter-wave and terahertz technologies have been attracting attention from the wireless research community since they can offer large underutilized bandwidths which can enable the support of ultra-high-speed connections in future wireless communication systems. While the high signal attenuation occurring at these frequencies requires the adoption of very large (or the so-called ultra-massive) antenna arrays, in order to accomplish low complexity and low power consumption, hybrid analog/digital designs must be adopted. In this paper we present a hybrid design algorithm suitable for both mmWave and THz multiuser multiple-input multiple-output (MIMO) systems, which comprises separate computation steps for the digital precoder, analog precoder and multiuser interference mitigation. The design can also incorporate different analog architectures such as phase shifters, switches and inverters, antenna selection and so on. Furthermore, it is also applicable for different structures, namely fully-connected structures, arrays of subarrays (AoSA) and dynamic arrays of subarrays (DAoSA), making it suitable for the support of ultra-massive MIMO (UM-MIMO) in severely hardware constrained THz systems. We will show that, by using the proposed approach, it is possible to achieve good trade-offs between spectral efficiency and simplified implementation, even as the number of users and data streams increases.

Keywords: millimeter wave (mmWave); Terahertz (THz); multiuser ultra-massive-MIMO; hybrid precoding and combining; antenna arrays

Citation: Pavia, J.P.; Velez, V.; Ferreira, R.; Souto, N.; Ribeiro, M.; Silva, J.; Dinis, R. Low Complexity Hybrid Precoding Designs for Multiuser mmWave/THz Ultra Massive MIMO Systems. *Sensors* **2021**, *21*, 18. https://doi.org/10.3390/s21186054

Academic Editor: Luís Castedo Ribas

Received: 14 July 2021
Accepted: 8 September 2021
Published: 9 September 2021

1. Introduction

Over the last few years, significant advances have been made to provide higher-speed connections to users in wireless networks, with several novel technologies being proposed to achieve this objective. However, future generations of communication systems will have to fulfil more demanding requirements that cannot be met by the methods adopted in today's communications systems. This

motivates the exploration of other candidate technologies, like the millimeter wave (mmWave) and Terahertz (THz) bands, where many applications that require ultra-high data rates can be designed. These bands offer great underutilized bandwidths and also allow for a simplified implementation of large antenna arrays, which are crucial to combat the severe signal attenuation and path losses that occurs at these frequencies [1–4]. The first applications of the THz band were limited to imaging and sensing due to the unavailability of efficient devices that can work on these frequencies. However, recent advances in the field of THz devices give us strong indications that THz communications will be feasible in the near future [3]. These technologies (THz systems in particular), are expected to ease the spectrum limitations of today's systems. They face several issues, such as the reflection and scattering losses through the transmission path, the high dependency between distance and frequency of channels at the THz band and the need for controllable time-delay phase shifters, since the phase shift will vary with frequencies based on the signal traveling time, which will also affect the system performance. These limitations require not only the proper system design, but also the definition of a set of strategies to enable communications [5,6].

The exploration of the potentialities of millimeter and sub-millimeter wavelengths is closely related to the paradigm of using very large arrays of antennas in beamforming architectures. This gives rise to so-called ultra-massive multiple-input multiple-output (UM-MIMO) systems. Still, to achieve the maximum potential of these systems, it is necessary to consider the requirements and the challenges related not only to the channel characteristics but also to the hardware component, especially regarding THz circuits [5,7,8]. Considering that high complexity and power usage are pointed out as major constraints of large-antenna systems, it is unfeasible to implement UM-MIMO schemes with a dedicated RF chain per antenna element in the mmWave and THz bands. Therefore, instead of fully-digital precoders and combiners, it becomes crucial to adopt hybrid digital/analog architectures as these require a reduced number of dedicated RF chains. By adopting this type of design, the signal processing is split into two separate parts: a low-dimensional digital part and a complementary analog part. This approach can enable a substantial reduction in the overall circuit complexity and power consumption [9]. By adopting a proper problem formulation, the analog design part can then be reduced to a simple projection operation in a flexible precoding or combining algorithm that can cope with different architectures, as we proposed in [10,11]. Despite the ultra-wide bandwidths available in mmWave and THz bands, and besides considering the problem of distance limitation, MIMO systems should take into account the operation in frequency selective channels [12]. To make the development of hybrid schemes for these systems a reality, it is necessary to handle the fading caused by multiple propagation paths typical in these types of channels [13]. Therefore, solutions inspired on multi-carrier schemes, such as orthogonal frequency division multiplexing (OFDM), are often adopted to address such problems [14].

Spectral Efficiency (SE) of point-to-point transmissions is a major concern in SingleUser (SU) and MultiUser (MU) systems. To achieve good performances, it is necessary to develop algorithms that are specially tailored to the architecture of these systems. Several hybrid precoding schemes have been proposed in the literature [15–19]. The authors of [15] proposed two algorithms for low-complexity hybrid precoding and beamforming for MU mmWave systems. Even though they assume only one stream per user, i.e., the number of data streams (N_s) is equal to the number of users (N_u), it is shown that the algorithms achieve interesting results when compared to the fully-digital solution. The concept of precoding based on adaptive RF-chain-to-antenna was only introduced in [16] for SU scenarios, but showed promising results. In [17], a nonlinear hybrid transceiver design relying on Tomlinson–Harashima precoding was proposed. Their approach only considers Fully-Connected (FC) architectures but can achieve a performance close to the fully-digital transceiver. A Kalman-based Hybrid Precoding method was proposed for MU scenarios in [18]. While designed for systems with only one stream per user and based on fully-connected structures, the performance of the algorithm is competitive with other existing solutions. A hybrid MMSE-based precoder and combiner design with low complexity was proposed in [19]. The algorithm is designed for MU-MIMO systems in narrowband channels, and it presents lower complexity and better results when compared to Kalman's precoding. Most of the hybrid solutions for mmWave systems aim to achieve near-optimal performance using FC structures, resorting to phase shifters or switches. However, the difficulty of handling the hardware constraint imposed by the analog phase shifters or by switches in the THz band is an issue that limits the expected performance in terms of SE.

Array-of-Subarrays (AoSAs) structures have gained particular attention over the last few years as a more practical alternative to FC structures, especially for the THz band. In contrast to FC structures, in which every RF chain is connected to all antennas via an individual group of phase shifters (which is prohibitive for higher frequencies), the AoSA approach allows us to have each RF chain connected to only a reduced subset of antennas. The adoption of a disjoint structure with fewer phase shifters reduces the system complexity, the power consumption and the signal power loss. Moreover, all of the signal processing can be easily carried out at the subarray level by using an adequate number of antennas [6].

Following the AoSA approach, it was shown in [20] that, to balance SE and power consumption in THz communications, adaption and dynamic control capabilities should be included in the hybrid precoding design. Therefore, Dynamic Arrays-of-Subarrays (DAoSAs) architectures could be adopted. The same authors proposed a DAoSA hybrid precoding architecture which can intelligently adjust the connections between RF chains and subarrays through a network of switches. Their results showed that it is possible to achieve a good trade-off for the balancing between the SE and power consumption.

Within the context of multiuser downlink scenarios, the authors of [21] studied some precoding schemes considering THz massive MIMO systems for Beyond 5th Generation (B5G) networks. Besides showing the impact on EE and SE performance, carrier frequency, bandwidth and antenna gains, three different precoding schemes were evaluated and compared. It was observed that the hybrid precoding approach with baseband Zero Forcing for multiuser interference mitigation (HYB-ZF) achieved much better results than an Analog-only Beamsteering (AN-BST) scheme with no baseband precoder. In fact, this approach was capable of better approaching the upper bound defined by the singular value decomposition precoder (SVD-UB). The other relevant conclusion is that the design of precoding algorithms should be adapted to the communication schemes. While considering all the specific constraints may allow the maximization of the system performance of the system, formulating and solving the corresponding optimization problem may not be so simple. Motivated by the work above, in this paper we developed an algorithm for hybrid precoding design which can accommodate different low-complexity architectures suitable for both mmWave and THz MU-MIMO systems. It is based on the idea of accomplishing a near-optimal approximation of the fully-digital precoder for any configuration of antennas, RF chains and data streams through the application of the alternating direction method of multipliers (ADMM) [22]. ADMM is a well-known and effective method for solving convex optimization problems but can also be a powerful heuristic for several non-convex problems [22,23]. To use it effectively within the context of MU-MIMO, THE proper formulation of the hybrid design problem as a multiple constrained matrix factorization problem is first presented. Using the proposed formulation, an iterative algorithm comprising several reduced complexity steps is obtained.

The main contributions of this paper can be summarized as follows:

- We propose a hybrid design algorithm with near fully-digital performance, where the digital precoder, analog precoder and multiuser interference mitigation are computed separately through simple closed-form solutions. Even though the hybrid design algorithm is developed independently of a specific channel or antenna configuration, it is particularly suitable for mmWave and THz systems where, on the one hand, very large antenna arrays are required to overcome distance limitations but, on the other hand, current hardware constraints in terms of cost and power consumption make the adoption fully-digital precoders/combiners with one dedicated RF chain per antenna element unviable. Whereas our previous work [10] also proposed a hybrid design algorithm for mmWave, it did not address multiuser systems, and in particular the MIMO broadcast channel. Therefore, it does not include any step for inter-user interference mitigation within its design. As we show here, for this multiuser channel, the hybrid design method must also deal with the residual inter-user interference as it can degrade system performance, particularly at high Signal Noise Ratios (SNRs);
- Due to the separability of the different steps (analog precoder, digital precoder and interference suppression), the proposed algorithm can incorporate different architectures, making it suitable for supporting UM-MIMO in severely hardware-constrained systems typical in the THz band. Unlike [10], where we only considered the adoption of phase shifters, in this paper we present explicit solutions for some of the most common architectures, namely FC, AoSA and DAoSA structures based in either Unquantized Phase Shifters

(UPS), Quantized Phase Shifters (QPS), Switches (Swi), Switches and Inverters (SI), Antenna Selection (AS) or Double Phase Shifters (DPS);

- To cope with the large bandwidths available in mmWave/THz bands, where practical MIMO systems likely have to operate in frequency selective channels, the proposed hybrid design considers the application in a multicarrier context, where the same analog precoder is applied at different frequencies;
- We explicitly show how the proposed design can be applied to a DAoSAs approach where a reduced number of switches are inserted at each AoSA panel, which allows the connections to the RF chains to be dynamically adjusted. Through extensive simulations, it is shown that our proposed solution is capable of achieving good trade-offs between spectral efficiency, hardware complexity and power consumption, proving to be a suitable solution for the deployment of UM-MIMO, especially in hardware-constrained THz systems.

The paper is organized as follows: Section II presents the adopted system model. The adopted formulation of the hybrid design problem for the MU-MIMO scenario and the proposed algorithm are described in detail in Section III, which includes the implementation of the algorithm for different analog architectures. Performance results are then presented in Section IV. Finally, the conclusions are outlined in Section V.

Notation: Matrices and vectors are denoted by uppercase and lowercase boldface letters, respectively. The superscript $(.)^T$ and $(.)^H$ denote the transpose and conjugate transpose of a matrix/vector, $\|\cdot\|_p$ is the ℓ_p - norm of a vector, $\|\cdot\|_0$ is its cardinality (i.e., the number of non-zero elements in a vector which is sometimes referred to as the ℓ_0 - norm in the literature) and $\boldsymbol{I}_n$ is the $n \times n$ identity matrix.

2. System Model

In this section, we present the system and channel models adopted for the design of the hybrid precoding algorithm. Let us consider the OFDM base system illustrated in Figure 1. In this case, we have a mmWave/THz hybrid multiuser MIMO system, where a base station (BS) is equipped with N_{tx} antennas and transmits to N_u users equipped with N_{rx} antennas over F carriers, as can be seen in Figure 1. On each subcarrier, N_s data streams are transmitted to each user which are represented as $\mathbf{s}_k = \left[\mathbf{s}_{k,1}^T ... \mathbf{s}_{k,N_u}^T\right]^T$, with $\mathbf{s}_{k,u} \in \mathbb{C}^{N_s \times 1}$. Instead of a fully-digital design which would require a dedicated RF chain per antenna element, both the precoder and combiner comprise separate digital and analog processing blocks. This approach allows for the use of reduced digital blocks with only a few RF chains, which are complemented by the analog blocks, that can be supported solely on networks of phase shifters and switches. Since the analog precoder (combiner) is located after (before) the IFFT (FFT) blocks, it is shared between the different subcarriers, as in [24,25]. Regarding the analog precoder and combiner, which are represented by matrices $\mathbf{F}_{\mathrm{RF}} \in \mathbb{C}^{N_{tx} \times N_{RF}^{tx}}$ and $\mathbf{W}_{\mathrm{RF}_u} \in \mathbb{C}^{N_{rx} \times N_{RF}^{rx}}$ with u=1,…,N_u, it is assumed that $N_u N_s \le N_{RF}^{tx} \le N_{tx}$ and $N_s \le N_{RF}^{rx} \le N_{rx}$, where N_{RF}^{tx} and N_{RF}^{rx} are the number of RF chains at the BS and each user, respectively. The received signal model at subcarrier k after the combiner can be written as

$$\mathbf{Y}_{k,u} = \sqrt{\rho_u}\mathbf{W}_{\mathrm{BB}_{k,u}}^H \mathbf{W}_{\mathrm{RF}_u}^H \mathbf{H}_{k,u} \mathbf{F}_{\mathrm{RF}} \mathbf{F}_{\mathrm{BB}_k} \mathbf{s}_k + \mathbf{W}_{\mathrm{BB}_{k,u}}^H \mathbf{W}_{\mathrm{RF}}^H \mathbf{n}_{k,u}, \quad (1)$$

where $\mathbf{H}_{k,u} \in \mathbb{C}^{N_{rx} \times N_{tx}}$ is the frequency domain channel matrix (assumed to be perfectly known at the transmitter and receiver) between the base station and the uth receiver at subcarrier k. Vector $\mathbf{n}_{k,u} \in \mathbb{C}^{N_{rx} \times 1}$ contains independent zero-mean circularly symmetric Gaussian noise samples with covariance $\sigma_n^2 \mathbf{I}_{N_{rx}}$ and ρ_u denotes the average received power. The digital baseband precoders and combiners are denoted by $\mathbf{F}_{\mathrm{BB}_k} \in \mathbb{C}^{N_{RF}^{tx} \times N_u N_s}$ and $\mathbf{W}_{\mathrm{BB}_{k,u}} \in \mathbb{C}^{N_{RF}^{rx} \times N_s}$, respectively.

Regarding the channel model, it is important to note that even though the mmWave and THz bands share a few commonalities, the THz channel has several peculiarities that distinguish it from the mmWave channel. For example, the very high scattering and diffraction losses in the THz band will typically result in a much sparser channel in the angular domain with fewer multipath components (typically less than 10) [21]. Furthermore, the gap between the line of sight (LOS) and non-line

of sight (NLOS) components tends to be very large, making it often LOS-dominant with NLOS-assisted [25]. An additional aspect relies on the much larger bandwidth of THz signals which can suffer performance degradation due to the so-called beam split effect, where the transmission paths squint into different spatial directions depending on the subcarrier frequency [20]. In light of this, in this paper we consider a clustered wideband geometric channel, which is commonly adopted both in the mmWave [15] and THz literature [20,25–28] However, it should be noted that the hybrid precoding/combining approach proposed in this paper is independent of a specific MIMO channel. In this case, the frequency domain channel matrices can be characterized as

$$\mathbf{H}_{k,u} = \gamma\left(\alpha_u^{LOS}\mathbf{a}_r\left(\phi_u^{r,LOS},\theta_u^{r,LOS}\right)\mathbf{a}_t\left(\phi_u^{t,LOS},\theta_u^{t,LOS}\right)^H + \right.$$

$$\left. + \sum_{i=1}^{N_{cl}}\sum_{l=1}^{N_{ray}}\alpha_{i,l,u}\mathbf{a}_r\left(\phi_{i,l,u}^{r},\theta_{i,l,u}^{r}\right)\mathbf{a}_t\left(\phi_{i,l,u}^{t},\theta_{i,l,u}^{t}\right)^H\right)e^{-j2\pi\tau_{i,u}f_k}, \tag{2}$$

where N_{cl} denotes the scattering clusters with each cluster i having a time delay of $\tau_{i,u}$ and N_{ray} propagations paths. α_u^{LOS} and $\alpha_{i,l,u}$ are the complex gains of the LOS component and of the lth ray from cluster i. Index u is the user (u=1,…, N_u), $f_k = f_c + \frac{B}{F}\left(k-1-\frac{F-1}{2}\right)$ (k=1,…, F) is the k^{th} subcarrier frequency, B is the bandwidth, f_c is the central frequency and γ is a normalizing factor such that $\mathrm{E}\left[\left\|\mathbf{H}_{k,u}\right\|_F^2\right] = N_{tx}N_{rx}$. Vectors $\mathbf{a}_t\left(\phi_{i,l,u}^{t},\theta_{i,l,u}^{t}\right)$ and $\mathbf{a}_r\left(\phi_{i,l,u}^{r},\theta_{i,l,u}^{r}\right)$ represent the transmit and receive antenna array responses at the azimuth and elevation angles of $\left(\phi_{i,l,u}^{t},\theta_{i,l,u}^{t}\right)$ and $\left(\phi_{i,l,u}^{r},\theta_{i,l,u}^{r}\right)$, respectively. Vectors $\mathbf{a}_t\left(\phi_u^{t,LOS},\theta_u^{t,LOS}\right)$ and $\mathbf{a}_r\left(\phi_u^{r,LOS},\theta_u^{r,LOS}\right)$ have similar meanings but refer to the LOS path angles $\left(\phi_u^{t,LOS},\theta_u^{t,LOS}\right)$ and $\left(\phi_u^{r,LOS},\theta_u^{r,LOS}\right)$. By carefully selecting the parameters of the channel model we can make it depict a mmWave or a THz channel. Considering Gaussian signaling, the spectral efficiency achieved by the system for the transmission to MS-u in subcarrier k is [28]

$$\mathbf{R}_{k,u} = \log_2\left|\mathbf{I}_{N_{RF}^{rx}} + \mathbf{R}_u^{-1}\mathbf{W}_{\mathrm{BB}_{k,u}}^H\mathbf{W}_{\mathrm{RF}_u}^H\mathbf{H}_{k,u}\mathbf{F}_{\mathrm{RF}}\mathbf{F}_{\mathrm{BB}_{k,u}}\times\right.$$
$$\left.\times\mathbf{F}_{\mathrm{BB}_{k,u}}^H\mathbf{F}_{\mathrm{RF}}^H\mathbf{H}_{k,u}{}^H\mathbf{W}_{\mathrm{RF}_u}\mathbf{W}_{\mathrm{BB}_{k,u}}\right|, \tag{3}$$

where $\mathbf{R}_{k,u}$ is the covariance matrix of the total inter-user interference plus noise at MS-u, which is characterized by

$$\mathbf{R}_{k,u} = \mathbf{W}_{\mathrm{BB}_{k,u}}^H\mathbf{W}_{\mathrm{RF}_u}^H(\mathbf{H}_{k,u}\sum_{j\neq u}^{N_u}\mathbf{F}_{\mathrm{RF}}\mathbf{F}_{\mathrm{BB}_{k,j}}\mathbf{F}_{\mathrm{BB}_{k,j}}^H\mathbf{F}_{\mathrm{RF}}^H\mathbf{H}_{k,u}{}^H +$$
$$+\sigma^2\mathbf{I}_{N_{rx}})\mathbf{W}_{\mathrm{RF}_u}\mathbf{W}_{\mathrm{BB}_{k,u}}. \tag{4}$$

3. Proposed Hybrid Design Algorithm

In this section, we will introduce the algorithm for the hybrid precoding problem and show how it can be adapted to different architectures. Although we will focus on the precoder design, a similar approach can be adopted for the combiner. However, since our design assumes that inter-user interference suppression is applied at the transmitter, only single-user detection is required at the receiver and therefore the algorithm reduces to the one described in [10].

3.1. Main Algorithm

Although there are several problem formulations for the hybrid design proposed in the literature, one of the most effective relies on the minimization of the Frobenius norm of the difference between the fully-digital precoder and the hybrid precoder [22,29–31]. In this paper we follow this matrix approximation-based

approach. First, we compute fully-digital precoders, which we assume to be designed so as to enforce zero inter-user interference, using, for example, the block-diagonalization (BD) approach described in [32].

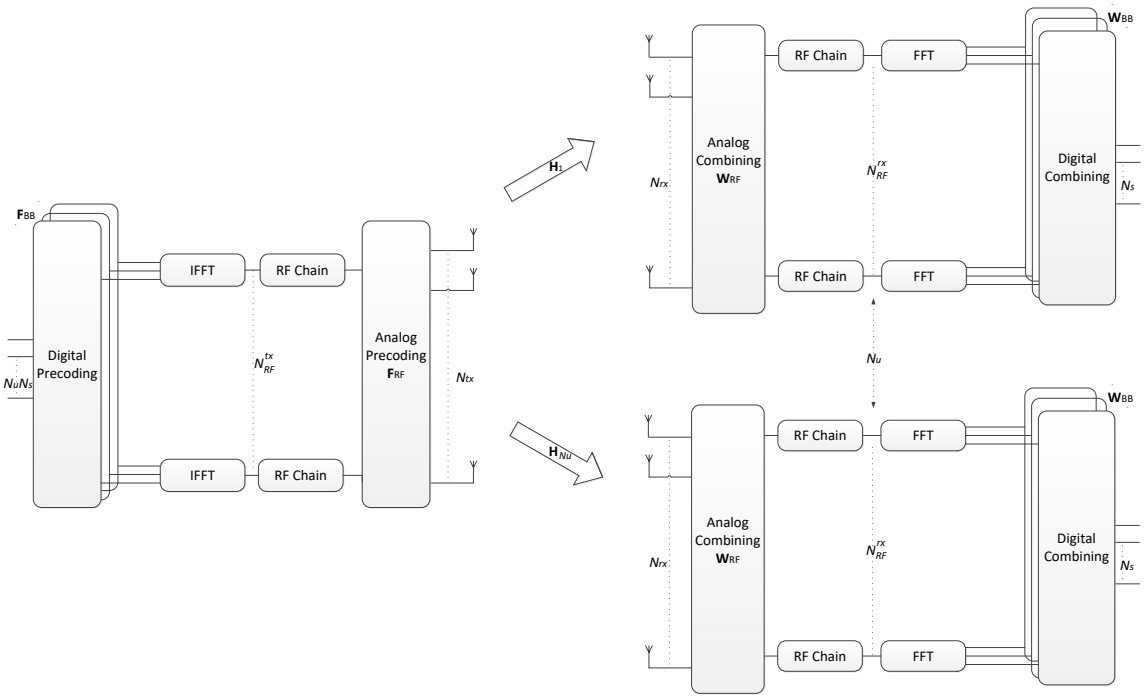

Figure 1. A multiuser OFDM mmWave/THz MIMO system with hybrid precoding.

Using the BD procedure, we obtain one different digital precoder matrix for each subcarrier, $\mathbf{F}_{\text{opt}_k}$ (with k=1,…, F, and $\mathbf{F}_{\text{opt}_k}=\left[\mathbf{F}_{\text{opt}_{k,1}},\cdots,\mathbf{F}_{\text{opt}_{k,N_u}}\right]$), which satisfy $\mathbf{H}_{k,u}\mathbf{F}_{k,u}=0$ for all $u'\neq u$ (u,u'=1,…,N_u), thus guaranteeing no inter-user interference. Using these digital precoder matrices, we design the hybrid digital/analog precoder by solving a matrix approximation problem formulated as

$$\min_{\mathbf{F}_{\text{RF}},\mathbf{F}_{\text{BB}_k}} \sum_{k=1}^{F}\left\|\mathbf{F}_{opt_k}-\mathbf{F}_{\text{RF}}\mathbf{F}_{\text{BB}_k}\right\|_F^2 \tag{5}$$

$$\text{subject to } \mathbf{F}_{\text{RF}}\in\mathcal{C}_{N_{tx}\times N_{RF}^{tx}} \tag{6}$$

$$\left\|\mathbf{F}_{\text{RF}}\mathbf{F}_{\text{BB}_k}\right\|_F^2=N_uN_s\,, \tag{7}$$

where equation (7) enforces the transmitter's total power constraint and $\mathcal{C}_{N_{tx}\times N_{RF}}$ is the set of feasible analog precoding matrices, which is defined according to the adopted RF architecture (it will be formally defined for several different

architectures in the next subsection). Matrix $\mathbf{F}_{\text{opt}_k}$ denotes the fully-digital precoder. Even if $\mathbf{F}_{\text{opt}_k}$ is selected in order to cancel all interference between users, the hybrid design resulting as a solution of equations (5)–(7) will correspond to an approximation and, as such, residual inter-user interference will remain. To avoid the performance degradation that will result from this, an additional constraint can be added to the problem formulation, namely

$$\sum_{\substack{u'=1\\u'\neq u}}^{N_u}\mathbf{H}_{k,u'}\mathbf{F}_{\text{RF}}\mathbf{F}_{\text{BB}_{k,u}}=0,\quad k=1,...,F,\quad u=1,...,N_u \tag{8}$$

where $\mathbf{F}_{\mathrm{BB}_{k,u}} = \mathbf{F}_{\mathrm{BB}_k}[:,(u-1)N_s+1:uN_s]$. This restriction is equivalent to enforcing $\mathbf{F}_{\mathrm{RF}}\mathbf{F}_{\mathrm{BB}_{k,u}}$ to lie in the null space of $\bar{\mathbf{H}}_{k,u} \in \mathbb{C}^{(N_u-1)N_{rx}\times N_{tx}}$ ($\bar{\mathbf{H}}_{k,u}$ is a matrix corresponding to $\mathbf{H}_k$ with the N_{rx} lines of user u removed) which we denote as $\mathcal{N}(\bar{\mathbf{H}}_{k,u})$. The overall optimization problem can be then expressed as

$$\min_{\mathbf{F}_{\mathrm{RF}},\mathbf{F}_{\mathrm{BB}_k}} \sum_{k=1}^{F} \left\| \mathbf{F}_{\mathrm{opt}_k} - \mathbf{F}_{\mathrm{RF}}\mathbf{F}_{\mathrm{BB}_k} \right\|_F^2 \tag{9}$$

$$\text{subject to } \mathbf{F}_{\mathrm{RF}} \in \mathcal{C}_{N_{tx}\times N_{RF}^{tx}} \tag{10}$$

$$\left\| \mathbf{F}_{\mathrm{RF}}\mathbf{F}_{\mathrm{BB}_k} \right\|_F^2 = N_u N_s \tag{11}$$

$$\mathbf{F}_{\mathrm{RF}}\mathbf{F}_{\mathrm{BB}_{k,u}} \in \mathcal{N}(\bar{\mathbf{H}}_{k,u}),\ \ k=1,\ldots,F,\ \ u=1,\ldots,N_u\,. \tag{12}$$

To derive a hybrid precoder/design algorithm that can cope with the different RF architectures, we can integrate the RF constraint directly into the objective function of the optimization problem. This can be accomplished through the addition of an auxiliary variable, **R**, combined with the use of the indicator function. The indicator function for a generic set $\mathcal{A}$ is defined as $I_{\mathcal{A}}(\mathbf{x})$, returning 0 if $\mathbf{x} \in \mathcal{A}$ and +∞ otherwise. A similar approach can be adopted for integrating the other constraints, equations (11) and (12), also into the objective function. The optimization problem can then be rewritten as

$$\min_{\mathbf{F}_{\mathrm{RF}},\mathbf{F}_{\mathrm{BB}_k},\mathbf{R},\mathbf{B}_k,\mathbf{F}_{\mathrm{aprox}_{k,u}}} \sum_{k=1}^{F} \left\| \mathbf{F}_{\mathrm{opt}_k} - \mathbf{F}_{\mathrm{RF}}\mathbf{F}_{\mathrm{BB}_k} \right\|_F^2 + \mathrm{I}_{\mathcal{C}}(\mathbf{R}) +$$

$$+\sum_{k=1}^{F} \mathrm{I}_{\|\cdot\|_F^2 = N_u N_s}(\mathbf{B}_k) + \sum_{k=1}^{F}\sum_{u=1}^{N_u} \mathrm{I}_{\mathcal{N}(\bar{\mathbf{H}}_{k,u})}(\mathbf{F}_{\mathrm{aprox}_{k,u}}) \tag{13}$$

$$\text{subject to } \mathbf{R} = \mathbf{F}_{\mathrm{RF}} \tag{14}$$

$$\mathbf{B}_k = \mathbf{F}_{\mathrm{RF}}\mathbf{F}_{\mathrm{BB}_k} \tag{15}$$

$$\mathbf{F}_{\mathrm{aprox}_{k,u}} = \mathbf{F}_{\mathrm{RF}}\mathbf{F}_{\mathrm{BB}_k}\,, \tag{16}$$

where $\mathbf{F}_{\mathrm{aprox}_k} = \left[\mathbf{F}_{\mathrm{aprox}_{k,1}},\cdots,\mathbf{F}_{\mathrm{aprox}_{k,N_u}}\right]$. The augmented Lagrangian function (ALF) for equations (13)–(16) can be written as

$$L_{\rho,\eta,\mu}(\mathbf{F}_{\mathrm{RF}},\mathbf{F}_{\mathrm{BB}},\mathbf{R},\mathbf{B},\mathbf{F}_{\mathrm{aprox}},\mathbf{\Lambda},\mathbf{\Psi},\mathbf{\Gamma}) = \sum_{k=1}^{F} \left\| \mathbf{F}_{\mathrm{opt}_k} - \mathbf{F}_{\mathrm{RF}}\mathbf{F}_{\mathrm{BB}_k} \right\|_F^2 + I_{\mathcal{C}_{N_{tx}\times N_{RF}^{tx}}}(\mathbf{R}) +$$

$$+\sum_{k=1}^{K} \mathrm{I}_{\|\cdot\|_F^2 = N_u N_s}(\mathbf{B}_k) + \sum_{k=1}^{F}\sum_{u=1}^{Nu} \mathrm{I}_{\mathcal{N}(\bar{\mathbf{H}}_{k,u})}(\mathbf{F}_{\mathrm{aprox}_{k,u}}) + 2\,\mathrm{Re}\{\mathrm{tr}(\mathbf{\Lambda}^H(\mathbf{F}_{\mathrm{RF}} - \mathbf{R}) +$$

$$+ \mathrm{tr}(\Psi_k{}^H \sum_{k=1}^{F}(-\mathbf{B}_k + \mathbf{F}_{\mathrm{RF}}\mathbf{F}_{\mathrm{BB}_k})) + \mathrm{tr}(\Gamma_k{}^H \sum_{k=1}^{F}(-\mathbf{F}_{\mathrm{aprox}_k} + \mathbf{F}_{\mathrm{RF}}\mathbf{F}_{\mathrm{BB}_k}))\} +$$

$$+\rho\left\|\mathbf{F}_{\mathrm{RF}}-\mathbf{R}\right\|_F^2+\eta\sum_{k=1}^{F}\left\|-\mathbf{B}_k+\mathbf{F}_{\mathrm{RF}}\mathbf{F}_{\mathrm{BB}_k}\right\|_F^2+\mu\sum_{k=1}^{F}\left\|-\mathbf{F}_{\mathrm{aprox}_k}+\mathbf{F}_{\mathrm{RF}}\mathbf{F}_{\mathrm{BB}_k}\right\|_F^2, \tag{17}$$

where $\mathbf{\Lambda}\in\mathbb{C}^{N_{\mathrm{Tx}}\times N_{RF}}$, $\mathbf{\Psi}\in\mathbb{C}^{N_{\mathrm{Tx}}\times N_{RF}}$ and $\mathbf{\Gamma}\in\mathbb{C}^{N_{\mathrm{Tx}}\times N_{RF}}$ are dual variables and ρ, η, μ are penalty parameters. After some straightforward algebraic manipulation and working with scaled dual variables $\mathbf{U}=\mathbf{\Lambda}/\rho$, $\mathbf{W}_k=\mathbf{\Psi}/\eta$ and $\mathbf{Z}_k=\mathbf{\Gamma}_k/\mu$ we can rewrite the ALF as

$$L_{\rho,\eta,\mu}(\mathbf{F}_{\mathrm{RF}},\mathbf{F}_{\mathrm{BB}},\mathbf{R},\mathbf{B},\mathbf{F}_{\mathrm{aprox}},\mathbf{U},\mathbf{W},\mathbf{Z})=\sum_{k=1}^{K}\left\|\mathbf{F}_{\mathrm{opt}_k}-\mathbf{F}_{\mathrm{RF}}\mathbf{F}_{\mathrm{BB}_k}\right\|_F^2+I_{\mathcal{C}_{N_{\mathrm{Tx}}\times N_{RF}^{\mathrm{Tx}}}}(\mathbf{R})+$$

$$+\sum_{k=1}^{F}\mathbf{I}_{\|\mathbf{F}\|_F^2=N_uN_s}(\mathbf{B}_k)+\sum_{k=1}^{F}\sum_{u=1}^{Nu}\mathbf{I}_{\mathcal{N}(\bar{\mathbf{n}}_{k,u})}(\mathbf{F}_{\mathrm{aprox}_k,u})+\rho\left\|\mathbf{F}_{\mathrm{RF}}-\mathbf{R}+\mathbf{U}\right\|_F^2-\rho\left\|\mathbf{U}\right\|_F^2+$$

$$+\eta\sum_{k=1}^{F}\left\|-\mathbf{B}_k+\mathbf{F}_{\mathrm{RF}}\mathbf{F}_{\mathrm{BB}_k}+\mathbf{W}_k\right\|_F^2-\eta\sum_{k=1}^{F}\left\|\mathbf{W}_k\right\|_F^2+$$

$$+\mu\sum_{k=1}^{F}\left\|-\mathbf{F}_{\mathrm{aprox}_k}+\mathbf{F}_{\mathrm{RF}}\mathbf{F}_{\mathrm{BB}_k}+\mathbf{Z}_k\right\|_F^2-\mu\sum_{k=1}^{F}\left\|\mathbf{Z}_k\right\|_F^2. \tag{18}$$

In the following, we apply ADMM [22] as a heuristic for solving problem Formulation (13)–(16). To accomplish this, we can apply the gradient ascent to the dual problem involving the ALF, which allows us to obtain an iterative precoding algorithm comprising the following sequence of steps. We start with the minimization of the ALF over $\mathbf{F}_{\mathrm{RF}}$ for iteration *t*+1 defined as

$$\mathbf{F}_{\mathrm{BB}}^{(t+1)}=\min_{\mathbf{F}_{\mathrm{BB}}}L_{\rho,\eta,\mu}(\mathbf{F}_{\mathrm{RF}}^{(t)},\mathbf{F}_{\mathrm{BB}},\mathbf{R}^{(t)},\mathbf{B}^{(t)},\mathbf{F}_{\mathrm{aprox}}^{(t)},\mathbf{U}^{(t)},\mathbf{W}^{(t)},\mathbf{Z}^{(t)}), \tag{19}$$

which can be obtained from

$$\nabla_{\mathbf{F}_{\mathrm{RF}}{}^{H}}L_{\rho,\eta,\mu}(\mathbf{F}_{\mathrm{RF}},\mathbf{F}_{\mathrm{BB}}{}^{(t)},\mathbf{R}^{(t)},\mathbf{B}^{(t)},\mathbf{F}_{\mathrm{aprox}}{}^{(t)},\mathbf{U}^{(t)},\mathbf{W}^{(t)},\mathbf{Z}^{(t)})=0 \tag{20}$$

leading to the closed form expression

$$\mathbf{F}_{\mathrm{RF}}^{(t+1)}=\left[\sum_{k=0}^{F-1}[\mathbf{F}_{\mathrm{opt}_k}+\eta(\mathbf{B}_k^{(t)}-\mathbf{W}_k^{(t)})+\mu(\mathbf{F}_{\mathrm{aprox}_k}^{(t)}-\mathbf{Z}_k^{(t)})]\mathbf{F}_{\mathrm{BB}_k}^{(t)\,H}+\rho\left(\mathbf{R}^{(t)}-\mathbf{U}^{(t)}\right)\right]\times$$
$$\times[(1+\eta+\mu)\sum_{k=0}^{F-1}\mathbf{F}_{\mathrm{BB}_k}^{(t)}\mathbf{F}_{\mathrm{BB}_k}^{(t)\,H}+\rho\mathbf{I}_{N_{RF}^{\mathrm{Tx}}}]^{-1},\ k=0,\ldots,F-1. \tag{21}$$

After obtaining the expression for $\mathbf{F}_{\mathrm{RF}}$, $\mathbf{F}_{\mathrm{BB}}{}^{(t+1)}$ can be found by following the same methodology. In this case the minimization is expressed as

$$\mathbf{F}_{\mathrm{BB}}{}^{(t+1)}=\min_{\mathbf{F}_{\mathrm{BB}}}L_{\rho,\eta,\mu}(\mathbf{F}_{\mathrm{RF}}{}^{(t)},\mathbf{F}_{\mathrm{BB}},\mathbf{R}^{(t)},\mathbf{B}^{(t)},\mathbf{F}_{\mathrm{aprox}}{}^{(t)},\mathbf{U}^{(t)},\mathbf{W}^{(t)},\mathbf{Z}^{(t)}), \tag{22}$$

which can be obtained from

$$\nabla_{\mathbf{F}_{\mathrm{BB}}{}^{H}}L_{\rho,\eta,\mu}(\mathbf{F}_{\mathrm{RF}}{}^{(t)},\mathbf{F}_{\mathrm{BB}},\mathbf{R}^{(t)},\mathbf{B}^{(t)},\mathbf{F}_{\mathrm{aprox}}{}^{(t)},\mathbf{U}^{(t)},\mathbf{W}^{(t)},\mathbf{Z}^{(t)})=0 \tag{23}$$

and leads to the closed form expression

$$\mathbf{F}_{\mathrm{BB}_k}{}^{(t+1)}=(1+\eta+\mu)\left(\mathbf{F}_{\mathrm{RF}}^{(t+1)H}\mathbf{F}_{\mathrm{RF}}^{(t+1)}\right)^{-1}\mathbf{F}_{\mathrm{RF}}^{(t+1)H}\cdot$$
$$\cdot\left(\mathbf{F}_{\mathrm{opt}_k}+\eta(\mathbf{B}_k^{(t)}-\mathbf{W}_k^{(t)})+\mu(\mathbf{F}_{\mathrm{aprox}_k}^{(t)}-\mathbf{Z}_k^{(t)})\right),k=1,\ldots,F. \tag{24}$$

The next steps consist of the minimization over $\mathbf{R}$ and $\mathbf{B}_k$. The minimization of equation (18) with respect to $\mathbf{R}$ and $\mathbf{B}_k$ can be written as

$$\begin{aligned}\mathbf{R}^{(t+1)} &= \min_{\mathbf{R}} \left\{ \mathrm{I}_{\mathcal{C}_{N_{Tx} \times N_{RF}}}(\mathbf{R}) + \rho \left\| \mathbf{F}_{RF}^{(t+1)} - \mathbf{R} + \mathbf{U}^{(t)} \right\|_F^2 \right\} \\ &= \prod_{\mathcal{C}_{N_{Tx} \times N_{RF}}} \left(\mathbf{F}_{\mathrm{RF}}^{(t+1)} + \mathbf{U}^{(t)} \right),\end{aligned} \tag{25}$$

and

$$\begin{aligned}\mathbf{B}_k^{(t+1)} &= \min_{\mathbf{R}} \left\{ \mathrm{I}_{\|\mathbf{B}\|_F^2 = N_u N_s}(\mathbf{B}_k) + \eta \left\| \mathbf{F}_{\mathrm{RF}}^{(t+1)} \mathbf{F}_{\mathrm{BB}_k}^{(t+1)} - \mathbf{B}_k + \mathbf{W}^{(t)} \right\|_F^2 \right\} \\ &= \prod_{\|\mathbf{B}\|_F^2 = N_u N_s} \left(\mathbf{F}_{\mathrm{RF}}^{(t+1)} \mathbf{F}_{\mathrm{BB}_k}^{(t+1)} + \mathbf{W}^{(t)} \right), \ k = 1, \ldots, F ,\end{aligned} \tag{26}$$

where $\prod_{\mathcal{C}_{a \times b}}(\cdot)$ and $\prod_{\|\mathbf{B}\|_F^2 = N_u N_s}(\cdot)$ denote the projection onto set $\mathcal{C}_{a \times b}$ and onto the set of matrices whose squared Frobenius norm is $N_u N_s$, respectively. While the former projection depends on the adopted analog architecture and will be explained in the next subsection, the second projection is simply computed as

$$\mathbf{B}_k^{(t+1)} = \frac{\left(\mathbf{F}_{\mathrm{RF}}^{(t+1)} \mathbf{F}_{\mathrm{BB}_k}^{(t+1)} + \mathbf{W}^{(t)} \right) \sqrt{N_u N_s}}{\left\| \mathbf{F}_{\mathrm{RF}}^{(t+1)} \mathbf{F}_{\mathrm{BB}_k}^{(t+1)} + \mathbf{W}^{(t)} \right\|_F^2} . \tag{27}$$

The minimization of (18) with respect of $\mathbf{F}_{\mathrm{aprox}_{k,u}}$ can be written as

$$\begin{aligned}\mathbf{F}_{\mathrm{aprox}_{k,u}}^{(t+1)} &= \min_{\mathbf{F}_{\mathrm{aprox}_{k,u}}} \{ \mathrm{I}_{\mathcal{N}(\bar{\mathbf{H}}_{k,u})}(\mathbf{F}_{\mathrm{aprox}_{k,u}}) + \\ &+ \mu \left\| \mathbf{F}_{\mathrm{RF}}^{(t+1)} \mathbf{F}_{\mathrm{BB}_{k,(u-1)N_s+1:uN_s}}^{(t+1)} - \mathbf{F}_{\mathrm{aprox}_{k,u}} + \mathbf{Z}_{k,(u-1)N_s+1:uN_s}^{(t)} \right\|_F^2 \} \\ &= \prod_{\mathcal{N}(\bar{\mathbf{H}}_{k,u})} \left(\left(\mathbf{F}_{\mathrm{RF}}^{(t+1)} \mathbf{F}_{\mathrm{BB}_k}^{(t+1)} \right)_{k,(u-1)N_s+1:uN_s} + \mathbf{Z}_{k,(u-1)N_s+1:uN_s}^{(t)} \right),\end{aligned} \tag{28}$$

which also involves a projection, $\prod_{\mathcal{N}(\bar{\mathbf{H}}_{k,u})}(\cdot)$, but in this case onto the null-space of $\bar{\mathbf{H}}_{k,u}$. Let us use $\mathbf{A}$ to denote $\mathbf{A} = \mathbf{F}_{\mathrm{RF}}^{(t+1)} \mathbf{F}_{\mathrm{BB}_{k,u}}^{(t+1)} + \mathbf{Z}_{k,(u-1)N_s+1:uN_s}^{(t)}$. The procedure to compute the projection of matrix $\mathbf{A}$ onto the null-space of $\bar{\mathbf{H}}_{k,u}$ can be formulated as another optimization problem, which can be expressed as

$$\min \ \sum_{i=1}^{N_s} \left\| \mathbf{A}_{:,i} - \mathbf{X}_{:,i} \right\|_F^2 \tag{29}$$

$$\text{subject to} \ \ \bar{\mathbf{H}}_{k,u} \mathbf{X}_{:,i} = 0 . \tag{30}$$

The general solution for this problem is presented in [29] corresponding to

$$\mathbf{X}_{:,i} = \left(\mathbf{I}_{N_{Tx}} - \bar{\mathbf{H}}_{k,u}^{H} \left(\bar{\mathbf{H}}_{k,u} \bar{\mathbf{H}}_{k,u}^{H} \right)^{-1} \bar{\mathbf{H}}_{k,u} \right) \mathbf{A}_{:,i}, \ \ i = 1, \ldots, N_s . \tag{31}$$

Reordering the column vectors in the original matrix form results in the final expression which can be rewritten as

$$\begin{aligned}\mathbf{X} &= \left(\mathbf{I}_{N_{Tx}} - \bar{\mathbf{H}}_{k,u}^{H} \left(\bar{\mathbf{H}}_{k,u} \bar{\mathbf{H}}_{k,u}^{H} \right)^{-1} \bar{\mathbf{H}}_{k,u} \right) \mathbf{A} \\ &= \left(\mathbf{I}_{N_{Tx}} - \bar{\mathbf{V}}_{k,u}^{(1)} \left(\bar{\mathbf{V}}_{k,u}^{(1)} \right)^{H} \right) \mathbf{A} .\end{aligned} \tag{32}$$

In this expression, $\bar{\mathbf{V}}_{k,u}^{(1)}$ denotes the matrix containing the right singular vectors corresponding to the non-zero singular values associated with the singular value decomposition (SVD) given by $\bar{\mathbf{H}}_{k,u} = \bar{\mathbf{U}}_{k,u} \bar{\mathbf{\Lambda}}_{k,u} \left[\bar{\mathbf{V}}_{k,u}^{(1)} \ \bar{\mathbf{V}}_{k,u}^{(0)} \right]^{H}$.

Therefore, to compute matrix **X**, one can perform a single value decomposition of $\bar{\mathbf{H}}_{k,u}$ and then use this to remove the projection of **A** onto the row space of $\bar{\mathbf{H}}_{k,u}$. Finally, the expressions for the update of dual variables **U**, **W** and **Z** are given by

$$\mathbf{U}^{(t+1)} = \mathbf{U}^{(t)} + \mathbf{F}_{\mathrm{RF}}^{(t+1)} - \mathbf{R}^{(t+1)}, \tag{33}$$

$$\mathbf{W}_k^{(t+1)} = \mathbf{W}_k^{(t)} + \mathbf{F}_{\mathrm{RF}}^{(t+1)}\mathbf{F}_{\mathrm{BB}_k}^{(t+1)} - \mathbf{B}_k^{(t+1)}, \tag{34}$$

$$\mathbf{Z}_k^{(t+1)} = \mathbf{Z}_k^{(t)} + \mathbf{F}_{\mathrm{RF}}^{(t+1)}\mathbf{F}_{\mathrm{BB}_k}^{(t+1)} - \mathbf{F}_{\mathrm{aprox}_k}^{(t+1)}. \tag{35}$$

Appropriate values for the penalty parameters can be obtained in a heuristic manner by performing numerical simulations. Regarding the initialization and termination of the algorithm, the same approach described in [10] can be adopted. The whole algorithm is summarized in Table 1.

Table 1. General Iterative Hybrid Design Algorithm.

1: **Input:** $\mathbf{F}_{\mathrm{opt}_k}$, $\mathbf{F}_{\mathrm{RF}}^{(0)}$, $\mathbf{F}_{\mathrm{BB}_k}^{(0)}$, $\mathbf{R}^{(0)}$, $\mathbf{B}_k^{(0)}$, $\mathbf{F}_{\mathrm{aprox}_{k,u}}^{(0)}$, ρ, Q

2: **for** t = 0, 1, …, Q−1 **do**

3: Compute $\mathbf{F}_{\mathrm{RF}}^{(t+1)}$ using (21).

4: Compute $\mathbf{F}_{\mathrm{BB}_k}^{(t+1)}$ using (24), for all k = 1,..., F.

5: Compute $\mathbf{R}^{(t+1)}$ using (25).

6: Compute $\mathbf{B}_k^{(t+1)}$ using (26), for all k = 1,..., F.

7: Compute $\mathbf{F}_{\mathrm{aprox}_{k,u}}^{(t+1)}$ using (28), for all k = 1,..., F and u = 1, …, N_u.

8: Update $\mathbf{U}^{(t+1)}$ using (33).

9: Update $\mathbf{W}_k^{(t+1)}$ using (34), for all k = 1,..., F.

10: Update $\mathbf{Z}_k^{(t+1)}$ using (35), for all k = 1,..., F.

11: **end for.**

12: $\hat{\mathbf{F}}_{\mathrm{RF}} \leftarrow \mathbf{R}^{(Q)}$.

13: $\hat{\mathbf{F}}_{\mathrm{BB}_k} \leftarrow \left(\hat{\mathbf{F}}_{\mathrm{RF}}{}^{H}\hat{\mathbf{F}}_{\mathrm{RF}}\right)^{-1}\hat{\mathbf{F}}_{\mathrm{RF}}{}^{H}\mathbf{F}_{\mathrm{aprox}_k}^{(Q)}$, for all k = 1,..., F.

14: $\hat{\mathbf{F}}_{\mathrm{BB}_k} \leftarrow \sqrt{N_u N_s}\left\|\hat{\mathbf{F}}_{\mathrm{BB}_k}{}^{H}\hat{\mathbf{F}}_{\mathrm{BB}_k}\right\|_F^{-1}\hat{\mathbf{F}}_{\mathrm{BB}_k}$.

15: **Output:** $\hat{\mathbf{F}}_{\mathrm{RF}}$, $\hat{\mathbf{F}}_{\mathrm{BB}}$.

In this table, Q denotes the maximum number of iterations. The projection operation is the only step specific to the implemented architecture, as will be explained in the next subsection.

3.2. Analog RF Precoder/Combiner Structure

The projection required for obtaining matrix **R** in step 5 of the precoding algorithm has to be implemented according to the specific analog beamformer [6,20,33–37]. This makes the proposed scheme very generic, allowing it to be easily adapted to different RF architectures. In the following, we will consider a broad range of architectures that can be adopted for the RF precoder for achieving reduced complexity and power consumption implementations. We will consider FC, AoSA and DAoSA structures as illustrated in Figure 2, where we assume single phase shifters (SPS). Besides SPS, we will also consider other alternative implementations for these structures, as illustrated in Figure 3 for AoSA. The different solutions either rely on selectors, switches, inverters or phase shifters, or combinations of these. The overall analog structure is defined as a combination of one of the architectures in Figure 2 with either SPS or one of the alternatives illustrated in Figure 3.

(1) Unquantized Phase Shifters (UPS)

In the first case, we consider the use of infinite resolution phase shifters which, while being ideal, are often used as a reference benchmark. For this architecture the RF constraint set is given by

$$\mathcal{C}_{a\times b} = \left\{\mathbf{X} \in \mathbb{C}^{a\times b} : \left|X_{i,j}\right| = 1\right\} \tag{36}$$

and the corresponding projection can be performed simply using

$$\mathbf{R}^{(t+1)} = \left(\mathbf{F}_{\mathrm{RF}}^{(t+1)} + \mathbf{W}^{(t)}\right) \oslash \left|\mathbf{F}_{\mathrm{RF}}^{(t+1)} + \mathbf{W}^{(t)}\right|, \tag{37}$$

where $\oslash$ denotes the Hadamard (i.e., element-wise) division.

(2) Quantized Phase Shifters (QPS)

The second case considers a more realistic scenario, in which phase shifters can be digitally controlled with N_b bits. These devices allow the selection of 2^{N_b} different quantized phases and the RF constraint set becomes

$$\mathcal{C}_{a\times b} = \left\{\mathbf{X} \in \mathbb{C}^{a\times b} : X_{i,j} = e^{2\pi k i/2^{N_b}},\ k=0,\ldots,2^{N_b}-1\right\}. \tag{38}$$

The implementation of the projection in line 5 of Table 1 can be obtained as the following element-wise quantization

$$R_{i,j}^{(t+1)} = e^{\min\limits_{k=0,\ldots,2^{N_b}-1}\left\{\mathrm{angle}\left(F_{\mathrm{RF}_{i,j}}^{(t+1)}+W_{i,j}^{(t)}\right)-2\pi k/2^{N_b}\right\}},\ i=1,\ldots,N_{tx},\ j=1,\ldots,N_{RF}^{tx}. \tag{39}$$

Phase shifters are typically one of the best solutions for analog processing blocks but also have a higher implementation cost and power consumption, especially when they have high resolutions.

(3) Double Phase Shifters (DPS)

Another appealing architecture relies on the use of double phase shifters (DPS) since these remove the constant modulus restriction on the elements of $\mathbf{F}_{\mathrm{RF}}$, following the idea in [37]. The main difference between SPS and DPS structures relies on the number of phase shifters in use to compose each connection from an RF chain to a connected antenna element, which in this case is doubled. Even though it increases the implementation complexity and power consumption, this solution can increase the spectral efficiency and approach the performance of the fully-digital one [37].

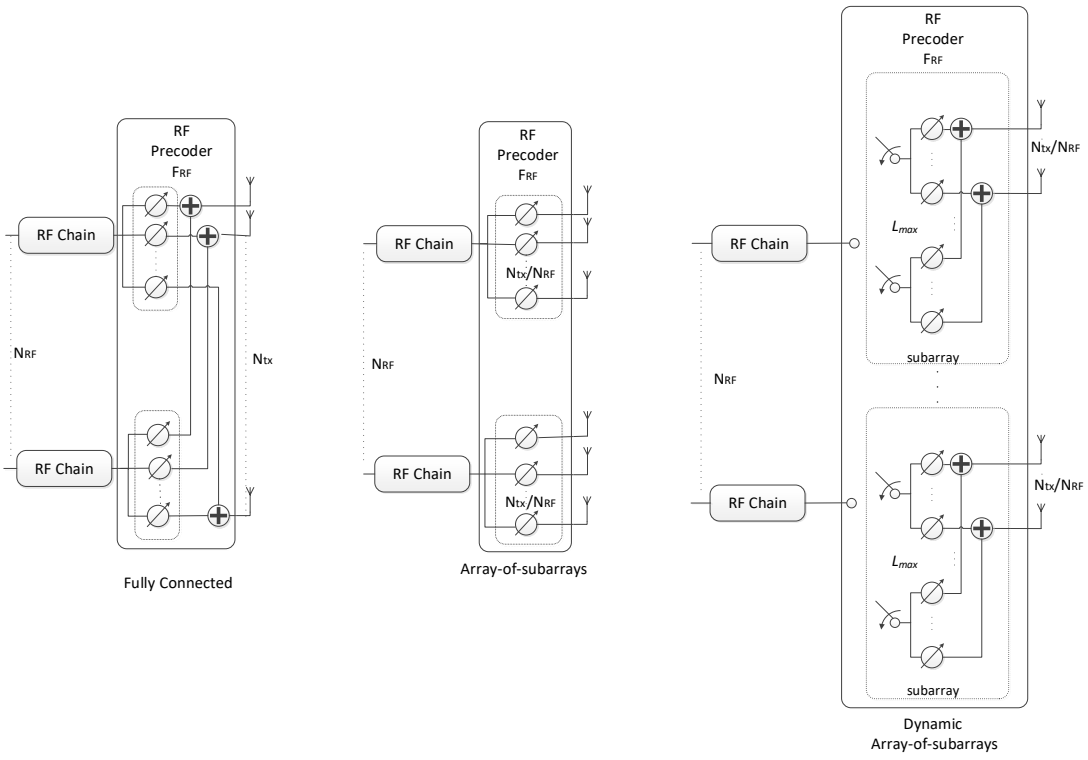

Figure 2. Different precoder architectures for a mmWave/THz MIMO system based on phase shifters.

In this case, the projection can be implemented element-wise simply as

$$R_{i,j}^{(t+1)} = \left(F_{\mathrm{RF}_{i,j}}^{(t+1)} + W_{i,j}^{(t)}\right) - e^{i\cdot\mathrm{angle}\left(F_{\mathrm{RF}_{i,j}}^{(t+1)}+W_{i,j}^{(t)}\right)} \times \max\left(0, \left|F_{\mathrm{RF}_{i,j}}^{(t+1)} + W_{i,j}^{(t)}\right| - 2\right). \tag{40}$$

Similarly to other architectures, DPS can be used not only in the fully-connected approach but also in the AoSA and DAoSA cases, replacing the constant modulus setting operation.

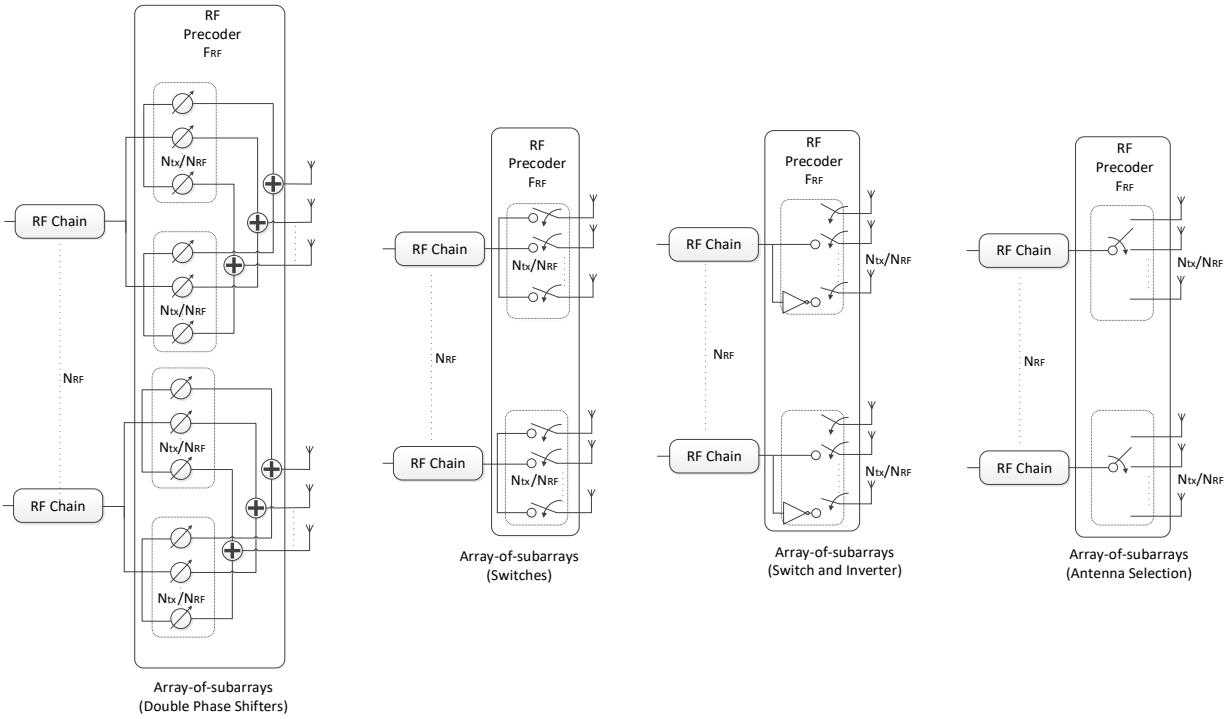

Figure 3. Alternative implementations to single phase shifters based on array-of-subarrays for a mmWave/THz MIMO system.

(4) Switches (Swi)

In an architecture based on switches, each of the variable phase shifters can be replaced by a switch which typically consumes less power [34]. This simplification results in a network of switches connecting each RF chain to the antennas. The RF constraint set can be represented as

$$\mathcal{C}_{a\times b} = \left\{ \mathbf{X} \in \mathbb{R}^{a\times b} : X_{i,j} = 0 \text{ or } X_{i,j} = 1 \right\} \tag{41}$$

(set of matrices having solely '0's or '1's as elements) and the projection can be implemented element-wise as

$$R_{i,j}^{(t+1)} = 1/2 + 1/2 \cdot \text{sign}\left(2\text{Re}\left[F_{\text{RF}_{i,j}}^{(t+1)} + W_{i,j}^{(t)} \right] - 1 \right). \tag{42}$$

(5) Switches and Inverters (SI)

Assuming that N_b=1, then each variable phase shifter of the QPS architecture can be replaced by a pair of switched lines, including also an inverter. The corresponding constraint set can be reduced to

$$\mathcal{C}_{a\times b} = \left\{ \mathbf{X} \in \mathbb{R}^{a\times b} : X_{i,j} = \pm 1 \right\}. \tag{43}$$

and the implementation of the projection simplifies to

$$R_{i,j}^{(t+1)} = \text{sign}\left(\text{Re}\left[F_{\text{RF}_{i,j}}^{(t+1)} + W_{i,j}^{(t)} \right] \right). \tag{44}$$

(6) Antenna Selection (AS)

The simplest scenario that we can consider corresponds to an architecture, where each RF chain can be only connected to a single antenna (and vice-versa). Antenna selection is a low-cost low-complexity alternative where only a specified subset of antennas are active at any given time [34]. The RF constraint set will comprise a matrix with only one non-zero element per column and per row, i.e.,

$$\mathcal{C}_{a\times b}=\left\{\mathbf{X}\in\mathbb{R}^{a\times b}:X_{i,j}=0 \text{ or } X_{i,j}=1,\left\|X_{i,:}\right\|_0=1,\left\|X_{:,j}\right\|_0=1\right\}. \quad (45)$$

In the definition, $\|\cdot\|_0$ represents the cardinality of a vector (sometimes referred to as the ℓ_0-norm in the literature). Defining $\mathbf{X}=\mathbf{F}_{\mathrm{RF}}^{(t+1)}+\mathbf{W}^{(t)}$, the projection can be approximately implemented by setting all the elements in **X** as 0 except for $X_{t_j,j}=1$, where t_j is the row position with the highest real component in column *j*:

$$t_j=\arg\max_{i=1,\ldots,N_{tx}}\left\{\mathrm{Real}\left[X_{i,j}\right]\right\}. \quad (46)$$

The computation of t_j is performed for all columns j = 1, …, N_{RF}^{tx}, sorted by descending order in terms of highest real components. It should be noted that during this operation, the same row cannot be repeated.

(7) Array-of-Subarrays (AoSAs)

Within the context of UM-MIMO, one of the most appealing architectures for keeping the complexity acceptable relies on the use of AoSA, where each RF chain is only connected to one or more subsets of antennas (subarrays). Denoting the number of subarrays as n_{SA}, which is typically set as $n_{SA}=N_{RF}$, and the size of each subarray as N_{tx}^{SA}, then we have $N_{tx}^{SA}=\frac{N_{tx}}{n_{SA}}=\frac{N_{tx}}{N_{RF}}$. To limit the complexity of the architecture, each RF chain can connect to a maximum of $L_{\max}$ consecutive subarrays.

In this case, the RF constraint set comprises matrices where each column has a maximum of $L_{\max}$ blocks of N_{tx}^{SA} constant modulus elements, with all the remaining elements being zero. Defining $\mathbf{X}=\mathbf{F}_{\mathrm{RF}}^{(t+1)}+\mathbf{W}^{(t)}$, the projection can be implemented by setting all the elements in **X** as 0 except for the subblocks in each column *j* which fulfill

$$\left\|\mathbf{X}_{[(j-1)N_{tx}^{SA}+(i-1)N_{tx}^{SA}+1:(j-1)N_{tx}^{SA}+iN_{tx}^{SA}]-1)\bmod N_{tx}]+1,j}\right\|_1>\frac{N_{tx}^{SA}}{2} \quad (47)$$

with i=1,…, L_{max} and j=1,…, N_{RF}. In this case, the corresponding elements of **R** are set as $R_{i,j}^{(t+1)}=\left(X_{i,j}\right)/\left|X_{i,j}\right|$, assuming UPS in these connections. Clearly, the phase shifters can be replaced by any of the other alternatives presented previously.

(8) Dynamic Array-of-Subarrays (DAoSAs)

As a variation of the previous AoSA architecture, we also consider an implementation where each subarray can be connected to a maximum of $L_{\max}$ RF chains (which can be non-adjacent). In this case, the constraint set comprises matrices where each $N_{tx}^{SA}\times N_{RF}$ component submatrix contains a maximum of $L_{\max}$ columns with constant modulus elements. The rest of the matrix contains only zeros. In this case, starting with X = 0, the projection can be obtained by selecting the $L_{\max}$ columns of

$$\left\|\mathbf{X}_{[(j-1)N_{tx}^{SA}+(i-1)N_{tx}^{SA}+1:(j-1)N_{tx}^{SA}+iN_{tx}^{SA}]-1)\bmod N_{tx}]+1,j}\right\|_1>\frac{N_{tx}^{SA}}{2} \quad (48)$$

where j=1,…, n_{SA} with the largest ℓ_1-norm and setting the corresponding elements of R as $R_{i,j}^{(t+1)}=\left(X_{i,j}\right)/\left|X_{i,j}\right|$, assuming the use of UPS. Care must be taken to guarantee that at least one sub-block will be active in every column of *R*. Similarly to the AoSA, the phase shifters can be replaced by any of the other presented alternatives.

3.3. Complexity

In the proposed algorithm, the $\mathbf{F}_{\mathrm{RF}}^{(t+1)}$ and $\mathbf{F}_{\mathrm{BB}}^{(t+1)}$ updates (steps 3 and 4 in Table 1) are defined using closed-form expressions that encompass several matrix multiplications, sums and an $N_{RF}\times N_{RF}$ matrix inverse (with an assumed complexity order of $\mathcal{O}\left(N_{RF}{}^3\right)$. These steps require a complexity order of $\mathcal{O}\left(QN_uN_sN_{RF}N_{tx}+F^{-1}QN_{RF}{}^2N_{tx}\right)$ and $\mathcal{O}\left(QN_uN_sN_{RF}N_{tx}+QN_{RF}{}^2N_{tx}\right)$, respectively.

The $\mathbf{R}^{(t+1)}$ update (step 5) involves simple element-wise division (assuming UPS) with $\mathcal{O}(QN_{RF}N_{tx})$ while variable $\mathbf{B}_k^{(t+1)}$ (step 6) comprises a Frobenius norm computation with $\mathcal{O}(QN_uN_sN_{RF}N_{tx})$. Step 7, the $\mathbf{F}_{\text{aprox}_{k,u}}^{(t+1)}$ update, has a complexity order of $\mathcal{O}\left(QN_{tx}{}^2N_uN_s+N_u{}^3N_{tx}N_{rx}{}^2+N_u{}^4N_{rx}{}^3\right)$, whereas the dual variables updates (steps 8–10) have a complexity of $\mathcal{O}\left(QN_uN_sN_{RF}N_{tx}+QN_{RF}{}^2N_{tx}\right)$. Therefore, keeping only the dominant terms, the overall complexity order for the proposed algorithm is $\mathcal{O}\left(Q\left(N_{tx}{}^2N_uN_s+N_{RF}{}^2N_{tx}\right)+N_u{}^3N_{tx}N_{rx}{}^2+N_u{}^4N_{rx}{}^3\right)$. Table 2 presents the total complexity order of the proposed method and compares it against other existing low-complexity alternatives, namely AM – Based [15], LASSO – Based Alt-Min (SPS and DPS) [14] and element-by-element (EBE) [20] algorithms. Taking into account that in UM-MIMO, N_{tx} will tend to be very large, it means the algorithms with higher complexity will typically be EBE and the one proposed in this paper due to the terms $\mathcal{O}\left(QN_{tx}{}^2\right)$ and $\mathcal{O}\left(QN_{tx}{}^2N_uN_s\right)$. It is important to note, however, that while the computational complexity of these two design methods may be higher, both algorithms can be applied to simple AoSA/DAoSA architectures. In particular, the proposed approach directly supports structures with lower practical implementation complexity (and are more energy-efficient) such as those based on switches. Furthermore, in a single-user scenario, the interference cancellation step of the proposed algorithm is unnecessary, and the complexity reduces to $\mathcal{O}\left(Q\left(N_uN_sN_{RF}N_{tx}+N_{RF}{}^2N_{tx}\right)\right)$. Regarding the other algorithms, they have similar complexities. However, the AM-based algorithm is designed for single stream scenarios whereas the others consider multiuser multi-stream scenarios.

Table 2. Overall Complexity of Different Hybrid Precoding Algorithms (per subcarrier).

AM—Based	
Operation	Complexity Order
Overall [15]	$\mathcal{O}\left(Q\left(N_uN_sN_{RF}N_{tx}+N_{RF}{}^2N_uN_s+F^{-1}N_{RF}{}^3\right)\right.$ $\left.F^{-1}N_{RF}{}^2N_{tx}+N_u{}^3N_s{}^3\right)$
LASSO—Based Alt-Min (SPS)	
Operation	Complexity Order
Overall [14]	$\mathcal{O}\left(Q\left(N_uN_sN_{RF}N_{tx}+N_{RF}{}^2N_uN_s+F^{-1}N_{RF}{}^3\right)\right.$ $\left.+N_u{}^2N_sN_{RF}N_{tx}+N_u{}^4N_s{}^3\right)$
ADMM	
Operation	Complexity Order
Overall [10]	$\mathcal{O}\left(Q\left(N_sN_{RF}N_{tx}+N_{RF}{}^2N_{tx}\right)\right)$
EBE	
Operation	Complexity Order
Overall [20]	$\mathcal{O}\left(QN_{tx}{}^2\right)$
Proposed	
Operation	Complexity Order
$\mathbf{F}_{\text{RF}}$	$\mathcal{O}\left(QN_uN_sN_{RF}N_{tx}+F^{-1}QN_{RF}{}^2N_{tx}\right)$
$\mathbf{F}_{\text{BB}}$	$\mathcal{O}\left(QN_uN_sN_{RF}N_{tx}+QN_{RF}{}^2N_{tx}\right)$
$\mathbf{R}$	$\mathcal{O}\left(QN_{RF}N_{tx}\right)$
$\mathbf{B}$	$\mathcal{O}\left(QN_uN_sN_{RF}N_{tx}\right)$
$\mathbf{F}_{\text{aprox}}$	$\mathcal{O}\left(QN_{tx}{}^2N_uN_s+N_u{}^3N_{tx}N_{rx}{}^2+N_u{}^4N_{rx}{}^3\right)$
U, W, Z	$\mathcal{O}\left(QN_uN_sN_{RF}N_{tx}+QN_{RF}{}^2N_{tx}\right)$
Overall	$\mathcal{O}\left(Q\left(N_{tx}{}^2N_uN_s+N_{RF}{}^2N_{tx}\right)+N_u{}^3N_{tx}N_{rx}{}^2+N_u{}^4N_{rx}{}^3\right)$

4. Numerical Results

In this section, the performance of the proposed algorithm will be evaluated and compared against other existing alternatives from the literature, considering multiuser MIMO systems. We consider that both the transmitter and receivers are equipped with uniform planar arrays (UPAs) with $\sqrt{N_{tx}}\times\sqrt{N_{tx}}$ antenna elements at the transmitter and $\sqrt{N_{rx}}\times\sqrt{N_{rx}}$ at the receiver. The respective array response vectors are given by

$$\mathbf{a}_{t/r}\left(\phi_{i,l,u}^{t/r},\theta_{i,l,u}^{t/r}\right)=\frac{1}{\sqrt{N_{tx/rx}}}\times\left[1,\ldots,e^{j\frac{2\pi}{\lambda}d\left(p\sin\phi_{i,l,u}^{t/r}\sin\theta_{i,l,u}^{t/r}+q\cos\theta_{i,l,u}^{t/r}\right)},\right.$$

$$\left.\ldots,e^{j\frac{2\pi}{\lambda}d\left(\left(\sqrt{N_{tx/rx}}-1\right)\sin\phi_{i,l,u}^{t/r}\sin\theta_{i,l,u}^{t/r}+\left(\sqrt{N_{tx/rx}}-1\right)\cos\theta_{i,l,u}^{t/r}\right)}\right]^{T}, \tag{49}$$

where p, q=0, …., $\sqrt{N_{tx/rx}}-1$ are the antenna indices, λ is the signal wavelength and d is the inter-element spacing, which we assume to be $d=\lambda/2$. We consider a sparse channel with limited scattering where N_{ray}=4 and N_{cl}=6. The angles of departure and arrival were selected according to a Gaussian distribution whose means are uniformly distributed in [0, 2π] and whose angular spreads are 10 degrees. While we include a few results for a NLOS channel, which is often considered a possible scenario in mmWave communications [14,15,25,31], we also present results for a channel with a LOS component which is more realistic, especially in the THz band. In the scenarios with a LOS component, a ratio of $E\left[\left|\alpha_u^{LOS}\right|^2\right]\Big/\sum_{i=1}^{N_{cl}}\sum_{l=1}^{N_{ray}}E\left[\left|\alpha_{i,l,u}\right|^2\right]=10$ is assumed (in this case we are admitting very weak NLOS paths compared to LOS which is typical in the THz band [27]). A fully-digital combiner was considered at each receiver and all simulation results were computed with 5000 independent Monte Carlo runs.

4.1. Fully-Connected Structures

First, we evaluate the performance assuming a fully-connected structure. Simulation results for a scenario where a base station with N_{tx}=100 antennas transmits a single data stream (N_s=1) to N_u=4 users with N_{rx}=4 antennas are shown in Figure 4 for F=1 and Figure 5 for F=64. The number of RF chains in the transmitter (N_{RF}^{tx}) is equal to N_uN_s. Besides our proposed precoder, several alternative precoding schemes are compared against the fully-digital solution, namely the LASSO-Based Alt-Min, the AM-Based and ADMM-Based precoding [10,14,15].

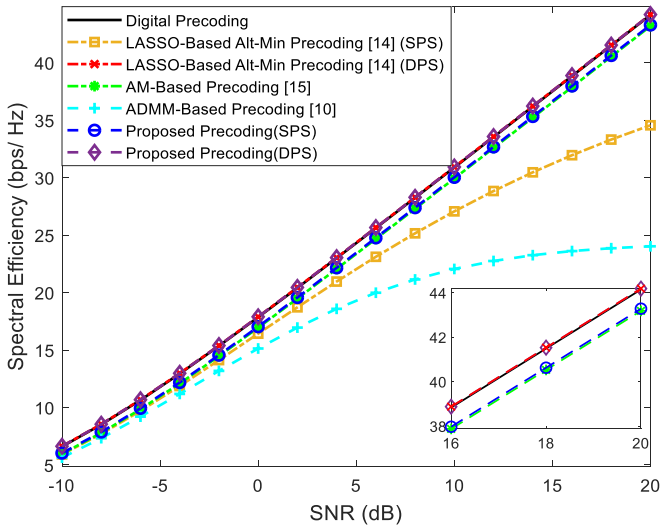

Figure 4. Spectral efficiency versus SNR achieved by different methods with N_u=4, N_s=1, $N_{RF}^{tx}=4$, F=1, N_{tx}=100 and N_{rx}=4 (only NLOS).

It can be observed that when F=1, only the LASSO-Based Alt-Min with SPS and the ADMM-Based precoder from [10] (which does not remove the inter-user interference) lie far from fully-digital precoder. All the others achieve near optimum results and, in fact, can even match them when adopting DPS (proposed approach and LASSO-based Alt-Min). As explained in Section II, whereas for F=1 we have $\mathbf{F}_{BB}$ and $\mathbf{F}_{RF}$ designed for that specific carrier, when F=64, $\mathbf{F}_{RF}$ has to be common to all subcarriers. While this reduces the implementation complexity, it also results in a more demanding restriction that makes the approximation of $\mathbf{F}_{opt_k}$ (problems (5)–(7)) to become worse. Additionally, when this approximation worsens, there can also be increased interference between users. Therefore, it can be observed in the results of Figure 5, that the gap between the fully-digital precoder and all the different hybrid algorithms is substantially wider. Still, the proposed precoder manages to achieve the best results.

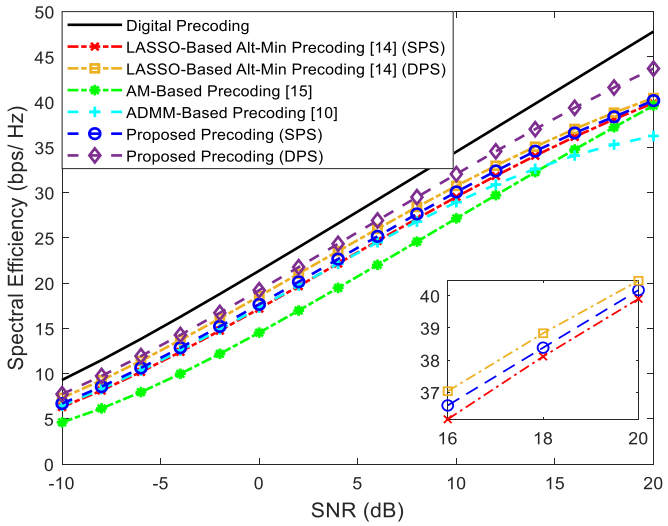

Figure 5. Spectral efficiency versus SNR achieved by different methods with N_u=4, N_s=1, $N_{RF}^{tx}=8$, F=64, N_{tx}=100 and N_{rx}=4 (only NLOS).

Given the performances of the different approaches, it is important to keep in mind that the AM-based precoding algorithm has the lowest performance in wideband but also one of the lowest computational complexities (see Table 2 of Section 3.3). In general, the proposed precoding algorithm is the one that can achieve better results at the cost of some additional computational complexity. Later on, we will address strategies based on lower complexity architectures that will allow for reducing the power consumption associated with its complexity.

In Figure 6, we consider a scenario where the BS employs a larger array with N_{tx}=256 antennas to transmit N_s=2 simultaneous streams to each user, where N_u=2. To better fit this scenario to a typical communication in the THz band, we consider the existence of a LOS component, a center frequency of f_c=300 GHz and a bandwidth of B=15 GHz (it is important to note that the beam split effect is also considered in the channel model). The AM precoder from [15] requires a single stream per user and thus was not included in the figure. It is important to note that in this scenario the use of F=64 with only 4 RF chains results in a more demanding restriction that makes the approximation to $\mathbf{F}_{opt_k}$ (equation (5)) more difficult, thus widening the gap between all the schemes and the fully-digital curve. Still, the LASSO-based Alt-Min precoding schemes present a performance substantially lower when compared to the proposed approaches. Furthermore, the best performance is achieved with the use of double phase shifters, as expected. Once again, in comparing the curves of the proposed precoder against the ADMM-based precoder from [10], the advantage of adopting an interference-cancellation-based design over a simple matrix approximation one is clear.

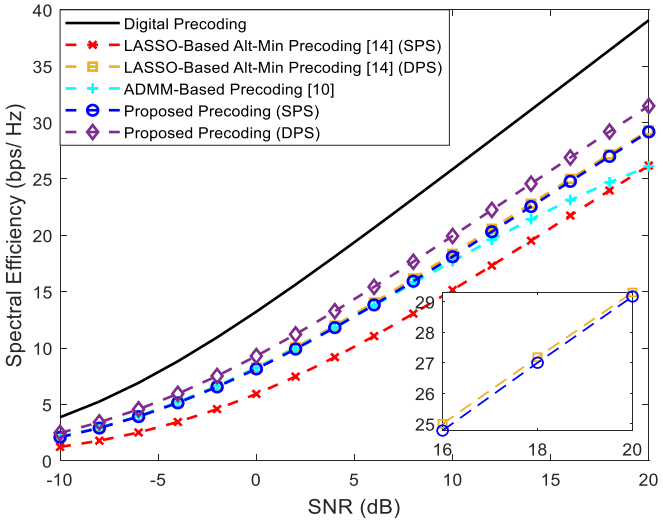

Figure 6. Spectral efficiency versus SNR achieved by different methods with N_u=2, N_s=2, $N_{RF}^{tx}=4$, F=64, N_{tx}=256 and N_{rx}=4 (with LOS component).

4.2. Reduced Complexity Architectures

Next, we will focus on the adoption of different reduced complexity architectures according to the typologies presented in Section 3.2. The objective is to evaluate the performance degradation when simpler architectures are adopted.

Figure 7 considers a scenario in which we have more than one data stream (N_s=2) being sent from the BS to each user (N_u=4) in a system with $N_{RF}^{tx}=N_u N_s$, F=1, N_{tx}=256 and N_{rx}=4. We considered the same penalty parameters configuration: $\rho=0.05$, $\mu=1$ and $\eta=\rho$. This figure is placed in a perspective of simplifying the implementation of the analog precoder but keeping a fully-connected structure. We can observe that the versions based on DPS and single UPS achieve the best results, as expected. Considering the more realistic QPS versions, the results can worsen but it is visible that it is not necessary to use high resolution phase shifters since, with only 3 bits resolution, the results are already very close to the UPS curve. It can also be observed that the simplest of the architectures, AS, results in the worst performance but the SE improves when the antenna selectors are replaced by a network of switches, or, even better, if branches with inverters are also included.

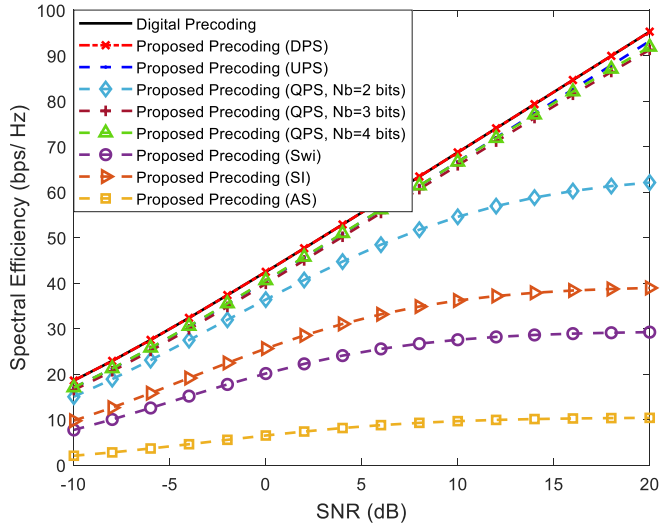

Figure 7. Spectral efficiency versus SNR achieved by the proposed precoder using different fully-connected architectures for N_u=4, N_s=2, $N_{RF}^{tx}=8$, F=1, N_{tx}=256 and N_{rx}=4 (only NLOS).

In Figure 8, we intend to simplify the implementation even further with the adoption of AoSAs. In this case we considered that the maximum number of

subarrays that can be connected to an RF chain (L_{max}) is only one. This imposes a very demanding restriction on matrix $\mathbf{F}_{RF}$ since most of it will be filled with zeros, thus substantially deteriorating the approximation to $\mathbf{F}_{opt_k}$ (equation (5)). The scenario is the same in Figure 7 but considers the existence of a LOS component with a few weak NLOS paths.

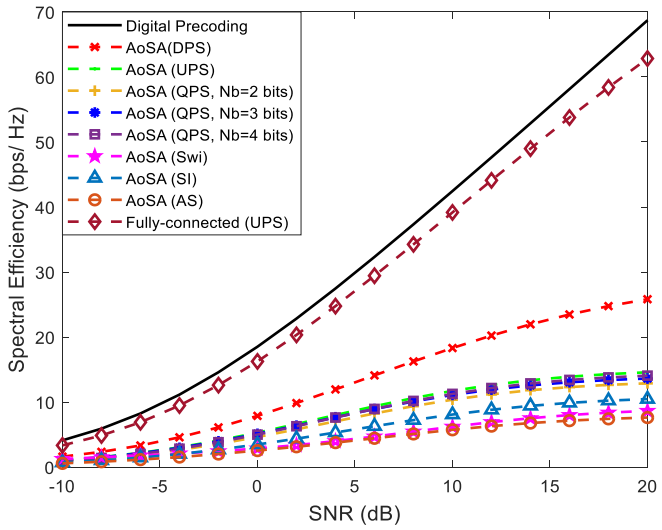

Figure 8. Spectral efficiency versus SNR achieved by the proposed precoder using different AoSA architectures with L_{max} = 1, N_u=4, N_s=2, $N_{RF}^{tx}=8$, F=1, N_{tx}=256 and N_{rx}=4 (with LOS component).

In fact, hereafter, the existence of an LOS component is assumed for the remaining figures of the paper in order to fit the AoSA/DAoSA results to a more typical scenario in the THz band. We can observe that for AoSA structures, the degradation of the SE is notorious, since all candidate versions present worse results when compared to the corresponding fully-connected design and are all far from the fully-digital solution. To reduce the large performance loss due to the adoption of a simple AoSA architecture, we can allow the dynamic connection of more subarrays to each RF chain by adopting a DAoSA structure, as introduced in Section 3.2.

In Figure 9, we study the effect of increasing the maximum number of subarrays that can be connected to an RF chain (L_{max}) in the performance of these schemes. Each subarray has a size of 32 antennas (n_t). Curves assuming the use of SPS as well as of DPS are included. It can be observed that the increase in the number of connections to subarrays, L_{max}, has a dramatic effect on the performance, resulting in a huge improvement by simply going from L_{max}=1 to L_{max}=2. Increasing further to L_{max}=4, the results become close to the fully-connected case, showing that the DAoSA can be a very appealing approach for balancing spectral efficiency with hardware complexity and power consumption. Combining the increase in L_{max} with the adoption of DPS can also improve the results but the gains become less pronounced for L_{max}>1. It is important to note that the penalty parameters can be fine-tuned for different system configurations.

One of the objectives of adopting these low-complexity solutions is to reduce overall power consumption. Based on [20], we can calculate the total power consumption of each precoding scheme using

$$P_C = P_{BB}N_{BB} + \left(P_{DAC} + P_{OS} + P_M\right)N_{RF}^{tx} + P_{PA}N_{tx} + P_{PC}N_{tx} + P_{PS}N_{PS} + P_{SWI}N_{SWI} + P_{tx}, \quad (50)$$

where P_{BB} is the power of the baseband block (with N_{BB} = 1), P_{DAC} is the power of a DAC, P_{OS} is the power of an oscillator, P_M is the power of a mixer, P_{PA} is the power of a power amplifier, P_{PC} is the power of a power combiner, P_{PS} is the power of a phase shifter, P_{SWI} is the power of a switch and P_{tx} denotes the transmit power. The N_x variable represents the number of elements of each device used in the precoder configuration.

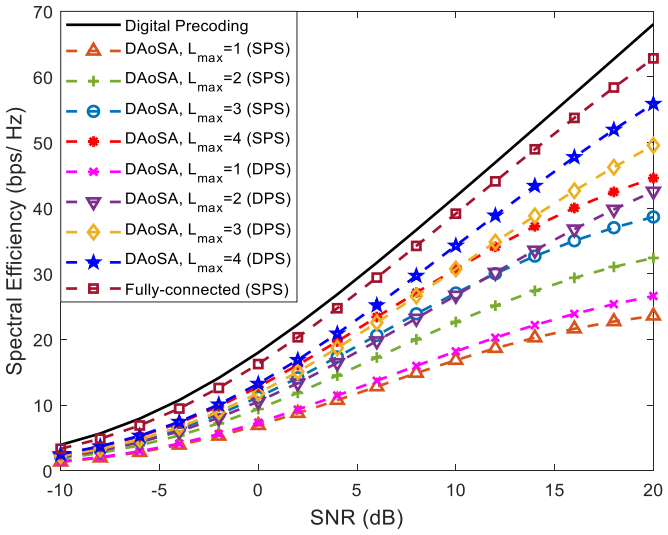

Figure 9. Spectral efficiency versus SNR achieved by the proposed precoder considering an architecture based on DAoSAs and the variation of the maximum number of subarrays that can be connected to an RF chain (L_{max}) for N_u=4, N_s=2, $N_{RF}^{tx}=8$, F=1, N_{tx}=256 and N_{rx}=4 (with LOS component).

Based on the values provided in [20, 38] for the power consumption of individual devices in the 300 GHz band, we adopt the following values: P_{BB} = 200 mW, P_{DAC} = 110 mW, P_{OS}=4 mW, P_M=22 mW, P_{PA}=60 mW, P_{PC}=6.6 mW, P_{SWI}=24 mW and P_I=100 mW.

Regarding the phase shifters, we assume values of P_{PS} = 10, 20, 40 and 100 mW for 1, 2, 3 and 4 quantization bits. Considering the same configuration scenario as Figures 7–9 with N_u=4, N_s=2, $N_{RF}^{tx}=N_uN_s$, F=1 and N_{tx}=256, we provide the values of power consumption for different precoder configurations in Table 3.

For the fully-connected structure with UPS, we assumed that P_{PS}=100 mW, which corresponds to quantized phase shifters with N_b=4 bits [38]. For the remaining phase-shifter-based precoder structures, we assumed that P_{PS}=40 mW, which corresponds to quantized phase shifters with N_b=3 bits, since with only 3 bits resolution the results are already very close to the UPS curve (see Figure 7). As can be seen from this table, the use of architectures based on DAoSAs allows us to reduce considerably the amount of power that is consumed by the precoder. In fact, we can reduce the amount of consumed power up to 55% if we consider a precoder scheme based on DAoSA with DPS and L_{max}=4 versus an FC structure precoder based on UPS, with only a small performance penalty (Figure 9). This reduction increases to 73% if the DPS structure is replaced by an SPS one.

In the particular case of architectures based on quantized phase shifters, we observed that by decreasing the number of quantization bits, it is possible to substantially reduce the power consumption without excessively compromising the complexity (as seen in Figure 7). This conclusion is corroborated by [20,38], since the architectures based on low resolution QPS, AoSAs and DAoSAs present superior energy efficiency when compared to the fully-connected structure with UPS.

In Figures 10 and 11, we provide a comparison between our proposed precoder and the EBE precoder from [20], considering an architecture based on DAoSAs (with SPS) and a scenario configuration similar to Figure 9, i.e., with N_s=2, $N_{RF}^{tx}=8$, F=1, N_{tx}=256 and N_{rx}=4.

These figures present various curves where the maximum number of subarrays that can be connected to an RF chain, L_{max}, is changed. Figure 10 refers to an SU scenario (N_u=1) whereas Figure 11 corresponds to an MU scenario with N_u=4. In the SU case, the proposed precoder achieves results very close to the fully-digital precoder, even with only L_{max}=2. Compared to the proposed algorithm, EBE shows a wider gap even though it has a smaller complexity (as presented in Table 2 of Section 3.3).

Table 3. Power Consumption for Different Implementations of the Proposed Precoder for N_u=4, N_s=2, $N_{RF}^{tx}=8$, F=1, N_{tx}=256.

Precoder		Estimated Power Consumption [W]
Fully-Connected	DPS	428.04
	UPS	223.24
	QPS (N_b=2)	59.4
	QPS (N_b=3)	100.36
	SWI	67.59
	SI	38.92
DAoSA SPS	L_{max}=1	28.87
	L_{max}=2	39.30
	L_{max}=3	49.73
	L_{max}=4	60.17
DAoSA DPS	L_{max}=1	39.11
	L_{max}=2	59.78
	L_{max}=3	80.45
	L_{max}=4	101.13

When we increase the number of users from N_u=1 to N_u=4, we can clearly observe that the EBE algorithm suffers a substantial degradation compared to the proposed solution which can be explained by the lack of inter-user interference cancellation (it was not specifically designed for MU scenarios).

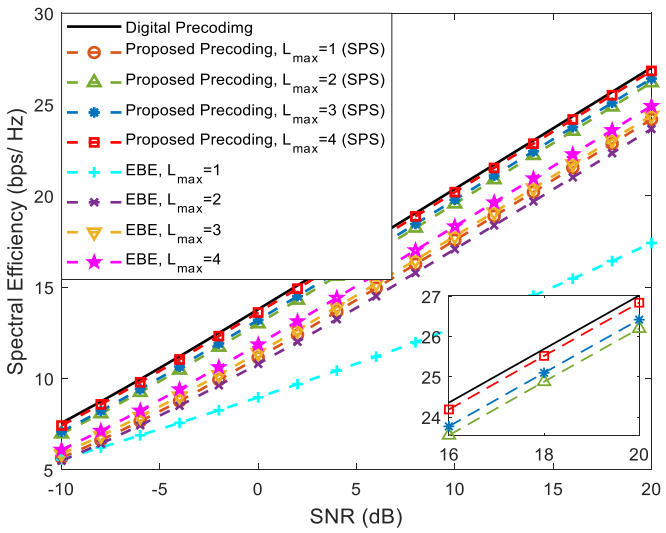

Figure 10. Spectral efficiency versus SNR achieved by the proposed precoder and by the EBE algorithm considering an architecture based on DAoSAs and the variation of the maximum number of subarrays that can be connected to an RF chain (L_{max}) for N_u=1, N_s=2, $N_{RF}^{tx}=8$, F=1, N_{tx}=256 and N_{rx}=4 (with LOS component).

Even though a sub-6 GHz system often adopts fully-digital processing [39], where each antenna element has a dedicated RF chain, it is possible to apply the proposed hybrid design algorithm to a sub-6 GHz channel since it is independent of a specific MIMO channel (as are the other alternative algorithms that we used as benchmarks and which are targeted at solving the matrix approximation problem). To exemplify, Figure 12 presents the simulated results obtained for the same scenario of Figure 4 but considering an ideal uncorrelated channel which approximates a rich scattering environment that is typical in sub-6 GHz bands.

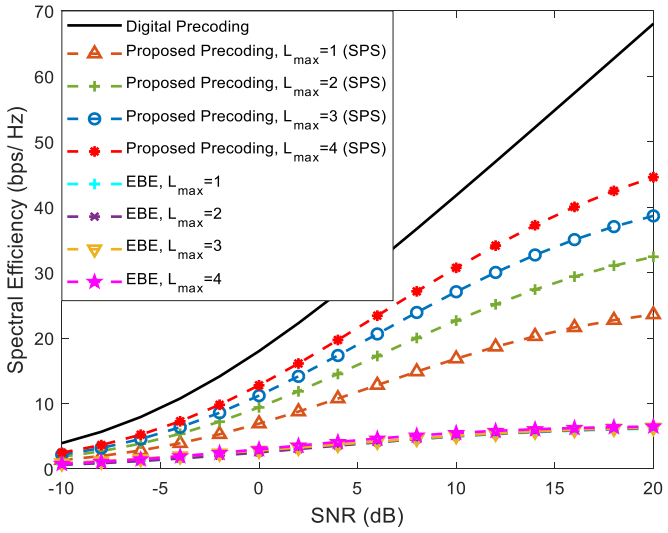

Figure 11. Spectral efficiency versus SNR achieved by the proposed precoder and by the EBE algorithm considering an architecture based on DAoSAs and the variation of the maximum number of subarrays that can be connected to an RF chain (L_{max}) for a mmWave/THz system with N_u=4, N_s=2, $N_{RF}^{tx}=8$, F=1, N_{tx}=256 and N_{rx}=4 (with LOS component).

It can be observed that the proposed approach displays similar behavior to the ones in the upper-bands channel, showing that it can also be used for this particular type of channel (even though it may require a higher number of RF chains to achieve a good approximation of the fully-digital solution in some scenarios, due to the channel not being sparse, as noted in [40]). It is important to highlight that even though the proposed approach can be applied to other channels, the algorithm was designed with the aim of dealing with architectures with a very large number of antennas and with large hardware constraints, making it especially interesting for mmWave and THz.

While we have shown how the proposed approach can deal with several relevant types of analog precoders/combiners, it is important to note that are other alternative structures that have been recently proposed in the literature. For example, some authors have considered precoding paradigms based on time-delayer structures for THz systems [27,41]. One of the most notorious is the Delay Phase Precoding (DPD), which consists in the use of a Time-Delay (TD) network between the RF chains and the traditional phase shifters network in order to convert phase-controlled analog precoding into delay-phase-controlled analog precoding. The main advantage related to this type of precoding is that the time delays in the TD network are carefully designed to generate frequency-dependent beams which are aligned with the spatial directions over the whole bandwidth [41]. While we do not address the adoption of time-delay structures in this paper, it should be possible to derive a projection algorithm that simultaneously takes into account the constraints imposed in both analog-precoding steps: time-delay networks and frequency-independent phase shifters.

While we have shown how the proposed approach can deal with several relevant types of analog precoders/combiners, it is important to note that are other alternative structures that have been recently proposed in the literature. For example, some authors have considered precoding paradigms based on time-delayer structures for THz systems [27,41]. One of the most notorious is the Delay Phase Precoding (DPD), which consists in the use of a Time-Delay (TD) network between the RF chains and the traditional phase shifters network in order to convert phase-controlled analog precoding into delay-phase-controlled analog precoding.

The main advantage related to this type of precoding is that the time delays in the TD network are carefully designed to generate frequency-dependent beams which are aligned with the spatial directions over the whole bandwidth [41]. While we do not address the adoption of time-delay structures in this paper, it should be possible to derive a projection algorithm that simultaneously takes into account the constraints imposed in both analog-precoding steps: time-delay networks and frequency-independent phase shifters.

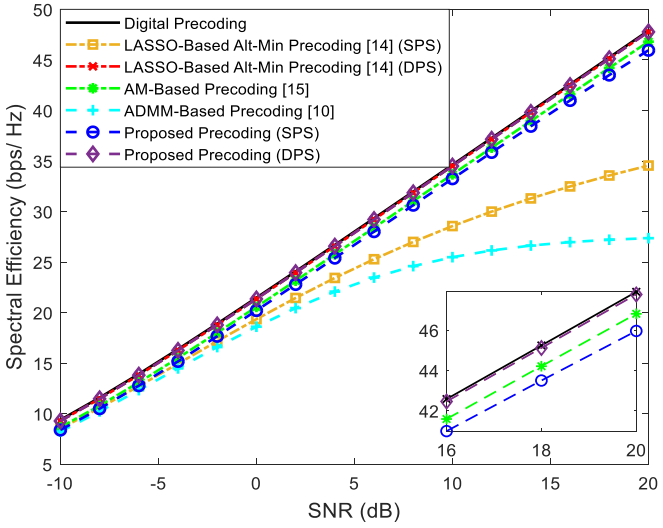

Figure 12. Spectral efficiency versus SNR achieved by different methods for a mmWave/THz MIMO-OFDM system with N_u=4, N_s=1, $N_{RF}^{tx}=4$, F=1, N_{tx}=100 and N_{rx}=4 considering an uncorrelated channel.

5. Conclusions

In this paper, we proposed an iterative algorithm for hybrid precoding design which is suitable for multiuser UM-MIMO systems operating in mmWave and THz bands. The adopted approach replaces unfeasible fully-digital precoders/combiners relying on a dedicated RF chain per antenna with a hybrid architecture comprising low dimension digital blocks with only a few RF chains which are complemented by analog blocks supported solely on networks of phase shifters and switches. The proposed hybrid design algorithm is based on the approximation of the fully-digital approach whose problem formulation is split into a sequence of smaller subproblems with closed-form solutions and can work with a broad range of configuration of antennas, RF chains and data streams. The separability of the design process allows for the adaptability of the algorithm to different architectures, making it suitable for implementation with low-complexity AoSA and DAoSA structures, which are particularly relevant for the deployment of UM-MIMO in hardware-constrained THz systems. It was shown that good trade-offs between SE and hardware implementation complexity can in fact be achieved by the proposed algorithm for several different architectures. Numerical results showed that the use of architectures based on DAoSAs allows us to reduce considerably the amount of power that is consumed at the precoder. In fact, in a reference scenario, we showed that it was possible to reduce the amount of consumed power up to 55% if we consider a precoder scheme based on DAoSAs with DPS and L_{max} = 4 versus an FC structure based on UPS, with only a small performance penalty. This reduction increases to 73% if the DPS structure is replaced by an SPS one.

Author Contributions: Conceptualization, J.P.P. and N.S.; methodology, J.P.P., N.S. and R.D.; software, J.P.P. and N.S.; validation, J.P.P., N.S., M.R. and R.D.; formal analysis, J.P.P., V.V., R.F. and N.S.; investigation, J.P.P., V.V., R.F. and N.S.; resources, N.S. and M.R.; data curation, J.P.P.; writing—original draft preparation, J.P.P. and N.S.; writing—review and editing, J.P.P., V.V., R.F., N.S., M.R., J.S. and R.D; visualization, J.P.P. and N.S.; supervision, N.S. and M.R.; project administration, N.S., M.R., J.S. and R.D.; funding acquisition, N.S and R.D. All authors have read and agreed to the published version of the manuscript.

Funding: This work was supported by the FCT—Fundação para a Ciência e Tecnologia under the grant 2020.05621.BD. The authors also acknowledge the funding provided by FCT/MCTES through national funds and when applicable co-funded EU funds under the project UIDB/50008/2020.

Institutional Review Board Statement: Not applicable.

Informed Consent Statement: Not applicable.

Data Availability Statement: The data presented in this study are available on request from the corresponding author. The data are not publicly available due to privacy.

Conflicts of Interest: The authors declare no conflict of interest.

References

1. Rappaport, T.S.; Sun, S.; Mayzus, R.; Zhao, H.; Azar, Y.; Wang, K.; Wong, G.; Schulz, J.K.; Samimi, M.; Gutierrez, F. Millimeter Wave Mobile Communications for 5G Cellular: It Will Work! *IEEE Access* **2013**, *1*, 335–349, https://doi.org/10.1109/access.2013.2260813.
2. Uwaechia, A.N.; Mahyuddin, N.M. A Comprehensive Survey on Millimeter Wave Communications for Fifth-Generation Wireless Networks: Feasibility and Challenges. *IEEE Access* **2020**, *8*, 62367–62414, https://doi.org/10.1109/access.2020.2984204.
3. Akyildiz, I.F.; Kak, A.; Nie, S. 6G and Beyond: The Future of Wireless Communications Systems. *IEEE Access* **2020**, *8*, 133995–134030, https://doi.org/10.1109/access.2020.3010896.
4. Tan, J.; Dai, T. THz Precoding for 6G: Applications, Challenges, Solutions, and Opportunities. *arXiv Prepr.* **2020**, arXiv:2005.10752. Available online: https://arxiv.org/abs/2005.10752 (accessed on 2 July 2021).
5. Sarieddeen, H.; Alouini, M.-S.; Al-Naffouri, T.Y. An Overview of Signal Processing Techniques for Terahertz Communications. *Proc. IEEE* **2021**, 1–38, https://doi.org/10.1109/jproc.2021.3100811.
6. Lin, C.; Li, G.Y.L. Terahertz Communications: An Array-of-Subarrays Solution. *IEEE Commun. Mag.* **2016**, *54*, 124–131, https://doi.org/10.1109/mcom.2016.1600306cm.
7. Ahmed, I.; Khammari, H.; Shahid, A.; Musa, A.; Kim, K.S.; De Poorter, E.; Moerman, I. A Survey on Hybrid Beamforming Techniques in 5G: Architecture and System Model Perspectives. *IEEE Commun. Surv. Tutorials* **2018**, *20*, 3060–3097, https://doi.org/10.1109/comst.2018.2843719.
8. Chataut, R.; Akl, R. Massive MIMO Systems for 5G and beyond Networks—Overview, Recent Trends, Challenges, and Future Research Direction. *Sensors* **2020**, *20*, 1–35.
9. Sohrabi, F.; Yu, W. Hybrid Digital and Analog Beamforming Design for Large-Scale Antenna Arrays. *IEEE J. Sel. Top. Signal Process.* **2016**, *10*, 501–513, https://doi.org/10.1109/jstsp.2016.2520912.
10. Souto, N.N.; Silva, J.; Pavia, J.; Ribeiro, M. An alternating direction algorithm for hybrid precoding and combining in millimeter wave MIMO systems. *Phys. Commun.* **2019**, *34*, 165–173.
11. Pavia, J.P.; Souto, N.; Ribeiro, M.; Silva, J.; Dinis, R. Hybrid Precoding and Combining Algorithm for Reduced Complexity and Power Consumption Architectures in mmWave Communications. In Proceedings of the 2020 IEEE 91st Vehicular Technology Conference: VTC2020-Spring, Antwerp, Belgium, 25–28 May 2020; pp. 1–5, https://doi.org/10.1109/vtc2020-spring48590.2020.9128553.
12. Guan, K.; Li, G.; Kuerner, T.; Molisch, A.F.; Peng, B.; He, R.; Hui, B.; Kim, J.; Zhong, Z. On Millimeter Wave and THz Mobile Radio Channel for Smart Rail Mobility. *IEEE Trans. Veh. Technol.* **2016**, *66*, 5658–5674, https://doi.org/10.1109/tvt.2016.2624504.
13. Alkhateeb, A.; Mo, J.; Gonzalez-Prelcic, N.; Heath, R. MIMO Precoding and Combining Solutions for Millimeter-Wave Systems. *IEEE Commun. Mag.* **2014**, *52*, 122–131, https://doi.org/10.1109/mcom.2014.6979963.
14. Yu, X.; Zhang, J.; Letaief, K.B. Alternating minimization for hybrid precoding in multiuser OFDM mmWave systems. In Proceedings of the 2016 50th Asilomar Conference on Signals, Systems and Computers, Pacific Grove, CA, USA, 6–9 November 2016; pp. 281–285, https://doi.org/10.1109/acssc.2016.7869042.
15. Yuan, H.; An, J.; Yang, N.; Yang, K.; Duong, T.Q. Low Complexity Hybrid Precoding for Multiuser Millimeter Wave Systems Over Frequency Selective Channels. *IEEE Trans. Veh. Technol.* **2018**, *68*, 983–987, https://doi.org/10.1109/tvt.2018.2880787.
16. Liu, F.; Kan, X.; Bai, X.; Du, R.; Liu, H.; Zhang, Y. Hybrid precoding based on adaptive RF-chain-to-antenna connection for millimeter wave MIMO systems. *Phys. Commun.* **2020**, *39*, 100997, https://doi.org/10.1016/j.phycom.2019.100997.
17. Xu, K.; Cai, Y.; Zhao, M.; Niu, Y.; Hanzo, L. MIMO-Aided Nonlinear Hybrid Transceiver Design for Multiuser Mmwave Systems Relying on Tomlinson-Harashima Precoding. *IEEE Trans. Veh. Technol.* **2021**, *70*, 6943–6957, https://doi.org/10.1109/tvt.2021.3087651.
18. Vizziello, A.; Savazzi, P.; Chowdhury, K.R. A Kalman Based Hybrid Precoding for Multi-User Millimeter Wave MIMO Systems. *IEEE Access* **2018**, *6*, 55712–55722, https://doi.org/10.1109/access.2018.2872738.
19. Elmagzoub, H.M. On the MMSE-based multiuser millimeter wave MIMO hybrid precoding design. *Int. J. Commun. Syst.* **2020**, *33*, e4409, https://doi.org/10.1002/dac.4409.
20. Yan, L.; Han, C.; Yuan, J. A Dynamic Array-of-Subarrays Architecture and Hybrid Precoding Algorithms for Terahertz Wireless Communications. *IEEE J. Sel. Areas Commun.* **2020**, *38*, 2041–2056, https://doi.org/10.1109/jsac.2020.3000876.
21. Busari, S.; Huq, K.; Mumtaz, S.; Rodriguez, J. Terahertz Massive MIMO for Beyond-5G Wireless Communication. In Proceedings of the ICC 2019-2019 IEEE International Conference on Communications (ICC), Shanghai, China, 11–22 March 2019.
22. Boyd, S.; Parikh, N.; Chu, E.; Peleato, B.; Eckstein, J. Distributed Optimization and Statistical Learning via the Alternating Direction Method of Multipliers. *Found. Trends Mach. Learn.* **2010**, *3*, 1–122, https://doi.org/10.1561/2200000016.
23. Wang, Y.; Yin, W.; Zeng, J. Global Convergence of ADMM in Nonconvex Nonsmooth Optimization. *J. Sci. Comput.* **2018**, *78*, 29–63, https://doi.org/10.1007/s10915-018-0757-z.

24. Alkhateeb, A.; Heath, R.W. Frequency Selective Hybrid Precoding for Limited Feedback Millimeter Wave Systems. *IEEE Trans. Commun.* **2016**, *64*, 1801–1818.
25. Yuan, H.; Yang, N.; Yang, K.; Han, C.; An, J. Hybrid Beamforming for Terahertz Multi-Carrier Systems Over Frequency Selective Fading. *IEEE Trans. Commun.* **2020**, *68*, 6186–6199, https://doi.org/10.1109/tcomm.2020.3008699.
26. Tarboush, S.; Sarieddeen, H.; Chen, H.; Loukil, M.H.; Jemaa, H.; Alouini, M.S.; Al-Naffouri, T.Y. TeraMIMO: A Channel Simulator for Wideband Ultra-Massive MIMO Terahertz Communications. *arXiv Prepr.* **2021**, arXiv:2104.11054. Available online: https://arxiv.org/abs/2104.11054 (accessed on 2 July 2021).
27. Lin, C.; Li, G.Y.; Wang, L. Subarray-Based Coordinated Beamforming Training for mmWave and Sub-THz Communications. *IEEE J. Sel. Areas Commun.* **2017**, *35*, 2115–2126, https://doi.org/10.1109/jsac.2017.2720038.
28. Nguyen, D.D.; Le, L.; Le-Ngoc, T.; Heath, R. Hybrid MMSE Precoding and Combining Designs for mmWave Multiuser Systems. *IEEE Access* **2017**, *5*, 19167–19181.
29. Bertsekas, D. *Nonlinear Programming*; Athena Scientific: Belmont, MA, USA, 2016.
30. El Ayach, O.; Rajagopal, S.; Abu-Surra, S.; Pi, Z.; Jr, R.W.H. Spatially Sparse Precoding in Millimeter Wave MIMO Systems. *IEEE Trans. Wirel. Commun.* **2014**, *13*, 1499–1513, https://doi.org/10.1109/twc.2014.011714.130846.
31. Yu, X.; Shen, J.-C.; Zhang, J.; Letaief, K.B. Alternating Minimization Algorithms for Hybrid Precoding in Millimeter Wave MIMO Systems. *IEEE J. Sel. Top. Signal Process.* **2016**, *10*, 485–500, https://doi.org/10.1109/jstsp.2016.2523903.
32. Spencer, Q.; Swindlehurst, A.L.; Haardt, M. Zero-Forcing Methods for Downlink Spatial Multiplexing in Multiuser MIMO Channels. *IEEE Trans. Signal Process.* **2004**, *52*, 461–471, https://doi.org/10.1109/tsp.2003.821107.
33. Mendez-Rial, R.; Rusu, C.; Gonzalez-Prelcic, N.; Alkhateeb, A.; Heath, R. Hybrid MIMO Architectures for Millimeter WaveCommunications: Phase Shifters or Switches? *IEEE Access* **2016**, *4*, 247–267.
34. Lee, J.; Lee, Y.H. AF relaying for millimeter wave communication systems with hybrid RF/baseband MIMO processing. In Proceedings of the 2014 IEEE International Conference on Communications (ICC), Sydney, Australia, 10–14 June 2014; pp. 5838–5842, https://doi.org/10.1109/icc.2014.6884253.
35. Payami, S.; Ghoraishi, M.; Dianati, M.; Sellathurai, M. Hybrid Beamforming with a Reduced Number of Phase Shifters for Massive MIMO Systems. *IEEE Trans. Veh. Technol.* **2018**, *67*, 4843–4851, https://doi.org/10.1109/tvt.2018.2807921.
36. Tian, M.; Zhang, J.; Zhao, Y.; Yuan, L.; Yang, J.; Gui, G. Switch and Inverter Based Hybrid Precoding Algorithm for mmWave Massive MIMO System: Analysis on Sum-Rate and Energy-Efficiency. *IEEE Access* **2019**, *7*, 49448–49455, https://doi.org/10.1109/access.2019.2910094.
37. Yu, X.; Zhang, J.; Letaief, K.B. Doubling Phase Shifters for Efficient Hybrid Precoder Design in Millimeter-Wave Communication Systems. *J. Commun. Inform. Netw.* **2019**, *4*, 51–67.
38. Yan, L.; Han, C.; Yang, N.; Yuan, J. Dynamic-subarray with Quantized- and Fixed-phase Shifters for Terahertz Hybrid Beamforming. In Proceedings of the GLOBECOM 2020-2020 IEEE Global Communications Conference, Taipei, Taiwan, 7–11 December 2020; pp. 1–6, https://doi.org/10.1109/globecom42002.2020.9348113.
39. Li, Z.; Zhang, C.; Lu, I.-T.; Jia, X. Hybrid Precoding Using Out-of-Band Spatial Information for Multi-User Multi-RF-Chain Millimeter Wave Systems. *IEEE Access* **2020**, *8*, 50872–50883, https://doi.org/10.1109/access.2020.2979712.
40. Park, S.; Alkhateeb, A.; Jr., R.W.H. Dynamic Subarrays for Hybrid Precoding in Wideband mmWave MIMO Systems. *IEEE Trans. Wirel. Commun.* **2017**, *16*, 2907–2920, https://doi.org/10.1109/twc.2017.2671869.
41. Tan, J.; Dai, L. Delay-Phase Precoding for THz Massive MIMO with Beam Split. In Proceedings of the 2019 IEEE Global Communications Conference (GLOBECOM), Big Island, Hawaii, USA, 9–13 December 2019; pp. 1–6, https://doi.org/10.1109/globecom38437.2019.9014304.

Chapter 5 – System-Level Assessment of Low-Complexity Hybrid Precoding Designs for Downlink MIMO Transmissions for Beyond 5G

THz communication represents one of the possible technologies to explore in order to achieve bitrates above 100 Gbps and an extremely low latency. However, a proper design for the communication systems is required due to a set of challenges that may affect their performance, such as the reflection and scattering losses through the transmission path, the high dependency with distance and the severe hardware constraints at the THz band. One key approach for overcoming some of these challenges relies on the use of massive/ultramassive antenna arrays combined with hybrid precoders based on fully connected or partially connected phase-shifters architectures. Although, these solutions can help to overcome some of the limitations of THz communications, a lack between link level and system level analysis is commonly verified. In this paper, a C-RAN for B5G systems operating at mmWave/THz bands where the access points support multi-user MU-MIMO transmission using massive/ultra-massive antenna arrays is presented. To enable the implementation of this scheme, the use of low-complexity hybrid precoding-based designs was considered. Numerical evaluation of the link and system-level for the proposed C-RAN downlink scheme integrated into a B5G system showed that it is possible to obtain a performance close to the digital precoding when considering scenarios with a larger number of subcarriers and users. Assessment of the C-RAN deployments in two indoor office scenarios showed the capability of achieving significant improvements in terms of throughput performance and coverage over typical cellular networks.

Some paper details:

- Title: System-Level Assessment of Low-Complexity Hybrid Precoding Designs for Downlink MIMO Transmissions for Beyond 5G;
- Date of publication: 09 March 2022;
- Journal: Applied Sciences;
- Scimago/Scopus Journal Ranking: Quartile 2;
- Publisher: MDPI.

applied sciences

MDPI

Article

System-Level Assessment of Low Complexity Hybrid Precoding Designs for Massive MIMO Downlink Transmissions in Beyond 5G Networks

João Pedro Pavia [1,2,*], Vasco Velez [1,2], Nuno Souto [1,2], Marco Ribeiro [1,2], Pedro Sebastião [1,2] and Américo Correia [1,2]

[1] Department of Information Science and Technology, ISCTE-Instituto Universitário de Lisboa, 1649-026 Lisboa, Portugal; Vasco_Velez@iscte-iul.pt (V.V.); Renato_Ferreira@iscte-iul.pt (R.F.); Nuno.Souto@iscte-iul.pt (N.S.); Marco.Ribeiro@iscte-iul.pt (M.R.); Pedro.Sebastiao@iscte-iul.pt (P.S.); Americo.Correia@iscte-iul.pt (A.C.)

[2] Instituto de Telecomunicações, 1049-001 Lisboa, Portugal;

* Correspondence: jpavia@lx.it.pt (J.P.P)

Applied Sciences 2022, 12(6), 2812; https://doi.org/10.3390/app12062812

Received: 03 February 2022 / Revised: 28 February 2022 / Accepted: 07 March 2022 / Published: 09 March 2022

Abstract: The fast growth experienced by the telecommunications field along the last decades have been motivating the academy and the industry to invest in the design, testing and deployment of new evolutions of wireless communication systems. Terahertz (THz) communication represents one of the possible technologies to explore in order to achieve the desired achievable rates above 100Gbps and the extremely low latency required in many envisioned applications. Despite the potentiali-ties, it requires proper system design, since working at the THz band brings a set of challenges such as the reflection and scattering losses through the transmission path, the high dependency with distance and the severe hardware constraints. One key approach for overcoming some of these challenges relies on the use of massive/ultramassive antenna arrays combined with hybrid pre-coders based on fully connected phase-shifters architectures or partially connected architectures, such as arrays of subarrays (AoSAs) or dynamic AoSAs (DAoSAs). Through this strategy, it is possible to obtain very high-performance gains while drastically simplifying the practical im-plementation and reducing the overall power consumption of the system when compared to a fully digital approach. Although this type of solutions have been previously proposed to address some of the limitations of mmWave/THz communications, a lack between link level and system level analysis is commonly verified. In this paper, we present a thorough system level assessment of a cloud radio access network (C-RAN) for beyond 5G (B5G) systems where the access points (APs) operate in the mmWave/THz bands, supporting multi-user MIMO (MU-MIMO) transmission with massive/ultra-massive antenna arrays combined with low-complexity hybrid precoding archi-tectures. Results showed that the C-RAN deployments in two indoor office scenarios for the THz were capable of achieving good throughput and coverage performances, with only a small compromise in terms of gains when adopting reduced complexity hybrid precoders. Furthermore, we observed that the indoor mixed office scenario can provide higher throughput and coverage performances independently of the cluster size, when compared to the indoor open office scenario.

Citation: Pavia, J.P. et al. System-Level Assessment of Low Complexity Hybrid Precoding Designs for Massive MIMO Downlink Transmissions in Beyond 5G Networks. *Appl. Sci.* **2022**, *12*,2812.https://doi.org/10.3390/app12062812

Academic Editor: Mário Marques da Silva

Received: 03 February 2022
Accepted: 07 March 2022
Published: 09 March 2022

Keywords: Terahertz (THz); multiuser Ultra-Massive-MIMO; hybrid precoder design; system level simulation; cloud radio access network (C-RAN); Beyond 5G (B5G); 6G.

1. Introduction

In the recent years we have been witnessing the increasing deployment of the fifth generation of wireless communications (5G). This generation represents a significant mark in the way we communicate, enabling new applications that would be otherwise infeasible with the technology of previous generations. Therefore, several new technolo-gies were incorporated into 5G which were crucial to achieve all the requirements that are needed for the operation of these systems. However, the telecommunications field is experiencing a fast growth along the last decades, which have been motivating the academy and the industry to invest in the design, testing and deployment of the next generation of wireless communications (6G). Within this context, terahertz (THz) communications have been attracting more and more attention, being referred by research community as one of the most promising research fields on the topic, not only for the availability of spectrum but also because of the achievable rates that can be offered to the users [1,2].

THz systems are becoming feasible due to the recent advances in the field of THz de-vices, and they are expected to ease the spectrum limitations of today's systems [3]. How-ever, there are several issues that can affect the system performance, such as the reflection and scattering losses through the transmission path, the high dependency between range and frequency of channels at the THz band and also the need for controllable time-delay phase shifters. Such limitations require not only the proper system design, but also the definition of a set of strategies to enable communications [4,5]. According to the literature, some of the challenges for beyond 5G networks (B5G) are the fabrication of plasmonic nano array antennas, channel estimation, precoding, signal detection, beamforming, and beamsteering [6]. To overcome the distance limitation in THz communications, one can take advantage of the very large antenna arrays that can be implemented at these bands while minimizing interference between multiple users. However, when working with massive/ultra-massive arrays of antennas, a fully digital precoder is often not feasible and hybrid designs must be used instead. Regarding hybrid precoder, it is necessary to adopt the most adequate architecture in order to maintain the intended trade-off between per-formance and complexity. Fully-connected (FC) structures based on phase shifters, arrays of subarrays (AoSAs) and dynamic arrays of subarrays (DAoSAs) represent some of the most referred architectures in the literature [7-11]. From the energy efficiency (EE) and power consumption perspective which are particularly relevant and the mmWave/THz bands, the use of partially connected (PC) structures such as AoSAs and DAoSAs, can be more efficient than fully connected structures. In particular, DAoSAs represent a much more appealing solution, since they can offer a good compromise (in terms of perfor-mance) between fully connected structures which have a higher implementation com-plexity (especially with a massive number of antennas) and AoSAs which are lighter but can suffer significant degradation in performance. When concerning about this topic, one can find on the literature a wide range of schemes for multiple input multiple output (MIMO) systems considering both uplink and downlink scenarios [7-11], but there is a significant imbalance between the number of approaches aimed at those scenarios for hybrid precoding at higher frequencies. The authors of [12] proposed two algorithms for low-complexity hybrid precoding and beamforming for multi-user (MU) mmWave systems. Even though they assume only one stream per user, i.e., the number of data streams (Ns) is equal to the number of users (Nu), it is shown that the algorithms achieve interesting results when compared to the fully-digital solution. The concept of precoding based on adaptive RF-chain-to-antenna was only introduced in [13] for single user (SU) scenarios but showed promising results. In [14], a nonlinear hybrid transceiver design re-lying on Tomlinson–Harashima precoding was proposed. Their approach only considers FC architectures but can achieve a performance close to the fully-digital transceiver. Most of the hybrid solutions for mmWave systems aim to achieve near-optimal performance using FC structures, resorting to phase shifters or switches. However, the difficulty of handling the hardware constraint imposed by the analog phase shifters or by switches in the THz band is an issue that limits the expected performance in terms of SE. In [15] the authors proposed a low complexity design

based on the alternating direction method of multipliers (ADMM) that can approximate the performance of a hybrid precoder to the fully-digital performance. It is targeted to the millimeter wave (mmWave)/THz bands and can incorporate different architectures at the analog component of the precoder, making it suitable for supporting ultra-massive MIMO (UM-MIMO) in severely hard-ware-constrained systems that are typical at these bands. There are some recent experimental demonstrations of hybrid precoding schemes in for MIMO mmWave communications as mentioned in [16,17]. However, these implementations still have limitations in the size of the adopted arrays and number of RF chains. Regarding the applications of these schemes in the THz band, the technology is still in early stages and there are still no UM-MIMO implementations with hybrid precoding/beamforming. Nevertheless, there are already some simpler MIMO implementations in THz as the ones mentioned in [18,19].

When transitioning from a link level perspective to a system level analysis, we must deal with several other issues such as distance limitation, signal-to-noise ratio (SNR) degradation, weak coverage areas and blind zones which are particularly relevant when working in the high frequency spectrum [11,20,21]. This is the main reason why network and resource allocation planning are crucial when deploying these systems for cellular communications, independently of the scenario under study [11, 22]. There are few sys-tem-level evaluations of mmWave schemes in the literature, such as the ones mentioned in [23,24], but beyond all the proposals in the field of system level analysis very few ex-amples have been extended to 5G New Radio (5G NR) standard of the 3rd Generation Partnership Project (3GPP) and for the THz level (e.g. 100 GHz) as we cover in this paper. This standard suggests the use of deterministic cluster delay lines (CDLs) for link-level simulations, which requires the definition of average angles of departure (AODs) and ar-rival (AOAs) and also a tapped delay line (TDL). For system-level simulations, a full three-dimensional (3D) modelling of a radio channel is recommended since this type of analysis requires a statistical approach [25,26].

Motivated by the work above, in this paper we study a cloud radio access network (C-RAN) for 5G and beyond systems which is based on the adoption of low complexity hybrid precoding designs for massive and ultra-massive multi-user MIMO (MU-MIMO) schemes operating in the mmWave/THz bands. As far as the authors are aware there are no previous studies similar to the one presented in this paper focusing on system-level evaluation of robust hybrid algorithms with different architectures (FC, AoSA, DAoSA, etc.) at the THz band. The C-RAN studied in this paper assumes that each access point (AP) uses the precoder to remove the multi-user interference (MUI) generated at the receivers, breaking the MU communication into equivalent small SU links which enables a lower complexity at the receiver side. We consider a virtualized C-RAN, where the network determines which APs are to be associated with each terminal. The cell moves with and always surrounds the terminal in order to provide a cell-center experience throughout the entire network. Each terminal designated as user equipment (UE) is served by its pre-ferred set of APs. The actual serving set for a UE may contain one or multiple APs and the terminal's data is partially or fully available at some cluster with potential serving APs. The AP controller (Central Processor) will accommodate each UE with its preferred cluster and transmission mode at every communication instance while considering load and channel state information (CSI) knowledge associated with the cluster of APs [27].

The main contributions of this paper can be summarized as follows:

- Thorough system level assessment of a virtualized C-RAN with two clusters sizes, namely, size 1 and 3, where the APs operate in the mmWave/THz bands with mas-sive/ultra-massive antenna arrays combined with low-complexity hybrid precoding ar-chitectures. The system level simulations were performed based on link level results be-tween the APs and multiple terminals, where it is considered that the ADMM algorithm from [15] is applied for hybrid precoding design at the transmitter side.
- System level evaluation of the proposed C-RAN in two 5G NR three-dimension (3D) scenarios, namely, the indoor mixed office (InD-MO) and indoor open office (InD-OO).
- System level assessment of the proposed based C-RAN with the fifth numerology of 5G NR in the 3D indoor mixed office scenario with different parameters, such as, number of transmitted antennas per user and number of subcarriers, with the results benchmarked against two alternative MU-MIMO schemes.

Table 1. Table of acronyms.

Acronym	Designation
3D	Three-dimensional
3GPP	The 3rd Generation Partnership Project
5G	The fifth generation of wireless communications
5GNR	5G New radio
6G	The sixth generation of wireless communications
ADMM	Alternating direction method of multipliers
AM	Alternating minimization
AOA	Average angle of arrival
AOD	Average angle of departure
AoSA	Array of subarrays
AP	Access point
B5G	Beyond 5G
BER	Bit error rate
BLER	Block error rate
CDL	Cluster delay line
C-RAN	Cloud radio access network
CSI	Channel state information
DAoSA	Dynamic array of subarrays
DPS	Double phase shifters
EC	Energy consumption
EE	Energy efficiency
FC	Fully-connected
InD-MO	Indoor-mixed office
InD-OO	Indoor-pen office
LASSO	Least absolute shrinkage and selection operator
LOS	Line-of-sight
MIMO	Multiple Input Multiple Output
MU	Multi-user
MUI	Multi-user interference
MU-MIMO	Multi-user MIMO
mmWave	Millimeter wave
NLOS	Non-line of sight
PC	Partially-connected
QPS	Quantized phase shifters
UM-MIMO	Ultra-massive MIMO
SE	Spectral efficiency
SNR	Signal-to-noise ratio
SPS	Single phase shifters
SU	Single-user
TDL	Tapped delay line
TRP	Transmission and reception point
THz	Terahertz
UE	User equipment

System level evaluation demonstrates that low-complexity hybrid precoding-based C-RAN deployments in an indoor scenario can enable the practical implementation of those schemes, which rely on massive/ultra-massive antenna arrays to combat distance limitation and minimize the MUI. While these hybrid designs sacrifice some performance, significant throughput performance and coverage improvements can still be achieved over typical cellular networks.

In Table 1, we present a list of acronyms adopted along the text in order to improve the readability of the paper. The paper is organized as follows: Section 2 presents the model for the low-complexity hybrid precoding system and the system level scenario that is considered in the evaluation. Section 3 presents and discusses the system level simulations results, whereas the conclusions are outlined in Section 4.

Notation: Matrices and vectors are denoted by uppercase and lowercase boldface letters, respectively. (.)T and (.)H denote the transpose and conjugate transpose of a matrix/vector, $\|\cdot\|_p$ is the ℓ_p -norm of a vector, $\|\cdot\|_0$ is its cardinality, $\lfloor\cdot\rfloor$ is the floor function and $\boldsymbol{I}_n$ is the n × n identity matrix.

2. System Model

2.1. Transmitter and receiver model

Let us consider a mmWave/THz hybrid MU-MIMO system, where an AP is equipped with N_{tx} antennas that transmit to N_u users simultaneously over F carriers. Each user is equipped with N_{tx} antennas that transmits to N_u users simultaneously. Each user is equipped with N_{rx} antennas over F carriers, as the one described in Figure 1. N_s data streams are transmitted to each user and to each subcarrier, which can be represented as $\mathbf{s}_k = \left[\mathbf{s}_{k,1}^T \ldots \mathbf{s}_{k,N_u}^T\right]^T$, with $\mathbf{s}_{k,u} \in \mathbb{C}^{N_s \times 1}$. Since a fully digital design would require a dedicated RF chain per antenna element, both the digital and analog processing blocks of the precoder and combiner are separated. By following this approach, it is possible to use reduced digital blocks with only a few radio frequency (RF) chains, which can be complemented by the analog blocks that are based on networks of phase-shifter and switches solely. It is assumed that $N_u N_s \le N_{RF}^{tx} \le N_{tx}$ and $N_s \le N_{RF}^{rx} \le N_{rx}$, where N_{RF}^{tx} and N_{RF}^{rx} are the number of RF chains at the AP and each user, respectively. The received signal model at user u and subcarrier k after the combiner can be written as

$$\mathbf{Y}_{k,u} = \sqrt{\rho_u}\mathbf{W}_{\mathrm{BB}_{k,u}}^H \mathbf{W}_{\mathrm{RF}_u}^H \mathbf{H}_{k,u} \mathbf{F}_{\mathrm{RF}} \mathbf{F}_{\mathrm{BB}_k} \mathbf{s}_k + \mathbf{W}_{\mathrm{BB}_{k,u}}^H \mathbf{W}_{\mathrm{RF}}^H \mathbf{n}_{k,u}, \quad (1)$$

where $\mathbf{H}_{k,u} \in \mathbb{C}^{N_{rx} \times N_{tx}}$ is the frequency domain channel matrix (assumed to be perfectly known at the transmitter and receiver) between the AP and the u^{th} receiver at subcarrier k. $\mathbf{F}_{\mathrm{RF}} \in \mathbb{C}^{N_{tx} \times N_{RF}^{tx}}$ and $\mathbf{W}_{\mathrm{RF}_u} \in \mathbb{C}^{N_{rx} \times N_{RF}^{rx}}$ represent the analog precoder and combiner, with u=1, …, N_u, ρ_u denotes the average received power and vector $\mathbf{n}_{k,u} \in \mathbb{C}^{N_{rx} \times 1}$ contains independent zero-mean circularly symmetric Gaussian noise samples with covariance $\sigma_n^2 \mathbf{I}_{N_{rx}}$. The digital baseband precoders are denoted by $\mathbf{F}_{\mathrm{BB}_k} \in \mathbb{C}^{N_{RF}^{tx} \times N_u N_s}$ and the combiners by $\mathbf{W}_{\mathrm{BB}_{k,u}} \in \mathbb{C}^{N_{RF}^{rx} \times N_s}$. In order to maintain the complexity of the implementation limited, the analog component is the same for all subcarriers, which means that $\mathbf{F}_{\mathrm{RF}}$ and $\mathbf{W}_{\mathrm{RF}}$ will be the same for all subcarriers.

Considering the major issues related to spectral efficiency (SE), energy consumption and hardware implementation for THz pointed in introduction, in this study we considered the architectures depicted in Figure 2 [15, 28–31]. The FC architecture is the closest to the performance of the digital architecture, but it is also the most power consuming of the hybrid architectures. This is the main motivation for the development of partially connected architectures (AoSAs and DAoSAs) with the aim of trying to achieve similar performances to FC structures, but with lower energy consumption. The AoSAs architectures, especially the ones based on phase shifters, can be divided into two categories, namely, the ones based on single phase shifters (SPS) and the ones based on double phase shifters (DPS). Increasing the number of phase shifters connected to each antenna results in an improved performance but entails a higher energy consumption.

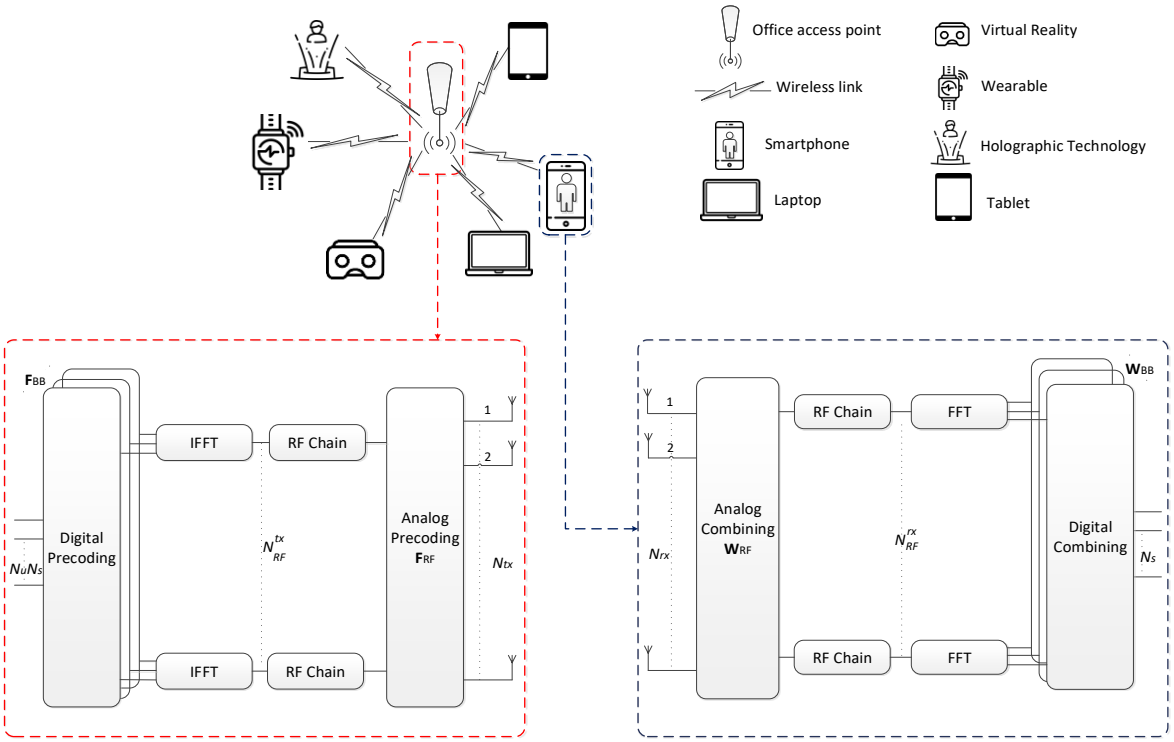

Figure 1. Transmitter and receiver structure of a multiuser OFDM mmWave/THz MIMO system with hybrid precoding for an InD scenario.

On the other hand, DAoSAs represent a much more appealing solution due the good compromise between performance and energy consumption (EC). However, the choice of the most suitable architecture depends on several aspects, which are related to the calculation of the $\mathbf{F}_{\mathrm{RF}}$ and $\mathbf{F}_{\mathrm{BB}}$ matrices. When considering a FC structure with SPS, the $\mathbf{F}_{\mathrm{RF}}$ will be dense with all elements having unit amplitude. Nevertheless, if we consider the case of AoSA architecture, the $\mathbf{F}_{\mathrm{RF}}$ elements also have unit amplitude, but the matrix structure is

$$\mathbf{F}_{\mathrm{RF}} = \mathrm{blkdiag}\{\mathbf{f}^{RF,1},\ldots,\mathbf{f}^{RF,N_{RF}}\} = \begin{bmatrix} \mathbf{f}^{RF,1} & \cdots & 0 \\ \vdots & \ddots & \vdots \\ 0 & \cdots & \mathbf{f}^{RF,N_{RF}} \end{bmatrix}, \tag{2}$$

with $\mathbf{f}^{RF,i} = \begin{bmatrix} f_1^{RF,i},\ldots,f_{\frac{N_{tx}}{N_{RF}}}^{RF,i} \end{bmatrix} \in \mathcal{U}_{N_{tx}/N_{RF,1}}$ for i=1, …, N_{RF}. In the case of the DAoSA architecture, the matrix is similar to case of AoSA but can have a number of non-null columns in each row of up to the maximum number of subarrays that can be connected to an RF chain (L_{max}). If we consider DPS-based architectures, the amplitude of the elements becomes less than or equal to 2.

Several schemes have been proposed in the literature to calculate the matrices $\mathbf{F}_{\mathrm{RF}}$ and $\mathbf{F}_{\mathrm{BB}}$, such as [12,29]. The approach suggested in [15], can calculate $\mathbf{F}_{\mathrm{RF}}$ and $\mathbf{F}_{\mathrm{BB}}$ by approximation of the digital F for any of these four structures. The overall optimization problem can be then expressed as

$$\min_{\mathbf{F}_{\mathrm{RF}},\mathbf{F}_{\mathrm{BB}_k}} \sum_{k=1}^{F} \left\| \mathbf{F}_{\mathrm{opt}_k} - \mathbf{F}_{\mathrm{RF}}\mathbf{F}_{\mathrm{BB}_k} \right\|_F^2 \tag{3}$$

$$\text{subject to } \mathbf{F}_{\mathrm{RF}} \in \mathcal{C}_{N_{tx} \times N_{RF}^{tx}} \tag{4}$$

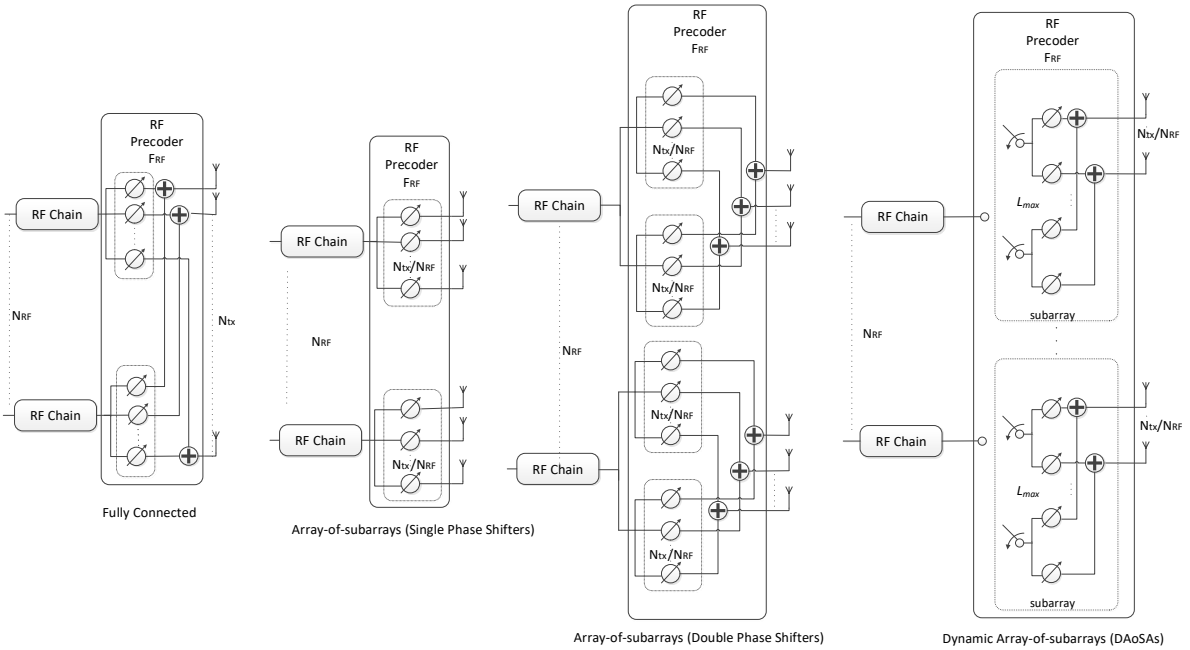

Figure 2. Different precoder architectures for a mmWave/THz MIMO system based on phase shifters.

$$\left\| \mathbf{F}_{\mathrm{RF}} \mathbf{F}_{\mathrm{BB}_k} \right\|_F^2 = N_u N_s \,. \tag{5}$$

In this formulation matrix $\mathbf{F}_{\mathrm{opt}_k}$ denotes the fully-digital precoder and the equation (5) enforces the transmitter's total power constraint and $\mathcal{C}_{N_{tx} \times N_{RF}}$ is the set of feasible analog precoding matrices, which is defined according to the adopted RF architecture. In order to enforce $\mathbf{F}_{\mathrm{RF}} \mathbf{F}_{\mathrm{BB}_{k,u}}$ to lie in the null space of $\bar{\mathbf{H}}_{k,u} \in \mathbb{C}^{(N_u - 1) N_{rx} \times N_{tx}}$, we write the following restriction to the overall optimization problem expressed in (3) to (5)

$$\mathbf{F}_{\mathrm{RF}} \mathbf{F}_{\mathrm{BB}_{k,u}} \in \mathcal{N}\left(\bar{\mathbf{H}}_{k,u}\right), \tag{6}$$

with k=1, …, F and u=1, …, N_u. $\bar{\mathbf{H}}_{k,u}$ is a matrix corresponding to $\mathbf{H}_k$ with the N_{rx} lines of user u removed which we denote as $\mathcal{N}\left(\bar{\mathbf{H}}_{k,u}\right)$. Other RF constraints can be directly integrated into the objective function of the optimization problem in order to cope with the different RF architectures.

2.2. Channel model

Even though mmWave and THz bands share a few similarities, the THz channel presents several unique features that differentiate it from the mmWave channel. In the THz band, the very high scattering and diffraction losses tend to result in a much sparser channel in the angular domain with fewer multipaths components (typically less than 10) [20]. Because of the referred phenomenon, the gap between the line of sight (LOS) and non-line of sight (NLOS) components tends to be very large, which often makes LOS-dominant with NLOS-assisted [28]. An additional aspect relies on the much larger bandwidth of THz signals which can suffer performance degradation due to the so-called beam split effect, where the transmission paths squint into different spatial directions depending on the subcarrier frequency [29]. In light of this, in this paper we consider a clustered wideband geometric channel, which is commonly adopted both in mmWave [12] and THz literature [5,6,30,31]. However, it should be noted that the hybrid precoding/combining approach proposed in this paper is independent of a specific MIMO channel. In this case the frequency domain channel matrices can be characterized as

$$\mathbf{H}_{k,u} = \gamma\left(\alpha_u^{LOS}\mathbf{a}_r\left(\phi_u^{r,LOS},\theta_u^{r,LOS}\right)\mathbf{a}_t\left(\phi_u^{t,LOS},\theta_u^{t,LOS}\right)^H + \right.$$
$$\left. + \sum_{i=1}^{N_{cl}}\sum_{l=1}^{N_{ray}}\alpha_{i,l,u}\mathbf{a}_r\left(\phi_{i,l,u}^{r},\theta_{i,l,u}^{r}\right)\mathbf{a}_t\left(\phi_{i,l,u}^{t},\theta_{i,l,u}^{t}\right)^H\right)e^{-j2\pi\tau_{i,u}f_k}, \quad (7)$$

where N_{cl} denotes the number of scattering clusters with each cluster i, having a time delay of $\tau_{i,u}$ and N_{ray} is the number of propagation paths per cluster. α_u^{LOS} and $\alpha_{i,l,u}$ are the complex gains of the LOS component and of the l^{th} ray from cluster i. Index u is the user (u=1, …, N_u), $f_k = f_c + \frac{B}{F}\left(k - 1 - \frac{F-1}{2}\right)$ (k=1, …, F) is the k^{th} subcarrier frequency, B is the bandwidth, f_c is the central frequency and γ is a normalizing factor such that Vectors $\mathbf{a}_t\left(\phi_{i,l,u}^{t},\theta_{i,l,u}^{t}\right)$ and $\mathbf{a}_r\left(\phi_{i,l,u}^{r},\theta_{i,l,u}^{r}\right)$ represent the transmit and receive antenna array responses at the azimuth and elevation angles of $\left(\phi_{i,l,u}^{t},\theta_{i,l,u}^{t}\right)$ and $\left(\phi_{i,l,u}^{r},\theta_{i,l,u}^{r}\right)$, respectively. Vectors $\mathbf{a}_t\left(\phi_u^{t,LOS},\theta_u^{t,LOS}\right)$ and $\mathbf{a}_r\left(\phi_u^{r,LOS},\theta_u^{r,LOS}\right)$ have similar meanings but refer to the LOS path angles $\left(\phi_u^{t,LOS},\theta_u^{t,LOS}\right)$ and $\left(\phi_u^{r,LOS},\theta_u^{r,LOS}\right)$. By carefully selecting the parameters of the channel model it is possible to make it depict a mmWave or a THz channel. As represented in (7), this channel model includes both LOS and NLOS components. In the case of the NLOS components, we consider complex gaussian distributed paths gains, as in [32]. Radio propagation measurements have shown that this type of clustered based channel models can yield good agreements with real channel behavior at mmWave and subTHz frequencies [33].

2.3. System level scenario

The indoor hotspot deployment scenario focuses on small cells and high user density in buildings. This scenario, described in Table 2, represents InDs with a total area of 120 m×50 m. There are 12 small tri-sectored cells which are deployed with an inter-site distance (ISD) of 20 m. In this case the AP antenna height is 3 m. The coverage radius of the APs is R=6.7 m. The carrier frequency option is 100 GHz (THz waves). The bandwidth chosen is B_t=400 MHz corresponding to numerology five of 5G NR. Up to 16 carriers can be aggregated up to 6.4 GHz of bandwidth. It is important to note that in case of the number of users and wireless devices increasing relative to the numbers considered here, the expected behavior of the overall system will remain the same as long as carrier aggregation is used, and they will not cause inter-interference as long as they operate in different bands. A total of 15 users per AP are distributed uniformly and all users are indoors with 3 km per hour velocity as can be seen in Figure 3. Full buffer model is assumed. Our 3D simulation channel model considers the 5G NR indoor office wireless propagation environment in terms of physical aspects of mmWave and THz waves. For this particular scenario in any considered operating frequency, the number of clusters, number of subarrays (scatterers) per cluster, and the positions of the clusters are determined by the detailed steps and procedures of [25].

According to the 5G 3GPP 3D channel models, the number of clusters and scatterers are determined using the Poisson and uniform distributions with specific parameters. Since, we extend the operating frequency range up to 100 GHz, specific multi-antenna solutions and techniques need to be employed depending on the utilized spectrum. For higher frequency bands, the transmission is characterized by a considerable signal attenuation that limits the network coverage. To overcome this limitation, one of the key features is the adoption of a very large number of multi-antenna elements having a given aperture to increase the transmission/reception capability of MU-MIMO and beamforming. Since, managing transmissions in higher frequency bands is complicated, beam management is necessary to establish the correspondence between the directions of the transmitter and the receiver-side beams by identifying the most suitable beam pair for both downlink and uplink.

Table 2. Evaluation parameters for indoor-office scenario.

Parameters		Indoor – office
Layout	Room size (WxLxH)	120 mx50 mx3 m
	ISD	20m
AP antenna height h_{AP}		3 m (ceiling)
UE location	LOS/NLOS	LOS and NLOS
	Height h_{UE}	1.5 m
UE mobility (horizontal plane only)		3 km/h
Min. AP - UE distance (2D)		0
UE distribution (horizontal)		Uniform

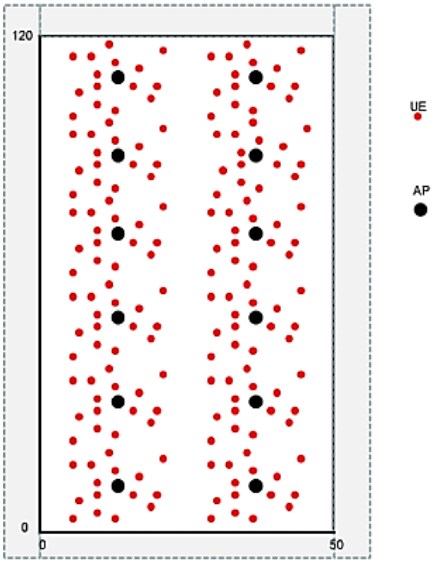

Figure 3. Indoor Office scenario layout.

3. Numerical Results

In this section we present the numerical assessment of both the link and system level of a massive/ultra-massive MU-MIMO downlink scheme operating in the mmWave/THz band integrated into a 5G NR system, where the APs are based on the low complexity ADMM-based hybrid precoding designs. Link level results are presented in terms of bit error rate (BER) and measure the performance of the signal across the entire communication chain, from transmitter to receivers. Both the link and system level diagrams can be found in references [15,27].

3.1. Link Level Simulations

Considering that both the transmitter and receivers are equipped with uniform planar arrays (UPAs) with $\sqrt{N_{tx}} \times \sqrt{N_{tx}}$ antenna elements at the transmitter and $\sqrt{N_{rx}} \times \sqrt{N_{rx}}$ at the receiver, the respective array response vectors are given by

$$\mathbf{a}_{t/r}\left(\phi_{i,l,u}^{t/r}, \theta_{i,l,u}^{t/r}\right) = \frac{1}{\sqrt{N_{tx/rx}}} \times \left[1, \ldots, e^{j\frac{2\pi}{\lambda}d\left(p\sin\phi_{i,l,u}^{t/r}\sin\theta_{i,l,u}^{t/r} + q\cos\theta_{i,l,u}^{t/r}\right)}, \right.$$
$$\left. \ldots, e^{j\frac{2\pi}{\lambda}d\left(\left(\sqrt{N_{tx/rx}}-1\right)\sin\phi_{i,l,u}^{t/r}\sin\theta_{i,l,u}^{t/r} + \left(\sqrt{N_{tx/rx}}-1\right)\cos\theta_{i,l,u}^{t/r}\right)}\right]^T, \tag{8}$$

where λ is the signal wavelength, d is the inter-element spacing (a $d = \lambda/2$ is assumed) and p, q=0, …., $\sqrt{N_{tx/rx}} - 1$ are the antenna indices. We consider a sparse channel with limited scattering where N_{ray}=1 and N_{cl}=9. The angles of departure and arrival were selected according to a Gaussian distribution whose means are uniformly distributed in [0, 2π] and whose angular spreads are 10 degrees. The

results are presented for a NLOS and LOS channel. This last case considers a ratio of $E\left[\left|\alpha_u^{LOS}\right|^2\right] \Big/ \sum_{i=1}^{N_{cl}} \sum_{l=1}^{N_{ray}} E\left[\left|\alpha_{i,l,u}\right|^2\right] = 10$, which means we are admitting very weak NLOS paths when compared to LOS.

In a first approach, we compared several solutions available in the literature concerning the hybrid precoding, such as AM [12], LASSO [34] and ADMM [15] based precoding. In Figure 4, we assumed a scenario with N_{tx}=100, N_{rx}=4, $N_{RF}^{tx} = 12$, N_u=4 and N_s=2, in which we change the number of subcarriers. To ensure a fair comparison, all schemes have a SE close to 2 bits per channel use (bpcu) per user. In this study, we considered that the hybrid precoding algorithms (LASSO and ADMM) can be applied to an architecture based on SPS or DPS, as proposed by [35] .

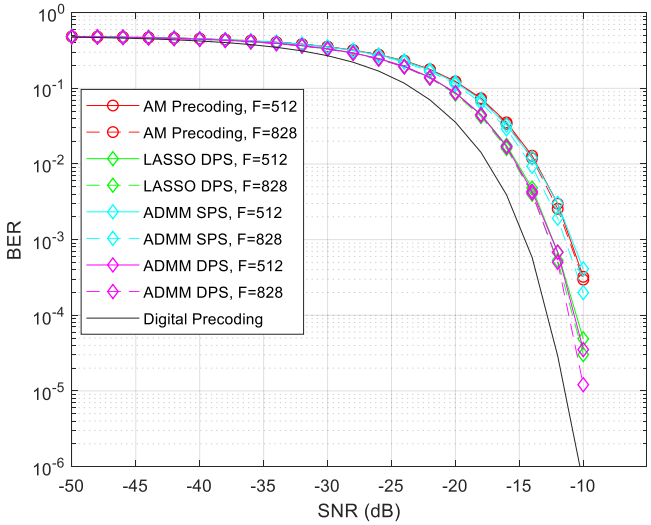

Figure 4. BER performance versus SNR achieved by different methods by changing the number of subcarriers and considering a system with N_{tx}=100, N_{rx}=4, $N_{RF}^{tx} = 12$, N_u=4 and N_s=2 (only NLOS component).

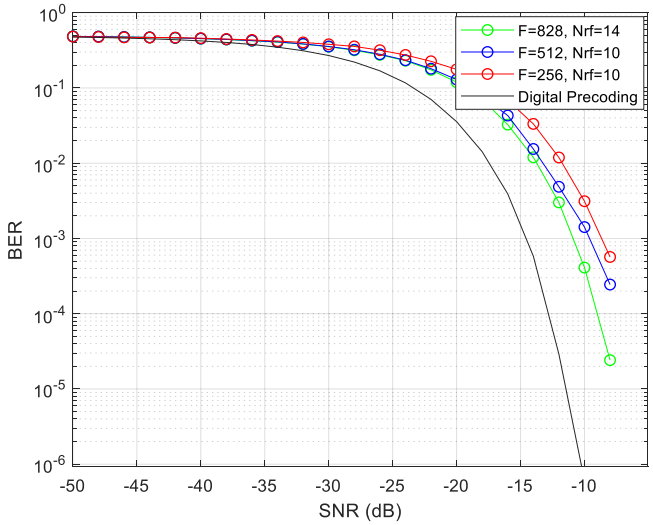

Figure 5. BER performance versus SNR achieved by the proposed precoder with N_{tx}=256, N_{rx}=4, N_u=4, and N_s=2, by changing the number of subcarriers and the number of RF chains (only NLOS component).

It can be observed that the ADMM based on a DPS scheme outperforms both versions of AM and LASSO (SPS/DPS), and the gains tend to be slightly greater when the symbols are distributed over a larger number of subcarriers (F). However, the larger the number of subcarriers the greater will be the number of the required RF chains to maintain a good performance. In general, the ADMM precoding algorithm is the one that can achieve the best results at the cost of some additional computational complexity and it is also the most flexible since it can cope with different architectures, as explained in [15]. At the next subsection of the paper, we will compare these three methods based on system level simulations.

In order to understand how many RF chains are necessary to maintain a good performance as the number of subcarriers increases, we simulated the ADMM algorithm for a scenario with N_{tx}=256, N_{rx}=4, N_u=4 and N_s=2 and we changed the number of subcarriers, as can be seen in Figure 5. By maintaining the same number of RF chains as the number of subcarriers increases, some performance degradation results as can be seen when we compare the curves of F=256 and F=512. In fact, in the case of F=828, 10 RF chains were insufficient to provide acceptable performance and therefore 14 RF chains were employed.

After studying the performance of the ADMM precoder considering the variation of the number subcarriers, F, and RF chains, it is important to understand the main differences in terms of performance when considering architectures based on SPS, DPS as well as the impact of quantized phase shifters (QPS). The results are shown in Figure 6. It can be seen that a better performance can be achieved when considering a design based on a DPS over the SPS. It is important to remember, however, that the architecture based on DPS provides a better performance but requires the use of twice the number of phase shifters in the implementation.

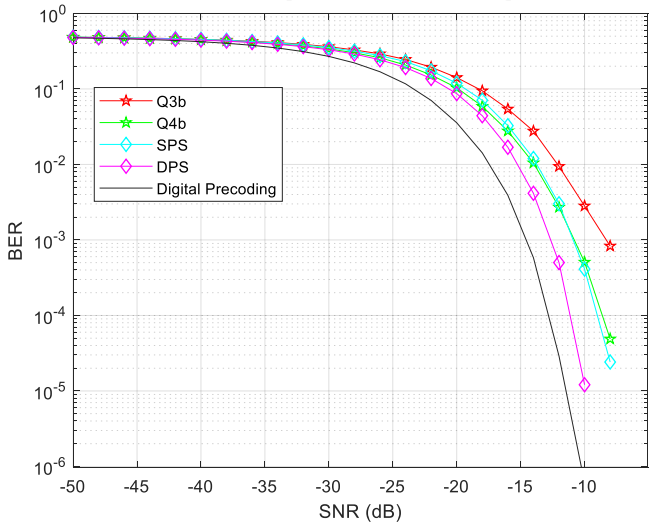

Figure 6. BER performance versus SNR achieved by the proposed precoder with N_{tx}=256, N_{rx}=4, N_u=4, $N_{RF}^{tx}=14$, F=828 and N_s=2, considering several versions of the algorithm (only NLOS component).

In this same figure, we include QPS curves, which corresponds to the SPS architecture with quantized phase shifters. It can be observed that, as expected, there is a performance loss when comparing the QPS curves against the ideal SPS, but this degradation is greatly reduced when using phase shifters with only 4 bits of quantization. Beyond, the choice of the parameters of the scenario, the BER performance can be improved by increasing the number of iterations of precoding algorithms.

3.2. System Level Simulations

Bit and block error rate (BER/BLER) results obtained from link level simulations are used as input for the system level evaluation. As presented in the system model section, we consider an indoor office virtualized C-RAN, where the network determines which APs are to be associated with each UE. The total number of sites with APs is 12, which are equally spaced. Each site with APs consists of three transmission and reception points (TRPs), each one equipped with UPAs with N_{tx} antennas, while UEs also have one UPA with N_{rx} antennas. The number of antennas N_{tx} of each array is 100 or 256 antennas whereas the separation between antennas of the array is half wavelength. The signal-to-noise ratio (SNR) in dB considered in the system level simulations is obtained from $\text{SNR} = (E_s/N_0) + 10\,log(R_s/B)$ dB, where R_s is the total transmitted symbol rate per antenna and user, B is the total bandwidth, and E_s/N_0 is the ratio of symbol energy to noise spectral density in dB. Values of E_s/N_0 are obtained from the link level BLER results. The BLER can expressed using the BER, according to the following expression

$$\text{BLER}=1-(1-\text{BER})^L \quad (9)$$

where L is the length of the block in bits. L can be calculated as L=2×F, since the selected modulation is quadrature phase shift keying (QPSK) and each subcarrier transports a symbol with 2 bits. By maintaining the reference BLER (BLER_{ref}) equal to 0.1 as the F increases, we must decrease the respective reference BER (BER_{ref}). We considered the fifth numerology of 5G NR with spacing between the subcarriers of 480 KHz. The transmission time interval (*TTI*) of this numerology is 31.25 μs and the total bandwidth is B_T= 400 MHz. Up to 16 carriers can be aggregated if more bandwidth and higher binary rates, according to the 5G NR specifications, are to be achieved. We used the 3D InD-MO channel model specified by 3GPP [25] which has a LOS probability (P_{LOS}) equal to 1 for a distance lower than 1.2 m between the AP and terminals. The probability of NLOS components is $P_{NLOS} = 1 - P_{LOS}$ and depends on the distance between the AP and the terminals. Previously, we started our study by comparing several solutions available in the literature concerning hybrid precoding algorithms in terms of BER versus SNR.

Based on those results, we decided to analyze the performance of a system, where the APs operate in the mmWave/THz bands with massive/ultra-massive antenna arrays combined with those different hybrid precoding architectures. For this evaluation, first we start by considering that the cluster size is equal to 1. When RAN cluster size is one (1C), we have the traditional cellular network where each AP generates inter-site interference. When RAN cluster size is 3, the network is partitioned into three adjacent site sets and each user is served at the same time by three TRPs generating much less inner interference. It is important to note that the throughput presented in the following figures concerns the average throughput value of the various UEs moving randomly throughout the 200 seconds of simulation. Initially, the terminals are placed uniformly distributed inside each sector served by an UPA antenna. The movement of the terminals is "Random waypoint around AP". At every 0.5 ms of simulation the SNR at all terminals is calculated. Those blocks which are received with SNR > $\mathrm{SNR}_{\mathrm{target}}$ are considered in the throughput calculation. The blocks that are received with SNR < $\mathrm{SNR}_{\mathrm{target}}$ are not counted in the throughput due to the throughput definition itself. $\mathrm{SNR}_{\mathrm{target}}$ is the SNR value for BLER_{ref}=0.1. In practical terms, each block received with SNR < $\mathrm{SNR}_{\mathrm{target}}$ would be retransmitted until it is correctly received. However, we do not consider this situation in the simulations.

Figure 7 is based on the link level simulation of Figure 4 presented in the previous subsection. In general, it is observed that the greater the number of subcarriers, the greater will be the throughput. As expected, the digital precoder is the one which presents the best performance in terms of throughput as the number of subcarriers and users increases. However, it is possible to approach its performance by considering the use of hybrid algorithms and their different architectures. The ADMM based on a SPS scheme is the one, which presents the worst performance for a lower number of subcarriers, but when this parameter is increased it obtains a similar performance to the AM precoding algorithm. The LASSO precoding algorithm with DPS and F=512 can obtain a slightly higher performance when compared to the ADMM DPS with F=512. However, by increasing the number of subcarriers we observe that both algorithms obtain very similar performances. The blue curves represent the theoretical curves of average throughput value expected to be obtained based on the formula $\mathrm{Throughput} = R_{b_{\max}}(1 - \mathrm{BLER}_{ref})$, where BLER_{ref}=0.1 and $R_{b_{\max}}$ is the maximum binary transmission rate considered for the two cases F=512 and F=828.

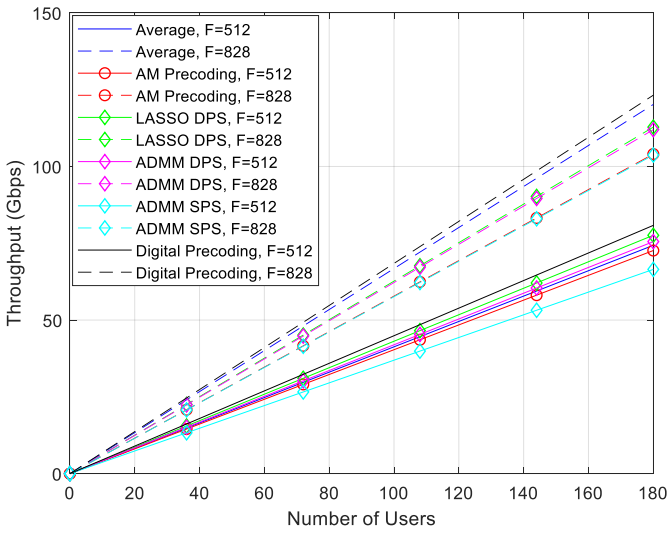

Figure 7. Throughput (Gbps) vs number of users for different methods with N_{tx}=100, N_{rx}=4, $N_{RF}^{tx}=12$ and N_s=2, by changing the number of subcarriers (only NLOS component).

Contrary to what it can be seen for F=512, a loss of performance of the algorithms for F=828 when compared to the curve of average throughput value expected for the case of F=828, is observed. Moreover, we observe that with a fixed number of RF chains, the throughput of hybrid schemes tends to be closer to digital with *F*=512 than with *F*=828. When considering the digital precoding for *F*=828 and 3C, a maximum SE of 1.9 bps/Hz/user can be obtained. Note that, this fact is also verified in the later graphs.

Following the study on the required number of RF chains to accommodate an increasing number of subcarriers discussed in Figure 5, it is necessary to understand how the system behaves when considering different RAN cluster sizes. In Figure 8, we can conclude that by increasing the number of RF chains for higher values of *F* allow us to reach greater levels of throughput. Furthermore, when the cluster size increases to 3 (3C), as the number of users increases, the difference becomes more notorious due to the lesser inner interference caused by the network partitioning. When we have N_u=180, the achieved throughput increases from 105.7 Gbps to 133.3 Gbps if the cluster size triples. It must be noted that for smaller blocks, such as *F*=16 up to 128, the system performance is independent of cluster size. When *F* presents higher values, we observed that the performance difference of 1C and 3C increases with block size.

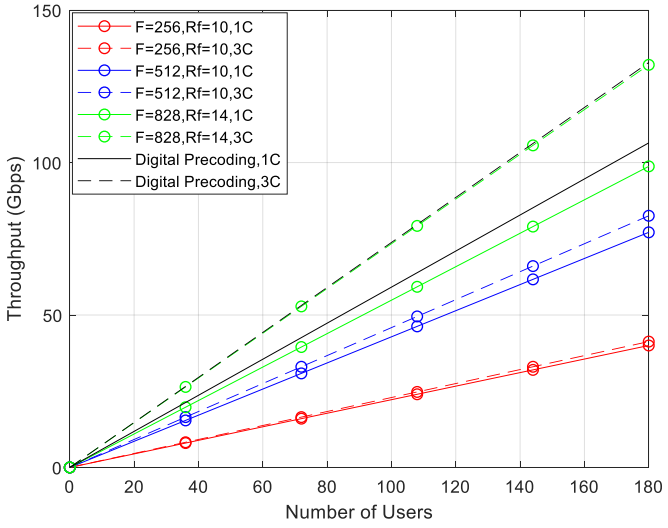

Figure 8. Throughput (Gbps) vs number of users for different number of subcarriers, RF chains and cluster sizes, considering the proposed precoder with N_{tx}=256, N_{rx}=4 and N_s=2 (only NLOS component).

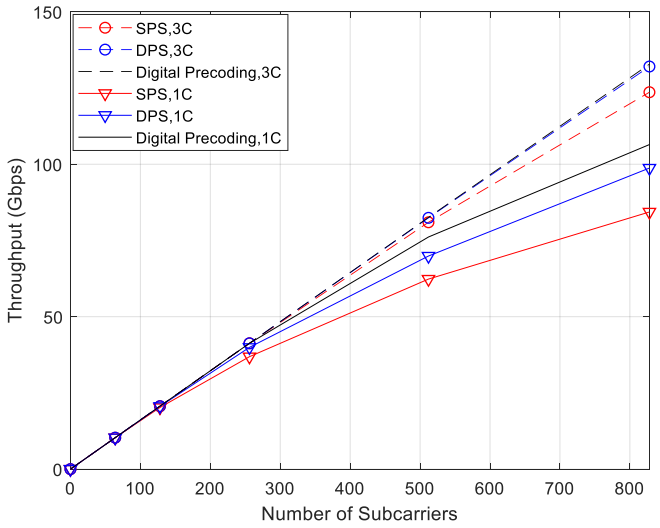

Figure 9. Throughput (Gbps) vs number of subcarriers for different versions of the algorithm (SPS and DPS) and cluster sizes, considering the proposed precoder with N_{tx}=256, N_{rx}=4, N_{RF}^{tx} =14 , N_s=2 and N_u=180 (with LOS component).

At this point, we already know that the throughput increases as the number of subcarriers increases and the ADMM precoding algorithm constitutes as an interesting alternative, since it can present a good performance and can cope with different architectures, facilitating their implementation. However, it is worth to understand how the system behaves when the AP antennas are combined with different architectures based on phase shifters, as can be seen in Figure 9. Independently of the adopted architecture, it is observed that the throughput increases as the number of subcarriers increases. However, the adoption of a DPS architecture can provide a higher throughput when compared to an architecture based on SPS. This difference is even more notorious when we increase the cluster size from 1 to 3. Considering a F=828 and 1C the version of the algorithm based on SPS can reach a throughput of 85.79 Gbps whereas the one based on DPS can reach a throughput of 99.99 Gbps. When we have 3C, both versions of the algorithm can obtain a significant improvement over the values obtained for 1C. The first one can reach a throughput around 127.3 Gbps and the latter one reaches 132 Gbps. In fact, the version based on a DPS architecture with 3C is the one who can closely approach the digital precoding curve.

After previously analyzing two different solutions based on phase shifters, we now evaluate the performance of the system in terms of throughput and coverage with more realistic phase shifters, i.e., phase shifters with quantization. Figure 10 is based on the link level simulation of Figure 6 presented in the previous subsection. From this figure, we observe that, as expected, by increasing the number of quantization (QPS curves) it is possible to approach the performance of the ideal unquantized version of the algorithm (SPS curve). Furthermore, it can also be seen that by increasing the cluster size, the throughput can almost double when the number of subcarriers is large. Moreover, we observe that by increasing the cluster size from 1C to 3C that the hybrid precoders curves get closer to the digital precoder curve. A lower throughput loss, due to the quantization effect, is also observed.

Following the conclusions about the previous figure concerning the impact of quantized phases shifter in the hybrid architectures, we decided to study the system performance using the same hybrid architecture in the InD-MO and the InD-OO scenarios. The throughput per user results of Figure 11 and the average coverage results of Figure 12, were simulated considering a precoder based on QPS with N_b = 3 and 4 bits. It can be observed in Figure 11 for the InD-MO scenario, that by increasing the cluster size the throughput will improve and if we consider the effect of using more quantization bits the difference becomes more notorious. When the cluster size increases from 1 to 3, we can observe at 100 mW that the throughput doubles in both cases of quantization. If we consider the InD-OO scenario, the obtained gains present a similar behavior as the power increases but the throughput we can reach will be significatively lower. The difference between these two scenarios lies in the relative weight of the LOS and NLOS components, as the attenuation losses associated with them are the same in both scenarios. In the InD-MO scenario the P_{LOS} is 1 up to 1.2 m and decreases to 0.368 at 6.5 m.

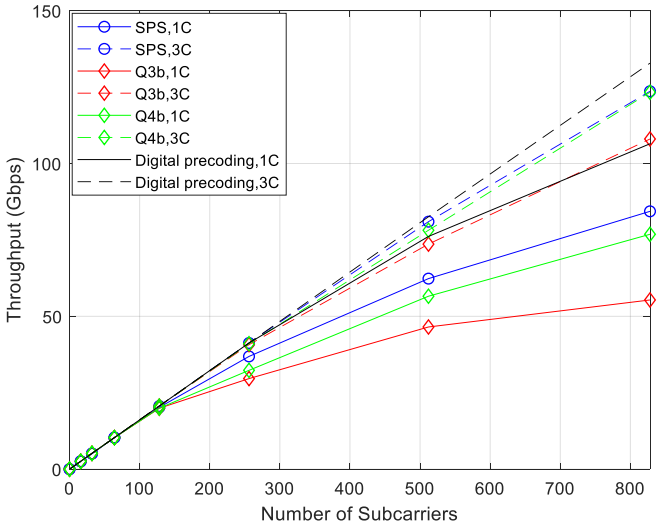

Figure 10. Throughput (Gbps) vs number of subcarriers for different versions of the algorithm (with and without quatization) and cluster sizes, considering the proposed precoder with N_{tx}=256, N_{rx}=4, $N_{RF}^{tx}=14$, N_s=2 and N_u=180 (only NLOS component).

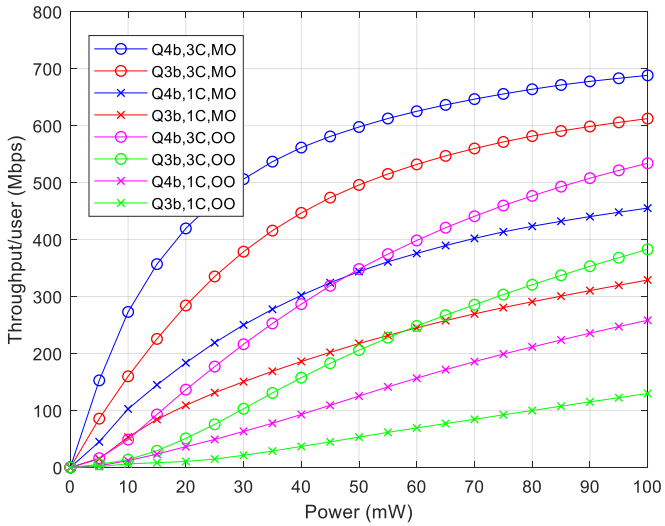

Figure 11. Throughput (Mbps) versus mean value of power required by each user (mW), considering the proposed precoder with N_{tx}=256, N_{rx}=4, $N_{RF}^{tx}=14$, N_s=2, F=828 and the quantization effect (with LOS component).

In the InD-OO scenario the P_{LOS} is 1 up until 5.0 m and decreases to 0.538 at 49.0 m. Knowing that the P_{NLOS} is equal to $1-P_{LOS}$, we realize that in the InD-MO scenario the weight of the NLOS component will be greater than that of the LOS component. Since the attenuation losses of NLOS are much higher than those of the LOS component, the received power of the APs decreases rapidly with distance. Therefore, in the case of the InD-OO scenario, the weight of the LOS component is greater than the one of the NLOS component, so the transmitted power of the APs decreases very slowly with distance generating a strong inter-site interference, which affects the maximum throughput and coverage that can be reached. Moreover, the channel can influence the results since with a stronger LOS component the multipaths (NLOS component) become weaker, which worsens the spatial multiplexing and the spatial diversity effects.

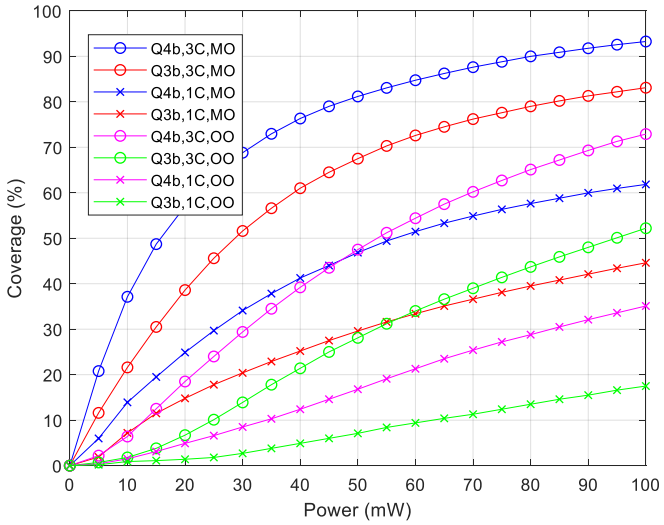

Figure 12. Coverage (%) versus mean value of power required by each user (mW), considering the proposed precoder with N_{tx}=256, N_{rx}=4, $N_{RF}^{tx}=14$, N_s=2, F=828 and the quantization effect (with LOS component).

Figure 12 exhibits a similar behaviour when compared to the previous figure, since the greater the cluster size and the number of quantization bits, the greater will be the achieved coverage. With 3 and 4 bits of quantization at 100 mW and when the cluster size increases from 1 to 3, we obtain a significant improvement which almost doubles the initial coverage. If we consider the InD-OO scenario, the obtained gains in terms of coverage present a similar behavior as the power increases but we can no longer obtain more than 73% of coverage (N_b=4 bits and 3C).

In order to understand the influence of the variation of the transmitted power (P_t) of the APs on the system-level simulation results, we considered two InD scenarios with the proposed precoder based on a DPS architecture with N_{tx}=256, N_{rx}=4, $N_{RF}^{tx}=14$, N_s=2 and F=828. In Table 3, we present the results of average throughput per user for both InD-OO and InD-MO scenarios when we vary the transmitted power (P_t) of each AP. We considered that $P_t \in \{10,100,1000\}$ mW. As expected, based on Figures 11 and 12, the performance of scenario MO is higher than OO due to less inter-cell interference. For the same reason cluster 3C presents higher performance than cluster 1C. We can check that independently of the scenario and cluster size there is an optimum value of P_t, which is 100 mW. The highest values of throughput occur for 100 mW. This value of P_t was considered in all system level simulation of this paper. It corresponds to the best tradeoff between transmitted power and inter-cell interference. For cluster size one (1C) and InD-OO, the performance with 10 mW tends to be higher than 1000 mW due to the high inter-interference of this cluster. However, for cluster size (3C) occurs the opposite because of lower inter-interference of this cluster.

Table 3. Influence of the variation of the transmitted power of the APs on the system results.

Transmitted Power (mW)	Cluster size	Average Throughput (Mbps)	
		MO	OO
10	1C	542.6	388.3
10	3C	725.6	648.2
100	1C	551.6	411.6
100	3C	733.4	662.8
1000	1C	526.3	376.3
1000	3C	722.3	665.8

To reduce the large performance loss due to the adoption of a simple AoSA architecture, we can allow the dynamic connection of more subarrays to each RF chain by adopting a DAoSA structure and study the impact of the use of SPS and

DPS architectures, from a system level perspective. The goal of these structures is to try to reach a compromise between fully connected structures which are more complex to implement (especially with a massive number of antennas) and AoSAs (L_{max}=1) which are lighter but typically suffer a large performance loss.

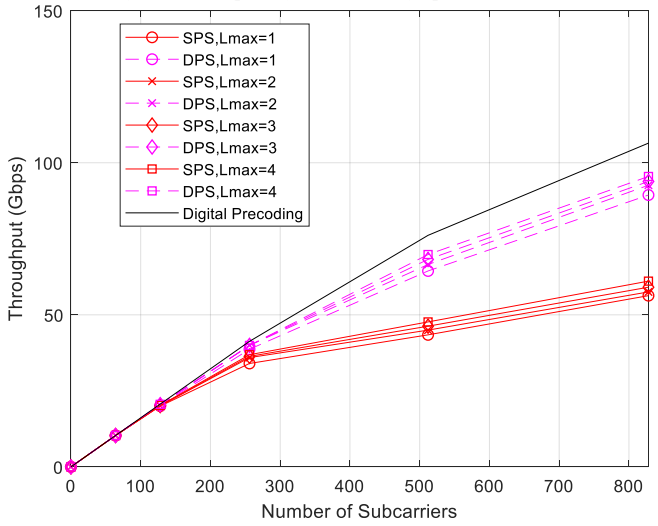

Figure 13. Throughput (Gbps) vs number of subcarriers for different versions of the algorithm (SPS or DPS) as a function of L_{max}, considering the proposed precoder with N_{tx}=256, N_{rx}=4, N_{RF}^{tx}=14 , N_s=2 and N_u=180 (with LOS component) and 1C.

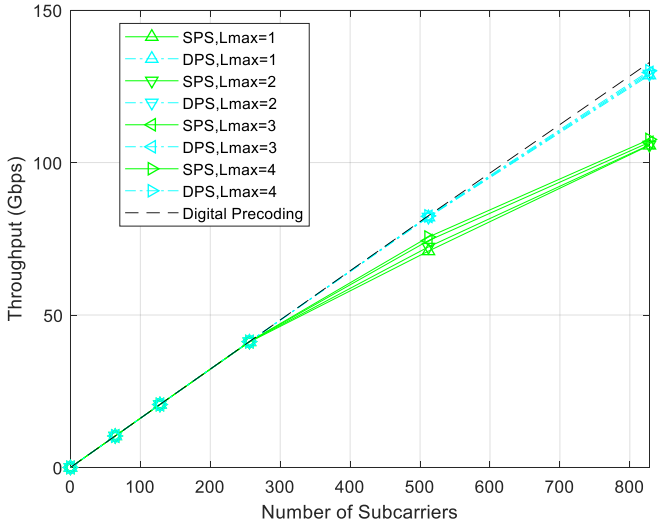

Figure 14. Throughput (Gbps) vs number of subcarriers for different versions of the algorithm (SPS or DPS) as a function of L_{max}, considering the proposed precoder with N_{tx}=256, N_{rx}=4, N_{RF}^{tx}=14 , N_s=2 and N_u=180 (with LOS component) and 3C.

It possible to conclude, through Figure 13 and Figure 14, that the performance of the system can be improved as the L_{max} increases. The use of DPS instead of using SPS architectures can provide higher throughputs but the difference between the gains tend to reduce when the cluster size increases. When we have 1C the gains of the DPS over the SPS can surpass 50% and with 3C we obtain gains around 20%. In general, by combining the increase in L_{max} with the adoption of DPS and the cluster size, it is possible to improve the results, but the gains become less pronounced for L_{max}>1. A performance close to the digital precoding can be achieved when considering the use of a DPS scheme for L_{max}=4 and a cluster size of 3. When compared to the cluster size 1C, with 3C it is observed that the throughput loss is lesser when adopting the hybrid schemes instead of the digital one.

4. Conclusions

In this paper we described a cloud radio access network aimed at operating at the mmWave/THz bands in beyond 5G systems where the access points support

multi-user MU-MIMO transmission using massive/ultra-massive antenna arrays. In order to make the implementation of this scheme feasible, low-complexity hybrid precoding based on several analog architectures, namely fully connected, array of subarrays and dynamic array of subarrays combined with single or double phase shifters, was considered. Numerical evaluation of both the link and system level for the proposed cloud radio access network downlink scheme integrated into a beyond 5G system showed that it is possible to obtain a performance close to the digital precoding when considering scenarios with a larger number of subcarriers and users. The use of partially connected architectures (array of subarrays and dynamic array of subarrays) when compared with fully connected structures tends to achieve good performances in terms of the trade-off between spectral efficiency and energy consumption.

Assessment of the cloud radio access network deployments in two indoor office scenarios at the THz band showed on the capability of achieving significant improvements in terms of throughput performance and coverage over typical cellular networks. Indoor-mixed office scenario provides higher throughput and coverage performances in comparison to the indoor-open office scenario independently of the cluster size, due to less inter-site interference. The variation of the transmitted power of the access points can impact the system results, since in order to obtain a better performance an optimal value of transmitted power around 100 mW must be considered. Furthermore, it was observed that the use of a larger cluster size, namely using 3C instead of 1C, tends to result in a lower throughput penalty when replacing a fully digital implementation by a lower complexity hybrid scheme (fully connected or dynamic array of subarrays).

Author Contributions: Conceptualization, J.P.P., A.C. and N.S.; methodology, J.P.P., A.C. and N.S.; software, J.P.P., A.C., V.V. and N.S.; validation, J.P.P., A.C., V.V., M.R., P.S. and N.S.; formal analysis, J.P.P., A.C., V.V., M.R., P.S. and N.S.; investigation J.P.P., A.C., V.V., M.R., P.S. and N.S.; resources, A.C., M. R., P.S. and N.S.; data curation, J.P.P. and A.C.; writing—original draft preparation J.P.P., A.C., V.V., M.R., P.S. and N.S.; writing—review and editing, J.P.P., A.C., V.V., M.R., P.S. and N.S.; visualization, J.P.P. and A.C.; supervision, A.C., M.R. and N.S.; project administration, A.C. and N.S.; funding acquisition, A.C. and N.S. All authors have read and agreed to the published version of the manuscript.

Funding: This work was supported by the FCT—Fundação para a Ciência e Tecnologia under the grant 2020.05621.BD. The authors also acknowledge the funding provided by FCT/MCTES through national funds and when applicable co-funded EU funds under the project UIDB/50008/2020.

Institutional Review Board Statement: Not applicable.

Informed Consent Statement: Not applicable.

Data Availability Statement: The data presented in this study are available on request from the corresponding author. The data are not publicly available due to privacy.

Conflicts of Interest: The authors declare no conflict of interest.

References

1. Dang, S.; Amin, O.; Shihada, B. and Alouini, M. S. "What should 6G be?," Nature Electronics 2020, 3, 1, 20–29.
2. Saad, W.; Bennis, M. and Chen, M. "A Vision of 6G Wireless Systems: Applications, Trends, Technologies, and Open Research Problems," *IEEE Network* **2020**, 34, 3, 134–142.
3. Akyildiz, I.F.; Kak, A.; Nie, S. 6G and Beyond: The Future of Wireless Communications Systems. *IEEE Access* **2020**, *8*, 133995–134030.
4. Sarieddeen, H.; Alouini, M.-S.; Al-Naffouri, T.Y. An Overview of Signal Processing Techniques for Terahertz Communications. *Proc. IEEE* **2021**, 1–38.
5. Lin, C.; Li, G.Y.L. Terahertz Communications: An Array-of-Subarrays Solution. *IEEE Commun. Mag.* **2016**, *54*, 124–131.
6. Faisal, A.; Sarieddeen, H.; Dahrouj, H.; Al-Naffouri, T.; Alouini, M. Ultramassive MIMO Systems at Terahertz Bands: Prospects and Challenges. *IEEE Vehicular Technology Magazine* **2020**, *15*, 33-42.
7. Castaneda, E.; Silva, A.; Gameiro, A.; Kountouris, M. An Overview on Resource Allocation Techniques for Multi-User MIMO Systems. *IEEE Commun. Surv. Tutor.* **2017**, *19*, 239–284.
8. Zu, K.; de Lamare, R.; Haardt, M. Generalized Design of Low-Complexity Block Diagonalization Type Precoding Algorithms for Multiuser MIMO Systems. *IEEE Trans. Commun.* **2013**, *61*, 4232–4242.
9. Lopes, P.; Gerald, J. Leakage-based precoding algorithms for multiple streams per terminal MU-MIMO systems. *Digit. Signal Process.* **2018**, *75*, 38–44.
10. Guerreiro, J.; Dinis, R.; Montezuma, P.; Marques da Silva, M. On the Achievable Performance of Nonlinear MIMO Systems. *IEEE Commun. Lett.* **2019**, *23*, 1725–1729.

11. Chataut, R.; Akl, R. Massive MIMO Systems for 5G and beyond Networks—Overview, Recent Trends, Challenges, and Future Research Direction. *Sensors* **2020**, *20*, 2753.
12. Yuan, H.; An, J.; Yang, N.; Yang, K.; Duong, T.Q. Low Complexity Hybrid Precoding for Multiuser Millimeter Wave Systems Over Frequency Selective Channels. *IEEE Trans. Veh. Technol.* **2018**, *68*, 983–987.
13. Liu, F.; Kan, X.; Bai, X.; Du, R.; Liu, H.; Zhang, Y. Hybrid precoding based on adaptive RF-chain-to-antenna connection for millimeter wave MIMO systems. *Phys. Commun.* **2020**, *39*, 100997.
14. Xu, K.; Cai, Y.; Zhao, M.; Niu, Y.; Hanzo, L. MIMO-Aided Nonlinear Hybrid Transceiver Design for Multiuser Mmwave Systems Relying on Tomlinson-Harashima Precoding. *IEEE Trans. Veh. Technol.* **2021**, *70*, 6943–6957.
15. Pavia, J.; Velez, V.; Ferreira, R.; Souto, N.; Ribeiro, M.; Silva, J.; Dinis, R. Low Complexity Hybrid Precoding Designs for Multiuser mmWave/THz Ultra Massive MIMO Systems. *Sensors* **2021**, *21*, 6054.
16. Payami, S.; Khalily, M.; Araghi, A.; Loh, T.; Cheadle, D.; Nikitopoulos, K.; Tafazolli, R. Developing the First mmWave Fully-Connected Hybrid Beamformer With a Large Antenna Array. *IEEE Access* **2020**, *8*, 141282-141291.
17. Loh, T.; Cheadle, D.; Payami, S.; Khalily, M.; Nikitopoulos, K.; Tafazolli, R. Experimental Evaluation of a Millimeter-wave Fully-Connected Hybrid Beamformer with a Large Antenna Array. In Proceedings of the 2021 15th European Conference on Antennas and Propagation (EuCAP), Dusseldorf, Germany, 22–26 March 2021.
18. Li, X.; Yu, J.; Wang, K.; Kong, M.; Zhou, W.; Zhu, Z.; Wang, C.; Zhao, M.; Chang, G. 120 Gb/s Wireless Terahertz-Wave Signal Delivery by 375 GHz-500 GHz Multi-Carrier in a 2 × 2 MIMO System. *Journal of Lightwave Technology* **2019**, *37*, 606-611.
19. Jia, S.; Zhang, L.; Wang, S.; Li, W.; Qiao, M.; Lu, Z.; Idrees, N.; Pang, X.; Hu, H.; Zhang, X.; Oxenlowe, L.; Yu, X. 2 × 300 Gbit/s Line Rate PS-64QAM-OFDM THz Photonic-Wireless Transmission. *Journal of Lightwave Technology* **2020**, *38*, 4715-4721.
20. Busari, S.; Huq, K.; Mumtaz, S.; Rodriguez, J. Terahertz Massive MIMO for Beyond-5G Wireless Communication. In Proceedings of the ICC 2019-2019 IEEE International Conference on Communications (ICC), Shanghai, China, 11–22 March 2019.
21. Akyildiz, I.F.; Han, C.; Hu, Z.; Nie, S.; Jornet, J.M. TeraHertz Band Communication: An Old Problem Revisited and Research Directions for the Next Decade. arXiv **2021**, arXiv: 2112.13187v1. Available online: https://arxiv.org/abs/2112.13187v1 (accessed on 2 July 2021).
22. Godinho, A.; Fernandes, D.; Soares, G.; Pina, P.; Sebastião, P.; Correia, A.; Ferreira, L.S. A Novel Way to Automatically Plan Cellular Networks Supported by Linear Programming and Cloud Computing. *Appl. Sci.* **2020**, *10*, 3072.
23. Jao, C.; Wang, C.-Y.; Yeh, T.-Y.; Tsai, C.-C.; Lo, L.-C.; Chen, J.-H.; Pao, W.-C.; Sheen, W., "WiSE: A System-Level Simulator for 5G Mobile Networks," in *IEEE Wireless Communications* **2018**, 25, 2, 4-7.
24. Riviello, D.G.; Di Stasio, F.; Tuninato, R. Performance Analysis of Multi-User MIMO Schemes under Realistic 3GPP 3-D Channel Model for 5G mmWave Cellular Networks. *Electronics* **2022**, 11, 330.
25. 3rd Generation Partnership Project (3GPP). TR 38.901 v14.1.1, Study on channel model for frequencies from 0.5 to 100 GHz, Release 14. July **2017**. Available online: www.3gpp.org/ftp/Specs/archive/38_series/38.901/38901-g10.zip (accessed on 01 November 2021).
26. Bechta, K.; Kelner, J.; Ziółkowski, C.; Nowosielski, L. Inter-Beam Co-Channel Downlink and Uplink Interference for 5G New Radio in mm-Wave Bands. *Sensors* **2021**, *21*, 793.
27. Zaidi, S., Ben Smida, O., Affes, S., Vilaipornsawai, U., Zhang, L. and Zhu, P. User-Centric Base-Station Wireless Access Virtualization for Future 5G Networks. *IEEE Transactions on Communications*. **2019**, *67*, *7*, 5190-5202.
28. Yuan, H.; Yang, N.; Yang, K.; Han, C.; An, J. Hybrid Beamforming for Terahertz Multi-Carrier Systems Over Frequency Selective Fading. *IEEE Trans. Commun.* **2020**, *68*, 6186–6199.
29. Yan, L.; Han, C.; Yuan, J. A Dynamic Array-of-Subarrays Architecture and Hybrid Precoding Algorithms for Terahertz Wireless Communications. *IEEE J. Sel. Areas Commun*. **2020**, 38, 2041–2056.
30. Han, C.; Yan, L.; Yuan, J. Hybrid Beamforming for Terahertz Wireless Communications: Challenges, Architectures, and Open Problems. *IEEE Wireless Communications* **2021**, *28*, 198-204.
31. Ning, B.; Zhongbao, T.; Chen, Z.; Han, C.; Yuan, J.; Li, S. TeraMIMO Prospective Beamforming Technologies for Ultra-Massive MIMO in Terahertz Communications: A Tutorial. arXiv **2021**, arXiv: 2107.03032v2. Available online: https://arxiv.org/abs/2107.03032v2 (accessed on 2 January 2022).
32. Basar, E.; Yildirim, I. SimRIS Channel Simulator for Reconfigurable Intelligent Surface-Empowered Communication Systems, 2020 IEEE Latin-American Conference on Communications (LATINCOM), online, 18–20 November 2020, pp. 1-6.
33. Ju, S.; Xing, Y.; Kanhere, O.; Rappaport, T. S. Millimeter Wave and Sub-Terahertz Spatial Statistical Channel Model for an Indoor Office Building. arXiv **2021**, arXiv:2103.17127v1. Available online: https://doi.org/10.48550/arXiv.2103.17127(accessed on 26 February 2022).
34. Yu, X., Zhang, J. and Letaief, K., "Alternating minimization for hybrid precoding in multiuser OFDM mmWave systems", 2016 50th Asilomar Conference on Signals, Systems and Computers, Pacific Grove, CA, USA, 6–9 November 2016.
35. Yu, X., Zhang, J. and Letaief, K. B., "Doubling Phase Shifters for Efficient Hybrid Precoder Design in Millimeter-Wave Communication Systems", Journal of Communications and Information Networks **2019**, 4, pp. 51-67.

Chapter 6 – Conclusions and Future Work

In this chapter, a brief summary containing the main conclusions and possible work extensions are presented.

6.1. Summary

This thesis aimed to propose and to evaluate solutions to enable ultra-high-speed wireless communications in the THz band. Considering this main goal, three types of approaches were explored, covering the design of devices, the IM based schemes for B5G networks and the hybrid precoding designs for THz UM–MIMO systems.

As a result of this work, several contributions have been made and demonstrated in each of previously mentioned research areas, through models, methodologies or improvements. Considering the compelling need for new ways of producing sources, detectors and other devices such as filters, sensors and modulators for the THz domain, a reconfigurable THz filter design, using frequency selective structures based on metamaterial resonators was presented in chapter 2. By combining two arrays of gold wires, the proposed filter can provide greater cancellation of harmonics, higher dynamic range and enhanced frequency selectivity. Due to its simplicity and ease of control of energy transmission and reflection (which results from the careful tuning between the wire radius and the distance between wires), this filter design is especially suited for the implementation of reconfigurable THz filters and optical modulators, since it transits from situations in which it presents a full transparency ($|S_{11}|=0$) for a full opacity ($|S_{11}|=1$). Moreover, this approach can also be used for the implementation of STAR RIS.

Considering the expected requirements such as the SR, SE and EE for the next generation of wireless communications, a novel MIMO system where GSM symbols are transmitted simultaneously to multiple users was proposed in chapter 3. This approach is capable of improving the SE and EE, exploiting large antenna settings at the BS combined with high-order M-QAM constellations. In order to remove the inter-user interference a precoder is applied at the BS, while a reduced complexity iterative SU GSM detector is implemented at each receiver. We found, through simulation results, that our approach can achieve a very competitive and very promising performance compared to conventional MU-MIMO systems with identical SE, since system-level assessment showed potential gains of up to 155% in throughput and 139% in coverage when compared to traditional cellular networks, for a system with N_a=2 active indexes, N_{sc}=256

subcarriers, N_u=15 users, N_{tx}=17 transmission antennas/user, N_{rx}=16 reception antennas/user and 100% of transmitted power for all QAM constellations (assuming clustering where the network is partitioned into three adjacent RRU sets and each user is served by three RRUs).

Overcoming some of the limitations of the THz that can affect the system performance, requires not only a proper system design but also the definition of a set of strategies to enable communications. Considering this situation in chapter 4, an iterative algorithm for hybrid precoding design, which is suitable for multiuser UM-MIMO systems operating in mmWave and THz bands, was presented. This proposal is based on the approximation of the fully-digital approach whose problem formulation is split into a sequence of smaller subproblems with closed-form solutions and can function with a broad range of configuration of antennas, RF chains and data streams. The adaptability of the algorithm to different architectures can be achieve due to the separability of the design process, making it suitable for implementation with low-complexity AoSA and DAoSA structures. This kind of architectures are crutial for the deployment of UM-MIMO in hardware-constrained THz systems. Through our numerical study, we found out that good trade-offs between SE and hardware implementation complexity can be achieved for several different architectures. In fact, when considering the use of architectures based on DAoSAs, it is possible to reduce considerably the amount of power that is consumed at the precoder. Aditionally, we showed that it was possible to reduce the amount of consumed power up to 55% if we consider a precoder scheme based on DAoSAs with DPS and L_{max} = 4 versus an FC structure based on UPS with only a small performance penalty, for a reference scenario. Moreover, this reduction increases to 73% if the DPS structure is replaced by an SPS one. Based on the work developed and described on the previous chapter, in chapter 5 we presented a system-level assessment of low complexity hybrid precoding designs for massive MIMO downlink transmissions in B5G networks. A virtualized C-RAN, where the network determines which APs are to be associated with each terminal, was considered. We assumed that the cell was moving according to the terminal in order to provide a centre-cell experience across the network. Each UE was served by its preferred set of APs. The effective server set for a UE could contain one or several APs and the terminal data was partially or fully available in a cluster with potential server APs. Based on the previous assumptions, the AP controller was assumed to accommodate each UE with its cluster as well as the preferred

transmission mode in each communication instance, while considering the load and CSI knowledge associated with the cluster of APs. We showed that it is possible to obtain a performance close to the digital precoding when considering scenarios (with and without LoS component) with a large number of subcarriers and users, based on our numerical system level study for the proposed C-RAN downlink scheme integrated into a B5G system. The system performance was studied considering several hybrid architectures, such as fully connected, AoSAs (SPS and DPS) and DAoSAs. The impact of quantized phases shifter in the hybrid architectures was analyzed in two indoor office scenarios at the THz band, which were considered for the assessment of the C-RAN deployments. In both cases, the capability of achieving significant improvements in terms of throughput performance and coverage over typical cellular networks was verified. In general, the InD-MO scenario can deliver higher throughput and coverage performances in comparison to the InD-OO scenario independently of the cluster size, due to lower inter-site interference. We also found out that the variation of the transmitted power of the APs can impact the system results, since in order to obtain a better performance an optimal value of transmitted power of around 100 mW must be considered. This value corresponds to the best trade-off between transmitted power and inter-cell interference in the considered scenario. Furthermore, it was observed that the use of a larger cluster size, namely, using 3C instead of 1C, tends to result in a lower throughput penalty when replacing a fully digital implementation by a lower complexity hybrid scheme, namely, a FC or DAoSA.

In conclusion, several directions can be followed to provide solutions to the underlying problems of the THz band and this work aimed to provide some answers to them. Still, much remains to be done to make this type of communications feasible in the near future.

6.2. Future Work

This work has left several research topics that can be explored in the near future. Considering the research presented in this thesis, some improvements can be made to add even more value to this work, such as:

- Develop more accurate device models for the THz so that they can be used in the evaluation of communication schemes more realistically - the development of devices for the THz is a field that presents a wide range of possibilities. However,

more accurate device models for THz communications are still needed and their integration in communication schemes must be evaluated;

- Adoption of the proposed reconfigurable THz filter as base element for the implementation of STAR RIS - STAR RIS is a novel concept, which consists on the capability of the surface in reflecting and transmitting the incident wireless signal. Despite the potential of this new paradigm, new designs and otimization procedures are required to enable a full-space manipulation of the signal propagation for the communication schemes. The accomplishment of this task using the proposed reconfigurable THz filters may allow us to reach high throughput gains and good system performances;
- Proposal of new THz communication schemes incorporating the concept of RIS-based IM [61] - considering the work within the scope of IM and the recent trends in this field encompassing RIS, it would be interesting to explore new communication schemes. Problems associated with the reflection/scattering characteristics of the incident waves in these structures could be solved in order to improve the signal quality at the receiver as well as the spectral efficiency of the systems;
- Design of UM-MIMO THz transceiver schemes based on RIS, exploiting low complexity hybrid precoding architectures for MU scenarios - as it was mentioned on the first chapter, in order to compensate the propagation losses that occur at high frequencies, UM-MIMO can be used for high array gains by beamforming. However, since a large number of analogue phase shifters are required to perform analogue beamforming, THz communication encompassing UM-MIMO will have a considerably higher power consumption. In line with this issue, it would be interesting to propose and to evaluate a solution that can allow the replacement of those phase shifters by an energy efficient RIS to perform the analog beamforming of the hybrid precoding.

References

[1] ANACOM, "COVID-19 - Electronic communications traffic continues to rise and increase in relation to the previous week," 07 04 20220. [Online]. Available: https://www.anacom.pt/render.jsp?contentId=1521663. [Accessed 03 02 2022].

[2] ANACOM, "BEREC and European Commission release joint statement on traffic increase due to the COVID-19," 19 03 2020. [Online]. Available: https://www.anacom.pt/render.jsp?contentId=1519528. [Accessed 03 02 2022].

[3] ANACOM, "Voice and mobile internet traffic grows in 2020," 04 03 2021. [Online]. Available: https://www.anacom.pt/render.jsp?contentId=1603502. [Accessed 03 02 2022].

[4] ANACOM, "Fixed broadband Internet traffic grows a record 62.5%," 09 03 2021. [Online]. Available: https://www.anacom.pt/render.jsp?contentId=1603721. [Accessed 03 02 2022].

[5] ANACOM, "COVID-19 led to faster growth of over-the-top services," 17 01 2022. [Online]. Available: https://www.anacom.pt/render.jsp?contentId=1714063. [Accessed 03 02 2022].

[6] C. Wang, F. Haider, X. Gao, X. You, Y. Yang, D. Yuan, H. Aggoune, H. Haas, S. Fletcher and E. Hepsaydir, "Cellular architecture and key technologies for 5G wireless communication networks," *IEEE Communications Magazine,* vol. 52, no. 2, p. 122–130, 2014.

[7] M. H. Alsharif, M. A. M. Albreem, A. A. A. Solyman and S. Kim, "Toward 6G Communication Networks: Terahertz Frequency Challenges and Open Research Issues," *Computers, Materials & Continua,* vol. 66, pp. 2831-2842, 2021.

[8] I. F. Akyildiz, J. M. Jornet and C. Han, "Terahertz band: Next frontier for wireless communications," *Physical Communication,* vol. 12, p. 16–32, 2014.

[9] S. Mumtaz, J. M. Jornet, J. Aulin, W. H. Gerstacker, X. Dong and B. Ai, "Terahertz Communication for Vehicular Networks," *IEEE Transactions on Vehicular Technology,* vol. 66, no. 7, pp. 5617-5625, 2017.

[10] I. F. Akyildiz, S. Nie, S. Lin and M. Chandrasekaran, "5G roadmap: 10 key enabling technologies," *Computer Networks,* vol. 106, p. 17–48, 2016.

[11] H. Elayan, O. Amin and R. M. a. A. M. Shubair, "Terahertz communication: The opportunities of wireless technology beyond 5G," in *2018 International Conference on Advanced Communication Technologies and Networking (CommNet)*, Marrakech, 2018.

[12] H. Elayan, O. Amin, B. Shihada, R. Shubair and M. Alouini, "Terahertz Band: The Last Piece of RF Spectrum Puzzle for Communication Systems," *IEEE Open Journal of the Communications Society,* vol. 1, pp. 1-32, 2020.

[13] B. Ferguson and X. Zhang, "Materials for terahertz science and technology," *Nature Materials,* vol. 1, no. 1, pp. 26-33, 2002.

[14] S. Fathololoumi, E. Dupont, Z. Wasilewski, C. Chan, S. Razavipour, S. Laframboise, S. Huang, Q. Hu, D. Ban and H. Liu, "Effect of oscillator strength and intermediate resonance on the performance of resonant phonon-based

terahertz quantum cascade lasers," *Journal of Applied Physics,* vol. 113, no. 11, pp. 113109-1-113109-17, 2013.

[15] T. Akalin, "Terahertz sources: Powerful photomixers," *Nature Photonics,* vol. 6, pp. 81-81, 2012.

[16] M. Tonouchi, "Cutting-edge terahertz technology," *Nature Photonics,* vol. 1, pp. 97-105, 2007.

[17] S. Komiyama, "Single-photon detectors in the terahertz range," *IEEE Journal of Selected Topics in Quantum Electronics,* vol. 17, p. 54–66, 2011.

[18] J. Neu, B. Krolla, O. Paul, B. Reinhard, R. Beigang and M. Rahm, "Metamaterial-based gradient index lens with strong focusing in the thz frequency range," *Optics Express,* vol. 18, p. 27748–27757, 2010.

[19] O. Paul, R. Beigang and M. Rahm, "Highly selective terahertz bandpass filters based on trapped mode excitation," *Optics Express,* vol. 17, p. 18590–18595, 2009.

[20] X. Zhang and Z. Liu, "Superlenses to overcome the diffraction limit," *Nature Materials,* vol. 7, p. 435–441, 2008.

[21] R. Shelby, D. Smith and S. Schultz, "Experimental Verification of a Negative Index of Refraction," *Science,* vol. 292, no. 5514, pp. 77-79, 2001.

[22] K. Kanté, D. Germain and A. de Lustrac, "Experimental demonstration of a nonmagnetic metamaterial cloak at microwave frequencies," *Physical Review B,* vol. 80, no. 20, pp. 201104-201108, 2009.

[23] N. Kundtz, D. Smith and J. Pendry, "Electromagnetic design with transformation optics," *Proceedings of the IEEE,* vol. 99, pp. 1622-1633, 2011.

[24] M. Ribeiro and C. Paiva, "Transformation and moving media: a unified approach using geometric algebra," in *Nato Science Series: Metamaterials and Plasmonics: Fundamentals, Modelling and Applications*, Dordrecht, Springer, 2009, p. 63–74.

[25] M. Ribeiro and C. Paiva, "An equivalence principle for electromagnetics through Clifford's geometric algebras," *Metamaterials,* vol. 2, p. 77–91, 2008.

[26] T. Yen, W. Padilla, N. Fang, D. Vier, D. Smith, J. Pendry, D. Basov and X. Zhang, "Terahertz magnetic response from artificial materials," *Science,* vol. 303, no. 5663, pp. 1494-1496, 2004.

[27] H. Chen, S. Palit, T. Tyler, C. Bingham, J. Zide, J. OHara, D. Smith, A. Gossard, R. Averitt, W. Padilla, N. Jokerst and A. Taylor, "Hybrid metamaterials enable fast electrical modulation of freely propagating terahertz waves," *Applied Physics Letters,* vol. 93, p. 091117–091119, 2008.

[28] H. Chen, W. Padilla, J. Zide, S. Bank, A. Gossard, A. Taylor and R. Averitt, "Ultrafast optical switching of terahertz metamaterials fabricated on eras/gaas nanoisland superlattices," *Optics Letters,* vol. 32, no. 12, pp. 1620-1622, 2007.

[29] I. F. Akyildiz, C. Han and S. Nie, "Combating the Distance Problem in the Millimeter Wave and Terahertz Frequency Bands," *IEEE Communications Magazine,* vol. 56, no. 6, pp. 102-108, 2018.

[30] M. Saad, F. Bader, J. Palicot, A. Al Ghouwayel and H. Hijazi, "Single Carrier with Index Modulation for Low Power Terabit Systems," in *2019 IEEE Wireless Communications and Networking Conference (WCNC)*, Marrakech, Morocco, 2019.

[31] D. Li, D. Qiao and L. Zhang, "Achievable Rate of Indoor THz Communication Systems with Finite-Bit ADCs," in *2018 10th International Conference on Wireless Communications and Signal Processing (WCSP)*, Hangzhou, China, 2018.

[32] N. Ishikawa, S. Sugiura and L. Hanzo, "50 Years of Permutation, Spatial and Index Modulation: From Classic RF to Visible Light Communications and Data Storage," *IEEE Communications Surveys & Tutorials*, vol. 20, no. 3, pp. 1905-1938, 2018.

[33] H. Lopes and N. Souto , "Iterative Signal Detection for Large-Scale GSM-MIMO Systems," *IEEE Transactions on Vehicular Technology*, vol. 67, no. 8, pp. 7734 - 7738, 2018.

[34] K. Huq, S. Busari, J. Rodriguez, V. Frascolla, W. Bazzi and D. Sicker, "Terahertz-Enabled Wireless System for Beyond-5G Ultra-Fast Networks: A Brief Survey," *IEEE Network* , vol. 33, no. 4, pp. 89-95, 2019.

[35] T. Raddo, S. Rommel, B. Cimoli, C. Vagionas, D. Perez-Galacho, E. Pikasis, E. Grivas, K. Ntontin, M. Katsikis, D. Kritharidis, E. Ruggeri, I. Spaleniak, M. Dubov, D. Klonidis, G. Kalfas, S. Sales, N. Pleros and I. Tafur Monroy, "Transition technologies towards 6G networks," *EURASIP Journal on Wireless Communications and Networking*, vol. 1, no. 100, pp. 1-22, 2021.

[36] S. Zaidi, O. Ben Smida, S. Affes, U. Vilaipornsawai, L. Zhang and P. Zhu, "User-Centric Base-Station Wireless Access Virtualization for Future 5G Networks," *IEEE Trans. Commun.*, vol. 67, p. 5190–5202, 2019.

[37] D. Riviello, F. Di Stasio and R. Tuninato, "Performance Analysis of Multi-User MIMO Schemes under Realistic 3GPP 3-D Channel Model for 5G mmWave Cellular Networks," *Electronics*, vol. 11, no. 3, pp. 330-358, 2022.

[38] C. Jao, C. Wang, T. Yeh, C. Tsai, L. Lo, J. Chen, W. Pao and W. Sheen, "WiSE: A System-Level Simulator for 5G Mobile Networks," *IEEE Wireless Communications*, vol. 25, no. 4-7, 2018.

[39] N. Souto, J. Silva, J. P. Pavia and M. Ribeiro, "An alternating direction algorithm for hybrid precoding and combining in millimeter wave MIMO systems," *Physical Communication*, vol. 34, pp. 165 - 173, 2019.

[40] J. Pavia, N. Souto and M. Ribeiro, "Design of a Reconfigurable THz Filter Based on Metamaterial Wire Resonators with Applications on Sensor Devices," *Photonics*, vol. 7, no. 3, pp. 48-69, 2020.

[41] J. Pavia, V. Velez, B. Brogueira, N. Souto and A. Correia, "Precoded Generalized Spatial Modulation for Downlink MIMO Transmissions in Beyond 5G Networks," *Applied Sciences*, vol. 10, no. 18, pp. 6617-6636, 2020.

[42] V. Velez, J. Pavia, N. Souto, P. Sebastião and A. Correia, "A generalized space-frequency index modulation scheme for downlink MIMO transmissions with improved diversity," *IEEE Access*, vol. 9, pp. 118996-119009, 2021.

[43] J. Pavia, V. Velez, . R. Ferreira, N. Souto, M. Ribeiro, J. Silva and R. Dinis, "Low Complexity Hybrid Precoding Designs for Multiuser mmWave/THz Ultra Massive MIMO Systems," *Sensors*, vol. 21, no. 18, pp. 6054-6080, 2021.

[44] J. Praia, J. Pavia, N. Souto and M. Ribeiro, "Phase Shift Optimization Algorithm for Achievable Rate Maximization in Reconfigurable Intelligent Surface Assisted THz Communications," *Electronics*, vol. 11, no. 1, pp. 18-33, 2021.

[45] V. Velez, J. Pavia, C. Rita, C. Gonçalves, N. Souto, P. Sebastião and A. Correia, "System-Level Assessment of a C-RAN based on Generalized Space-Frequency Index Modulation for 5G New Radio and Beyond," *Applied Sciences,* vol. 12, no. 3, pp. 1592-1616, 2022.

[46] J. Pavia, V. Velez, N. Souto, M. Ribeiro, P. P. Sebastião and A. Correia, "System-Level Assessment of Low-Complexity Hybrid Precoding Designs for Downlink MIMO Transmissions for 5G New Radio and Beyond," *Applied Sciences,* vol. 12, no. 6, pp. 2812-2835, 2022.

[47] J. Pavia, N. Souto, M. Ribeiro, J. Silva and R. Dinis, "Hybrid Precoding and Combining Algorithm for Reduced Complexity and Power Consumption Architectures in mmWave Communications," in *2020 IEEE 91st Vehicular Technology Conference (VTC2020-Spring)*, Virtual Edition, 2020.

[48] B. Brogueira, J. Pavia, N. Souto and A. Correia, "Precoder and Combiner Design for Generalized Spatial Modulation based Multiuser MIMO Systems," in *2020 23rd International Symposium on Wireless Personal Multimedia Communications (WPMC)*, Virtual Edtition, 2020.

[49] D. Akbar, H. Altan, J. Pavia, M. Ribeiro, A. Sahin and C. Sarikaya, "Development of Stand- Off Imaging Systems using Low-Cost Plasma Detectors that Work in the GHz to THz range," in *Terahertz (THz), Mid Infrared (MIR) and Near Infrared (NIR) Technologies for Protection of Critical Infrastructures Against Explosives and CBRN, NATO Science for Peace and Security Series B: Physics and Biophysics*, Dordrecht, Springer, 2021, pp. 275-285.

[50] J. Pavia, M. Ribeiro and N. Souto, "Design of Frequency Selective Devices for the THz Domain with Applications on Structural Health Monitoring," in *2019 Thirteenth International Congress on Artificial Materials for Novel Wave Phenomena (Metamaterials)*, Rome, Italy, 2019.

[51] X. Mu, Y. Liu, L. Guo, J. Lin and R. Schober, "Simultaneously Transmitting And Reflecting (STAR) RIS Aided Wireless Communications," *IEEE Transactions on Wireless Communications,* 2021.

[52] N. H. Farhat and N. S. Kopeika, "A Low-Cost Millimeter-Wave Glow-Discharge Detector," *IEEE,* 1972.

[53] A. Abramovich and E. Farber, "Terahertz detection mechanism of inexpensive sensitive glow discharge detector," *J. Appl. Phys.,* vol. 103, p. 093306, 2008.

[54] N. Alasgarzade, T. Takan, I. U. Uzun-Kaymak, A. B. Sahin and H. Altan, "Modulation and frequency response of GDDs in the millimeter wave/THz region," in *Proc. SPIE*, 2015.

[55] W. Yuan, N. Wu, A. Zhang, X. Huang, Y. Li and L. Hanzo, "Iterative Receiver Design for FTN Signaling Aided Sparse Code Multiple Access," *IEEE Trans. Wirel. Commun.,* vol. 19, p. 915–928, 2020.

[56] X. Cheng, M. Zhang, M. Wen and L. Yang, "Index Modulation for 5G: Striving to Do More with Less," *IEEE Trans. Wirel. Commun.,* vol. 25, p. 126–132, 2018.

[57] A. Correia, N. Souto, P. Sebastiao, D. Gomez-Barquero and M. Fuentes, "Broadcasting Scalable Video with Generalized Spatial Modulation in Cellular Networks," *IEEE Access ,* vol. 8, p. 22136–22144, 2020.

[58] S. D. Tusha, A. Tusha, E. Basar and H. Arslan, "Multidimensional index modulation for 5G and beyond wireless networks," *Proc. IEEE,* vol. 109, no. 2, p. 170–199, 2021.

[59] I. Akyildiz, A. Kak and S. Nie, "6G and Beyond: The Future of Wireless Communications Systems," *IEEE Access*, vol. 8, pp. 133995-134030, 2020.

[60] A. Faisal, H. Sarieddeen, H. Dahrouj, T. Al-Naffouri and M. Alouini, "Ultramassive MIMO Systems at Terahertz Bands: Prospects and Challenges," *IEEE Vehicular Technology Magazine* , vol. 15, no. 4, pp. 33-42, 2020.

[61] E. Basar, "Reconfigurable Intelligent Surface-Based Index Modulation: A New Beyond MIMO Paradigm for 6G," *IEEE Transactions on Communications*, vol. 68, pp. 3187-3196, 2020.

[62] M. Saad, F. Bader, J. Palicot, A. C. Al Ghouwayel and H. Hijazi, "Single Carrier with Index Modulation for Low Power Terabit Systems," in *2019 IEEE Wireless Communications and Networking Conference (WCNC)*, Marrakech, Morocco, 2019.